Plasmonic enhanced pyroelectrics for microfluidic manipulation

Olurotimi Esan

September 2016

A thesis submitted to the

Division of Biomedical Engineering

School of Engineering

University of Glasgow

In fulfilment of the requirements for

The Degree of Doctor of Philosophy

Abstract

Plasmon enhanced micromanipulation addresses some of the drawbacks associated with more traditional optical based methods, particularly in regard to the nature of laser excitation required for actuation. The resonant electromagnetic field enhancement observed as a result of the plasmon resonance phenomenon, enables trapping of nanoscale objects, and reduces the risk of photoinduced sample damage by reducing excitation power required for trapping. Plasmon resonance introduces an unavoidable heating effect which hinders stable trapping in microfluidic environments as a result of phenomena such as convection. In this work, the heating associated with plasmon resonance is used constructively, to devise a new micromanipulation technique. Plasmonic nanostructures are patterned on pyroelectric substrates which create an electric field in response to changes in temperature. This electric field results in the generation of local and global electrokinetic phenomena which are used in high throughput trapping of suspended particles. To demonstrate the versatility of this technique, particles are patterned into arbitrary shapes. A suggested application for this technique is as an optically controlled photoresist free lithographic method for use in microfluidic environments

Table of Contents

List of Tables

List of Figures

Acknowledgements

I would like to thank Prof. Jon Cooper for the opportunity to perform this research in his group and for his supervision throughout the project. I would also like to thank Dr. Alasdair Clark for further supervision.

For their assistance and discussion, I would like to thank Dr. Andrew Glidle, Dr. Rab Wilson, Dr. Julien Reboud and Dr. Steven Neale. Thanks also go to the technical staff of the JWNC.

Finally, I would like to thank my friends and family for their support and encouragement.

Author's Declaration

The work presented in this thesis was conducted by the author and has not previously been submitted for a degree or diploma at this university or any other institution.

Glossary

AOT: Aerosol-OT

CAD: Computer aided design

CCD: Charge-coupled device

DC: Direct current

DCVJ: 9-(2,2-Dicyanovinyl) julolidine

DEP: Dielectrophoresis

DMABN: Dimethlyamino benzonitrile

DNA: Deoxyribonucleic acid

EHD: Electrohydrodynamic

EP: Electrophoresis

ET: Electrothermal

ETF: Electrothermal flow

EWF: Extra wide field

FEM: Finite element modelling

FFT: Fast Fourier transform

FWHM: Full width at half maximum

GDS: Graphic data systems

HFE: Hydrofluoroether

IPA: Isopropyl alcohol

IR: Infrared

ITO: Indium tin oxide

LN: Lithium niobate

LSPR: Localised surface plasmon resonance

LUT: Lookup table

MIBK: Methyl-isobutyl ketone

MSD: Mean squared displacement

NA: Numerical aperture

PMMA: Polymethyl methacrylate

PVA: Polyvinyl alcohol

PVDF: Polyvinylidene fluoride

RC: Resistor-capacitor

SEM: Scanning electron microscopy

SERS: Surface enhanced Raman spectroscopy

SLM: Spatial light modulator.....

SPP: Surface plasmon polaritons .....

SPR: Surface plasmon resonance.....

TICT: Twisted intramolecular charge transfer .....

UHR: Ultra high resolution.....

UV-VIS: Ultraviolet-visible.....

VRU: Variable resolution unit .....

1 Introduction

Summary

This chapter presents a brief introduction to optically induced manipulation techniques and discusses how the plasmonic effect is currently used to improve aspects of their operation. Drawbacks of current plasmon-assisted optical manipulation are also discussed as a means of elucidating the background leading to the development of a plasmon assisted pyroelectric manipulation technique.

1.1 Optically induced manipulation

1.1.1 Optical tweezing

Optically induced micromanipulation makes use of photonic forces (directly or indirectly) to control the motion of trapped objects. The ability to use light for the kinetic control of particles is of interest in the field of nano/microtechnology in general, and bio-engineering specifically. Optical manipulation confers the ability, due to the length scale of light, to perform complex actuation, which would otherwise not be possible using purely mechanical constructs. In addition, the actuation by its nature is temporary and reconfigurable, creating the possibility of programmable operations. Optical traps can be used as a means for elucidating the dynamics of nanoscale interactions. This technique has been useful in highlighting the operation of various biological systems (e.g. protein and DNA unfolding [1], [2], determination of single molecule dynamics [3], [4]).

The invention of the laser enabled investigations into optically induced micromanipulation. Prior to this, the radiation pressure of light had been predicted theoretically by Maxwell. This hypothesis was later experimentally verified independently by Lebedev [5], [6], and Nichols and Hull [5],[7], using thermal light sources. The observed effects of radiation pressure held little practical application without the ability to focus light to micrometric scales. In 1986, Arthur Ashkin and collaborators were able to reliably control the motion and confinement of microparticles in their single beam gradient force trap (latterly known as optical tweezers) [8]. Its operation can be explained by taking a ray optics approach (illustrated in Figure 1.1) to the interaction between light and particles (a sphere is considered for simplicity [9]). Light rays are refracted by the sphere, indicating a transfer in momentum from the sphere to the ray. Using classical mechanics

arguments (specifically Newton's third law), it can be shown that photons from the light rays transfer an equal amount of momentum to the sphere. The gradient in intensity creates a transverse optical force directed towards the centre of the light beam. A similar explanation can be made for an optical force acting in the axial plane (with additional consideration for the scattering force caused by the mismatch between the sphere and the suspension medium).

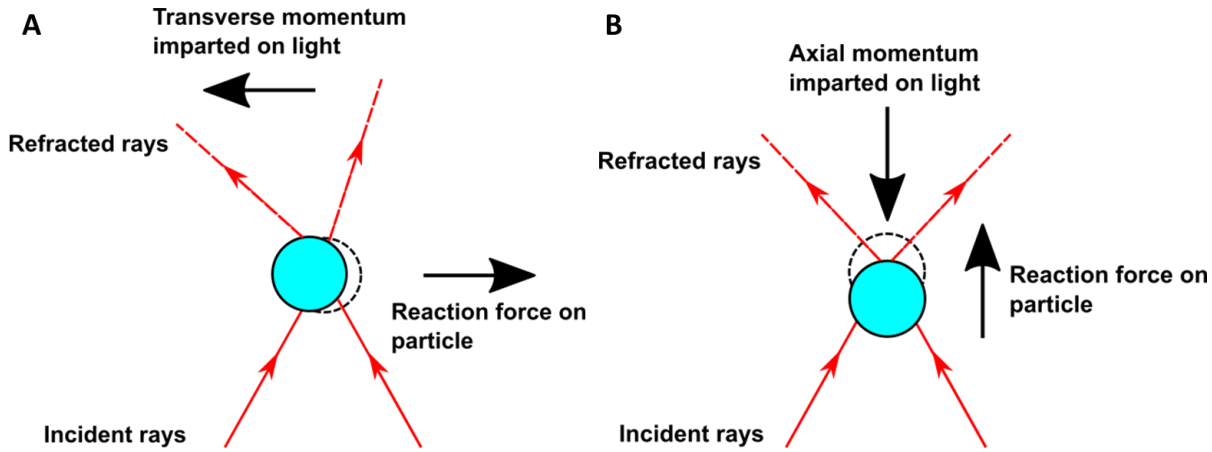

Figure 1.1: Ray optics origin of optical tweezing phenomenon adapted from [9]**. A) Transverse force on particle in an optical trap. B) Axial force on particle in an optical trap**

Stable trapping with optical tweezers requires a balance between the aforementioned gradient forces (which act in the direction of the laser beam's focus) and scattering forces (which act in the direction of laser beam propagation). The practical considerations for achieving this balance highlight a limitation of the technique: an objective with a large numerical aperture is necessary to create sufficiently strong gradient forces for trapping. The strong focussing creates a high intensity laser beam risking heat induced damage of materials (opticution), particularly when the wavelength of the exciting laser matches the peak absorption wavelength of the trapped material [10]. This drawback more acutely affects control of biological materials. In addition, there is limited scope for high throughput manipulation of multiple particles. Though it is possible to multiplex a laser beam for simultaneous trapping of particles, the methods used to achieve this multiplexing greatly impact the efficiency of the trapping mechanism. For instance, though spatial light modulators have been used to trap distinct particles in separate locations (holographic optical tweezers) [11], the number of traps cannot be increased arbitrarily without reducing their stiffness. Though it is possible to increase the input laser power, this again cannot be done indiscriminately as thermal breakdown of the SLM is risked. Similar limitations are noticed when multiplexing is achieved by rapidly cycling through a discrete set of trap locations (i.e. time-averaged multiplexing) [12]. In this case, the time spent away from the traps has to be less than

the time it takes for the particle to diffuse from its trapped location, a constraint which becomes more difficult to achieve when the distance the laser travels increases [9], [12], [13](i.e. the distance between two traps increases or the number of trap locations the laser visits becomes too great).

1.1.2 Optically assisted trapping

Indirect optical manipulation techniques were created largely in response to some of the limitations of optical tweezers. In optically assisted trapping schemes, light acts as an intermediary operator for the actual kinetic driver. As a consequence, the constraints on the nature of the light beam (i.e. strongly focussed, high intensity) can be relaxed; the light needs only be intense enough to induce enough of a secondary response to control particle movement.

A simple example of this principle is the use of thermally induced forces for the transportation of particles. Using the photothermal effect, (i.e. absorption of light in a material leads to heat generation) thermal gradients can be generated in a microfluidic environment. The nature of these thermal gradients can subsequently be used to control particle motion in different ways. Thermally induced density/buoyancy instabilities can be used to generate convection for the long range transportation of particles [14]–[16]. Thermophoresis (or the Soret effect) has been used to trap particles by creating inhomogeneous thermal fields in a microfluidic medium [17]. Particles tend to diffuse from high to low temperature regions. This tendency is a result of thermodynamics as the system increases its entropy in its approach to an equilibrium state. The diffusion process is a result of collisions between particles and the molecules of the suspending medium. Thus, through careful control of thermal gradients, enhancement or depletion of particles can be achieved [15], [18]. By inhomogeneously exciting particles, or engineering Janus particles, which have faces with differing thermal properties [19], thermal gradients can be created on the particle rather than in the fluid. Using this kind of excitation, particles can be attracted or repelled from the light source. Photothermally induced viscosity gradients can also be used for controlling fluid flow in microfluidics, or alternatively, the mass transport of various microparticles [20], [21]. The nature of the thermal properties exploited means that complex operations (e.g. separation of distinct populations of colloidal objects) can be difficult to control, as the physical phenomena operate on the bulk fluid as opposed to individual particles.

Optically assisted electrokinetics provides a good balance between the flexibility achieved with optical tweezing, and high-throughput seen with classical electrokinetic systems. In contrast to optical and photothermal kinetic actuation, there is less of a dependence on the optical and

thermal properties of the materials. Actuation is dependent on the nature of the electrical fields, and the electrical properties of the microfluidic environment and the objects to be moved. These can be modified simply, with minimal changes to other properties of fluids and particles which might be under investigation.

Optically assisted electrokinetic techniques rely on the ability of substrates to provide an electrical response to optical stimulation. Perhaps the most widely used of these methods is optoelectronic tweezing [22], [23]. In this technique, the microfluidic chamber is created using a photoconductive and electrically conductive layer sandwiching a fluidic region. These layers are biased with an external signal source. As the fluid and the photoconductive layer have a frequency dependent response, biasing is performed by an AC electric field. In the absence of illumination, the impedance of the photoconductor is greater than the fluid, and the majority of the applied electric field is dropped across the photoconductive layer. The impedance of the photoconductor is reduced at the point of illumination, allowing transmission of the electric field into the fluid. This change in impedance creates electric field gradients in a parallel plate configuration which can be used in different manners to control the motion of particles (through dielectrophoresis) or fluids (electrowetting on dielectric) [24]. Through control of the frequency of the electric field (and other parameters such as the conductivity of the fluid medium), complex trapping and sorting operations can be performed. As there is no need to balance scattering and gradient forces, simple light sources can be used enabling parallelisation with the use of commercially available digital projectors.

An experimental technique linked to, but distinct from, optoelectronic tweezing is rapid electrokinetic patterning. At low frequencies, the moderate temperature increase and subsequent temperature gradient caused by photonic absorption in the substrate creates a body force, because of the electrothermal effect. This produces a convective like vortex capable of trapping and transporting particles [25]. In contrast to optoelectronic tweezing, no photoconductive substrate is necessary (as with thermal actuation, absorption properties of the substrate are more crucial). Rapid electrokinetic patterning and optoelectronic tweezing address a number of the drawbacks related to optical tweezing, such as the intensity of excitation, and throughput of manipulated particles. The need for special substrates and a separate signal source means they cannot be used in all situations.

Photorefractive optoelectronic tweezing [26]–[30] exists as a response to the need for external signal sources characteristic of optoelectronic tweezing. In this scheme, the photoconductive substrate, characteristic of traditional optoelectronic tweezers, is replaced with a photovoltaic substrate capable of generating internal electric space charge fields. Inhomogeneous illumination of the photovoltaic substrate creates a non-linear electric field which can be exploited in the same

way as in conventional optoelectronic tweezing. Though the need for a signal source has been addressed, photorefractive optoelectronic tweezing is not as responsive as conventional optoelectronic tweezing due to the manner in which the electric field is generated. The substrate has to be optically excited continuously for relatively long periods of time to allow the migration of sufficient electrons (drift and diffusion dominated processes) to generate an electric field [27], [28].

1.1.3 Summary of optical micromanipulation

As has been demonstrated, there are a number of different techniques which provide optical micromanipulation. The variety is a result of the fact that each of these is not without a characteristic drawback (i.e. there is no universal optical micromanipulation solution). Plasmonic enhancements can be used to improve the operation of these techniques. Details on how these improvements have been made in the literature are given below.

Table 1.1: Table of optical micromanipulation techniques, advantages, and characteristic drawbacks

Manipulation technique	Advantages	Disadvantages
Optical tweezing	• Trapping in axial and lateral planes [9] • Femtonewton resolution [5]	• Opticution risk [10] • Diffraction limited [5]
Optoelectronic tweezing	• Reduced power [23] • Parallel manipulation of multiple particles [23]	• Additional signal source required [23]
Rapid electrokinetic patterning	• Reduced power [25] • No photoconductive substrate required [25]	• Additional signal source required [25]
Photorefractive optoelectronic tweezing	• No additional signal source required in typical configurations [30], [31]	• Slow response time [31] • Limited environment [31]
Photothermal	• Long range manipulation of objects [14], [21] • Diverse actuation approaches	• Bulk vs particle effect limits selectivity

1.2 Plasmonics

Plasmonics is the study and application of plasmon resonance; a coupled oscillation of an incident electromagnetic field (usually in the form of light) to the valence electrons of a material. Two distinct manifestations of plasmon resonance exist [32] defined by the manner in which the coupling of light to metal oscillation occurs; SPR (surface plasmon resonance also known as surface plasmon polaritons/SPP) in which propagating charge oscillations are confined to a metal-dielectric interface, and localised surface plasmon resonance (LSPR) where charge oscillations occur throughout the structure of a metal. Though the experimental configurations necessary for providing appropriate excitation for SPP are more cumbersome [32], the relative ease with which metallic thin films could be fabricated on planar surfaces meant that this form of plasmon resonance historically had been more widely deployed than LSPR [32], [33]. The advent of reliable nanofabrication techniques (e-beam lithography), coupled with the extremely high electric field enhancement (up to 1000 ×)[34], and the ability to engineer nanostructures with specific properties (such as the ability to support multiple resonant modes distinguished by wavelength or polarisation [35]–[39]), means that LSPR increasingly supersedes SPR for practical purposes.

Under appropriate excitation, plasmon resonances induce a localised electric field enhancement constrained to the interface between a metal and an adjacent dielectric. This localisation constitutes a subwavelength confinement, and the magnitude of the electric field enhancement can be controlled using the wavelength of the incident light. These three key characteristics of plasmon resonance (tuneable wavelength dependent, non-diffraction limited, electric-field/optical enhancement) generally define the more widely deployed plasmonic applications. For instance, the sub-wavelength, electric field enhancement characteristic of plasmonic structures has been used by researchers to create waveguides [40], modulators [41], and lenses [34] capable of operating beyond the diffraction limit [40], [42].

The sensitivity of optical enhancement to different environments and changes in geometry, coupled with the length scale of light, makes plasmonics a useful tool for biosensing [43]. Surface modified plasmonic structures will produce a characteristic shift in their optical response in the presence of an analyte, due to the modified geometry of the plasmonic structure. Tailoring of the surface modification process (through the use of antibodies or complementary DNA sequences for example) can be used to quantify/identify specific binding events [44], [45]. Similarly, the change in plasmonic activity seen in response to a change in refractive index can be used as a sensing event in its own right, without additional chemical modifications. The geometric

dependent resonant scattering of light means that in a dark-field configuration, plasmonic structures can be used for labelling purposes, without drawbacks such as photobleaching, which are associated with alternatives such as fluorescent tags [46], [47].

When used in conjunction with other applications, the plasmonic enhancement effect can be used to improve the performance of these technologies. In the most famous of such applications, surface enhanced Raman spectroscopy (SERS), plasmonic structures and thin films are used to enhance the inherently weak low energy/ vibrational signal associated with Raman scattering [48].

1.2.1 Plasmon assisted optical trapping

The plasmonic enhancement effect is increasingly used as a means to overcome some of the limitations associated with optically induced manipulation techniques [49]. When used with optical tweezers, the localised amplification of light produced as a result of plasmon resonance relaxes the requirement for a high intensity, tightly focussed laser beam coming out of the objective, thus reducing the risk of opticution [49]–[52]. Subwavelength localisation enables trapping of nanometre scale objects, as trapping is no longer diffraction limited [49].

The drawbacks associated with plasmon assisted optical trapping are often a result of the enhanced absorption characteristics observed because of plasmon resonance. The increased absorption creates a localised heating effect meaning plasmonic structures act as nano heat-sources. This heating effect has been used in chemistry, to control the speed of chemical reactions by increasing their activation temperature [53]. Plasmonic heating has also been used for fabrication purposes for the catalytic growth of semiconductor nanowires [54], [55]. Other emerging applications for the plasmonic heating effect include photothermal cancer therapy [56], photoacoustic imaging [57], and drug delivery [56], [58].

Heat generated in the course of optical manipulation creates convection currents in the fluid medium which affect stable trapping, a problem that can be controlled (e.g. by using heatsinking materials to suppress the amount of heat generated [50], [59]) but not curtailed entirely. In addition to this, the issue of throughput still remains as the relevant optical enhancement does not propagate beyond the region where the light beam is incident on the plasmonic nanostructure (i.e. this system is still to some extent reliant on diffusion to transport particles towards the trap). Though convection resulting from plasmonic heating can be used to transport particles towards the trap [60], [61], this requires a delicate balance such that the thermal forces do not completely overpower the optical forces [60].

Plasmonic heating can be used more advantageously for indirect optical manipulation based on thermal effects [62]–[64]. The ability to control the wavelength of absorption and generated temperature means that some of the limitations associated with conventional photothermal manipulation can be circumvented. However (barring plasmonic rapid electrokinetic patterning [65], which has its own set of associated limitations), the drawbacks of photothermal actuation remain (i.e. the relative lack of control over thermal associated properties).

1.3 Pyroelectric manipulation

Pyroelectric manipulation of microparticles and fluids operates by exploiting electrokinetic phenomena in a manner similar to optoelectronic tweezers. In such schemes, a thermal stimulus is applied to a pyroelectric substrate, which generates an electric field in response to this change in temperature. By controlling the magnitude and geometry of these electric fields, the induced electrokinetic phenomena can be used in a variety of applications. For instance, pyroelectrically controlled electrowetting has been used to create arrays of droplets that can be used as micro-lens arrays [66]. Nanoparticle self-assembly has been demonstrated using a similar pyroelectric device. A pyro-electrohydrodynamic effect has also been used for on-demand droplet and particle transfer [67].

Early pyroelectric manipulation experiments used conduction based heat sources (such as hot plates [66], [68] and soldering irons [69]), which heat a large area (on the order of mm) of the substrate, to provide thermal stimulus. As the electrokinetic phenomena exploited in these early experiments required large electric field gradients, distinct electric field regions were created using either external conductive layers [70], or by creating internal ferroelectric domains [68], [71]. By maximising the electric field gradient using the discontinuities between different regions, effects such as dielectrophoresis and interfacial surface tension can be used to manipulate fluid and particle motion. In another solution, the necessary electric field discontinuity is gotten when the pyroelectric substrate is delocalised from a reservoir of fluids or particles, which are used to pattern a target [69]. These modes of operation have persisted even when photonic sources have been used to provide thermal stimulus [72], [73]. As a result, these solutions did not offer the flexibility exhibited by some of the purely optically actuated techniques as the location of trapped objects is fixed by the position of the electrodes.

1.4 Outline of structure of thesis

This project introduces a different method for applying the plasmonic effect for optical actuation. In this thesis, plasmonic heating is used to create nano and microscale heat sources. These heat sources, which hinder stable trapping in conventional plasmon-enhanced optical manipulation schemes, are used to stimulate the pyroelectric effect on appropriate substrates. Crucially, experiments are performed in a self-contained microfluidic device allowing several electrokinetic phenomena to be activated simultaneously. This allows precise, high throughput manipulation of ensembles of particles. Arbitrary patterning of silica beads and metallic nanoparticles is performed, demonstrating the technique. A primary application of this patterning effect is as an optically controlled, photoresist free fabrication technique. Additionally, combining pyroelectric manipulation with plasmonics in this way provides a way to address the diffusion limit associated with the operation of other plasmonic applications, such as biosensors.

The thesis is structured as follows. Chapter 2 presents a theoretical background of the relevant physical phenomena exploited in this project. This includes a review of plasmon resonance with an emphasis on heat generation processes resulting from LSPR, the pyroelectric effect and its establishment in lithium niobate crystals and electrokinetic phenomena (particularly electrophoresis and dielectrophoresis and the relationship between particles and fluid surroundings i.e. the electrical double layer and the Claussius-Mossotti factor).

Chapter 3 details the experimental and numerical methods used to gain the results presented in the thesis. This chapter includes an overview of the materials used in experiments and for fabrication purposes.

Chapter 4 presents results from experiments performed using fluorescent molecular rotors to characterise the temperature generation of various plasmonic structures in different geometries and on different substrates. The chapter concludes with a discussion on the drawbacks on the technique used and possible changes which can be made to improve the accuracy of thermometry.

Chapter 5 presents a numerical analysis of the major forces induced in plasmonic enhanced pyroelectric field generation and how their presence affects stable particle trapping and kinetic actuation. The results from this chapter are used to present suggestions of necessary environmental prerequisites for performing electrokinetic microfluidic manipulation.

Chapter 6 details the results of experiments performing patterning of particles into arbitrarily defined shapes as a result of the capacitive nature of lithium niobate crystals. The influence of the surrounding microfluidic environment is considered.

Chapter 7 demonstrates plasmon enhanced pyroelectric trapping of silica beads. Particle tracking techniques are used to characterise the magnitude of the trapping force. The influence of bead size and the differences between pyroelectric trapping resulting from plasmonic heating in contrast to absorptive heating of lithium niobate, are discussed.

Chapter 8 summarises the results of the project and presents suggestions on the directions future work developing the technique presented might take.

1.5 References

[1] M. Aubin-Tam, A. O. Olivares, R. T. Sauer, T. A. Baker, and M. J. Lang, "Single-Molecule Protein Unfolding and Translocation by an ATP-Fueled Proteolytic Machine," *Cell*, vol. 145, no. 2, pp. 257–267, 2011.

[2] T. T. Perkins, S. R. Quake, D. E. Smith, and S. Chu, "Relaxation of a Single DNA Molecule Observed by Optical Microscopy," *Science*, vol. 263, pp. 822–827, 1994.

[3] K. Svoboda, C. F. Schmidt, B. J. Schnapp, and S. M. Block, "Direct observation of kinesin stepping optical trapping interferometry," *Nature*, vol. 365, pp. 721–727, 1993.

[4] J. T. Finer, R. M. Simmons, and J. A. Spudich, "Single myosin molecule mechanics: piconewton forces and nanometre steps," *Nature*, vol. 368, pp. 113–119, 1994.

[5] O. M. Maragò, P. H. Jones, P. G. Gucciardi, G. Volpe, and A. C. Ferrari, "Optical trapping and manipulation of nanostructures.," *Nat. Nanotechnol.*, vol. 8, no. 11, pp. 807–19, 2013.

[6] P. Lebedev, "Untersuchungen über die Druckkräfte des Lichtes," *Ann. Phys.*, vol. 311, no. 11, pp. 433–458, 1901.

[7] E. F. Nichols and G. F. Hull, "A preliminary communication on the pressure of heat and light radiation," *Phys. Rev. I*, vol. 13, no. 5, pp. 307–320, 1901.

[8] A. Ashkin, J. M. Dziedzic, J. E. Bjorkholm, and S. Chu, "Observation of a single-beam gradient force optical trap for dielectric particles.," *Opt. Lett.*, vol. 11, no. 5, p. 288, 1986.

[9] J. E. Molloy and M. J. Padgett, "Lights, action: optical tweezers," *Contemp. Phys.*, vol. 43, no. 4, pp. 241–258, 2002.

[10] K. Svoboda and S. M. Block, "Biological applications of optical forces," *Annu. Rev. Biophys. Biomol. Struct.*, vol. 23, pp. 247–285, 1994.

[11] E. R. Dufresne and D. G. Grier, "Optical tweezer arrays and optical substrates created with diffractive optics," *Rev. Sci. Instrum.*, vol. 69, no. 5, p. 1974, 1998.

[12] K. Sasaki, M. Koshioka, H. Misawa, N. Kitamura, and H. Masuhara, "Pattern formation and

flow control of fine particles by laser-scanning micromanipulation.," *Opt. Lett.*, vol. 16, no. 19, pp. 1463–1465, 1991.

[13] A. Lafong, W. J. Hossack, J. Arlt, T. J. Nowakowski, and N. D. Read, "Time-Multiplexed Laguerre-Gaussian holographic optical tweezers for biological applications.," *Opt. Express*, vol. 14, no. 7, pp. 3065–72, 2006.

[14] Y. Liu and A. W. Poon, "Flow-assisted Single-beam Optothermal Manipulation of Microparticles," *Opt. Express*, vol. 18, no. 7, pp. 18483–18491, Oct. 2010.

[15] D. Braun and A. Libchaber, "Trapping of DNA by Thermophoretic Depletion and Convection," *Phys. Rev. Lett.*, vol. 89, no. 18, p. 188103, Oct. 2002.

[16] E. Vela, C. Pacoret, S. Bouchigny, S. Regnier, K. Rink, and A. Bergander, "Non-contact mesoscale manipulation using laser induced convection flows," *2008 IEEE/RSJ Int. Conf. Intell. Robot. Syst.*, pp. 913–918, Sep. 2008.

[17] S. Duhr and D. Braun, "Optothermal Molecule Trapping by Opposing Fluid Flow with Thermophoretic Drift," *Phys. Rev. Lett.*, vol. 97, no. 3, p. 38103, Jul. 2006.

[18] S. Duhr and D. Braun, "Why molecules move along a temperature gradient.," *Proc. Natl. Acad. Sci. U. S. A.*, vol. 103, no. 52, pp. 19678–82, Dec. 2006.

[19] H. Jiang, N. Yoshinaga, and M. Sano, "Active Motion of a Janus Particle by Self-Thermophoresis in a Defocused Laser Beam," vol. 105, no. 26, p. 268302 (1-4), 2010.

[20] F. M. Weinert and D. Braun, "Optically driven fluid flow along arbitrary microscale patterns using thermoviscous expansion," *J. Appl. Phys.*, vol. 104, no. 10, p. 104701(1-10), 2008.

[21] F. M. Weinert and D. Braun, "An Optical Conveyor for Molecules," *Nano Lett.*, vol. 9, no. 12, pp. 4264–4267, 2009.

[22] C. Pei Yu, A. T. Ohta, and M. C. Wu, "Massively parallel manipulation of single cells and microparticles using optical images," *Nature*, vol. 436, no. 7049, pp. 370–372, 2005.

[23] M. C. Wu, "Optoelectronic Tweezers," *Nat. Photonics*, vol. 5, pp. 322–324, 2011.

[24] J. K. Valley, S. N. Pei, S. Ningpei, A. Jamshidi, H.-Y. Hsu, and M. C. Wu, "A unified platform for optoelectrowetting and optoelectronic tweezers.," *Lab Chip*, vol. 11, no. 7, pp. 1292–7, 2011.

[25] A. Kumar, J. S. Kwon, S. J. Williams, N. G. Green, N. K. Yip, and S. T. Wereley, "Optically modulated electrokinetic manipulation and concentration of colloidal particles near an electrode surface," *Langmuir*, vol. 26, no. 7, pp. 5262–5272, 2010.

[26] H. A. Eggert, F. Y. Kuhnert, K. Buse, J. R. Adleman, and D. Psaltis, "Trapping of dielectric particles with light-induced space-charge fields," *Appl. Phys. Lett.*, vol. 90, no. 24, p. 241909, 2007.

[27] J. Matarrubia, a García-Cabañes, J. L. Plaza, F. Agulló-López, and M. Carrascosa, "Optimization of particle trapping and patterning via photovoltaic tweezers: role of light modulation and particle size," *J. Phys. D. Appl. Phys.*, vol. 47, no. 26, p. 265101, Jul. 2014.

[28] C. Arregui, J. B. Ramiro, Á. Alcázar, Á. Méndez, H. Burgos, Á. García-Cabañes, and M. Carrascosa, "Optoelectronic tweezers under arbitrary illumination patterns: theoretical simulations and comparison to experiment," *Opt. Express*, vol. 22, no. 23, p. 29099, 2014.

[29] S. Glaesener, M. Esseling, and C. Denz, "Multiplexing and switching of virtual electrodes in optoelectronic tweezers based on lithium niobate.," *Opt. Lett.*, vol. 37, no. 18, pp. 3744–6,

Sep. 2012.

[30] M. Esseling, F. Holtmann, M. Woerdemann, and C. Denz, “Two-dimensional dielectrophoretic particle trapping in a hybrid crystal/PDMS-system.,” *Opt. Express*, vol. 18, no. 16, pp. 17404–11, 2010.

[31] M. Carrascosa, A. Garcia-Cabanes, M. Jubera, J. B. Ramiro, and F. Agullo-Lopez, “LiNbO3: A photovoltaic substrate for massive parallel manipulation and patterning of nano-objects,” *Appl. Phys. Rev.*, vol. 2, no. 4, 2015.

[32] S. A. Maier, *Plasmonics: Fundamentals and Applications*. Springer Science, 2007.

[33] K. A. Willets and R. P. Van Duyne, “Localized surface plasmon resonance spectroscopy and sensing.,” *Annu. Rev. Phys. Chem.*, vol. 58, pp. 267–97, Jan. 2007.

[34] K. Li, M. I. Stockman, and D. J. Bergman, “Self-Similar Chain of Metal Nanospheres as an Efficient Nanolens,” *Phys. Rev. Lett.*, vol. 91, no. 22, p. 227402(1-4), 2003.

[35] E. Petryayeva and U. J. Krull, “Localized surface plasmon resonance: nanostructures, bioassays and biosensing--a review.,” *Anal. Chim. Acta*, vol. 706, no. 1, pp. 8–24, Nov. 2011.

[36] K. L. Kelly, E. Coronado, L. L. Zhao, and G. C. Schatz, “The optical properties of metal nanoparticles: The influence of size, shape, and dielectric environment,” *J. Phys. Chem. B*, vol. 107, no. 3, pp. 668–677, 2003.

[37] G. W. Bryant, F. J. Garcıa de Abajo, J. Aizpurua, P. Hanarp, D. S. Sutherland, and M. Kall, “Optical Properties of Gold Nanorings,” *Phys. Rev. Lett.*, vol. 90, no. 5, pp. 5–8, 2003.

[38] S. Link and M. A. El-Sayed, “Size and Temperature Dependence of the Plasmon Absorption of Colloidal Gold Nanoparticles,” *J. Phys. Chem. B*, vol. 103, pp. 4212–4217, 1999.

[39] C. Rockstuhl, F. Lederer, M. Platz, C. Etrich, and H. Giessen, “On the reinterpretation of resonances in split-ring-resonators at normal incidence,” vol. 14, no. 19, pp. 65–68, 2006.

[40] A. Boltasseva, V. S. Volkov, R. B. Nielsen, E. Moreno, S. G. Rodrigo, and S. I. Bozhevolnyi, “Triangular metal wedges for subwavelength plasmon-polariton guiding at telecom wavelengths,” *Opt. Express*, vol. 16, no. 8, pp. 6323–6325, 2008.

[41] J. A. Schuller, E. S. Barnard, W. Cai, Y. C. Jun, J. S. White, and M. L. Brongersma, “Plasmonics for extreme light concentration and manipulation.,” *Nat. Mater.*, vol. 9, no. 3, pp. 193–204, Mar. 2010.

[42] D. K. Gramotnev and S. I. Bozhevolnyi, “Plasmonics beyond the diffraction limit,” *Nat. Photonics*, vol. 4, no. 2, pp. 83–91, 2010.

[43] J. N. Anker, W. P. Hall, O. Lyandres, N. C. Shah, J. Zhao, and R. P. Van Duyne, “Biosensing with plasmonic nanosensors.,” *Nat. Mater.*, vol. 7, no. 6, pp. 442–453, 2008.

[44] A. W. Clark, D. G. Thompson, D. Graham, and J. M. Cooper, “Engineering DNA binding sites to assemble and tune plasmonic nanostructures,” *Adv. Mater.*, vol. 26, no. 25, pp. 4286–4292, 2014.

[45] J. Liu and Y. Lu, “Fast colorimetric sensing of adenosine and cocaine based on a general sensor design involving aptamers and nanoparticles,” *Angew. Chemie - Int. Ed.*, vol. 45, pp. 90–94, 2005.

[46] S. Schultz, D. R. Smith, J. J. Mock, and D. A. Schultz, “Single-target molecule detection with nonbleaching multicolor optical immunolabels,” *Proc. Natl. Acad. Sci. U. S. A.*, vol. 97, no.

3, pp. 996–1001, 2000.

[47] J. Yguerabide and E. E. Yguerabide, “Light-Scattering Submicroscopic Particles as Highly Fluorescent Analogs and Their Use as Tracer Labels in Clinical and Biological Applications,” *Anal. Biochem.*, vol. 262, pp. 157–176, 1998.

[48] P. L. Stiles, J. A. Dieringer, N. C. Shah, and R. P. Van Duyne, “Surface-enhanced Raman spectroscopy.,” *Annu. Rev. Anal. Chem. (Palo Alto. Calif).*, vol. 1, pp. 601–26, Jan. 2008.

[49] A. N. Grigorenko, N. W. Roberts, M. R. Dickinson, and Y. Zhang, “Nanometric optical tweezers based on nanostructured substrates,” *Nat. Photonics*, vol. 2, no. 6, pp. 365–370, 2008.

[50] M. Righini, A. S. Zelenina, C. Girard, and R. Quidant, “Parallel and selective trapping in a patterned plasmonic landscape,” *Nat. Phys.*, vol. 3, no. 7, pp. 477–480, May 2007.

[51] M. Righini, P. Ghenuche, S. Cherukulappurath, V. Myroshnychenko, F. J. De García Abajo, and R. Quidant, “Nano-optical trapping of rayleigh particles and Escherichia coli bacteria with resonant optical antennas,” *Nano Lett.*, vol. 9, no. 10, pp. 3387–3391, 2009.

[52] M. Righini, G. Volpe, C. Girard, D. Petrov, and R. Quidant, “Surface plasmon optical tweezers: Tunable optical manipulation in the femtonewton range,” *Phys. Rev. Lett.*, vol. 100, no. 18, pp. 8–11, 2008.

[53] S. Mukherjee, F. Libisch, N. Large, O. Neumann, L. V Brown, J. Cheng, J. B. Lassiter, E. A. Carter, P. Nordlander, and N. J. Halas, “Hot Electrons Do the Impossible: Plasmon-Induced Dissociation of H2 on Au,” *Nano Lett.*, vol. 13, pp. 240–247, 2013.

[54] D. A. Boyd, L. Greengard, M. Brongersma, M. Y. El-naggar, and D. G. Goodwin, “Plasmon-Assisted Chemical Vapor Deposition,” *Nano Lett.*, vol. 6, no. 11, pp. 2592–2597, 2006.

[55] L. Cao, D. N. Barsic, A. R. Guichard, and M. L. Brongersma, “Plasmon-assisted local temperature control to pattern individual semiconductor nanowires and carbon nanotubes,” *Nano Lett.*, vol. 7, pp. 3523–3527, 2007.

[56] L. R. Hirsch, R. J. Stafford, J. A. Bankson, S. R. Sershen, B. Riviera, R. E. Price, J. D. Hazle, N. J. Halas, and J. L. West, “Nanoshell-mediated near-infrared thermal therapy of tumors under magnetic resonance guidance,” vol. 100, no. 23, pp. 13549–13554, 2003.

[57] J. A. Copland, M. Eghtedari, V. L. Popov, N. Kotov, N. Mamedova, M. Motamedi, and A. A. Oraevsky, “Nanoparticles as a Molecular Based Contrast Agent : Implications for Imaging of Deep Tumors Using Optoacoustic Tomography,” *Mol. Imaging Biol.*, vol. 6, no. 5, pp. 341–349, 2004.

[58] G. Baffou and R. Quidant, “Thermoplasmonics: using metallic nanostructures as nanosources of heat,” *Laser Photon. Rev.*, vol. 17, pp. 1–17, 2013.

[59] K. Wang, E. Schonbrun, P. Steinvurzel, and K. B. Crozier, “Trapping and rotating nanoparticles using a plasmonic nano-tweezer with an integrated heat sink.,” *Nat. Commun.*, vol. 2, p. 469, 2011.

[60] B. J. Roxworthy, K. D. Ko, A. Kumar, K. H. Fung, E. K. C. Chow, G. L. Liu, N. X. Fang, and K. C. Toussaint, “Application of plasmonic bowtie nanoantenna arrays for optical trapping, stacking, and sorting.,” *Nano Lett.*, vol. 12, no. 2, pp. 796–801, Feb. 2012.

[61] B. J. Roxworthy, A. M. Bhuiya, S. P. Vanka, and K. C. Toussaint, “Understanding and controlling plasmon-induced convection.,” *Nat. Commun.*, vol. 5, p. 3173, Jan. 2014.

[62] J. S. Donner, G. Baffou, D. McCloskey, and R. Quidant, “Plasmon-Assisted Optofluidics,”

ACS Nano, vol. 5, no. 7, pp. 5457–5462, Jul. 2011.

[63] G. L. Liu, J. Kim, Y. Lu, and L. P. Lee, "Optofluidic control using photothermal nanoparticles," *Nat. Mater.*, vol. 5, no. 1, pp. 27–32, Dec. 2005.

[64] M. Braun and F. Cichos, "Optically controlled thermophoretic trapping of single nano-objects.," *ACS Nano*, vol. 7, no. 12, pp. 11200–8, Dec. 2013.

[65] J. C. Ndukaife, A. Mishra, U. Guler, A. G. A. Nnanna, S. T. Wereley, and A. Boltasseva, "Photothermal heating enabled by plasmonic nanostructures for electrokinetic manipulation and sorting of particles.," *ACS Nano*, vol. 8, no. 9, pp. 9035–43, Sep. 2014.

[66] P. Ferraro, S. Grilli, L. Miccio, and V. Vespini, "Wettability patterning of lithium niobate substrate by modulating pyroelectric effect to form microarray of sessile droplets," *Appl. Phys. Lett.*, vol. 92, no. 21, p. 213107, 2008.

[67] V. Vespini, S. Coppola, S. Grilli, M. Paturzo, and P. Ferraro, "Pyroelectric Adaptive Nanodispenser (PYRANA) microrobot for liquid delivery on a target," *Lab Chip*, vol. 11, no. 18, p. 3148, 2011.

[68] S. Grilli and P. Ferraro, "Dielectrophoretic trapping of suspended particles by selective pyroelectric effect in lithium niobate crystals," *Appl. Phys. Lett.*, vol. 92, no. 23, p. 232902, 2008.

[69] S. Coppola, V. Vespini, S. Grilli, and P. Ferraro, "Self-assembling of multi-jets by pyro-electrohydrodynamic effect for high throughput liquid nanodrops transfer," *Lab Chip*, vol. 11, no. 19, pp. 3294–3298, 2011.

[70] O. Gennari, S. Grilli, S. Coppola, and V. Pagliarulo, "Spontaneous Assembly of Carbon-Based Chains in Polymer Matrixes through Surface Charge Templates," *Langmuir*, 2013.

[71] S. Grilli, S. Coppola, G. Nasti, V. Vespini, G. Gentile, V. Ambrogi, C. Carfagna, and P. Ferraro, "Hybrid ferroelectric–polymer microfluidic device for dielectrophoretic self-assembling of nanoparticles," *RSC Adv.*, vol. 4, no. 6, p. 2851, 2014.

[72] V. Vespini, S. Coppola, S. Grilli, M. Paturzo, and P. Ferraro, "Milking liquid nano-droplets by an IR laser: a new modality for the visualization of electric field lines," *Meas. Sci. Technol.*, vol. 24, no. 4, p. 45203, Apr. 2013.

[73] M. de Angelis, P. Matteini, F. Ratto, R. Pini, S. Coppola, S. Grilli, V. Vespini, and P. Ferraro, "Plasmon resonance of gold nanorods for all-optical drawing of liquid droplets," *Appl. Phys. Lett.*, vol. 103, no. 16, p. 163112, 2013.

2 Theory

Summary

This chapter presents the theoretical background of the phenomena exploited in this project. Beginning from elementary principles, the nature and major properties of these forces are discussed. These theoretical observations dictate the experimental framework used, and explain some of the seemingly counterintuitive results presented further on. More extensive derivations are included in Appendix B.

2.1 Thermoplasmonics

The proceeding sections discuss the origins of plasmonic heating in LSPR, excited using continuous wave illumination. Discussions regarding SPR and plasmonic heating induced by pulsed illumination can be found in Appendix A.

2.1.1 Plasmon resonance and the dielectric function of free electron gas

Plasmon resonance can be explained using a plasma model of electronic conduction (such as the Drude model). In this model, metals consist of a lattice of positively charged ions, surrounded by a plasma of freely moving electrons. The coupled collective fluctuation of this gas of electrons in response to an electric field is termed a plasmon.

Plasmon resonance is analogous to harmonic motion in classical mechanics, described using systems such as a pendulum or a mass on a spring (illustrated in Figure 2.1). An external perturbing force displaces an object from its equilibrium position, which subsequently experiences a restoring force proportional to this displacement. The restoring force is characteristic of the particular system being analysed: for a mass on a spring, the restoring force is proportional to the spring constant, and for a pendulum, it is inversely proportional to the length of the suspension. The resonance condition is obtained by solving the appropriate equations of motion.

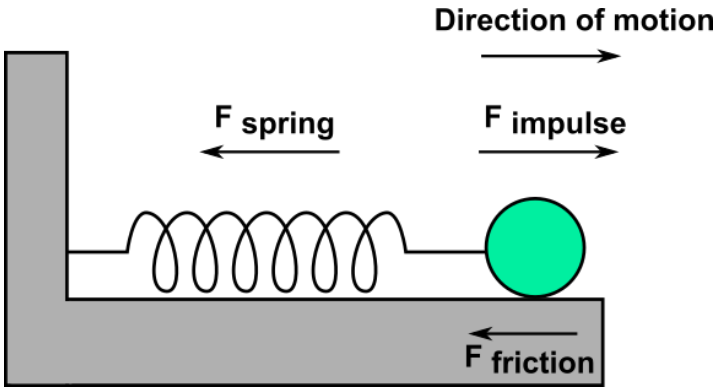

Figure 2.1: Mass on a spring. This mechanical system exhibits harmonic motion.

In the case of plasmon resonance, the perturbing force is the applied electromagnetic field, and the restoring force is a result of the free movement of the plasma of electrons. According to the Drude model, the material dependent plasmon frequency (which dictates the resonance condition) is given by:

$$\omega_{\mathrm{p}}^2 = \frac{ne^2}{\varepsilon_0 m}, \tag{2.1}$$

where n is the density of the gas of electrons, m is the effective optical mass of the electron, e is the elementary charge of an electron, and ε_0 is the vacuum dielectric constant. The plasmon frequency can be considered to be a measure of the characteristic response of electrons (i.e. charge carriers) to an applied electric field.

The dielectric response of a material is dependent on the motion of charge carriers. As a consequence of relativity, charge carriers cannot react instantaneously to an electric field: they are limited by the speed of light. The dielectric response of a material is thus a complex frequency dependent parameter in the form given below.

$$\varepsilon(\omega) = \varepsilon_1 + i\varepsilon_2 \tag{2.2}$$

The real part of (2.2) refers to the magnitude of polarisation [1] and the imaginary part refers to a phase shift (delay) in dielectric response [1], as a result of the inability to react instantaneously to electromagnetic fields. For metals, the "reaction limit" is the derived plasmon frequency. This dependence is reflected in the formulae for ε_1 and ε_2 given below.

$$\varepsilon_1 = 1 - \frac{\omega_p^2}{\omega^2 + \gamma^2} \tag{2.3}$$

$$\varepsilon_2 = \frac{\omega_p^2 \gamma}{\omega(\omega^2 + \gamma^2)}, \tag{2.4}$$

where ω is the frequency of the applied electric field, and γ is the characteristic electron collision frequency ($1/\tau$, τ is the average time between collisions), ~100 THz at room temperature.

2.1.2 Localised surface plasmon resonance

In localised surface plasmon resonance, the bulk plasmon is excited (in contrast to surface plasmon resonance where charge oscillations occur only at a metal's surface). For this to occur, the exciting electromagnetic wave interacts with all the electrons in the conduction band of the metal. As such, the characteristic length of a plasmonic structure needs to be less than the skin depth of the bulk metal at the frequency of excitation. The dislocation of electrons converts the metallic particle into an effective dipole, as positive and negative charges become separated (see Figure 2.2). The opposing charges induce a restoring force on the displaced bulk plasmon, the strength of which (by Coulomb's law) is dependent on the magnitude of electron displacement. Localised surface plasmon resonance occurs when the frequency of the exciting incident wave matches the oscillatory frequency of the metallic nanoparticle. Unlike in SPR, the resulting plasmon oscillations are confined to the nanoparticle (they do not propagate) and can be excited directly (i.e. no phase matching with an intermediary dielectric is required).

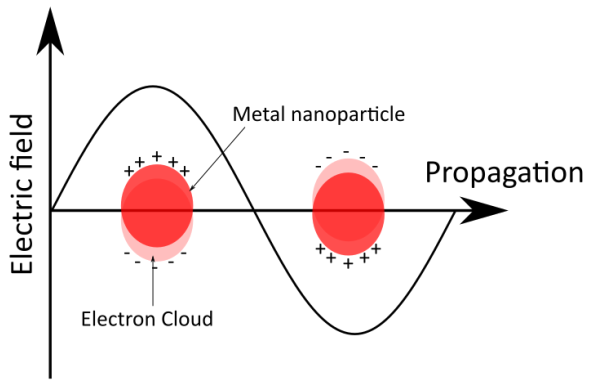

Figure 2.2: Schematic illustration of nanoparticle interaction with light inducing LSPR [2][3]**. Delocalisation of electron cloud by electric field creates a dipole resonance about the confines of the metal nanoparticle.**

The requisite condition for achieving plasmon resonance can be derived by considering the polarisability of the cloud of electrons surrounding a metallic nanoparticle. Assuming the nanoparticle is a sphere (for mathematical simplicity) with a diameter much less than the wavelength of the exciting light, a quasi-static approximation can be made (as the phase of the electromagnetic wave is effectively constant over the entire particle using these definitions), allowing the system to be analysed using an electrostatics approach by solving Laplace's equation for the effective dipole moment of the metallic nanoparticle. The relationship between polarisability and the dipole moment is given by:

$$p = \varepsilon\varepsilon_0 \alpha \boldsymbol{E}, \tag{2.5}$$

where α is the polarisability. Using this relationship and solving Laplace's equation for the dipole moment of the metal (using the approach detailed in [4]), the polarisability of the electron gas of a spherical nanoparticle is given as,

$$\alpha = 4\pi \frac{\varepsilon_\mathrm{p} - \varepsilon_\mathrm{m}}{\varepsilon_\mathrm{p} + 2\varepsilon_\mathrm{m}} R^3, \tag{2.6}$$

where R is the radius of the nanoparticle, ε_p is the relative permittivity of the metallic nanoparticle given by the previously derived complex dielectric function for metals, and ε_m is the electric permittivity of the medium surrounding the metallic nanoparticle. Resonance occurs at maximum polarisability i.e. when $|\varepsilon_\mathrm{p} + 2\varepsilon_\mathrm{m}|$ is at a minimum. Thus, the Frohlich condition [4] for dipolar surface plasmon resonance can be defined as,

$$Re\left[\varepsilon_\mathrm{p}\right] = -2\varepsilon_\mathrm{m} \tag{2.7}$$

Though the spherical assumption made is not valid for all geometries, it is often a good approximation for symmetrical particles and sufficiently details some important characteristics of LSPR. The sensitivity to environment is encompassed in the dependence of the polarisability on the electrical permittivity (and implicitly the refractive index) of the surrounding medium. The effect of geometry can be seen by noting the dependence of polarisability on the radius of a sphere; larger sized particles generally have a bigger polarisability and subsequently display greater LSPR. For particles beyond the limit of the quasistatic approximation (R>50 nm), the size of the particle begins to more noticeably affect the plasmon resonance frequency, as processes such as interband transitions, ignored in the quasistatic approximation, become more

pronounced. Geometrical transforms used to convert spheres to more arbitrary shapes also couple the metallic nanoparticle's characteristic length to frequency. Hence, size and shape can be used to tune plasmon wavelength. Increasing the size of a nanoparticle tends to redshift the plasmon resonance frequency.

The characteristic electromagnetic field enhancement occurs due to the fact that the dipole created as a result of the oscillations of the metal's bulk plasmon is able to induce an electric potential distinct from that created by the applied electric field (in the form of photonic excitation).

The electric field strength (in polar form) is thus [4],

$$\boldsymbol{E} = E_0 \cos\theta + \frac{g\, E_0 R^3 \cos\theta}{r^3}, \tag{2.8}$$

where E_0 is the electric field strength of the laser, $\cos\theta$ is the direction of laser polarisation, r is the radial coordinate, and g is the expression given by:

$$g = \frac{\varepsilon_\mathrm{p} - \varepsilon_\mathrm{m}}{\varepsilon_\mathrm{p} + 2\varepsilon_\mathrm{m}} \tag{2.9}$$

As g is in a similar form to the polarisability of the electron gas, it is clear that maximum electric field enhancement occurs at plasmon resonance. The dipole induced electric field, and subsequently the electromagnetic field enhancement, decays as $1/r^3$ with distance from the surface of the nanoparticle, highlighting the near-field nature of the LSPR effect.

The dipolar resonance of the metallic nanoparticle induces a re-radiation of the incident electromagnetic wave i.e. scattering of incident light. LSPR of particles can thus be determined by observing how efficiently light of different wavelengths is scattered. An extinction cross section quantifying the efficiency of LSPR is introduced by using the appropriate time averaged Poynting vector expression [5], and dividing by the intensity of the excitation. When the spherical assumption is made, the extinction cross section is defined as [4], [5],

$$\sigma_\mathrm{ext} = 9\frac{\omega}{c}\varepsilon_\mathrm{m}^{3/2} V \frac{\varepsilon_2}{[\varepsilon_1 + 2\varepsilon_\mathrm{m}]^2 + \varepsilon_2^2}, \tag{2.10}$$

where V is the volume of the sphere, and ε_1 and ε_2 are the real and imaginary parts of the metal's complex dielectric function, respectively. The extinction cross section represents the totality of energy transfer processes involved in LSPR and is comprised of a scattering cross section (which

quantifies radiative transfer processes) and an absorption cross section (which quantifies non-radiative transfer processes). The relationship between the three optical cross sections is given as [5],

$$\sigma_{\text{ext}} = \sigma_{\text{sca}} + \sigma_{\text{abs}} \tag{2.11}$$

Specific expressions for the scattering and absorption cross sections can be calculated using a similar Poynting vector technique to be [4], [5]:

$$\sigma_{\text{sca}} = \frac{8\pi}{3} k^4 R^6 \left| \frac{\varepsilon_{\text{p}} - \varepsilon_{\text{m}}}{\varepsilon_{\text{p}} + 2\varepsilon_{\text{m}}} \right|^2 \tag{2.12}$$

$$\sigma_{\text{abs}} = 4\pi k R^3 Im\left[\frac{\varepsilon_{\text{p}} - \varepsilon_{\text{m}}}{\varepsilon_{\text{p}} + 2\varepsilon_{\text{m}}} \right] \tag{2.13}$$

2.1.3 Heat power of plasmonic nanostructures

The internal energy transfer processes resulting from LSPR are expressed physically as heating of the nanoparticle. From elementary definitions, the energy absorption rate (calculated using the Poynting vector) is the heating power of the nanoparticle (since power is the rate of change of energy). This is given by [5]:

$$Q_{\text{abs}} = \iiint \boldsymbol{J} \cdot \boldsymbol{E} \, \mathrm{d}V, \tag{2.14}$$

where $\boldsymbol{J}$ refers to the internal current density of the nanoparticle and $\boldsymbol{E}$ is the electromagnetic field and V is a volume enclosing the particle.

The Ohmic nature of this value (as a result of its dependence on current density (current in macroscopic form) and electric field (voltage)) characterises plasmonic heating as a Joule heating process. From earlier discussions, the time averaged Poynting vector and absorption cross section are linked through the intensity of excitation (I). The heat power can thus be expressed using the absorption cross section as [6],

$$Q_{\text{abs}} = \sigma_{\text{abs}} I \tag{2.15}$$

By inspection (noting that a volume integral is performed to calculate the heat power of a plasmonic structure), the heat source density of a plasmonic nanostructure can be calculated as [6],

$$\boldsymbol{q} = \boldsymbol{J} \cdot \boldsymbol{E} \tag{2.16}$$

Redefining (2.16) for complex time harmonic functions gives [5], [6]:

$$\boldsymbol{q} = \frac{1}{2} Re[\boldsymbol{J}^* \cdot \boldsymbol{E}] \tag{2.17}$$

2.1.4 Heat generation by single plasmonic nanostructures

2.1.4.1 Continuous wave illumination

The temperature generated by a plasmonic nanostructure under excitation can be calculated using the heat conduction equation. To do this, the temperature outside the plasmonic nanoparticle due to internal absorption processes is considered. As there is no heat source in the medium (assuming heat generation processes are negligible compared to plasmonic heating and no phase changes occur), the steady state heat transfer equation outside the plasmonic structure is:

$$\nabla \cdot \kappa \nabla \boldsymbol{T} = 0 \tag{2.18}$$

Applying a Neumann style boundary condition at the interface of the surrounding medium and nanoparticle yields:

$$\kappa \nabla \boldsymbol{T} = \dot{q}, \tag{2.19}$$

where $\dot{q}$ is the heat flux density, i.e. the heat power per unit area delivered by the nanoparticle to its surroundings.

Due to the spatial inhomogeneity of the heat source density (and subsequently the heat flux density), the above expressions cannot be solved analytically without making some simplifications. As plasmonic heating is being considered, it can be reasonably assumed that the heat source is metallic, with electrons being the dominant energy carrier. Since the heat source is excited photonically, the surrounding environment can be assumed to be a dielectric, with

phononic vibrations dominating the energy transfer process. The heat conductivity of materials, from kinetic theory of gases, is given as [7]:

$$\kappa = \frac{1}{3} C_p v l, \tag{2.20}$$

where κ is the thermal conductivity, C_p is the specific heat capacity, v is the average velocity and l is the mean free path (i.e. the average distance between particle collisions). From (2.20), it can be shown that metals in general have a higher thermal conductivity than dielectrics, due to the greater velocity of electrons in comparison to phonons. As a result, thermalisation in the plasmonic particle occurs much faster than in the surrounding environment and nanoparticle temperatures can be considered uniform for practical purposes.

Using this uniform temperature approximation, appropriate surface integrals to the boundary equation can be applied yielding [8]:

$$Q_{\text{abs}} = \int \kappa \nabla \boldsymbol{T} \, \mathrm{d}A \tag{2.21}$$

To solve (2.21) analytically, particles are transformed into spheres described by an equivalent radius, R_{eq} (i.e. the radius of a sphere with the same volume as the particle), and β, a correction factor to account for the deviation from a spherical geometry. For general particle shapes, the temperature increase is estimated as [9]:

$$\Delta T = \frac{Q_{\text{abs}}}{4\pi \bar{\kappa} \beta R_{\text{eq}}}, \tag{2.22}$$

where $\bar{\kappa}$ is the thermal conductivity of the surrounding environment. For plasmonic nanoparticles at the interface between two different dielectrics e.g. a planar structure surrounded by a different medium, $\bar{\kappa}$ is defined as [10],

$$\bar{\kappa} = \frac{\kappa_1 + \kappa_2}{2}, \tag{2.23}$$

where κ_1 is the thermal conductivity of the supporting substrate, and κ_2 is the thermal conductivity of the surrounding medium.

The temperature distribution in the surrounding environment can be shown to decay with increasing distance from the nanoparticle. Thus, the spatially dependent temperature of the surrounding environment is [8]:

$$T(\boldsymbol{r}) = \frac{Q_{\text{abs}}}{4\pi\bar{\kappa}\beta|\boldsymbol{r} - \boldsymbol{r}_{\mathbf{i}}|}, \tag{2.24}$$

where $\boldsymbol{r}_{\mathbf{i}}$ is the centre of the particle, and $\boldsymbol{r}$ is any position external to the particle.

The uniform temperature approximation and the subsequent estimation of plasmonic heat generation considered here have focussed on steady state heating. The heat conduction equation as posed, suggests instantaneous thermal response of materials, which violates motion of energy carriers as defined by relativity, and invalidates the uniform temperature approximation. There is thus a characteristic time scale required for plasmonic nanoparticles to reach their steady state temperature. This can be gotten by considering the transient version of the heat conduction equation for internal processes:

$$\rho C_p \frac{\partial \boldsymbol{T}}{\partial t} + \nabla \cdot (\kappa \nabla \boldsymbol{T}) = -q \tag{2.25}$$

Through a dimensional analysis (separation of variables) the transient duration is given as [9]:

$$\tau \sim \frac{R_{\text{eq}}^2}{\alpha} = R_{\text{eq}}^2 \frac{\rho C_p}{\kappa}, \tag{2.26}$$

where α is the thermal diffusivity, ρ is the mass density of the nanoparticle, C_p is its heat capacity, and κ is the thermal conductivity of the surrounding area. For spherical nanoparticles of 1 μm diameter, the transient duration is on the order of 1 μs. This value can be used as a conservative estimate for the transient duration of heat generation by nanoparticles with resonance in the visible spectrum (i.e. between 400 and 800 nm), which, from previous derivations of LSPR, will have a characteristic length < 1 μm. Thus, the uniform temperature approximation gives a valid estimation of heat generated by nanoparticles excited with pulses exceeding 1 μs in duration.

2.1.5 Heat generation by collections of plasmonic nanostructures

Simultaneous excitation of multiple nanoparticles (as is often the case for practical purposes) increases the total temperature generated in comparison to single nanoparticle heating, as a

result of collective thermal effects. The temperature increase of a single nanoparticle in an assembly of multiple nanoparticles is given by the following expression [10]:

$$\Delta T = \Delta T_{\mathrm{s}} + \Delta T_{\mathrm{ext}}, \tag{2.27}$$

where ΔT_{s} is the temperature rise generated by the nanoparticle and ΔT_{ext} is the temperature rise generated by other surrounding nanoparticles. Due to the manner in which collective effects are manifested, there is no unique solution for this expression. However, by making some simplifications based on the nature of collections of nanoparticles, a valid solution can be gained.

To find an analytical expression for ΔT_{ext}, an array of lithographically fabricated nanostructures is considered. These structures have identical geometries and are spaced equally by a pitch (parameter –p). The final assumption is that the pitch of the array is such that single nanoparticles in this array are optically decoupled from each other.

The collective heating effects are the sum of the temperature increases due to surrounding particles. This temperature is at a maximum for a nanoparticle at the centre of an array. For a one dimensional array of equally spaced particles, uniformly irradiated particles, this sum can be written as [10],

$$\Delta T_{\mathrm{ext}} = \frac{Q_{\mathrm{abs}}}{4\pi\beta\bar{\kappa}p}\sum_{j\neq 0}^{N}\frac{1}{j}, \tag{2.28}$$

where N is the number of particles in the array, and j is the index of a particle's position in the array. The zeroth particle (i.e. $j = 0$) is defined as the particle at the centre of the array. By previously defined convention, the self-heating of the particle is considered separately and is thus ignored in the summation. This expression can be evaluated simply for small arrays of nanoparticles. For sufficiently large arrays (i.e. limit as N tends to infinity), the temperature due to collective heating effects is [10]:

$$\Delta T_{\mathrm{ext}} = \frac{Q_{\mathrm{abs}}}{2\pi\beta\bar{\kappa}}\frac{\ln(\gamma N)}{p}, \tag{2.29}$$

where γ is the Euler-Mascheroni constant ($\gamma \approx 0.577$).

Using similar summation (and integral) techniques, the following expressions for collective heating of various two dimensional array geometries and illumination conditions are gotten [10], where A is the area of a unit cell of an array (p^2 for a square array), P is the laser power, H is the

full width at half maximum (FWHM) of a Gaussian beam and D is the diameter of a uniformly distributed circular laser beam [10]. In these cases, it is assumed that the arrays are significantly bigger than the laser beam.

$$\Delta T_{\text{ext}} = \frac{\sigma_{\text{abs}} P}{\bar{\kappa}} \sqrt{\frac{\ln(2)}{4\pi}} \frac{1}{HA} \left(1 - \frac{4\sqrt{\ln(2)\, A}}{\pi H}\right) \tag{2.30}$$

$$\Delta T_{\text{ext}} = \frac{\sigma_{\text{abs}} P}{\bar{\kappa}} \frac{1}{\pi} \frac{1}{DA} \left(1 - \frac{2\sqrt{A}}{\sqrt{\pi} D}\right) \tag{2.31}$$

These expressions all show an implicit dependence on the array pitch. The general trend is given as [11],

$$\Delta T_{\text{ext}} \propto \Delta T_{\text{s}} \frac{R N^{(m-1)/m}}{p}, \tag{2.32}$$

where m is the dimensionality of the array of plasmonic structures. Thus for large, densely populated arrays of nanoparticles, the collective heating effects are more dominant than self-heating of a nanoparticle, and can be used as a more accurate estimate of the temperature of the array.

2.2 Pyroelectrics

2.2.1 Introduction to pyroelectricity

Dielectric materials (i.e. materials which become polarised in the presence of an applied electric field) can be divided into 32 crystal classes [12], the geometry of which dictates their characteristics. Ten of these 32 classes have a dipole in their unit cell and are non-centrosymmetric (have no centre of symmetry). Because of this particular asymmetry, these materials have a non-zero polarisation (spontaneous polarisation) in the absence of an electric field, and are subsequently referred to as the polar crystal classes.

The polar crystal classes (comprising the following point groups: 1, 2, m, mm2, 3, 3m, 4, 4mm, 6, 6mm [12]) display pyroelectric ability (i.e. temperature dependent polarisation). Thus, the two terms (polar crystals and pyroelectric crystal classes) are used interchangeably. In contrast to non-polar dielectric crystals, spontaneous polarisation of pyroelectric crystals cannot be measured directly with an electrometer, due to the fact that charge compensation occurs rapidly within the

crystal [12]. Under thermal equilibrium, spontaneous polarisation is neutralised by a screening charge. A change in temperature affects the moment of the dipole in the unit cell (in a manner particular to the specific pyroelectric material) such that the screening charge no longer compensates for the spontaneous polarisation. Hence, provided the change in temperature is fast enough, a current flows between the surfaces of the pyroelectric crystal (pyroelectric current), in an effort to neutralise the spontaneous polarisation (Figure 2.3).

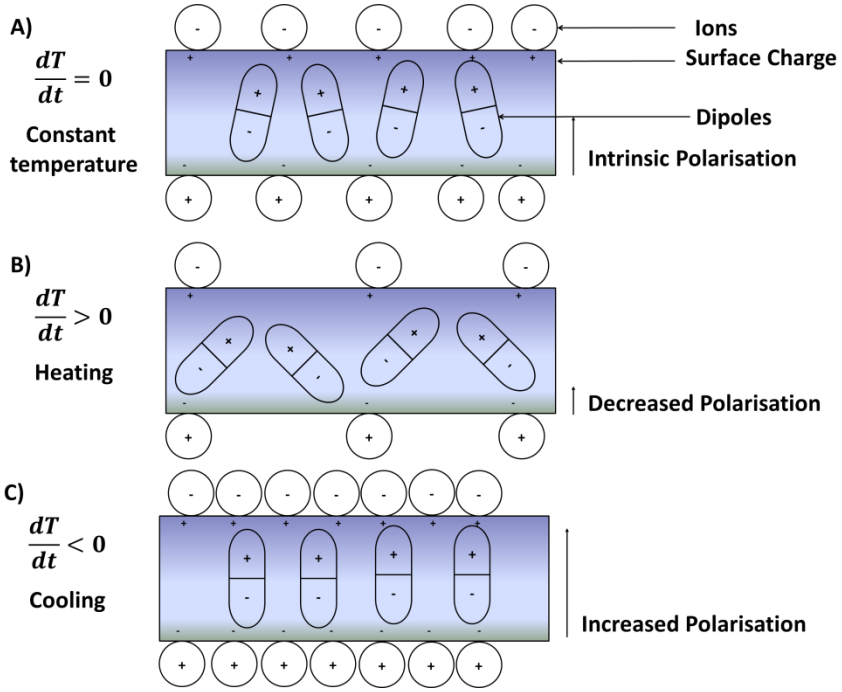

Figure 2.3: Schematic illustration of pyroelectric generation (adapted from [13]**). A) Surface charges are screened at constant temperature. B) Heating decreases polarisation. C) Cooling increases polarisation.**

With their structural anisotropy and spontaneous polarisation, pyroelectric crystals are electrically non-linear. As such, the electrical constitutive relationship is modified to accurately describe their behaviour:

$$\boldsymbol{D} = \boldsymbol{\varepsilon}_{\mathbf{r}}\varepsilon_0\boldsymbol{E} + \boldsymbol{Ps}, \tag{2.33}$$

where the electrical permittivity, $\boldsymbol{\varepsilon}_{\mathbf{r}}$, is a 3 × 3 matrix rather than a scalar value, due to the internal asymmetry of pyroelectric crystals, and the spontaneous polarisation, $\boldsymbol{Ps}$, is a temperature dependent parameter more accurately given by:

$$\boldsymbol{Ps} = \boldsymbol{\gamma}\Delta T \tag{2.34}$$

In this expression, the pyroelectric coefficient is a three-rowed vector with components in the x, y and z directions, and ΔT is the change in temperature.

As the spontaneous polarisation is a charge density, it follows that the pyroelectric charge can be estimated as,

$$Q = A\boldsymbol{\gamma}\Delta T, \tag{2.35}$$

where A is the area of the pyroelectric crystal undergoing thermal stimulation.

By noting that electrical current is the rate of change of generated charge, a pyroelectric crystal can be viewed as a temperature dependent current source. Appropriate modification of the above equation gives the magnitude of the generated current (and current density) as,

$$I = A\gamma\frac{\mathrm{d}T}{\mathrm{d}t} \tag{2.36}$$

$$J = \gamma\frac{\mathrm{d}T}{\mathrm{d}t} \tag{2.37}$$

There are capacitive elements to the electrical response of a thermally stimulated pyroelectric crystal; charges accumulate at the surface of the crystal and are separated by a dielectric as they do in a parallel plate capacitor. The intrinsic conductivity of the pyroelectric dictates that there is also a resistive element to the response. A pyroelectric crystal can thus be considered to be a temperature dependent current source in parallel with an RC circuit as in Figure 2.4 [14] [15]. The resistance, R_{cr}, and capacitance, C_{cr}, originate from the conductivity and permittivity of the pyroelectric substrate, respectively.

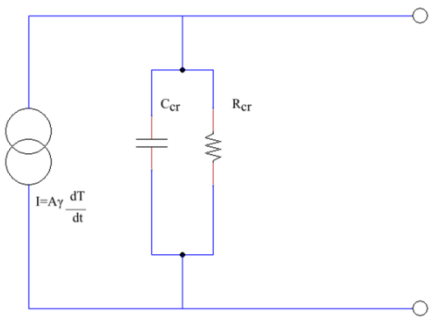

Figure 2.4: Equivalent circuit model of pyroelectric crystal. Capacitance and resistance are a result of intrinsic material properties.

2.2.2 Pyroelectricity in lithium niobate

Lithium niobate is a man-made dielectric crystal, with trigonal symmetry (possessing three-fold rotational symmetry), in the R3C space group (3m point group) [16]. The uniaxial symmetry of the trigonal crystal group means that lithium niobate has only two unique electrical permittivity values, with permittivity along the c axis (see Appendix B) differing from that along the other two orthogonal directions. The permittivity matrix of lithium niobate is of the form below.

$$\boldsymbol{\varepsilon}_{\mathbf{r}} = \begin{bmatrix} \varepsilon_{xx} & 0 & 0 \\ 0 & \varepsilon_{xx} & 0 \\ 0 & 0 & \varepsilon_{zz} \end{bmatrix}$$

The exact values of permittivity differ based on if the crystal is clamped or free during measurement (a result of the piezoelectricity of lithium niobate) [16]. When the crystal is unclamped, ε_{xx} is ~84 and ε_{zz} is ~30 [17], with the exact values dependent on the stoichiometry of the lithium, niobium, and oxygen. Clamped values of ε_{xx} and ε_{zz} are ~44 and ~ 29 [17] respectively. The equivalent capacitance is calculated using the permittivity of the axis perpendicular to the crystal's faces, a parameter which is dependent on the cut of the crystal.

Spontaneous polarisation in lithium niobate is a result of the movement of lithium and niobium ions within the crystal. As these ions move only in the direction parallel to the z/c axis, the temperature dependent spontaneous polarisation of lithium niobate is defined as a vector with non-zero components only in the z direction as,

$$\boldsymbol{\gamma} = \begin{bmatrix} 0 \\ 0 \\ \gamma \end{bmatrix},$$

where γ= -8.3× 10^{-5} C/K·m^2 [13]. The temperature dependent polarisation is negative to indicate that the positive z face becomes more negative (i.e. polarisation decreases), as the temperature increases.

2.2.3 Optical properties of lithium niobate

The anisotropic electrical permittivity of lithium niobate is responsible for its birefringence (since at optical frequencies, the refractive index is the square root of the electrical permittivity). Lithium niobate thus has an extraordinary refractive index parallel to its c axis and an ordinary

refractive index in the orthogonal directions [16], with specific values dependent on wavelength, as described by the Sellmeier equations (Appendix D). The birefringence of lithium niobate can be ignored if light propagates parallel to the optical axis, as the resulting polarisation is in the plane perpendicular to propagation; the ordinary refractive index, which is isotropic in this plane, is sufficient for explaining the interaction of light with matter.

Optical lithium niobate is transparent in the visible range between 300 nm and 5 µm. Absorption in this range is generally flat, with moderate peaks appearing at different wavelengths, due to polaron and bipolaron excitation caused by defects in the crystal lattice structure, as a result of non-ideal stoichiometry [17]. Beyond this range, lithium niobate is opaque due to absorption by the phononic lattice.

2.3 Forces on a particle in a microfluidic environment

Particles suspended in a microfluidic environment experience forces even in the absence of external stimulation. These intrinsic forces define the minimum levels of actuation required to control particle motion. Figure 2.5 depicts a free body diagram of the intrinsic forces acting on a microparticle. In this image, Brownian motion and drag are considered only in lateral dimensions for the purposes of clarity. The origin and nature of these forces are discussed in further detail in the proceeding sections.

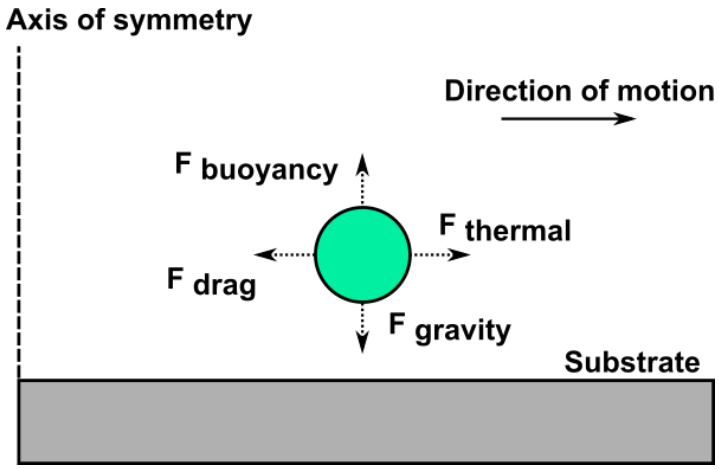

Figure 2.5: Free body diagram of intrinsic forces on a particle in a microfluidic system

2.3.1 Brownian motion

Brownian motion is the stochastic movement of particles in a fluid as a result of the thermal energy of a system. Particles are in constant collision with the molecules of the suspending medium, a process which dictates their motion. Using kinetic theory, it can be shown that an ensemble of microparticles has an average energy of $\frac{3}{2}kT$ in three dimensions (i.e. $\frac{1}{2}kT$ for a given axis). k is Boltzmann's constant and T is the thermodynamic temperature in Kelvin. The motion of individual particles is governed by collisions with other particles, as well as the boundaries of the microfluidic chamber. As such, particle energy follows a probability distribution (Boltzmann distribution), and particle motion is random. The mean squared displacement (i.e. characteristic change in position of a particle due to Brownian motion in a given time period) is the variance of this distribution and is given by the Einstein equation as,

$$\bar{x}^2 = 2dDt, \tag{2.38}$$

where d is the dimensionality of the observed system, and D is the diffusion coefficient, which is calculated through the Stokes-Einstein equation as,

$$D = \frac{kT}{6\pi\eta r} \tag{2.39}$$

where η is the viscosity of the fluid medium, and r is the radius of a spherical particle. In the absence of stimulation, Brownian motion is responsible for the translational motion of particles in two dimensions (i.e. particles are not necessarily stationary in the absence of stimulation). The mean squared displacement can be used to define the maximum allowable particle displacement characteristic of negligible external forces [18]. The standard deviation of the Gaussian distribution is the square root of the variance i.e.

$$\bar{x} = (2dDt)^{\frac{1}{2}} \tag{2.40}$$

2.3.2 Gravity and sedimentation

Downward motion (i.e. movement in the vertical/ z plane) of a particle in a microfluidic chamber is controlled primarily by gravitational acceleration. The total force on a particle is as a result of its

mass, and an opposing force due to the mass of the liquid (buoyancy) [19], [20]. This is calculated using the following expression:

$$F = \frac{4}{3}\pi r^3(\rho_{\mathrm{p}} - \rho_{\mathrm{m}})g, \tag{2.41}$$

where, $\frac{4}{3}\pi r^3$ is subsequently the volume of a spherical particle, ρ_{p} is the mass density of the particle, and ρ_{m} is the mass density of the fluid medium. g is the gravitational acceleration constant.

2.3.3 Drag

Particles in motion experience a restrictive force in opposition to their direction of travel as a result of viscous friction. Flow in a microfluidic system can typically be assumed to be laminar (as a result of the low Reynold's number associated with such systems). Thus, the drag force is of the form:

$$F = fv, \tag{2.42}$$

where v is the velocity of the particle, and f is the coefficient of friction, which depends on the material and its environment. For spherical particles freely moving in a solution, the friction force is given by Stokes's law as,

$$F = 6\pi\eta r v \tag{2.43}$$

In the context of particle motion, Stokes's drag is important for estimating the characteristic displacement of particles where only the magnitude of the applied force is known. In a microfluidic system, inertial forces are negligible and over short time periods, Stokes's drag equates to the applied force. Thus, the velocity of a particle can be used as a direct measurement of the applied force.

2.4 Electrokinetic phenomena

Electrokinetic phenomena originate from Coulomb's force (i.e. the force an electric field applies on a charge), with more specific mathematical and qualitative delineations arising when different boundary conditions and frames of reference (e.g. force in system vs free energy in system) are considered. As with all kinetic phenomena, motion is only achieved when Coulomb's force is greater than the cumulative opposing forces on the subject in question. Coulomb's force in vector form is given by:

$$\boldsymbol{F} = q \cdot \boldsymbol{E}, \tag{2.44}$$

where q is the charge on the test subject, and $\boldsymbol{E}$ is the electric field vector. This can be seen to be a solution to Coulomb's law where a charge has been replaced by the electric field it induces (which can be calculated a priori).

2.4.1 Electrophoresis

Electrophoresis is an electrokinetic phenomenon concerned with the motion of charged particles in a solution. Here, the expression for Coulomb's force can be considered to be synonymous with the electrophoretic force, with the caveat that the charge in the equation refers to the effective surface charge of the particle. The distinction between effective surface charge and native surface charge is required due to the ionisation that occurs when a particle is suspended in liquid medium. Ionisation processes can modify the magnitude, and cause a reversal of native surface charge (e.g. preferential adsorption of screening charges can switch polarity [20]). As a result of these modifications, electrophoresis is frequently described using the concept of the electrical double layer, which can be used to explain apparent anomalous responses of particles to electrical stimulation.

As Coulomb's force (and by extension, the electrophoretic force) deals with vector entities, electrophoresis can either attract or repel particles from/to high electric field regions. It is frequently described as a DC phenomenon as a consequence of this; alternately switching the sign of the electric field produces no net motion— particles oscillate as they are attracted to/repelled from electric field regions with equal force upon a change of sign [21].

2.4.1.1 Electrical double layer and zeta potential

The electrical double layer (illustrated in Figure 2.6) originates from the interactions between charges at the interface between a solid and a liquid. Solids in contact with a liquid gain a surface charge regardless of their previous neutrality (due to processes such as adsorption of ions and ion dissolution [20], [22]). This surface charge changes the local ionic distribution creating an electrical double layer of counter-ions separated from co-ions. The tendency for electroneutrality in the electrical double layer requires that a particle's surface charge is screened [22]; therefore, charges equal in magnitude and opposite in sign (counter-ions) are attracted to the solid surface. Due to the finite size of these counter ions, only a fraction of these are attached to the solid surface by specific adsorption. The rest of these ions approach to within an ionic radius of the solid surface (the Stern plane). A shear plane exists a short distance from this, defined as the point where liquid is no longer bound to the solid surface. Co-ions (charges of the same sign as the surface charge) are repelled and exist in a mobile phase in the liquid. In the immediate vicinity of the surface, co-ions are less abundant than counter-ions. The double layer thickness is defined by the distance from the surface where the concentration of co and counter-ions matches that of the bulk electrolyte.

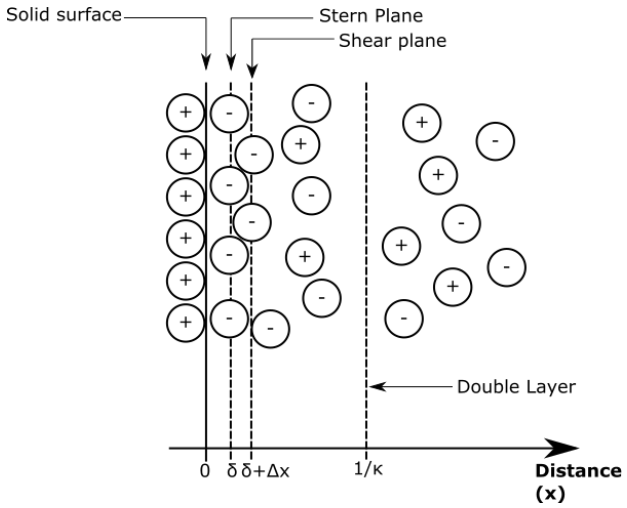

Figure 2.6: Schematic illustration of electrical double layer [20]**.**

Each plane has an associated potential: ψ_0 is defined as the surface potential, ψ_s is the Stern potential, and ζ is the potential at the shear plane. The existence of the shear plane indicates that during electrophoresis, a small amount of liquid moves along with the particle. The zeta potential

(ζ) can thus be used as a measure of the energy required to move the particle and the bound liquid, and is an important parameter for use in electrophoresis for this reason.

The total electrophoretic motion of a particle can be described by independently considering the electrically induced motion of the ions in the diffuse electrical double layer, and that of the particle itself [20]. The electrophoretic force can be described using Stokes's law as [20],

$$F_{\mathrm{e}} = 6\pi\eta v_{\mathrm{e}} a, \tag{2.45}$$

where a is the radius of the particle, and v_{e} is the electrophoretic velocity described as [20],

$$v_{\mathrm{e}} = E\mu_{\mathrm{e}}, \tag{2.46}$$

where E is the electric field, κ is the reciprocal of the double layer thickness ($\frac{1}{d}$), and μ_{e} is the electrophoretic mobility which is related to the zeta potential through the Henry equation [20].

2.4.2 Dielectrophoresis

A limit on electrophoresis is the requirement that particles are charged to allow for motion. In contrast to this, dielectrophoresis is the motion of dielectric materials in non-uniform electric fields as a consequence of their polarisability (Figure 2.7). In the simplest consideration, electric polarisation of dielectrics causes the separation of free charge carriers, creating an effective dipole. In uniform electric fields, there is no net Coulombic force on the dipole due to the symmetry of the charges and the electric field. In non-uniform electric fields, the magnitude of the electric field in different spatial regions varies. As a result, the Coulombic force on different sides of the dipole varies and as such, there is a net force on the particle. If the asymmetry of the electric field is sufficient, the net force on the particle is enough to induce motion.

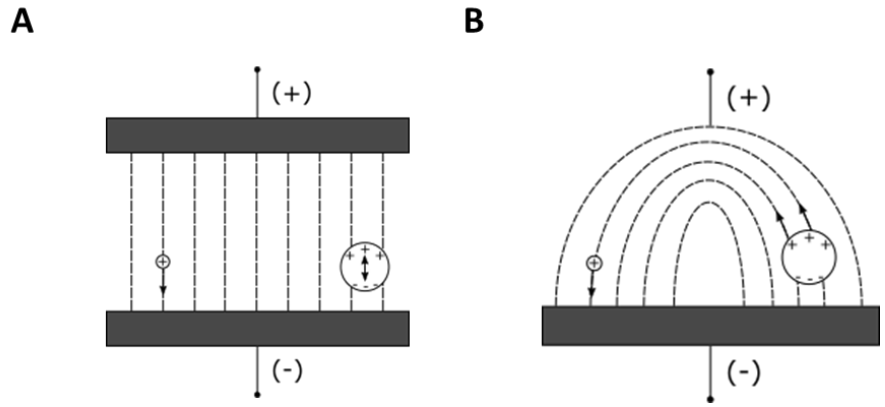

Figure 2.7: Electrokinetic motion of charged and neutral particles. A) Electrophoresis: charged particles move towards opposing terminal. Neutral particles remain stationary. B) Dielectrophoesis: charged particles move towards terminal of opposing polarity. Neutral, polarisable particles move in direction of high electric field gradient.

The DEP force as generally quoted is derived by considering a dipole of length d in a non-uniform electric field as in the illustration below (Figure 2.8):

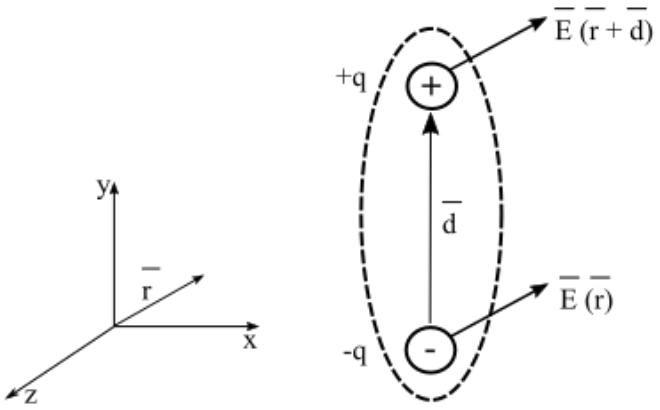

Figure 2.8: Illustration of the geometry used for calculating the net dielectrophoretic force on a dipole [23]**.**

The total force on the dipole in the geometry defined in Figure 2.8 can be calculated from the force on the charges at opposing ends of the dipole.

Provided the separation between the two charges (d) is sufficiently small, a Taylor series expansion can be used to express the electric field at $E(r + d)$ in terms of $E(r)$ [23].

By introducing the effective dipole moment, $p = qd$ and the gradient operator, ∇, the force on the dipole can be written as,

$$\boldsymbol{F} = p\nabla\boldsymbol{E} \tag{2.47}$$

Though this expression accurately calculates the dielectrophoretic force, the nature of a particle's interaction with the electric field, and how the particle's properties affect the dielectrophoretic force, is not apparent from the equation as written. An analytical expression for the dipole moment, for different particle geometries in terms of their electrical properties, does not always exist. However, the behaviour of a sphere is often times a good enough approximation for colloidal particles, and is thus used as a general expression for the DEP force. This is frequently written as [24],

$$\boldsymbol{F} = 2\,\pi\varepsilon_{\mathrm{m}}\,R^3 K\,\nabla|\boldsymbol{E}|^2, \tag{2.48}$$

where K (the Claussius-Mossotti factor) is defined as [24],

$$K = \frac{\varepsilon_{\mathrm{p}} - \varepsilon_{\mathrm{m}}}{\varepsilon_{\mathrm{p}} + 2\varepsilon_{\mathrm{m}}} \tag{2.49}$$

The more general expression for the DEP force (which includes excitation by time harmonic electric fields) is given as [24],

$$< \boldsymbol{F} > = 2\,\pi\varepsilon_{\mathrm{m}}\,R^3 Re[K^*]\nabla|\boldsymbol{E}_{\mathbf{rms}}|^2, \tag{2.50}$$

where <> represents the time average operator, $\boldsymbol{E}_{\mathbf{rms}}$ is the root mean squared value of the time harmonic electric field and K^* is the complex conjugate of the complex Claussius-Mossotti factor defined as [24],

$$K^* = \frac{\varepsilon_{\mathrm{p}}^* - \varepsilon_{\mathrm{m}}^*}{\varepsilon_{\mathrm{p}}^* + 2\varepsilon_{\mathrm{m}}^*} \tag{2.51}$$

The permittivities in this case have been replaced with the conjugate of their complex counterpart which is in the form [21]:

$$\varepsilon = \varepsilon' - i\,\varepsilon'' \tag{2.52}$$

The dielectrophoretic force is dependent on the electric field gradient (as opposed to the electric field magnitude), thus, repoling (changing the direction between positive and negative electric field regions) the electric field has no effect on the direction of particle travel.

2.4.2.1 Claussius-Mossotti factor and particle polarisability

The relative polarisability of a particle with respect to the immersed medium dictates the nature of particle motion in dielectrophoresis (in contrast to electrophoresis where it is the sign of the charge in relation to the electric field). The precise relationship is encapsulated in the Claussius-Mossotti factor. By considering the limits of particle permittivity (i.e. $\varepsilon_{\mathrm{p}} \rightarrow 0, \varepsilon_{\mathrm{p}} \rightarrow \infty$) it can be shown that, unlike charge, which can theoretically grow indefinitely, the Claussius-Mossotti lies in the range $-0.5 \leq K \leq 1$. Hence, negative dielectrophoresis (repulsion from high electric field gradient regions) is inherently weaker than positive dielectrophoresis [21].

The complex permittivity used to describe the Claussius-Mossotti factor can be viewed as a mathematical representation of the dielectric response of a material i.e. the motion of charges in an electric field. Polarisation or restricted charge motion is represented by the real part of the electrical permittivity while conduction (free charge motion) is represented by the imaginary part [21]. Using this definition, the complex permittivity in the Claussius-Mossotti factor is [21]:

$$\varepsilon = \varepsilon' - \frac{i\sigma'}{\omega}, \tag{2.53}$$

where ε is the frequency dependent electrical permittivity (originating from the different modes of polarisation available to a material due to its structure (micro/macroscopic), the diversity of charge carriers, and the ability of these to respond to electrical stimulation [21]), containing real and imaginary parts linked by Kramers-Kronig relations, and σ is the electrical conductivity of the material.

Consideration of the frequency dependent electrical permittivity shows that the limiting cases of the Claussius-Mossotti factor are written as [24],

$$K(\omega \rightarrow \infty) = \frac{\varepsilon_{\mathrm{p}} - \varepsilon_{\mathrm{m}}}{\varepsilon_{\mathrm{p}} + 2\varepsilon_{\mathrm{m}}} \tag{2.54}$$

$$K(\omega \rightarrow 0) = \frac{\sigma_{\mathrm{p}} - \sigma_{\mathrm{m}}}{\sigma_{\mathrm{p}} + 2\sigma_{\mathrm{m}}} \tag{2.55}$$

Particle conductivity (σ_{p}) is size dependent due to surface conductance effects, which are non-negligible when micrometre-sized particles are considered. The particle conductivity is more accurately given by [25]:

$$\sigma_{\mathrm{p}} = \sigma_{\mathrm{b}} + \frac{2\lambda}{R}, \tag{2.56}$$

where σ_b is the bulk conductivity of the particle and λ is the surface conductance.

Surface conductance is induced by the motion of charge carriers along and normal to a particle's surface. Using Ohm's law, it can be shown that surface conductance is related, through the tangential electric field, to charge carrier motion (which is a surface current) [25]. Based on this definition, the surface conductance can thus be calculated using the surface charge density and mobility of ions in the liquid medium [25]. As such, surface conductance can be viewed as an effect of the polarisation of the electrical double layer [25].

2.4.3 Electrohydrodynamic effects

Electrohydrodynamic effects are the result of the coupling between relevant electrical and mechanical properties of a fluid. This interaction induces a force on the fluid causing motion. EHD mechanisms can broadly be split into surface effects (interfacial effects) and body effects.

2.4.3.1 Surface effects

Electroosmosis occurs as a result of the formation of the electrical double layer at the interface between the pyroelectric substrate and the microfluidic environment. Ions in the shear plane move tangential to the surface of the substrate due to Coulombic interactions [21], [26]. As a result of Stokes's drag, there is a corresponding fluid movement in this layer giving rise to fluid motion in the bulk [21], [26]. Using this definition, the similarities between electroosmosis and electrophoresis can be noted.

The effect of electroosmosis on overall bulk motion can be calculated by imposing a slip condition at the solid-liquid boundary (i.e. the location of the electrical double layer). The slip velocity is given by [18]:

$$v = \frac{E_t \sigma_q}{\kappa \eta}, \tag{2.57}$$

where σ_q is the surface charge density, κ is the reciprocal of the double layer thickness, η is the viscosity of the fluid, and E_t is the tangential component of the electric field.

2.4.3.2 Electrothermal body effects

The electrohydrodynamic body force is given by the expression below [27]:

$$\boldsymbol{F} = \rho_{\mathrm{q}}\boldsymbol{E} - \frac{1}{2}\boldsymbol{E}^2\nabla\varepsilon, \tag{2.58}$$

where ρ_{q} is the volumetric charge density in the fluid and ε is the electrical permittivity.

In the expression above, the first term on the right hand side of the equation refers to Coulombic forces (i.e. electrical forces as a result of charge and conductivity interactions), and the second term refers to dielectric forces. The electrohydrodynamic body force is thus a consequence of the combination of electrophoretic and dielectrophoretic forces acting on the suspension medium (as opposed to the particle as previously described).

In this case, the electric field varies as a result of changes to temperature due to thermally induced motion of charge carriers. Perturbation theory is used to account for the small changes to charge density as a result of changes to temperature [28]. As a result, a new expression for the charge density is yielded [28]:

$$\rho = \left(\frac{\sigma\nabla\varepsilon - \varepsilon\nabla\sigma}{\sigma + i\omega\varepsilon}\right)\cdot E_0, \tag{2.59}$$

where $\nabla\varepsilon$ and $\nabla\sigma$ are the respective changes in dielectric response and conductivity due to temperature, and are given by [18]:

$$\nabla\varepsilon = \frac{\partial\varepsilon}{\partial T}\nabla T \tag{2.60}$$

$$\nabla\sigma = \frac{\partial\sigma}{\partial T}\nabla T \tag{2.61}$$

Substituting (2.59) into the body force expression yields [18]:

$$< F > = \frac{1}{2}Re\left[\left(\left(\frac{\sigma\nabla\varepsilon - \varepsilon\nabla\sigma}{\sigma + i\omega\varepsilon}\right)\cdot E_0\right)E_0 - \frac{1}{2}{E_0}^2\nabla\varepsilon\right] \tag{2.62}$$

The electrothermal force is thus given by [28]:

$$< f >= \frac{1}{2} Re\left[\left(\left(\frac{\sigma\varepsilon(\alpha-\beta)}{\sigma+i\omega\varepsilon}\right)(\nabla T \cdot E_0)\right)E_0 - \frac{1}{2}\varepsilon\alpha {E_0}^2 \nabla T,\right] \quad (2.63)$$

where α and β are dimensionless coefficients defined as [28],

$$\alpha = \frac{1}{\varepsilon}\frac{\partial\varepsilon}{\partial T} \quad (2.64)$$

$$\beta = \frac{1}{\sigma}\frac{\partial\sigma}{\partial T} \quad (2.65)$$

2.5 References

[1] C. F. Bohren and D. R. Huffman, *Absorption and Scattering of Light by Small Particles*. John Wiley & Sons, 1983.

[2] K. A. Willets and R. P. Van Duyne, "Localized surface plasmon resonance spectroscopy and sensing.," *Annu. Rev. Phys. Chem.*, vol. 58, pp. 267–97, Jan. 2007.

[3] K. L. Kelly, E. Coronado, L. L. Zhao, and G. C. Schatz, "The optical properties of metal nanoparticles: The influence of size, shape, and dielectric environment," *J. Phys. Chem. B*, vol. 107, no. 3, pp. 668–677, 2003.

[4] S. A. Maier, *Plasmonics: Fundamentals and Applications*. Springer Science, 2007.

[5] M. Quinten, *Optical Properties of Nanoparticle Systems: Mie and Beyond*. Weinheim: Wiley-VCH, 2011.

[6] G. Baffou and R. Quidant, "Thermoplasmonics: using metallic nanostructures as nanosources of heat," *Laser Photon. Rev.*, vol. 17, pp. 1–17, 2013.

[7] A. Bejan and A. D. Kraus, *Heat Transfer Handbook*. John Wiley & Sons.

[8] G. Baffou, R. Quidant, and C. Girard, "Thermoplasmonics modeling: A Green's function approach," *Phys. Rev. B*, vol. 82, no. 16, p. 165424, Oct. 2010.

[9] G. Baffou, R. Quidant, and F. G. de Abajo, "Nanoscale control of optical heating in complex plasmonic systems," *ACS Nano*, vol. 4, no. 2, pp. 709–716, 2010.

[10] R. Quidant, S. Monneret, G. Baffou, P. Berto, E. B. Urena, J. Polleux, and H. Rigneault, "Photoinduced Heating of Nanoparticle Arrays," *ACS Nano*, vol. 7, no. 8, pp. 6478–6488, 2013.

[11] A. O. Govorov, W. Zhang, T. Skeini, H. Richardson, J. Lee, and N. A. Kotov, "Gold nanoparticle ensembles as heaters and actuators: Melting and collective plasmon resonances," *Nanoscale Res. Lett.*, vol. 1, no. 1, pp. 84–90, 2006.

[12] J. C. Burfoot and G. W. Taylor, *Polar Dielectrics And Their Applications*. Macmillan, 1979.

[13] S. B. Lang, "Pyroelectricity: From Ancient Curiosity to Modern Imaging Tool," *Phys. Today*, vol. 58, no. 8, p. 31, 2005.

[14] T. Z. Fullem and Y. Danon, “Electrostatics of pyroelectric accelerators,” *J. Appl. Phys.*, vol. 106, no. 7, p. 74101, 2009.

[15] S. B. Lang and F. Steckel, “Method for the Measurement of the Pyroelectric Coefficient, dc Dielectric Constant, and Volume Resistivity of a Polar Material,” *Rev. Sci. Instrum.*, vol. 36, no. 7, p. 929, 1965.

[16] R. Weis and T. Gaylord, “Lithium niobate: summary of physical properties and crystal structure,” *Appl. Phys. A*, vol. 203, pp. 191–203, 1985.

[17] T. Volk and M. Wohlecke, *Lithium Niobate: Defects, Photorefraction and Ferroelectric Switching*. Springer-Verlag Berlin Heidelberg, 2008.

[18] A. Ramos, H. Morgan, N. G. Green, and A. Castellanos, “Ac electrokinetics: a review of forces in microelectrode structures,” *J. Phys. D. Appl. Phys.*, vol. 31, no. 18, pp. 2338–2353, 1999.

[19] S. Tao and H. Morgan, “AC Electrokinetic Micro- and Nano-particle Manipulation and Characterization,” in *Electrokinetics and Electrohydrodynamics in Microsystems*, A. Ramos, Ed. Springer Wien New York, 2011, pp. 1–28.

[20] D. J. Shaw, *Introduction to Colloid and Surface Chemistry*. Butterworth-Heinemann, 1992.

[21] H. A. Pohl, *Dielectrophoresis: The behaviour of neutral matter in nonuniform electric fields*. Cambridge University Press, 1978.

[22] R. Aveyard and D. A. Haydon, *An introduction to the principles of surface chemistry*. Cambridge University Press, 1973.

[23] T. B. Jones, *Electromechanics of Particles*. Cambridge University Press, 1995.

[24] R. Pethig, “Review article-dielectrophoresis: status of the theory, technology, and applications.,” *Biomicrofluidics*, vol. 4, no. 2, pp. 1–35, Jan. 2010.

[25] C. T. O’Konski, “Electric properties of macromolecules. V. Theory of ionic polarization in polyelectrolytes,” *J. Phys. Chem.*, vol. 64, no. 5, pp. 605–619, 1960.

[26] A. Ramos, “Electrohydrodynamic and Magnetohydrodynamic Micropumps,” in *Microfluidic Technologies for Miniaturized Analysis Systems*, S. Hardt and F. Schönfeld, Eds. Springer Science, 2007, pp. 59–115.

[27] A. Ramos, “Electrohydrodynamic Pumping in Microsystems,” in *Electrokinetics and Electrohydrodynamics in Microsystems*, A. Ramos, Ed. Springer Wien New York, 2011, pp. 127–156.

[28] N. G. Green, A. Ramos, A. González, A. Castellanos, and H. Morgan, “Electrothermally induced fluid flow on microelectrodes,” *J. Electrostat.*, vol. 53, no. 2, pp. 71–87, 2001.

3 Materials and methods

Summary

A range of numerical and experimental techniques were employed in the investigation of plasmonic enhanced pyroelectric manipulations. This chapter details the materials used in the experiments and an overview of the experimental and numerical procedures employed in the remainder of the thesis

3.1 Introduction

This section details the numerical and experimental techniques used in the course of the research discussed in this thesis. Specific implementations of the protocols are introduced in the relevant experimental chapters. Supplementary information relating to more detailed operation of various lithographic tools, as well as optical properties of materials used during finite element modelling, can be found in Appendix C and Appendix D.

3.2 Materials

Lithium niobate wafers (500 µm thick, 4 inch diameter) were obtained from the Roditi international company, London UK. Pyrex wafers (500 µm thick, 4 inch diameter) were obtained from University Wafer, Boston, USA.

Methanol, acetone, ethanol and IPA used primarily for solvent cleaning were obtained from Fisher-Scientific.

Gold used for electron beam evaporation was obtained from Pi-KEM, UK. Aluminium and titanium for electron beam evaporation were obtained from the Kurt J Lesker Company.

Polymethyl methacrylate (PMMA), 2010 (80k molecular weight) and 2041 (241k molecular weight), was obtained from Lucite International Inc. Microposit MFCD26 developer was obtained from Shipley company Inc. Methyl-isobutyl ketone (MIBK) was obtained from Merck Chemicals Ltd.

DCVJ was obtained from Ursa Bioscience LLC. Spectroscopic grade glycerol was obtained from Sigma-Aldrich. These materials, as well as methanol, were used for fluorescent thermometry of plasmonic particles.

Chloroauric acid and sodium citrate used in gold nanoparticle synthesis were obtained from Sigma-Aldrich.

Silica beads (1–4 µm, suspended in water, no surface charge) and silver nanowires (suspended in IPA) were obtained from Sigma-Aldrich. 5 µm silica beads (dry, neutral charged and carboxylated) were obtained from Bangs Labs. HFE-7500 was obtained from Acota UK. Mineral oil (heavy) and dioctyl sodium sulfosuccinate (Aerosol-OT/AOT), a charge stabilisation agent, were obtained from Sigma-Aldrich. Silicone oil was obtained from Fisher Scientific. Almond oil was obtained from Boots, UK.

3.3 Experimental setup

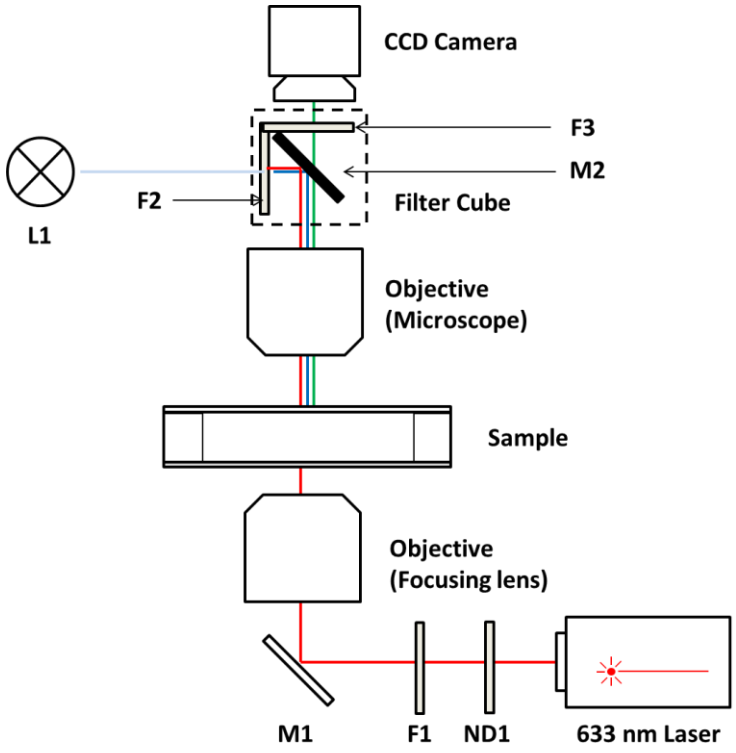

Figure 3.1: Schematic view of experimental setup

Simultaneous excitation and observation of plasmonic nanostructures, was achieved using a bespoke setup (illustrated schematically in Figure 3.1), built around an upright microscope with a

varying vertical column (Zeiss Axioscope A1.Vario), equipped with two independent and switchable light sources (L1). Bright field illumination is provided by a 100 W halogen lamp (Zeiss HAL 100 illuminator). Where necessary, fluorescence illumination is provided by a mercury arc lamp (Lumen Dynamics Excite 120q). The sample is placed on a motorized XY stage (Marzhauser Wetzlar Tango 2 desktop), which is fixed in the vertical position. Stage control is provided manually using the accompanying joystick, or automatically through software (MW Switchboard). Images are viewed and captured using a CCD camera (JAI BB-141GE) controlled with appropriate software (JAI-SDK tool). During brightfield illumination, a notch filter (Edmund Optics OD4) is placed in the light path (F3) for safety, and so that captured images are not flooded with laser light. M2 is a silvered glass reflector acting as a one way mirror. No filter is placed in position F2 during brightfield operation. Fluorescence illumination is required for thermometry purposes, where the intensity of DCVJ is imaged. During fluorescent illumination, an appropriate filter set (omega xf100-2, λ excitation = 475 nm (F2), λ emission = 525 nm (F3)) is used to provide spectrally coherent excitation. M2 is a dichroic mirror with a central wavelength at 475 nm. The optical density of the emission filter sufficiently attenuates laser excitation and performs the same function as the notch filter. DCVJ is excited at 455 nm and emits at 500 nm.

Plasmonic excitation is provided by a 633 nm diode pumped laser (Coherent Cube), which illuminates samples from below (i.e. substrate side first) through a steering mirror (M1). A continuous neutral density filter (ND1) is used to adjust the intensity of the excitation illumination. A bandpass filter (F1) centred at 630 nm is used to remove unwanted spectral components from the illumination. The laser beam is focussed using a 50× 0.5 NA objective placed on a translatable xyz mount (Thorlabs), to ensure the focal point of the illumination is coincident with plasmonic structures, regardless of minor variations in thickness between different substrates. The laser and neutral density filter are clamped to an optical riser (Newport), which is clamped to a breadboard (for major adjustments to beam alignment). The remaining optical elements are constructed using an optical cage system (Thorlabs 30 mm). The steering mirror is mounted on a gimbal with three degrees of freedom, for fine control of laser beam alignment.

The focal spot profile of the laser beam is measured using a single frame of video, analysed using a combination of ImageJ (pixel intensity) and Matlab (curve fitting). As a red laser is used, the value of the red pixel is used as a measure of the laser beam intensity. The laser beam fits a Gaussian profile with w_0 ($1/e^2$ radius) = 13 μm, as indicated below.

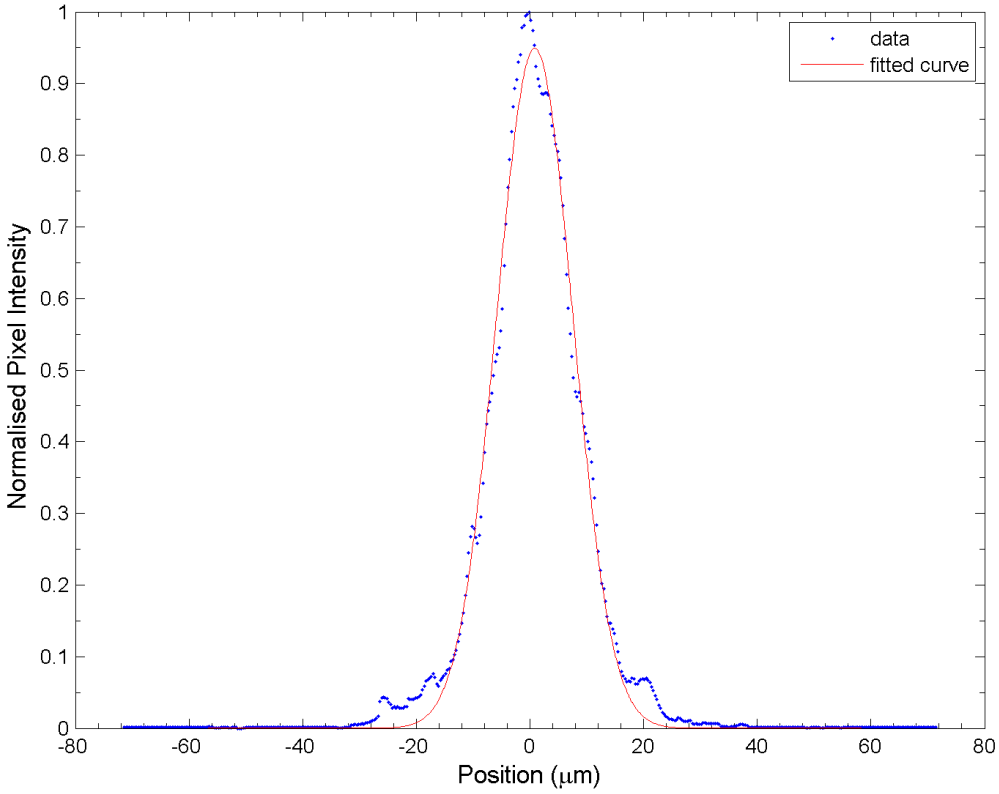

Figure 3.2: Measured distribution of laser beam intensity. Gaussian fit is plotted using a solid red line.

3.4 Fabrication of plasmonic nanostructures

3.4.1 Solvent cleaning of substrates

Pyrex and lithium niobate substrates were cleaned by ultrasonication for five minutes each in acetone, methanol, and isopropanol, and dried under nitrogen in a cleanroom environment. Prior to cleaning, substrates were cleaved to segments measuring approximately 15 mm × 10 mm.

3.4.2 Bottom up fabrication

Gold colloids fabricated using the Turkevich-Frens method (Section 3.4.2.1) are suspended in a 6% PVA matrix (4:1 dilution) [1]. Microlitre droplets are placed on cleaned substrates, and subsequently dried under vacuum conditions. Alternatively, for complete coverage of samples, the gold colloid solution is spun at 1000 rpm prior to drying.

3.4.2.1 Turkevich-Frens method

Colloidal gold particles (~17 nm diameter) were synthesised using a citrate reduction technique based on the Turkevich-Frens method [2]. Briefly, chloroauric acid ($HAuCl_4$) was diluted in water to a concentration of 1 mM, and heated at 97 °C. When condensation began, a 38 mM solution of sodium citrate in water was added to the chloroauric acid in a 10:1 solution of gold salt to citrate, and mixed using a magnetic stirrer. The solution was removed from the hotplate and cooled after ~40 minutes of stirring. The final concentration was determined using a combination of UV-VIS spectrometry (see 3.5.2), and Mie theory [3] to be (~10^{14} particles/mL or 1.3 mM). Colloid size was determined using dynamic light scattering and confirmed through scanning electron microscopy.

3.4.2.2 PVA matrix

PVA is introduced to deionised water heated at 80 °C, and stirred till it is completely dissolved. Evaporated water is replenished during mixing to ensure the final concentration of PVA is consistent with the initial weight measured.

3.4.3 Top down fabrication

Figure 3.3 shows a schematic of the processes involved in top-down fabrication (i.e. electron beam lithography) of plasmonic nanostructures. Detailed discussion of each process is given below.

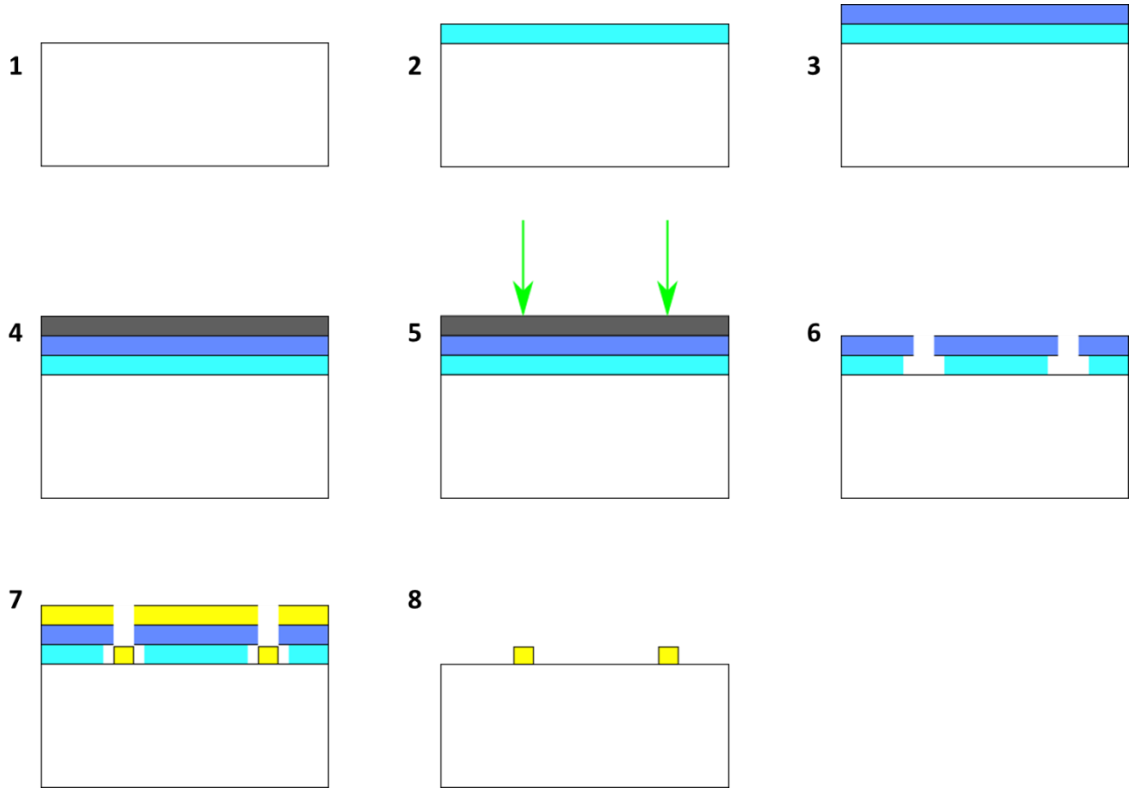

Figure 3.3: Electron beam fabrication process 1. Cleaned substrate. 2 and 3. Deposit bilayer of PMMA resists. 4. Evaporate 30 nm of aluminium charge conduction layer. 5. Expose substrate to electron beam. 6. Develop PMMA 7. Evaporate metal. 8. Perform lift-off.

3.4.3.1 Resist spinning

A positive tone resist (PMMA) was used for electron beam writing of nanostructures. A bilayer of resist was spun onto substrates comprising a low molecular weight PMMA on the bottom and a higher molecular weight PMMA solution on top (see Figure 3.3). This bilayer is required to gain the undercut profile necessary for achieving good metal lift off and good nanostructure definition [4], as since the lower molecular weight resist is more sensitive to the electron beam, a larger area receives the required clearing dose in this layer [4].

An initial layer of a 2.5% dilution of 2010 PMMA in o-xylene was spun onto substrates at 5000 rpm for one minute. This was followed by a two hour long baking step at 180 °C in an oven, for dehydration of the o-xylene solvent, leaving only the e-beam sensitive polymer. This process was repeated using a 2.5% dilution of 2041 PMMA in o-xylene. The dilution of the PMMA in o-xylene defines the resolution of the fabricated nanostructures as it affects the layer thickness. The 2.5% dilutions were used to gain highest resolution possible. The layer thicknesses, following spinning at the speeds and duration described, are approximately 40 nm and 50 nm, for 2010 and 2041 PMMA, respectively.

It was found to be necessary to incubate pyroelectric substrates at room temperature for at least 2 hours after baking, prior to applying the second layer of PMMA resist. Pyroelectric substrates acquire a surface charge in response to the heat applied in the initial bake step. This surface charge affects the adhesion of the second layer of resist to substrates. PMMA applied without this incubation period displayed an electrowetting effect which made the spin coating process difficult to control. Incubation was thus necessary to gain a uniform resist profile.

3.4.3.2 Charge conduction layer

Resist coated substrates were covered in a 30 nm aluminium layer prior to exposure in the electron beam writer. This was necessary to prevent build-up of charge on the surface of the non-conducting substrates. Such charge build-up deflects the electron beam path and can cause a significant deviation in the positioning of the described pattern. The aluminium layer was deposited using the Plassys MEB400s electron beam tool.

3.4.3.3 Electron beam lithography

Samples are patterned using the Vistec VB6 UHR EWF electron beam lithography tool. The instrument writes a pattern onto the substrate by selectively exposing it to a 100 kV electron beam at vectors detailed in a submitted design file. This design file is created using L-Edit CAD software, and exported as a graphic data systems (GDS) file for further processing. Layout beamer software converts designed geometries into smaller trapezoidal shapes (more compatible with the allowed shaping of the electron beam) in a process called fracturing.

The dose (charge density of the electron beam) for the structures used in this process was selected to be 1750 µC/cm, after performing dose tests between 500 and 3000 µC/cm to verify the reproducibility of each shape. Arrays were written in square arrays with 500 µm side length using a 1 nA, 4 nm diameter beam with a beam step size of 3.75 nm, and a VRU (variable resolution unit) of 3. These parameters are fixed using the belle software which collates this information with the fractured pattern for easy operation of the electron beam tool.

3.4.3.4 Resist development

Following beam-writing, substrates are incubated in Microposit CD26 developer for 2 minutes. This selective etchant removes the charge conducting aluminium layer, leaving the patterned PMMA resist intact. The sample is rinsed in deionised water and developed in 2.5:1 dilution of MIBK in IPA for 30 seconds. As PMMA is a positive tone resist, areas exposed to the electron beam are more soluble than unexposed areas and, as such, are washed away. The substrates are subsequently washed in IPA for 1 minute to stop development. Finally, samples are placed in a Gala Plasma Prep 5 oxygen barrel asher (pattern side up) for 30 seconds at 40 W, for plasma treatment. This removes unwanted resist inaccessible to the MIBK and IPA solvent during the development process, by etching ~2 nm of resist residue at the bottom of patterned features. This step thus aids uniform adhesion of metals to the substrates.

3.4.3.5 Gold metallisation and lift-off

Cleaned and developed substrates are metallised using the Plassys MEB400s electron beam evaporator. A 2 nm layer of titanium is deposited as an adhesion layer followed by a 25 nm layer of gold. The total thickness is chosen to be less than 40 nm (i.e. the thickness of the base PMMA layer) for easy removal of the undeveloped resist during the lift off process.

Metallised substrates were placed in a warm (50 °C) acetone bath for a two hour period to dissolve unwanted PMMA. Lift off was performed by agitating the acetone solution with a pipette. A one minute sonication step was necessary, if this agitation did not prove to be sufficient, to remove undeveloped PMMA. Substrates were cleaned by sonication in an IPA solution (to ensure removed metal aggregates were not redeposited onto the substrates), and dried under a stream of nitrogen prior to use, or storage under vacuum in a desiccator. An illustration of a substrate following the fabrication of plasmonic arrays is given in Figure 3.4. An alignment marker (circled) is patterned, the position of which is used to indicate the orientation of plasmonic structures relative to the polarisation of laser beam.

3.5 Characterisation of plasmonic nanostructures

3.5.1 SEM

Scanning electron micrographs of fabricated nanostructures were taken using a Hitachi S-4700 SEM tool. Prior to loading, samples were coated with gold/palladium (80/20) using an Agar sputter coater operating at 20 mA for 45 seconds. The agar sputter coater deposits metals at a rate of 9 nm per minute when the input current is 20 mA. The estimated final thickness of gold/palladium is thus 6.75 nm. Micrographs of colloidal structures were taken with the SEM tool operating at 5 kV. All other images were collected using a 10 kV acceleration voltage.

3.5.2 UV-VIS absorption spectrophotometry

Optical characterisation of fabricated plasmonic structures was carried out using a Shimadzu UV-3101 pc absorption spectrophotometer and a linear thin film polariser (where necessary). Planar samples were mounted on a bespoke holder with a 1 mm diameter pinhole. Fabricated arrays are aligned to this pinhole such that changes in light intensity at the detector are purely a result of the plasmonic activity of the aligned array. A plain piece of Pyrex is placed on an identical holder and placed on the reference arm. The system was operated between 400 and 800 nm.

Soluble samples (i.e. colloidal gold) were placed in a 3 mL cuvette and mounted at the sensing arm. Deionised water is placed in an identical cuvette and mounted at the reference arm. Operation is as with planar samples.

The spectrophotometer characterises plasmonic activity with an extinction type measurement (i.e. absorption and scattering losses are considered simultaneously). Rather than the previously defined extinction cross section, the instrument measures extinction using a transmittance value expressed either as a percentage or in a decibel format given by [5]:

$$T = \frac{I}{I_0} \times 100, \tag{3.1}$$

or [5],

$$Abs = -\log\frac{I}{I_0}, \tag{3.2}$$

where I is the transmitted light intensity (i.e. intensity of the light at the measurement arm), and I_0 is the incident light intensity (intensity of light at the reference arm).

An estimate of the extinction cross section can be made using the following relationship [6], [7]:

$$\sigma_{\text{ext}} N = 1 - T, \tag{3.3}$$

where N is the two dimensional particle density i.e. the number of particles per unit area considered. Using this relationship, experimentally derived plasmon resonance activity can be compared more readily to simulated data.

3.5.3 Dynamic light scattering

Dynamic light scattering was performed using a Malvern Zeta-sizer ZS90 tool to estimate the size and monodispersity of fabricated solutions of colloidal gold.

3.5.4 Dark field microscopy

Dark field microscopy was used as a quick non-destructive confirmation of the success of fabrication. The resonant scattering of plasmonic structures coupled with the high contrast of dark field microscopy enhances the visibility of sparsely populated arrays, as illustrated in Figure 3.4. Observation was performed using a Zeiss Axio Imager-A1 microscope with a Jenoptik ProgRes cf CCD camera capturing images.

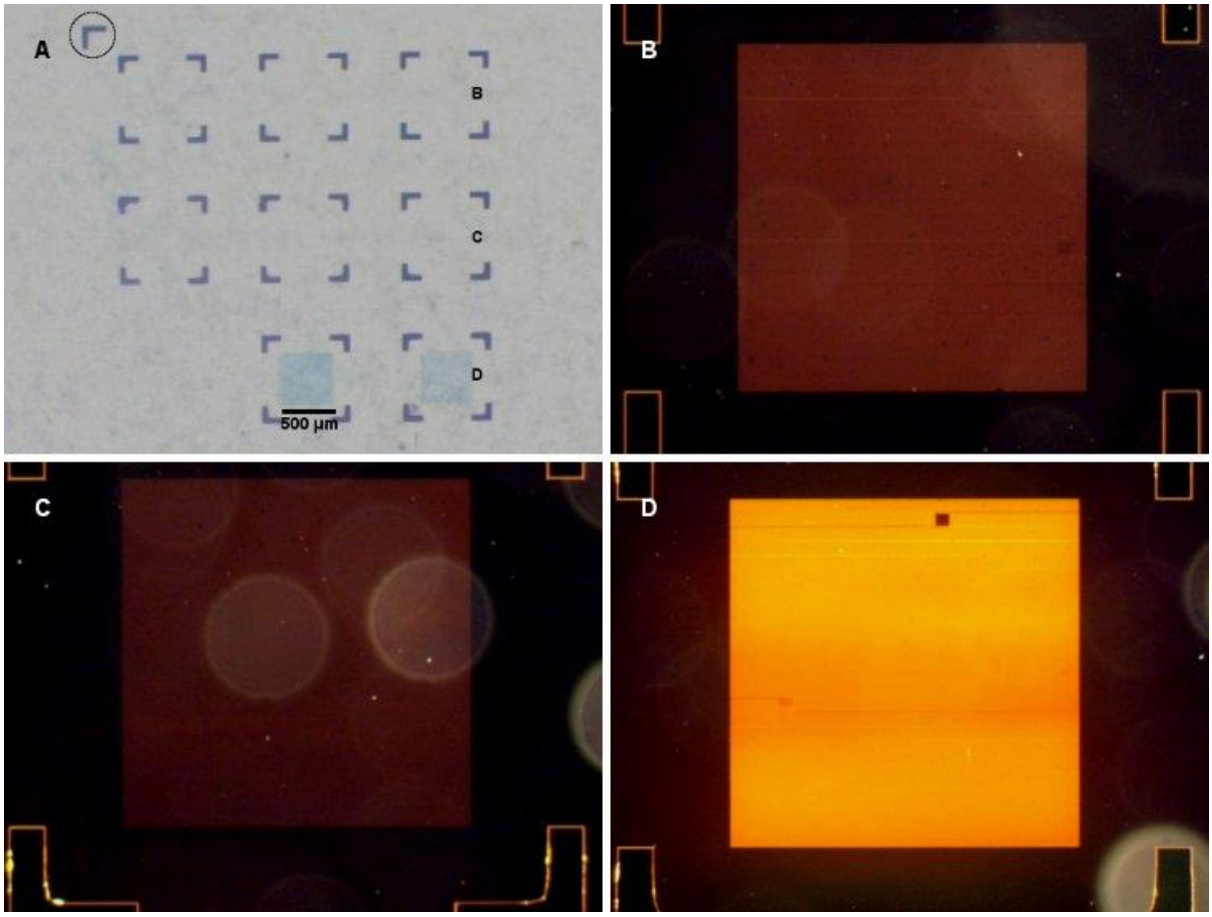

Figure 3.4: A) Bright field micrograph of a completed device showing alignment marker (circled) used for polarisation. B) Dark field micrograph of array labelled B. Resonant scattering of plasmonic structures enhances the visibility of the array in comparison to the bright field image. C) Dark field micrograph of array labelled C. D) Dark field micrograph of array labelled D.

3.6 Sample preparation

3.6.1 Microfluidic chamber construction

A microfluidic chamber (illustrated in Figure 3.5) is created by reversibly bonding a 180 µm thick coverslip to a 500 µm thick substrate (Pyrex or lithium niobate) with 100 µm thick double-side adhesive tape spacers. The chamber is constructed to be 10 mm wide, such that 4 plasmonic arrays fit within the microfluidic chamber with good clearance from the channel walls at each extremity.

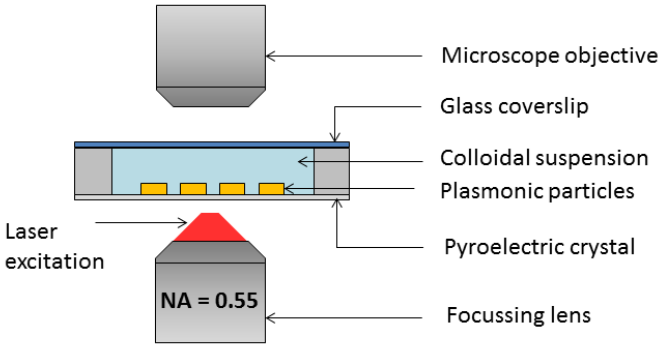

Figure 3.5: Illustrative image of completed microfluidic chamber undergoing stimulation. This image is not to scale

3.6.2 Solvent swap

Trapping experiments required the suspension of particles in non-polar, electrically insulating media (Chapter 5). To ensure miscibility, particles supplied in aqueous solvents are transferred through a solvent of intermediate polarity (ethanol). Particles are centrifuged for 5 minutes at 5000 rpm and re-suspended in ethanol. Centrifugation is repeated twice to wash particles and minimise the transfer of aqueous solvents to new media (solvent is renewed following each wash step).

3.6.3 Surface activity

Electrophoretic mobility and zeta potential of particles in a symmetric electrolyte (0.1 mM KCl) was checked using the Malvern Zeta-sizer ZS90 tool.

3.6.4 DCVJ reconstitution

1 mg vials of dry DCVJ (stored at -8 °C) are allowed to stand at room temperature for 15 minutes to equilibrate. 50 µL of the buffer, a 4:1 glycerol-methanol mix, is added to the vial and vortexed. 20 µL of this stock solution is added to 3 mL of buffer for use in fluorescent thermometry experiments. The final DCVJ concentration used in thermometry is 0.5 mM.

3.6.5 Calibrating thermal response of DCVJ

The response of the DCVJ solution is calibrated by plotting the fluorescence intensity from an average of 50 images against temperature. DCVJ is placed in a microfluidic chamber, and thermal stimulation is applied uniformly to the solution using a hot plate. The temperature is adjusted by 5 °C increments from room temperature (25 °C) to 90 °C. The temperature of the bulk DCVJ solution is independently verified using a thermal imaging camera (Flir E60bx).

Colour images (illustrated in Figure 3.6) were processed (converted to grayscale, time averaged and intensity profiled) using ImageJ to create the calibration curve (normalised against peak intensity at room temperature) displayed in Figure 3.7. The relationship is approximated by an exponential decay as suggested by the Forster-Hoffman relationship.

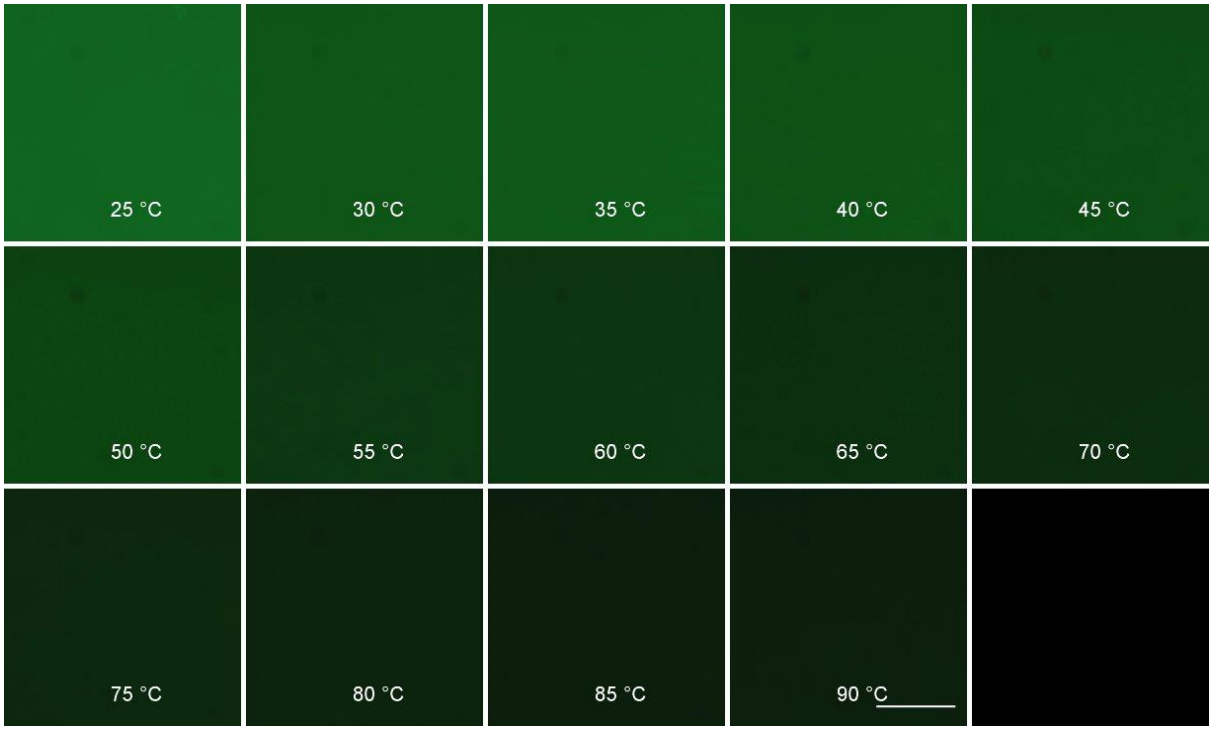

Figure 3.6: Colour images of DCVJ solution used to create calibration curve. Change in intensity is a result of increase in temperature. Scale bar is 50 µm

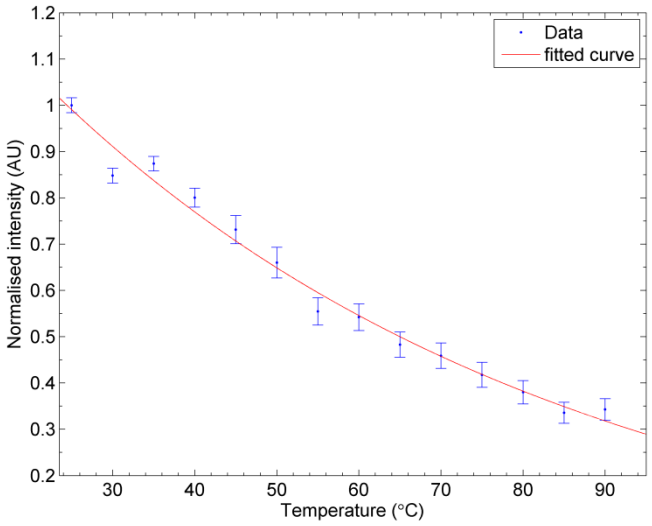

Figure 3.7: Calibration curve displaying normalised fluorescence intensity as a function of temperature. An exponential decay describes the relationship between temperature and fluorescence intensity. Error bars are the standard deviation of the intensity of fifty recorded images.

3.6.6 Fluorescent imaging

Fluorescent imaging of DCVJ solution was performed using a microscope operating with a 20× 0.5 NA objective. Fifty fluorescent images are collected at each laser power using a CCD operating at 30 Hz. Images are collected before, during and after laser stimulation. Camera gain, acquisition speed, and exposure time (33 ms), are set manually using the JAI-SDK tool, which also saves acquired images. Unless otherwise stated, plasmonic structures are stimulated for 1.5 seconds with continuous wave illumination. Baseline fluorescence intensity is gained by calculating the average fluorescence intensity before and after laser stimulation. The ratio of the fluorescence intensity during stimulation to this baseline is used to calculate the temperature change. The temperature reported is calculated from the average intensity of a sequence of 50 recorded images.

3.7 Simulation procedures

3.7.1 FEM of plasmon resonance

Finite element modelling of metallic structures was performed in order to estimate the magnitude and position of plasmon resonance peaks. Simulations were performed using the electromagnetic waves module in COMSOL 3.5a [8], which solves the harmonic wave equation.

The harmonic wave equation was solved in the visible region (i.e. between 400 and 800 nm) at 25 nm intervals.

Plasmonic scatterers are placed in three concentric spheres defining a near field boundary for the computation of the scattering cross section, and inner and outer boundaries of a perfectly matched layer (for the absorption of plane wave excitation at the edge of the simulation space) [9]. A scattering boundary condition is applied on the external boundaries. The simulation space is halved in the direction of wave propagation, to simulate transmission between two media.

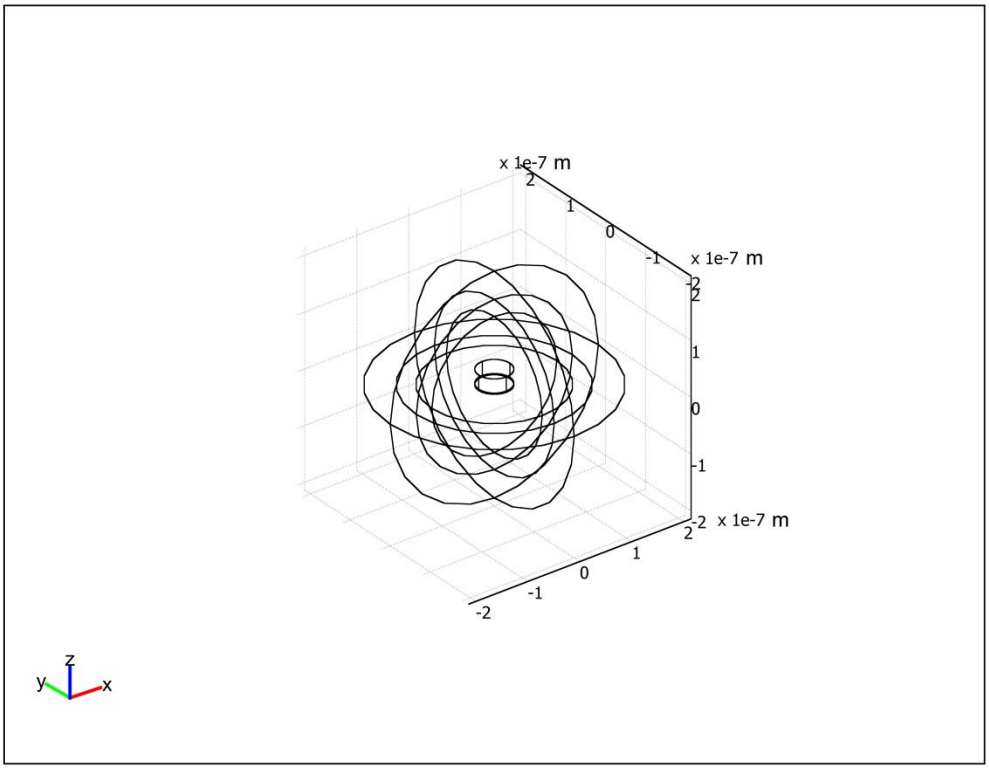

Figure 3.8: 3D projection of geometry of plasmonic simulation domain.

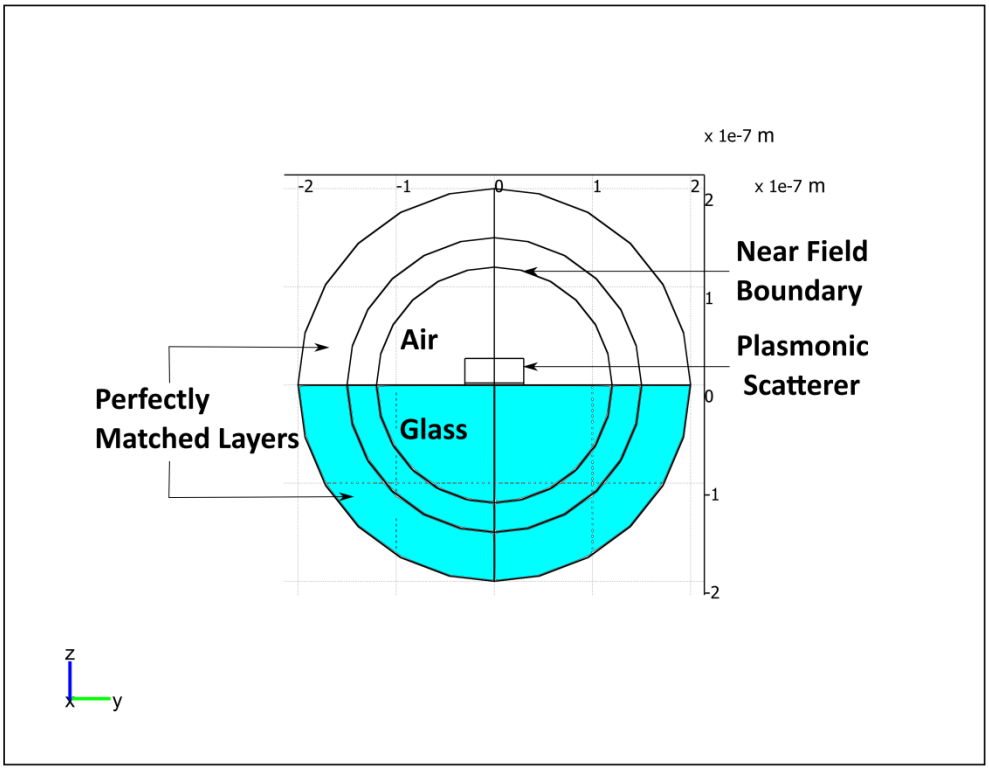

Figure 3.9: 2D projection of plasmonic simulation problem space. Labels depict relevant boundary conditions.

Laser excitation is approximated using a linearly polarised plane wave propagating in the z direction. The equation for an x-polarised wave is given as,

$$\boldsymbol{E} = E_0\, e^{-in_m k_0 z}\hat{x}, \tag{3.4}$$

where the relationship between I (irradiance) and E_0 is given by:

$$I = \frac{nc\varepsilon|E_0|^2}{2} \tag{3.5}$$

For a Gaussian beam, irradiance is related to laser power by:

$$I = \frac{2P_0}{\pi {w_0}^2}\exp -\frac{2(x^2+y^2)}{{w_0}^2}, \tag{3.6}$$

where w_0 is the beam radius and P_0 is the laser power.

To accurately model the effects of light transitioning between two boundaries, the Fresnel coefficients are used [10]:

$$r = \frac{1-m}{1+m} \tag{3.7}$$

$$t = \frac{2}{1+m} \tag{3.8}$$

$$m = \frac{n_2}{n_1}, \tag{3.9}$$

where r is the reflection coefficient and t is the transmission coefficient.

Excitation (i.e. background wave) in different halves of the simulation region is given by [10]:

$$\begin{aligned} a)\boldsymbol{E}_{|\boldsymbol{z<0}} &= (E_0\, e^{-in_1k_0z} + rE_0\, e^{in_1k_0z})\hat{x} \\ b)\ \boldsymbol{E}_{|\boldsymbol{z>0}} &= tE_0\, e^{-in_2k_0z}\hat{x}, \end{aligned} \tag{3.10}$$

when $n_1 = n_2$ (i.e. for a plasmonic scatterer in a homogenous medium), the equation above is identical to the plane wave equation previously described.

3.7.2 FEM of plasmonic heating

The heat generation module in COMSOL is used to solve the heat conduction equation in a stationary condition to model plasmonic heating. Infinite elements are used to simulate an unbounded background extending beyond the geometrically defined simulation space (in this way, they are analogous to the perfectly matched layers used previously). External boundaries are fixed to 25 °C. Heat power is defined using the internally calculated resistive loss. The expression used matches the derivative form of the volumetric heat source density defined in Chapter 2 (Equation (2.7)).

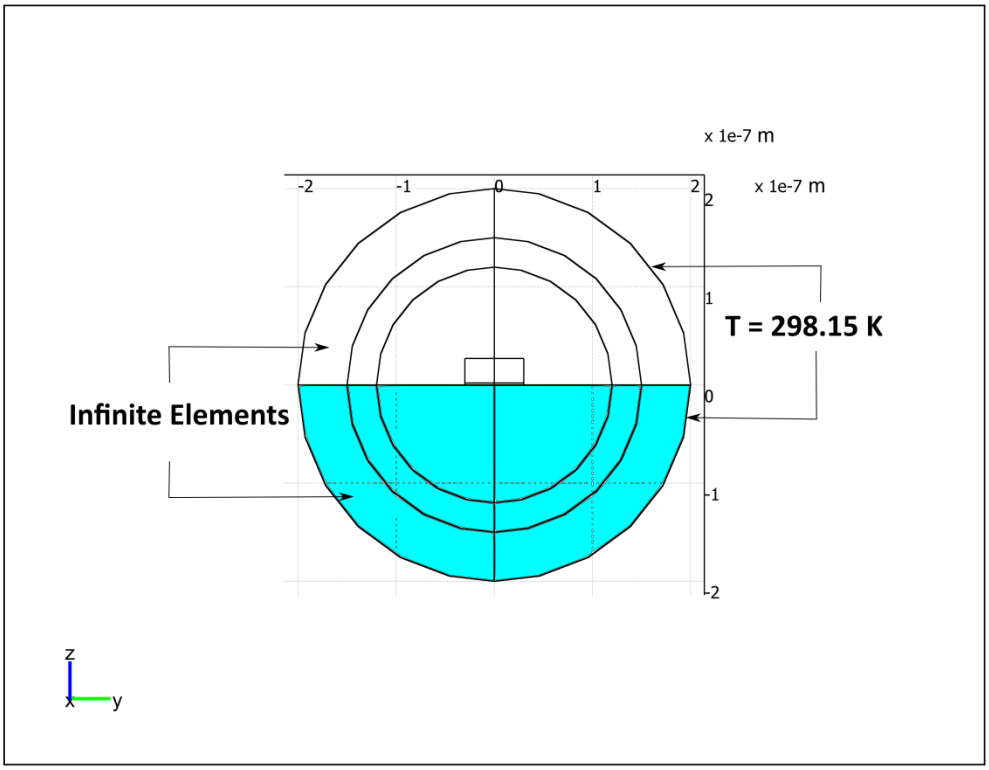

Figure 3.10: 2D projection of problem space used for modelling of single nanoparticle heating. This is identical to the plasmonic simulation space. Labels depict boundary conditions.

3.7.3 FEM of microfluidic system

The microfluidic system was modelled in two dimensions in order to avoid the complications associated with meshing discrete elements of vastly varying size (e.g. 500 µm substrate thickness compared with 25 nm nanoparticle thickness). The simulation geometry is illustrated in Figure 3.11 and is used to model the coupled thermodynamic, fluid dynamic, and electrical behaviour of the microfluidic system. By selecting appropriate boundary conditions, the influence of the array of plasmonic nanoparticles can be considered without rigorously solving the electromagnetic wave equation in three dimensions. The table below gives an overview of the boundary conditions used in solving the different partial differential equations describing electrical, thermal, and mechanical behaviour. These are discussed further in the sections below.

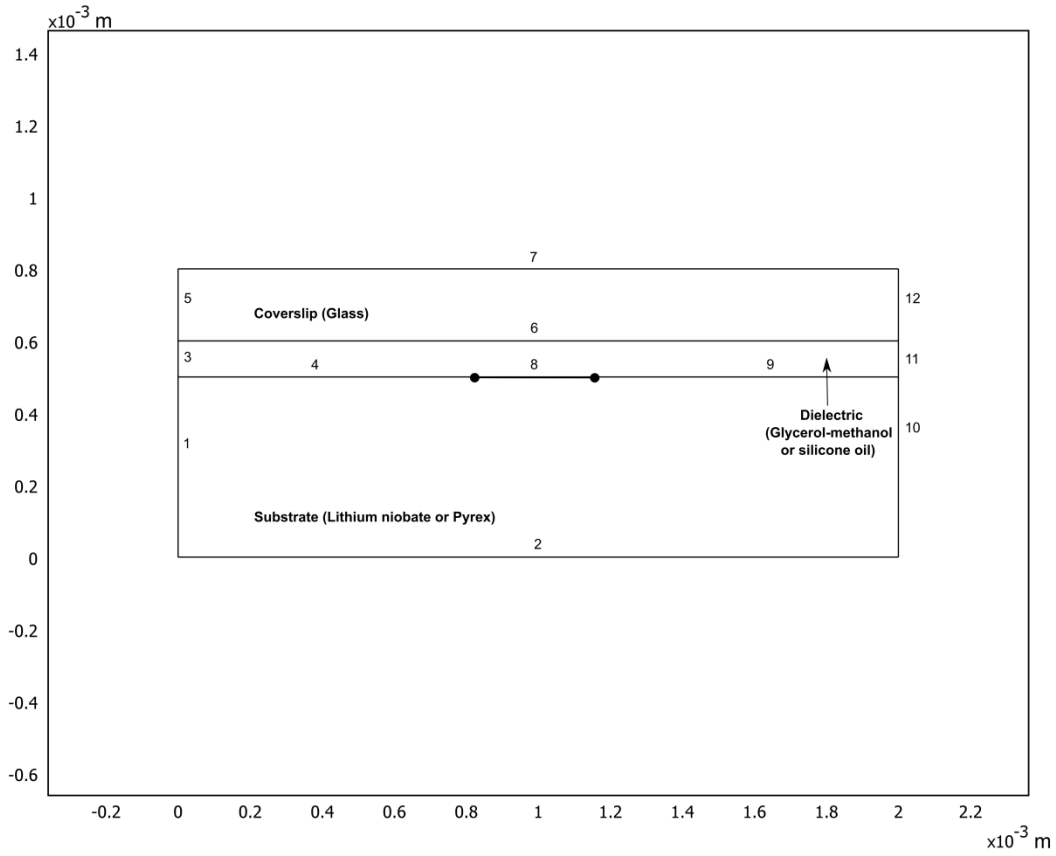

Figure 3.11: Geometry of problem space used for finite element modelling of microfluidic system. Boundaries are numbered, boundary conditions are discussed below.

Table 3.1: Boundary conditions used in finite element simulations associated with geometry defined in Figure 3.11.

Boundary index	Heat transfer	Electric field	Fluid mechanics
1	Insulation	Electrical insulation	N/A
2	Fixed temperature	Ground	N/A
3	Insulation	Electrical insulation	Open boundary
4	Continuity	Continuity	Wall (no slip)
5	Insulation	Electrical insulation	N/A
6	Continuity	Continuity	Wall (no slip)
7	Fixed temperature	Ground	N/A
8	Heat source (Highly conductive layer)	Continuity	Wall (no slip)
9	Continuity	Continuity	Wall (no slip)
10	Insulation	Electrical insulation	N/A
11	Insulation	Electrical insulation	Open boundary
12	Insulation	Electrical insulation	N/A

3.7.3.1 Heat generation

Plasmonic heating is estimated using a two dimensional heat generation model. External boundaries in the z direction are given a fixed temperature. External boundaries in the x direction are given an insulation condition, i.e. $\frac{dT}{dt} = 0$, as these boundaries do not conform to the actual edge of the experimental domain (i.e. simulation domain is truncated in the x direction). With the exception of boundary 8 (the plasmonic nanoarray/heat source), continuity of temperature change in the z direction is enforced at the internal boundaries. Boundary 8 is defined as a highly conductive 25 nm thick gold layer, used to simulate the array of plasmonic structures. Due to the pitch of the arrays considered, plasmonic self-heating is negligible. The plasmonic heat power is defined at this boundary as:

$$Q = \sigma_{\mathrm{abs}} N \cdot I, \tag{3.11}$$

where σ_{abs} is the absorption cross section of a single plasmonic nanoparticle, N is the two dimensional particle density and I is the spatially dispersive laser intensity modelled as a Gaussian beam whose equation is given by:

$$I = \frac{2P_0}{\pi {w_0}^2} \exp -\frac{2x^2}{{w_0}^2} \exp -az \tag{3.12}$$

The addition of an exponential decay function dependent on thickness is to account for absorption of the laser beam by the substrate. a is the Napierian absorption coefficient of a specific substrate. The magnitude of the predicted temperature increase is verified analytically using Equation (2.31).

3.7.3.2 Pyroelectric field generation

Pyroelectric field generation is modelled using the electrical currents module operating with a time harmonic formulation. As the model is setup in two rather than three dimensions, the z direction is synonymous with the polar plane in this configuration. Pyroelectric response is modelled as a remanent electrical displacement. To account for the temperature dependent nature of the pyroelectric field, this module is coupled to the heat generation module. Solutions for temperature generated by an array are used to evaluate the remanent electric displacement. This is used as an additional term in the constitutive equation i.e.

$$D = \varepsilon_0 \boldsymbol{\varepsilon}_\mathbf{r} \cdot E + \boldsymbol{D}_\mathbf{r} \tag{3.13}$$

$$\boldsymbol{D}_\mathbf{r} = \begin{bmatrix} 0 \\ \gamma_z \end{bmatrix} \Delta T, \tag{3.14}$$

where γ_z is the material specific pyroelectric coefficient (-8.3 × 10^{-5} C/ m·K for lithium niobate).

Using the above expression, the electric currents module solves Gauss's law for charge conservation in a quasi-static state to calculate the electric field accounting for the conductive and capacitive responses of the fluid and pyroelectric.

Similar to the heat transfer model, the edges of the simulation domain in the x direction do not conform to the edge of the simulation geometry. Hence, external boundaries are modelled as electrically insulating.

3.7.3.3 Fluid dynamics

Finite element modelling of fluid mechanical forces was performed to obtain the velocity field in the microfluidic system, by using the incompressible fluid module to solve the Navier-Stokes and mass-conservation equations given by:

$$\eta \nabla^2 u - \nabla p + f = 0 \tag{3.15}$$

$$\nabla \cdot u = 0, \tag{3.16}$$

where η is the fluid viscosity, u is the velocity field, p is the pressure, and f is a volumetric force (i.e. body force). The formulation of the Navier-Stokes equation assumes a low Reynold's number.

Solutions were computed only in the fluid domain i.e. substrate and coverslip domains are ignored. External boundaries in the z direction (in this case those at the substrate-fluid and coverslip-fluid interface) are modelled as a wall, with slip conditions applied where appropriate. External boundaries in the x direction are modelled as open boundaries. Body force terms are added depending on the particular effect being simulated (Chapter 5).

3.8 Particle tracking procedures

3.8.1 Image processing

Recorded image sequences are processed in ImageJ [11]. A region of interest (480 × 480 pixels) is cropped from the raw image sequence (the laser spot is located centrally). To suppress the filtered laser spot, the colour images are split into individual composite channels (red, green and blue) of which only the green channel is considered. The background is removed using a rolling ball correction method. The lookup table of the resulting imaging sequence is inverted so that particles appear white on a dark screen. Finally, the mean of the image sequence is subtracted from individual images, to remove static camera artefacts. Doing this allows easy isolation of particles in motion.

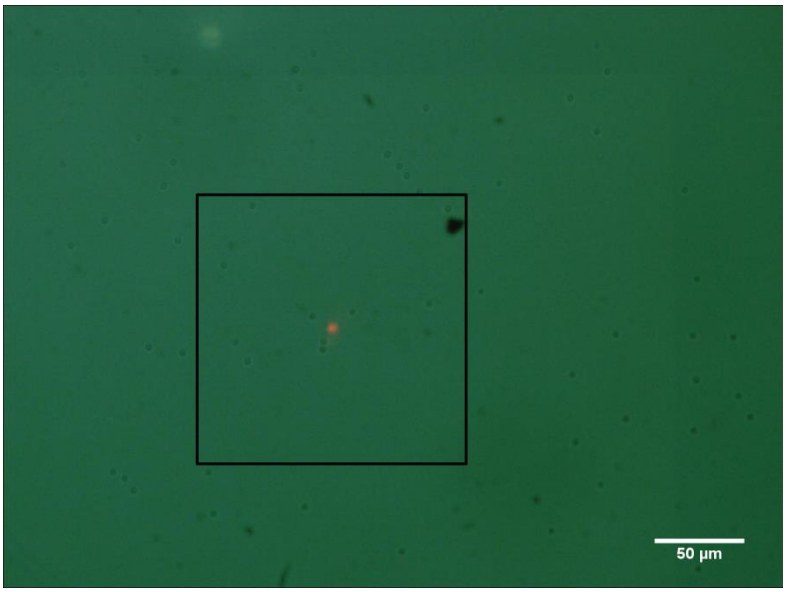

Figure 3.12: Illustration of a single frame of recorded video showing region of interest.

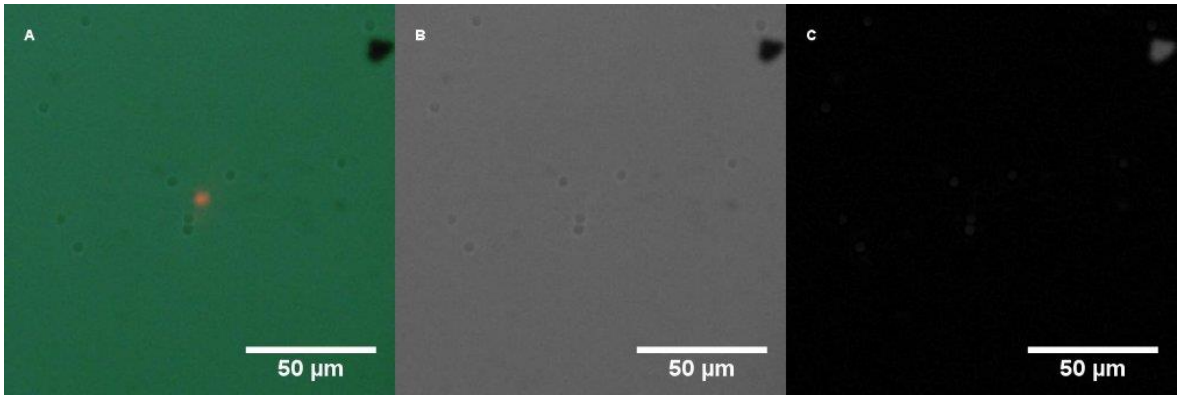

Figure 3.13: Results of image processing a region of interest of a frame of recorded footage A) Frame is cropped. B) Green channel is extracted. C) Background removal and LUT inversion yields grayscale image.

For processes where identification of individual particles is not necessary (i.e. ensemble behaviour is being considered), grayscale images are converted to binary using ImageJ's implementation of the triangle method, an algorithm described in [12]. Briefly, the algorithm constructs a right-angled triangle using the histogram of pixel intensities from the image. The height of this triangle is the frequency of the most abundant pixel intensity (i.e. the background), and the width is the range between the intensity of the background and the brightest pixel (see Figure 3.14). A series of lines coinciding with the histogram are drawn perpendicular to the hypotenuse of this triangle. The threshold is set where the length of this perpendicular line is maximised. Figure 3.15 displays a binary image produced using the triangle algorithm.

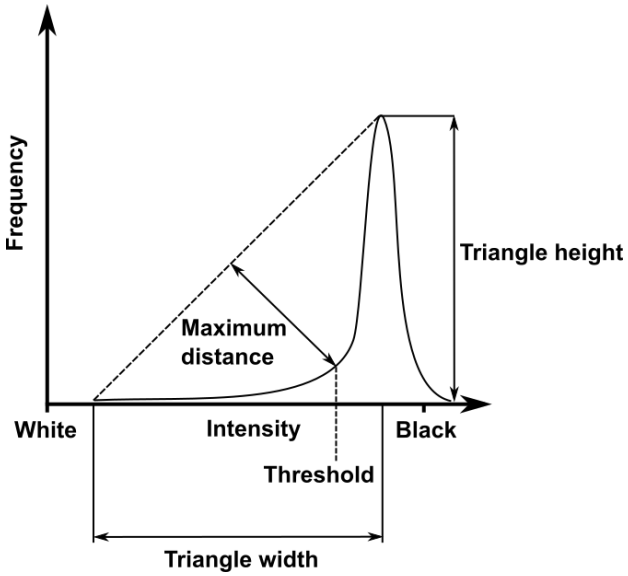

Figure 3.14: Determining threshold pixel intensities using the triangle algorithm. This illustration is adapted from [12]**.**

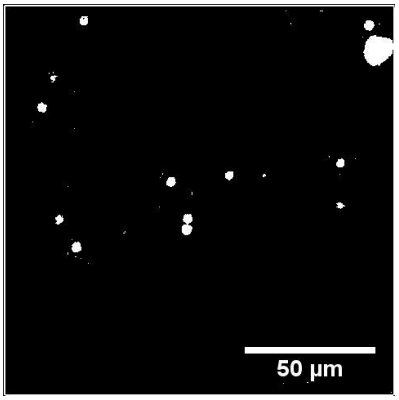

Figure 3.15: Binary image produced as a result of applying triangle algorithm.

3.8.2 Particle tracking

Particle tracking of processed image sequences is performed using Trackmate [13], an ImageJ plugin. Particle tracking occurs in two steps: particle identification and linking. Particles in image sequences are identified as significant changes in intensity (based on the magnitude and spatial extent) in the Fourier space. Identified particles are linked using a linear assignment problem algorithm (adapted from [14]), which searches for the best matches within a 25 µm radius. To ensure trajectories are continuous, a maximum frame gap (15 frames) is defined which details the acceptable period of time particles can be obscured from the field of view. The maximum gap closing distance (25 µm) details how far a particle is allowed to travel undetected before it is identified as a different particle. Edge features (e.g. particle size, location) are used to ensure trajectories are not spuriously linked.

Semi-automated particle tracking was necessary in some cases (e.g. for stationary mean-squared displacement measurements) where particles coincided with the laser beam, and image processing supressed their identification. In such instances, particle tracking was performed using Tracker [15], a Java based particle tracking program. Image sequences are spatially and temporally calibrated using a graphical user interface. Individual particles are identified manually by the user. Tracking is performed using a nearest neighbour algorithm with the user intervening when the software fails to find a good enough match in the radius defined.

3.9 References

[1] M. de Angelis, P. Matteini, F. Ratto, R. Pini, S. Coppola, S. Grilli, V. Vespini, and P. Ferraro, "Plasmon resonance of gold nanorods for all-optical drawing of liquid droplets," *Appl.*

Phys. Lett., vol. 103, no. 16, p. 163112, 2013.

[2] J. Turkevich, “Colloidal gold. Part I,” *Gold Bull.*, vol. 18, no. 4, pp. 125–131, 1985.

[3] W. Haiss, N. T. K. Thanh, J. Aveyard, and D. G. Fernig, “Determination of Size and Concentration of Gold Nanoparticles from UV - Vis Spectra,” *Anal. Chem.*, vol. 79, no. 11, pp. 4215–4221, 2007.

[4] Z. Cui, *Nanofabrication: Principles, Capabilities and Limits*. New York: Springer Science, 2008.

[5] U. Kreibig and M. Vollmer, *Optical Properties of Metal Clusters*. Springer-Verlag Berlin Heidelberg, 1995.

[6] C. Langhammer, Z. Yuan, I. Zoric, and B. Kasemo, “Plasmonic Properties of Supported Pt and Pd Nanostructures,” *Nano Lett.*, vol. 6, no. 4, 2006.

[7] G. W. Bryant, F. J. Garcıa de Abajo, J. Aizpurua, P. Hanarp, D. S. Sutherland, and M. Kall, “Optical Properties of Gold Nanorings,” *Phys. Rev. Lett.*, vol. 90, no. 5, pp. 5–8, 2003.

[8] “COMSOL Multiphysics Modeling Software.” [Online]. Available: https://www.comsol.com/.

[9] J. Berenger, “A perfectly matched layer for the absorption of electromagnetic waves,” *J. Comput. Phys.*, vol. 114, no. 2, pp. 185–200, Oct. 1994.

[10] C. F. Bohren and D. R. Huffman, *Absorption and Scattering of Light by Small Particles*. John Wiley & Sons, 1983.

[11] “ImageJ.” [Online]. Available: http://imagej.net/Welcome.

[12] E. Rogers, G. W. Zack, and S. A. Latt, “Automatic Measurement of Sister Chromatid Exchange Frequency,” *J. Histochem. Cytochem.*, vol. 25, no. 7, pp. 741–753, 1977.

[13] N. Perry, J. Tinevez, and J. Schindelin, “Trackmate - ImageJ.” [Online]. Available: http://imagej.net/TrackMate.

[14] K. Jaqaman, D. Loerke, M. Mettlen, H. Kuwata, S. Grinstein, S. L. Schmid, and G. Danuser, “Robust single-particle tracking in live-cell time-lapse sequences,” *Nat. Methods*, vol. 5, no. 8, pp. 695–702, 2008.

[15] D. Brown, “Tracker Video Analysis and Modeling Tool for Physics Education.” [Online]. Available: http://physlets.org/tracker/.

4 Fluorescence thermometry of plasmonic arrays

Summary

In this chapter, thermal generation of plasmonic nanostructures is investigated using a fluorescence intensity thermometry technique which allows for thermal imaging at the microscale. The influence of single particle geometry, inter-particle spacing, and supporting substrate on generated temperature are investigated experimentally and results are compared to analytical and numerical models. Possible reasons for discrepancies between the theoretically and experimentally derived results are discussed with emphasis placed on the impact this has on estimating the magnitude of the pyroelectric field. The chapter concludes with a discussion on possible experimental and computational improvements to the described technique which should improve the accuracy of results.

4.1 Introduction

The issue of temperature sensing to a micrometre scale and below is one which is crucial for determining the efficiency of thermal generation in plasmonic structures and by extension, the magnitude of generated pyroelectric field (in the context of this work). As heat (particularly in microfluidic environments) is diffusive/non-propagative [1], an intermediate conduit is required to quantitatively probe the thermal activity of a material of interest. This is made difficult by the operation of the traditionally used avenues (e.g. thermocouples, thermal resistors, IR imaging), whose resolution is broadly dependent on the size of their active element. As such, though they are able to sense temperature changes, the magnitude of these can be underestimated as these will need to be sufficiently large to register as more than just a fluctuation. In addition, where it is technically possible to fabricate such sensors with nanometre resolution (e.g. scanning thermal microscopy [2]), their operation is invasive (i.e. integration with plasmonic structures can affect their function) [3]. Hence, such techniques are often of little relevance to investigating plasmonic heating beyond a simple of confirmation of any thermal response of an array of plasmonic structures to laser excitation. More novel techniques have made use of the intrinsic properties of a variety of materials [3], [4] to detect local changes in temperature (e.g. fluorescence polarisation [5], [6], changes in refractive index [7], [8], phase changes in surrounding material [9]) to varying degrees of success. Fluorescence intensity thermometry [10] is frequently used for microfluidic thermal imaging due to the ease of deployment with conventional laboratory equipment.

In this chapter, fluorescent molecular rotors are used to perform fluorescence intensity thermometry on plasmonic structures in a manner which can be perceived to serve as a compromise between the ease of deployment (no additional optics required) of the more traditionally used fluorescence techniques, and the accuracy of anisotropy and lifetime spectroscopic based methods. In contrast to some of the other techniques mentioned, thermometry can be performed in environments more representative of those in which further experiments are performed. Results are compared to numerical predictions, and suggestions for the improvement of the technique are made.

4.2 Theoretical preamble

Fluorescence occurs when the return of a molecule's orbital electron from an excited singlet state to a ground state is accompanied by the emission of a photon. There are a number of different avenues (e.g. conformational changes) through which a molecule can relax to a ground state without the accompanying radiation of an emitted photon. Fluorescence only occurs if the lifetimes of these processes are not similar to, or shorter than the fluorescence lifetime (i.e. the time the electron spends in an excited state). A crucial distinction between fluorescence and other photoluminescence phenomena (e.g. phosphorescence) is the fact that transition to an intermediate triplet state (through non-radiative means), and subsequent relaxation from said state, does not occur.

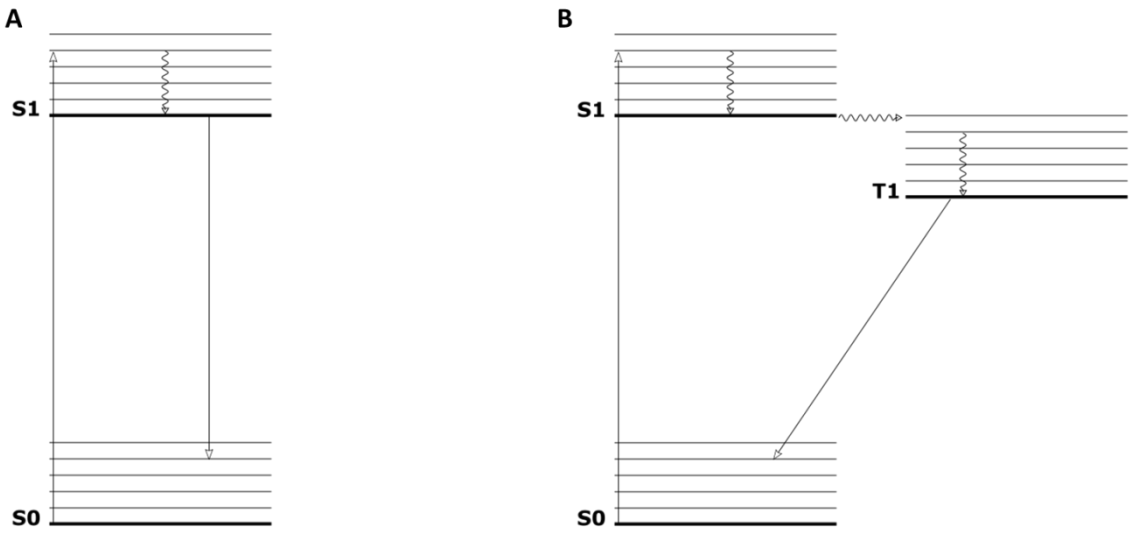

Figure 4.1: Jablonski diagrams depicting energy transfer in fluorescence (A) and phosphorescence (B) [11]**. A) Photoabsorption excites electrons to a higher electronic state. Internal conversion processes relax the electron to its**

lowest vibrational energy level in this electron state. Electrons return to a ground state accompanied by emission of a photon. B) Photoabsorption excites electrons to a higher electronic state. Isoenergetic levels of different electron states exist allowing for a transition between singlet and triplet electron levels. Vibrations occur bringing the electron to its lowest vibrational level in this triplet electron state before relaxation to the ground state accompanied by photon emission occurs.

An important characteristic of fluorescent molecules is quantum yield (Φ), which is the ratio of photons emitted after excitation to those absorbed during excitation i.e.

$$\Phi = \frac{N\ emitted\ photons}{N\ absorbed\ photons} \tag{4.1}$$

This can alternatively be written as:

$$\Phi = \frac{k_r}{k_r + k_{nr}}, \tag{4.2}$$

where k_r and k_{nr} are rate constants for radiative and non-radiative processes respectively. There is an intuitive link between quantum yield and fluorescent intensity. As fluorescence intensity (I_f) is simply a measure of the number of photons emitted as a result of fluorescence, the relationship between intensity and quantum yield can be written as:

$$I_f \approx k\Phi I_{A,} \tag{4.3}$$

where I_A is the intensity of absorbed light and k is an undefined constant of proportionality incorporating such things as instrument response. This relationship is valid for fluorescent probes with spectrally narrow emission characteristics [11].

Fluorescent molecular rotors form twisted intramolecular charge transfer (TICT) states upon photoexcitation [11], [12]. As a result, electronic relaxation from an excited state occurs primarily through photon emission, or through electron movement between electron donor and acceptor units in the molecule, a process which is frequently non-radiative. A key feature of molecular rotors is the predictability of this non-radiative pathway. While other fluorophores can lose energy non-radiatively, these processes are complex to define analytically (too many variables) and thus difficult to control experimentally. In contrast, the formation of a TICT state in a molecular rotor is predominantly controlled by the microenvironment, specifically, the viscosity of

the dispersant solvent. The quantum yield of a fluorescent molecular rotor is given by the Forster-Hoffman equation as [11], [12]:

$$\Phi \approx \eta^{x} \tag{4.4}$$

or equivalently:

$$\log \Phi = C + x \log \eta, \tag{4.5}$$

where η is the viscosity, and C and x are constants of proportionality that depend on the dispersal medium. Fluorescent quantum yield (and subsequently fluorescence intensity) of a molecular rotor is thus proportional to the viscosity of its microenvironment. This relationship can be explained qualitatively by noting that the twisting associated with molecular rotors is opposed in high viscosity environments, making electronic relaxation by photonic emission more energetically favourable. As changes in viscosity can be initiated by changes in temperature, the fluorescence intensity of molecular rotors can be used for thermometry. When this is done, the relationship between quantum yield and viscosity can be defined as:

$$\Phi \approx b\left(\frac{\eta}{T}\right)^{x} \tag{4.6}$$

In (4.6), b is a solvent dependent constant of proportionality. Hence, for molecular rotors, quantum yield and fluorescent intensity are inversely proportional to the temperature of their environment. Giving their size, they can be used to map inhomogeneous microscale temperature changes.

In the experiments detailed, the molecular-rotor, DCVJ (chosen for its high photostability and spectral characteristics (its absorption and emission wavelengths are distinct from the plasmonic excitation)) is dissolved in an 80% (v/v) glycerol-methanol mixture (as the viscosity of this is strongly temperature dependent). Temperature is subsequently characterised based on the resulting fluorescence intensity.

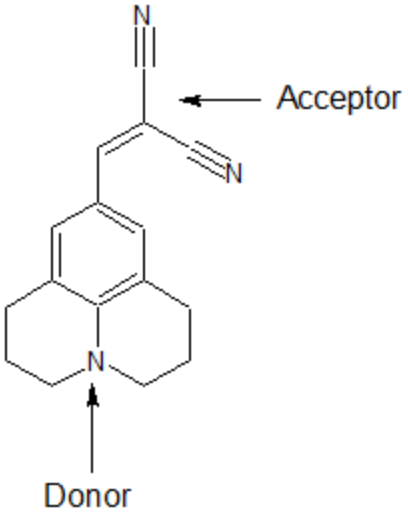

Figure 4.2: Illustration of DCVJ molecule [6] **drawn using ChemSketch.**

4.3 Materials and methods

4.3.1 Fabrication of plasmonic arrays

Arrays of plasmonic structures are fabricated using the method detailed in Section 3.4.3. The size of the structures is selected to gain a resonant response in the 635 nm region. (60 nm discs and 70 nm triangles are fabricated on glass and 40 nm discs and 50 nm triangles are fabricated on lithium niobate). Triangle dimers are spaced by 30 nm. Arrays with varying periodicity are fabricated, densely populated arrays in which the edge-edge distance is 100 nm, intermediate arrays, where the array pitch is 5× the characteristic length of a single structure (~300 nm on glass, ~200 nm on LN), and sparsely populated arrays with an edge-edge distance of 1 µm.

4.3.2 Preparation of DCVJ solution

DCVJ solution is prepared as detailed in Section 3.6.4.

4.3.3 Experimental setup

Simultaneous excitation and fluorescent imaging of plasmonic structures in DCVJ solution was performed using the setup described in Chapter 3. Laser powers were measured at the objective and vary between 0.1 and 7.6 mW. Focussed laser beam diameter is measured as 26 µm.

Fluorescent imaging of DCVJ solution was performed using the method described in Section 3.6.6.

4.3.4 FEM of plasmonic heating from single structures

Plasmonic heating of single nanostructures was simulated using a two-step finite element model detailed in Section 3.7.2. The electromagnetic wave equation is first solved at 633 nm to find the volumetric heat power density of a specific object. Laser excitation is described using a plane wave approximation with intensities matching those used experimentally. The stationary heat equation is then solved using the calculated heat power density. The thermal properties of glycerol, gold, titanium and glass are gotten from COMSOL's material library. The thermal properties of lithium niobate are gotten from [13]. The thermal properties of methanol are gotten from [14].

Table 4.1: Thermal properties of materials used in finite element simulation

Material	Mass density ρ (kg/m^3)	Specific heat capacity C_p (J/kg· K)	Thermal conductivity κ (W/m· K)
Glycerol-methanol (25 ° C)*	1174.54	2388.78	0.27
Lithium niobate	4648.5	633	4
Gold	19300	129	317
Titanium	4506	522	21.9
Glass	2203	703	1.38

* The thermal properties of the glycerol-methanol were calculated using an average from the mass fractions e.g. $\rho=\varphi_m\rho_m+\varphi_g\rho_g$

4.3.5 FEM of plasmonic heating from arrays of structures

Plasmonic heating of single nanostructures was simulated using the finite element model detailed in Section 3.7.3. The absorption cross section of a single plasmonic structure is calculated using the procedure described in Section 3.7.1. This is multiplied with the array density to approximate the absorption cross section of the array.

4.4 Results and discussion

4.4.1 Plasmon resonance characterisation

Plasmonic structures consisting of fundamental geometric elements were fabricated in order to test the effect of morphology on temperature generation. Structures in densely populated arrays (i.e. 100 nm edge-to-edge interparticle spacing) demonstrate collective plasmonic behaviour with optical coupling [15]; moderately populated arrays demonstrate collective plasmonic behaviour without optical coupling [16],[17], and sparse arrays demonstrate single plasmonic behaviour (for descriptive purposes, the triangle dimers are considered to be a single plasmonic element). Dimensions of structures deviate slightly from those defined in L-edit; mean triangle lengths are measured using ImageJ as 58 nm (nominal length 50 nm) and 82 nm (nominal length 70 nm). This broadening is more drastic with disc structures (60 nm vs 40 nm; 90 nm vs 60 nm), and is primarily a result of electron scattering in the fabrication process. Other processes which adversely affect estimation of the size of structures are uncorrected astigmatism in the scanning electron microscope. Though the binary conversion performed to enable automated geometry measurement is able to recover the true edges of the structure, this appears to be more difficult with circular structures. The plasmon resonance suggests that the dimensions of discs are closer to the nominal dimensions than indicated. Figure 4.3 depicts the uniformity of structures in a typical array; features calculated vary between 7.5 nm of the mean. Note that though the plasmonic structures fabricated are of the same morphology (i.e. disc and triangular elements), the characteristic dimensions differ depending on whether the supporting substrate was lithium niobate or glass. This change in dimension was necessary to achieve peak plasmon resonance in the 635 nm wavelength range on both substrates. Due to the large mismatch in refractive index between glass (n=1.45) and lithium niobate (n=~2.2) the position of the plasmon resonance peaks are redshifted on lithium niobate in comparison to glass. The dependence of the position of the plasmon resonance peak on refractive index, which is the square root of electrical permittivity, is implied in the Frohlich condition (Equation (2.7)). The larger refractive index of lithium niobate induces a greater displacement on a nanoparticle's plasmon. As a result, a greater reaction force is required to achieve resonance. According to Johnson and Christy [18], the relative permittivity of gold becomes more negative at longer wavelengths, providing this reaction force. Hence, the position of the plasmon resonance peak is redshifted for particles equal in volume.

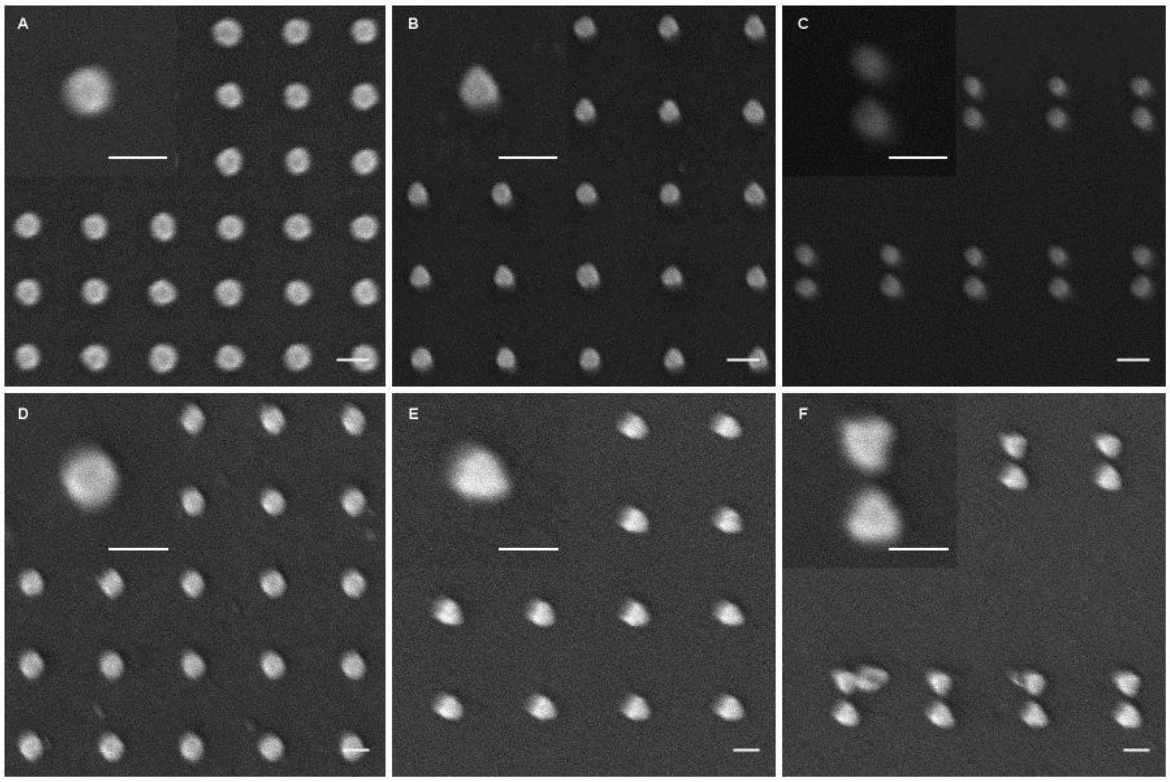

Figure 4.3: SEM images of fabricated plasmonic structures. A–C) Structures fabricated to achieve resonance at 635 nm region on lithium niobate. D–F) Structures fabricated to achieve resonance at 635 nm region on glass control. Scale bar: 100 nm.

Comparison of the experimentally derived plasmonic activity (extinction cross section) broadly mirrors the numerically predicted simulations with some caveats. For ease of visualisation, experimentally derived extinction cross section is presented alongside simulated absorption cross section. The scattering effects modelled using the finite element method obscured the position of plasmon resonance peaks in the simulated results. The position and magnitude of the experimentally derived plasmon resonance peaks do not match identically those simulated. This results from the changes between the computer defined geometry and the fabricated structure (noted previously), which causes deviations between the predicted and actual behaviour. Further explanations relate to the complex dielectric constants used to model the plasmonic structures. Johnson and Christy's [18], [19] refractive indices were used as exemplary values for the refractive indices of gold and titanium. The exact refractive indices change depending on the deposition technique used and, perhaps more relevantly, the purity of the metal, behaviours which are difficult to predict a priori. A similar explanation can be used to explain additional deviations on lithium niobate. The reduced Sellmeier equations [20] are used to model the refractive index on lithium niobate. This assumes subsequent plasmonic activity is measured at 24.5 °C. The typical room temperature at which plasmonic activity was measured was (~23 °C). It can be shown using the full Sellmeier equations that this change in temperature does not have a significant effect on the modelled refractive index. The refractive index at room temperature (23 °C) is identical to that

calculated using the reduced equation to nine significant figures. This error is not great enough to cause the deviations between experimental and modelled plasmonic activity. Of greater consequence is the stoichiometry of the lithium niobate wafer used [21], which, as with the purity of the metals, is more likely to deviate from the values presented as typical in the literature (as wafer growth processes differ depending on the supplier), causing slight but significant changes between the numerical and experimentally predicted values.

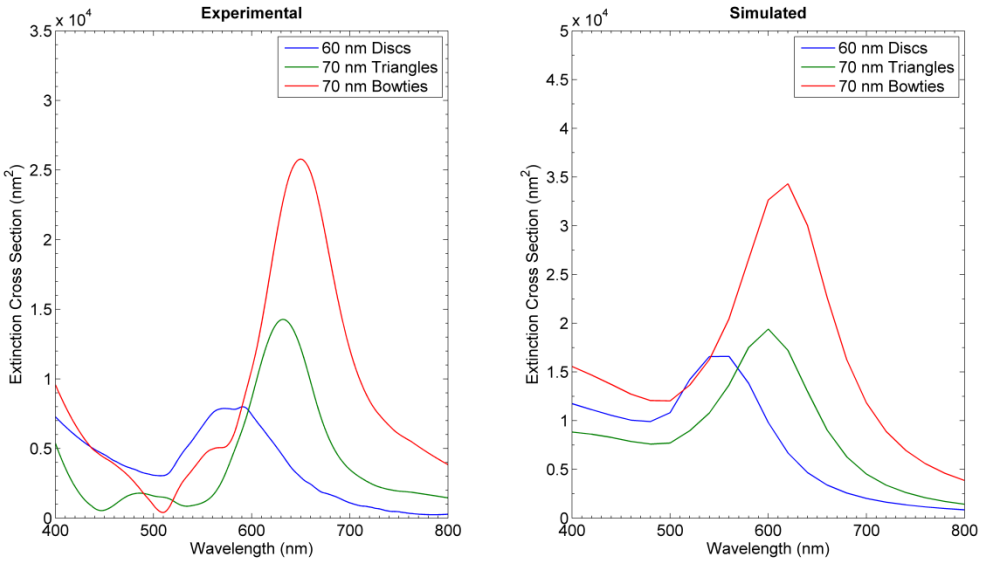

Figure 4.4: Comparison of experimentally derived and simulated plasmonic activity of structures fabricated on glass.

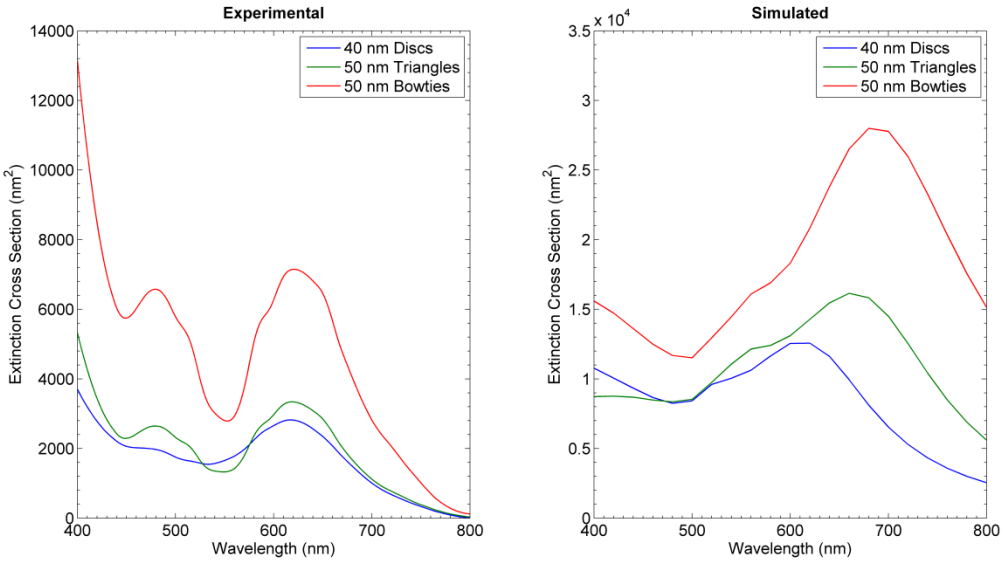

Figure 4.5: Comparison of experimentally derived and simulated plasmonic activity of structures fabricated on lithium niobate.

4.4.2 Finite element modelling of single plasmonic heating

The image below illustrates the temperature generated by single plasmonic entities on glass as a result of stimulation from a source with an on axis intensity of 2.76 kW/cm^2 (i.e. 7.6 mW Gaussian laser, w_0 = 13 µm). Excitation, as with the plasmonic characterisation experiments, is polarised parallel to the split in the bowties. For the intensities considered, temperature generated is limited to a maximum of 2 K (observed using discs) and is on the order of 1 K for triangles and triangle dimers. In spite of the inhomogeneity of the heat power, temperature is uniform in individual plasmonic structures (deviations observed in triangular geometries are artefacts resulting from the finite element meshing process and the sharp corners of these structures). Individual triangles in the bowtie act independently of each other (bottom triangle gets hotter than the top as a result of the position of the source of excitation). The distribution of the heat power suggests possible reasons for the changes in temperature generated associated with changes in geometry. Though maximum observed heat power is smaller in disc geometries (0.85 × 10^{17} W/m^3 vs 1 × 10^{17} W/m^3), this is distributed more evenly in the bulk (which is slightly more voluminous than triangle). In contrast, the bulk of the generated heat power in triangular geometries is confined to the edges, thus contributing to a smaller absorption cross section, and smaller temperature increase. A 1/r temperature decay is noted as distance from the plasmonic structure increases, validating the theoretical predictions of the nature of plasmonic heating made in Chapter 2.

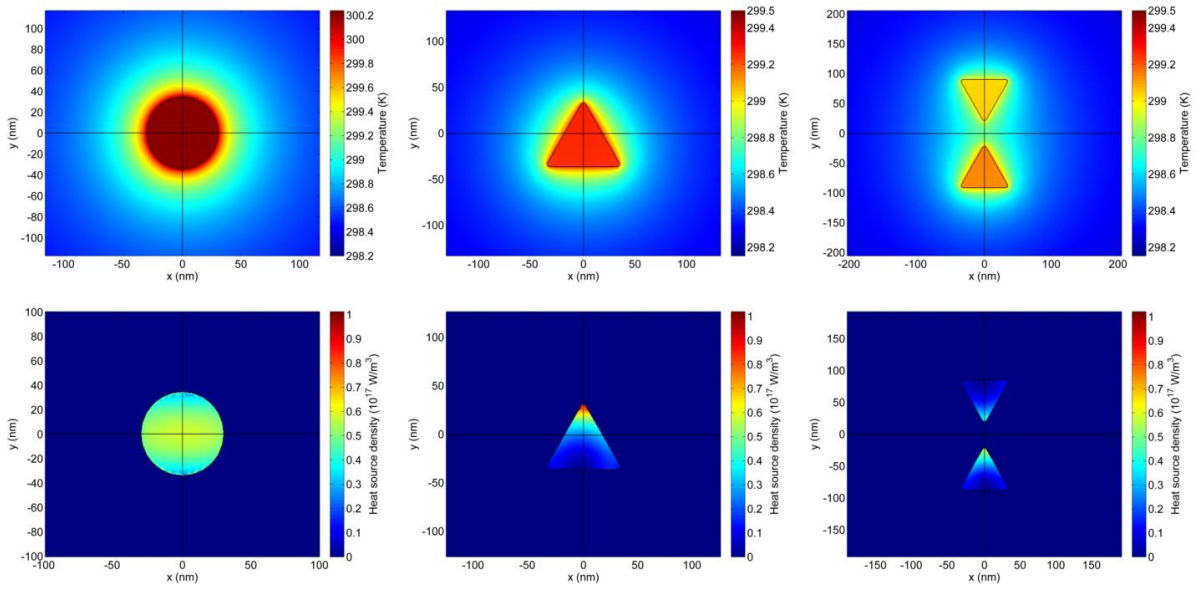

Figure 4.6: Results from finite element simulations of plasmonic heating on glass. Above) Temperature increase as a result of plasmonic stimulation. Below) Heat power distribution within nanostructures.

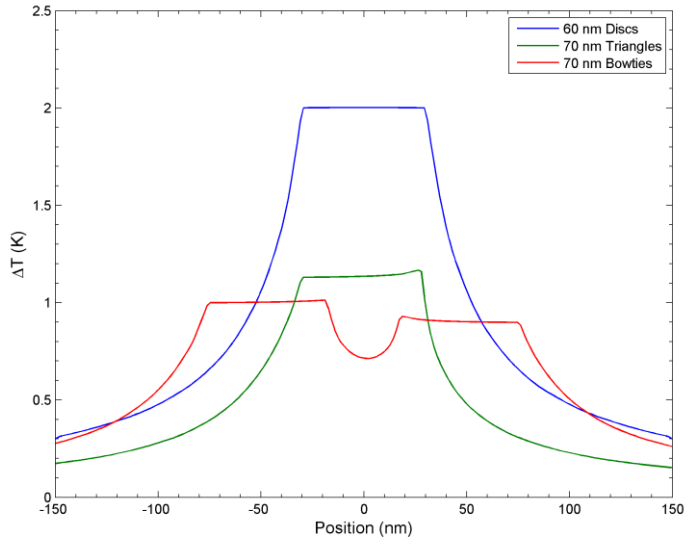

Figure 4.7: Spatial distribution of temperature generated by plasmonic structures on glass. Position refers to distance from the centre of the structure.

Figure 4.8 depicts the simulated heating of plasmonic structures on lithium niobate. The temperature increase is of a similar order of magnitude, in general, to that estimated on glass (the exception being discs where temperature increase is halved from 2 to 1 K). This is in spite of a general increase in the heatpower of the individual plasmonic elements (maximum of 3×10^{17} W/m^3 compared to 1×10^{17} on glass). The comparatively inefficient heating noted on lithium niobate, in comparison to glass, is attributable to its increased thermal conductivity (4 vs 1.38 K),

which gives a heatsinking effect. Hence, the magnitude of the temperatures generated on both substrates are broadly comparable in spite of the differences in plasmonic behaviour. As before, a 1/r temperature decay profile is depicted (Figure 4.9).

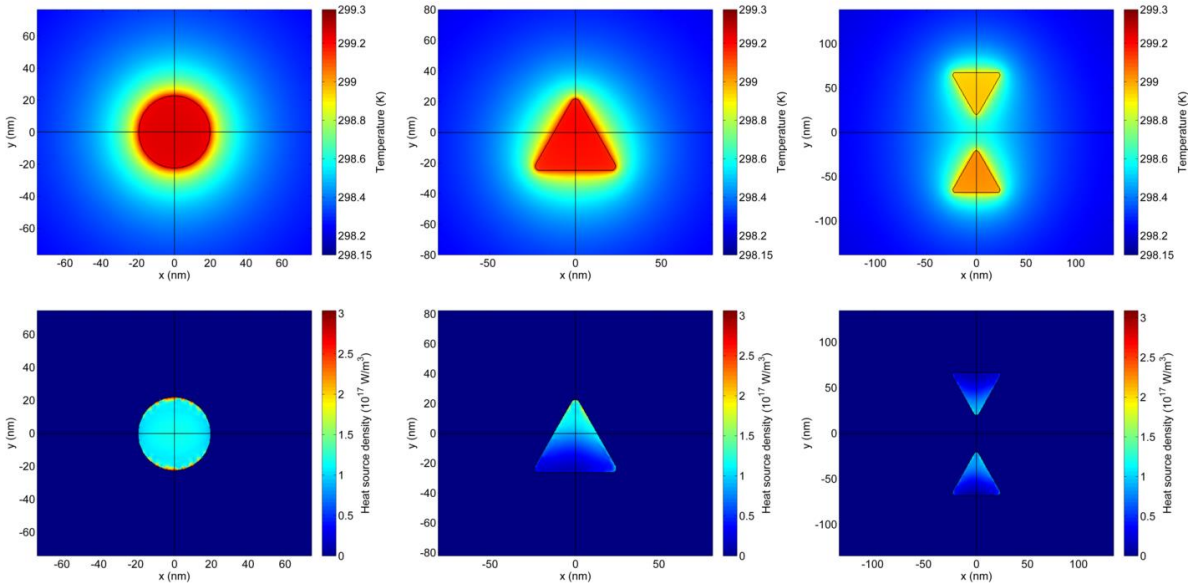

Figure 4.8: Results from finite element simulations of plasmonic heating on lithium niobate. Above) Temperature increase as a result of plasmonic stimulation. Below) Heat power distribution within nanostructures.

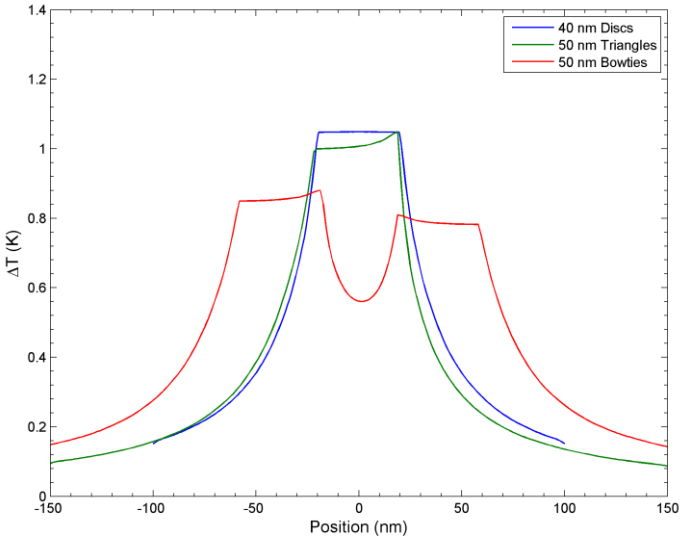

Figure 4.9: Spatial distribution of temperature generated by plasmonic structures on lithium niobate. Position refers to distance from the centre of the structure.

4.4.3 Simulation of heating from nanoparticle arrays

A simplified two dimensional model (described in Chapter 3) was used to predict the general nature of plasmonic heating from arrays of nanoparticles. The 1/r temperature decay noted with single nanoparticles is preserved, with the caveat that the characteristic length is now that of the laser beam (Figure 4.10). As a result of the diffusive nature of temperature, heating extends beyond the laser beam region, as illustrated in Figure 4.11. In general, a linear relationship between laser power and temperature generated is observed as suggested by the analytically described heat power term (Figure 4.12 and Figure 4.13). This is important in the context of pyroelectric field generation as it establishes that laser power and temperature can be considered to be synonymous i.e. the effect of changing the laser power is functionally identical to adjusting the temperature where pyroelectric field generation is concerned. From the simulations, the array density is the most important parameter in adjusting the magnitude of generated temperature. The most efficient heating with respect to input laser power, is observed with dense, 100 nm pitch arrays. In contrast 1 µm dense arrays generate similar temperatures to single NPs. The use of the two dimensional model means that some of the distinctions of inter-particle interactions are lost as temperature is considered on a macro-level. As the collective temperature is in general much larger than the temperature generated with a single nanoparticle, this simplification reasonably describes the observable behaviour of plasmonic heating.

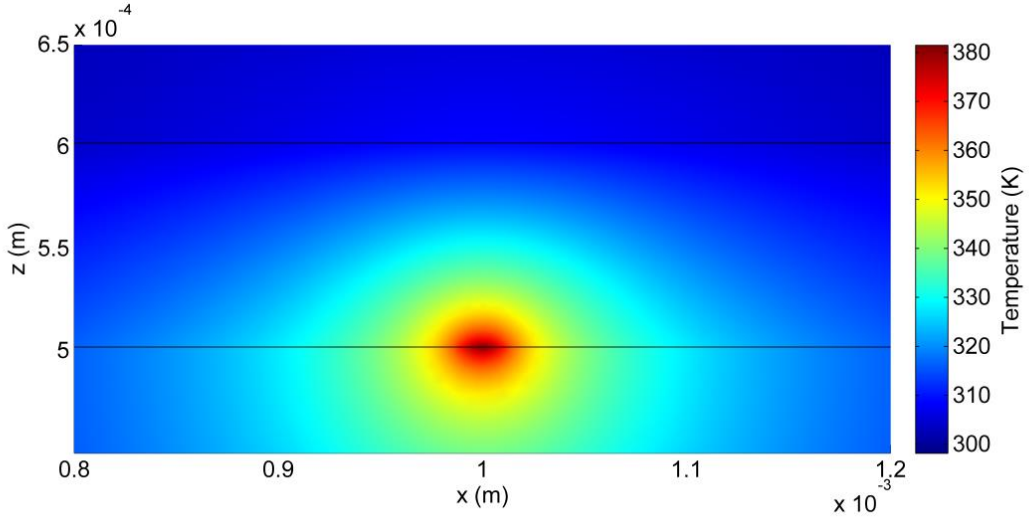

Figure 4.10: Representative image of plasmonic heating from an array of nanostructures. The image depicts the temperature generated as a result of stimulating an array of 40 nm discs with 140 nm pitch on lithium niobate.

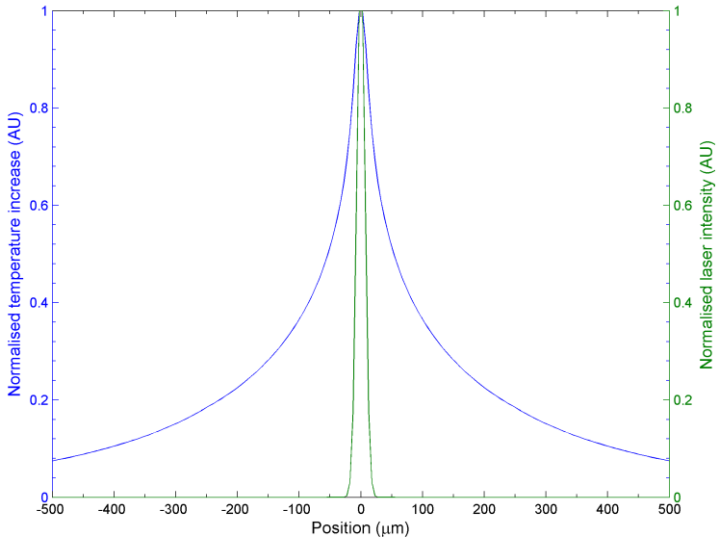

Figure 4.11: Spatial variation of temperature and laser intensity in microfluidic chamber at the solid-fluid interface. Position in x axis refers to distance from the centre of the laser beam. As these profiles are identical for all the simulations considered, values have been normalised to the maximum for illustrative purposes.

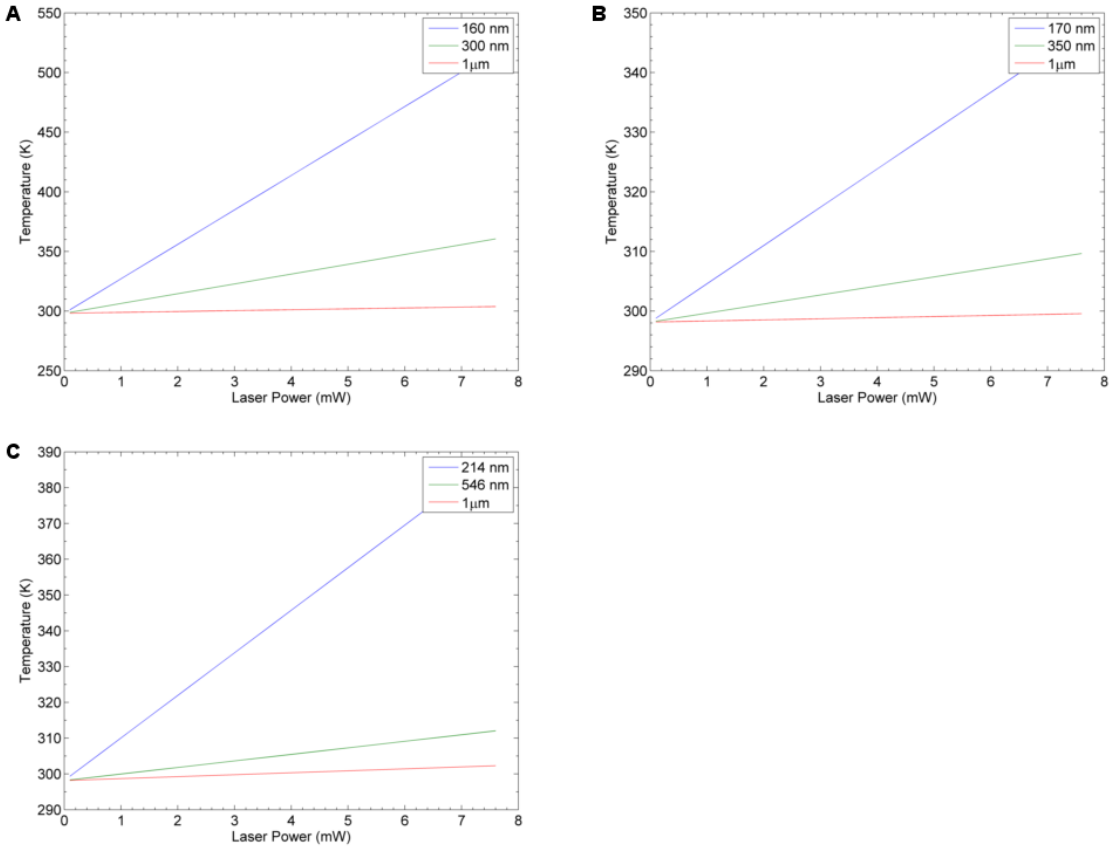

Figure 4.12: Simulated relationship between temperature and laser power for arrays of nanostructures on glass. Entries in legend refer to the side length of an equivalent square array. Results from simulations using: A) 60 nm discs, B) 70 nm triangles, and C) 70 nm bowties are depicted.

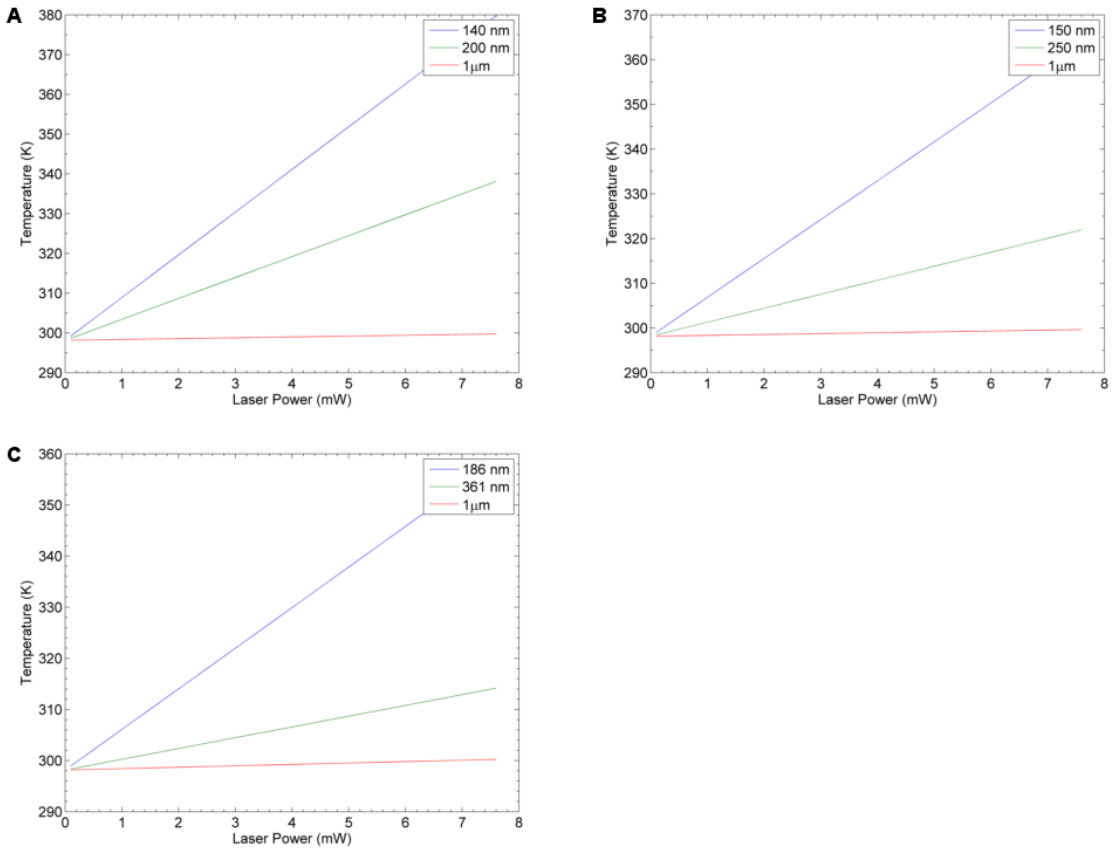

Figure 4.13: Simulated relationship between temperature and laser power for arrays of nanostructures on glass. Entries in legend refer to the side length of an equivalent square array. Results from simulations using: A) 40 nm discs, B) 50 nm triangles, and C) 50 nm bowties are depicted.

4.4.4 Verification of thermometry technique

DCVJ solution in microfluidic chamber is imaged under continuous fluorescent excitation at room temperature for ~4 minutes (1000 images are recorded). During this time, a marginal reduction in the fluorescent intensity is recorded attributable to photobleaching. Imaging experiments were subsequently performed to ensuring that fluorescent excitation time was kept at a minimum and was well below this limit. Hence, images were captured in 1.5 second periods.

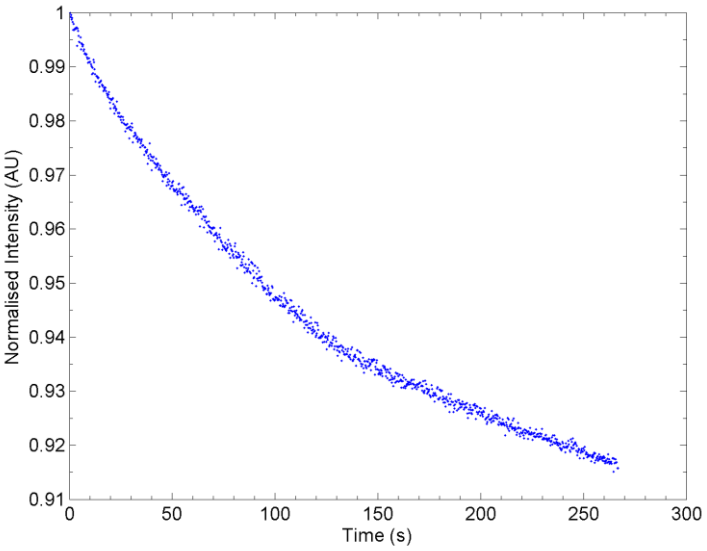

Figure 4.14: Decaying fluorescence intensity of DCVJ solution as a result of photobleaching. The intensity drops to 90% of its initial value after 4 minutes of stimulation.

According to theoretical considerations, a steady state temperature profile (i.e. $\frac{\mathrm{d}T}{\mathrm{d}t} = 0$) is expected as a result of continuous wave illumination of plasmonic structures. Figure 4.15 depicts the fluorescence intensity for a series of images recorded during plasmonic stimulation of an array of 60 nm discs (values are normalised to the maximum reported intensity in the image sequence). The results depict a random variation of fluorescence intensity over the observation period. The mean normalised intensity is 0.995 units and standard deviation is 0.0028. Crucially, intensity does not decrease with time, indicating photobleaching is minimal, and continued illumination of plasmonic structures does not lead to an increase in the temperature of the surrounding environment. This supports the assertion that during stimulation, temperature increase is stationary.

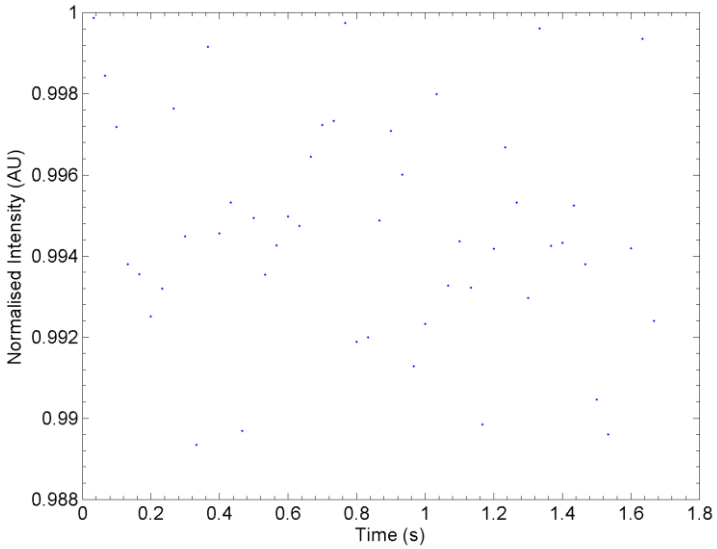

Figure 4.15: Temporal fluctuation of DCVJ intensity. Fluorescence intensity varies randomly during the observation period considered.

A video of DCVJ at room temperature, during, and after stimulation highlights the ability of the technique to elucidate the dynamics of plasmon-assisted photothermal heating (Figure 4.17). Figure 4.16 depicts the change in intensity of DCVJ in a 33 second span, during which laser stimulation is applied and then removed. A drop in DCVJ intensity is observed at 14.2 seconds (corresponding to the point when the laser is switched on), with the intensity recovering at 28.8 seconds (i.e. when the laser is switched off). According to this video, the transient region (thermal response time) is around 400 ms. Based on the properties of the surrounding fluid, this transient corresponds to a characteristic length of 200 µm (a transient of 1.73 ms is more representative of heating with a 26 µm diameter laser). The discrepancy between this calculated characteristic length and that dictated by the laser beam diameter appears to suggest that the temperature reported with this technique is that of the bulk fluidic region, and not the plasmonic structure. This is supported by the fact that the thickness of the microfluidic chamber is of the same order of magnitude as the calculated characteristic length. Thus, the observed transient is more consistent with heating of the bulk region.

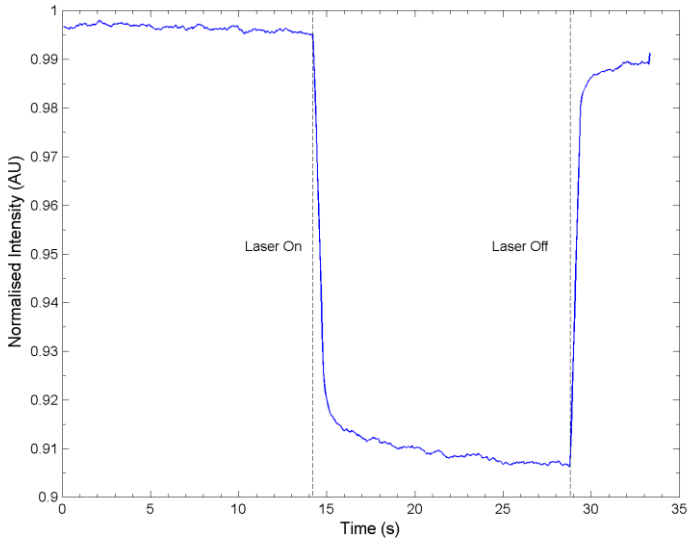

Figure 4.16: Change in fluorescence intensity before, during and after laser stimulation. Rise and fall time of graph are indicators of the thermal response of the fluid.

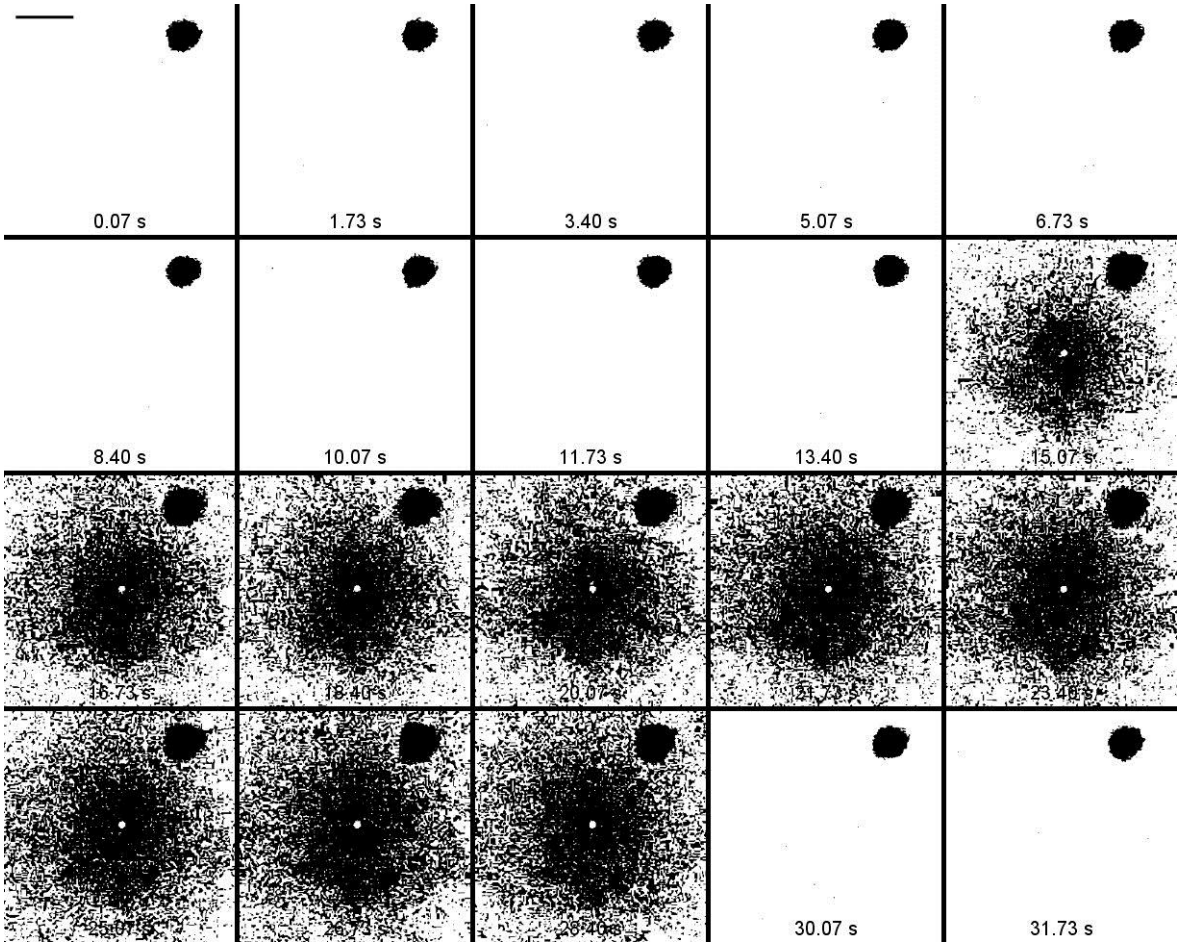

Figure 4.17: Montage of fluorescence recovery before and after plasmonic heating. The image sequence has been normalised for clarity. Scale bar is 50 µm.

4.4.5 Thermometry of plasmonic structures on glass substrate

Figure 4.18 depicts a false colour image illustrating the change in fluorescent intensity associated with laser stimulation of a dense array of 60 nm discs on glass. The laser is located at the (225,165)µm coordinate. The scale of the colour bar has been mapped so that changes in colour correspond to changes in temperature. The experiments show that temperature change is spatially dependent, with the magnitude decreasing with increasing distance from the laser spot, as predicted by analytical and numerical simulations. This behaviour is observed with all laser powers considered, as illustrated in Figure 4.19. The maximum temperature calculated (304 K at 7.6 mW) is much less than that simulated (530 K) for the same power on glass substrates. This (along with the larger than predicted thermal response time) further suggests that the temperature reported is that of the bulk. Image artefacts and competing optical processes obscure some of the detail uncovered during thermometry. The presence of a ring structure due to a shadow cast by the objective lens controlling the focus of the laser beam is observed. This appears as a region of elevated temperature when this is not the case. Similarly, a blemish appearing on the CCD sensor element of the camera appears as a localised hotspot at (250,200). In order to reduce the effects of these processes, the position of the laser beam in the image is located so that changes in temperature can be observed distinctly from these anomalies.

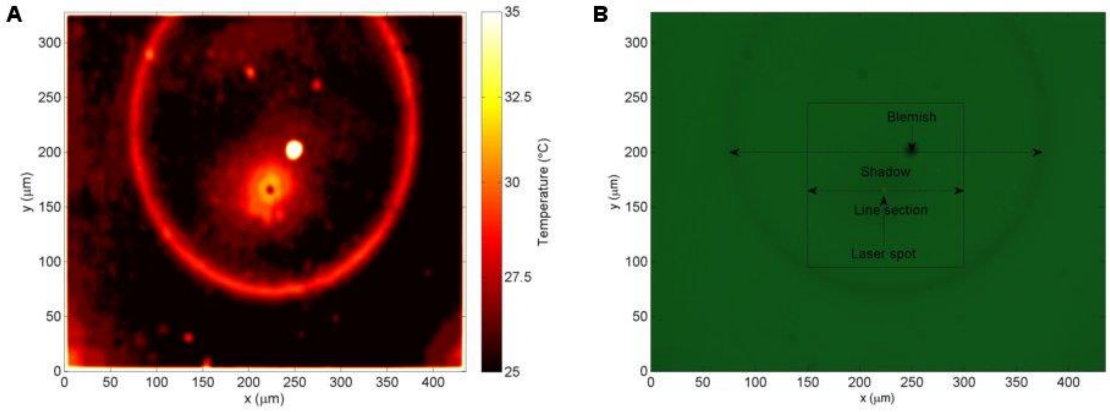

Figure 4.18: A) False colour image of change in DCVJ intensity as a result of stimulating an array of 60 nm discs on glass. Scale of colour bar is calculated temperature in °C. B) Raw image showing location of blemish, shadow and laser spot. As the pixel intensities differ markedly from the background in these locations, the algorithm reports anomalous changes in temperature at these points. The location of the line section over which the temperature profile is measured in the region of interest is also displayed.

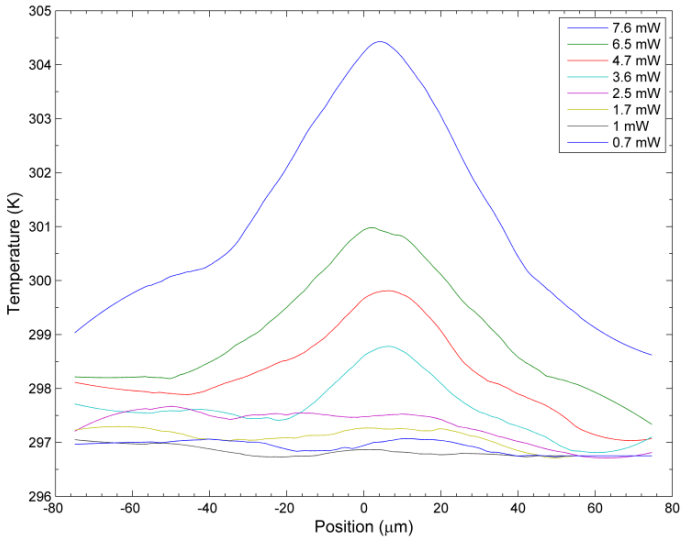

Figure 4.19: Spatial variation of temperature in microfluidic chamber for varying laser powers. Results depicted are due to laser stimulation of densely populated arrays of 60 nm discs. Similar trends are observed with other structures considered. Position refers to distance from laser beam centre.

Comparison of results from experiments performed with disc geometries to those performed with triangles and bowties show that for densely populated arrays, the temperature generated is of a similar magnitude. Though in absolute terms, arrays of triangles and bowties generate less heat at maximum power than discs (mirroring a trend observed with the numerically simulated results of plasmonic heating), this behaviour does not extend towards the entire range of powers considered. It appears that nanoparticle geometry has little effect on the temperature generated for the arrays considered. It should be noted that as before, a linear function appears to best describe the relationship between laser power and temperature as seen in Section 4.4.3. Temperatures were calculated from the mean of fifty recorded images using the calibration curve. The standard deviation of the image intensity of recorded sequences was used to estimate the error in the measurements. It should be noted that as a consequence of relying on the non-linear calibration curve to calculate temperature, there is an asymmetry in the estimated error of the measurements, seen most obviously with powers below 3.6 mW. The maximum error is thus +/- 4 K, which is observed at 7.6 mW. These results are illustrated in Figure 4.20. When the temperatures of all structures are averaged (n=3), the linear relationship is made more obvious, as can be seen in the image on the right of Figure 4.20. The intercept of the curve is at 296.4 K, mirroring the temperature of the room in which the experiment was performed. The maximum error is +/- 2 K.

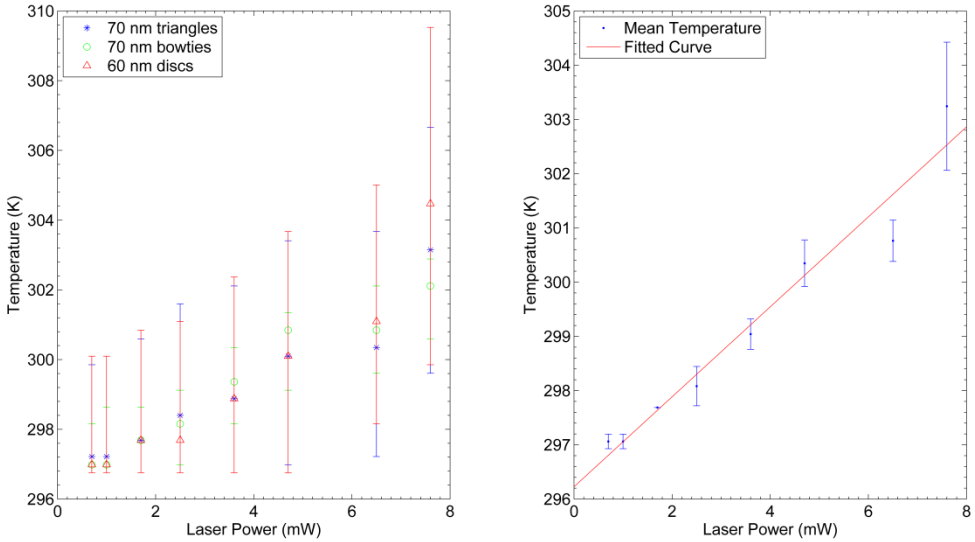

Figure 4.20: Maximum temperature generated at different laser powers resulting from plasmonic stimulation of arrays of nanostructures on lithium niobate. Left) Temperatures observed for distinct particles. Right) Mean of temperatures of all structures considered.

Array density is the most important parameter considered for controlling the amount of temperature generated by photonic means. Figure 4.21 depicts false colour images of plasmonic heating from 60 nm discs with densely (100 nm edge-edge), moderately (300 nm) and sparsely (1 µm) populated arrays. The area and magnitude of increased temperature decreases with increasing array pitch until there is no perceptible change in fluorescence intensity. Apart from validating a trend observed in FEM simulations, this further confirms that the change in fluorescent intensity is a result of plasmonic excitation and not simply laser stimulation (since the changing parameter in the cases presented is the array density). Figure 4.21D also illustrates the raw image recorded on the sparsely populated arrays. It is clear from this that laser stimulation is inconsequential. This behaviour highlights a further drawback with the technique. The inability to produce sufficient changes in intensities at low powers and/or on sparsely populated arrays means that the temperatures calculated in these conditions are subject to a large amount of uncertainty. Hence, without further validation, such results cannot be assumed to be representative of the actual behaviour of plasmonic heating.

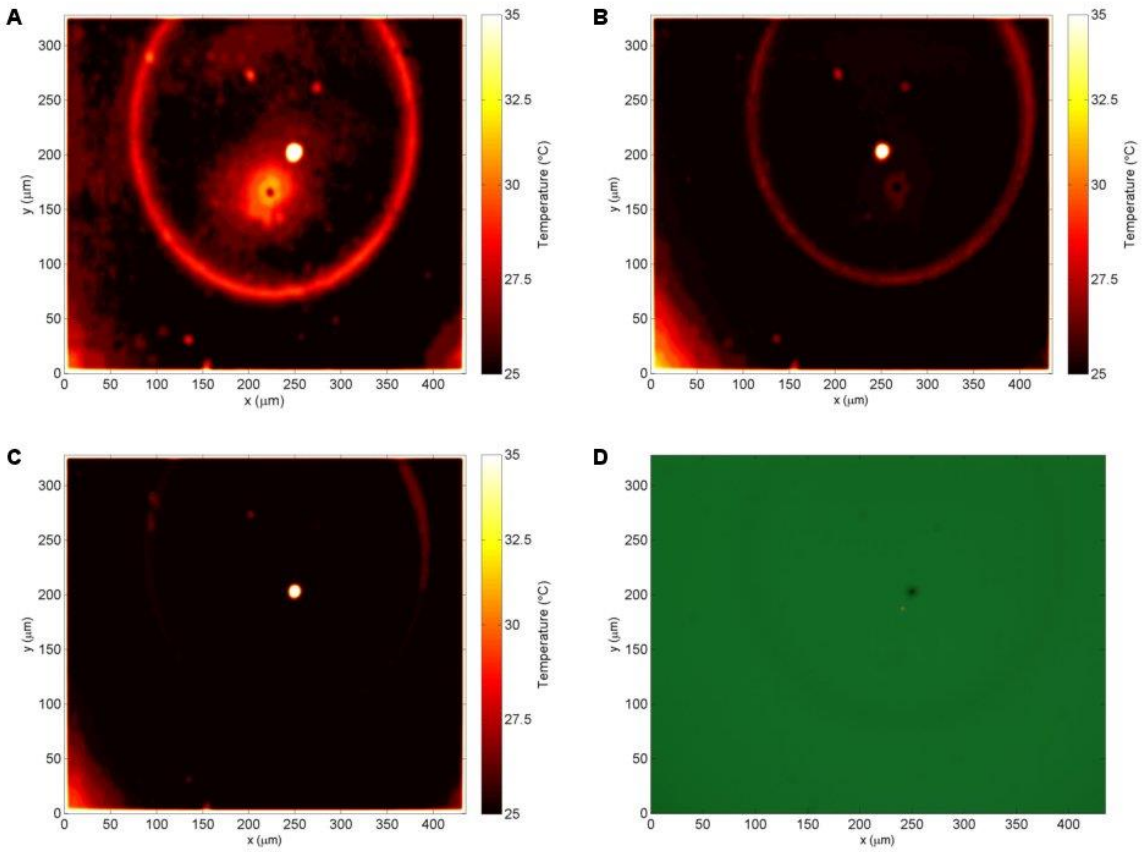

Figure 4.21: False colour images depicting change in intensity as a result of plasmonic stimulation of: A) dense (100 nm pitch), B) moderately (300 nm pitch), and C) sparsely (1 µm pitch) populated arrays of 60 nm discs on glass. D) Raw image recorded during stimulation of sparsely populated array of 60 nm discs. Image processing supresses the laser spot even though it is visible in the raw image.

4.4.6 Thermometry of plasmonic structures on lithium niobate

Fluorescence thermometry shows that plasmonic heating on lithium niobate behaves slightly differently from theory than anticipated. Temperatures were calculated as previously mentioned in Section 4.4.5. It appears that the absorption cross section calculated using finite element methods is an overestimation of the experimental value to a greater degree than experienced with structures fabricated on glass. Hence, the heat power generated on both substrates is of a similar magnitude. As a result, the heatsinking properties associated with the increased thermal conductivity of lithium niobate are more apparent. Figure 4.22 depicts false colour images of fluorescence intensity during laser stimulation (at 7.6 mW) of dense arrays of discs, triangles and bowties. In comparison to similar experiments performed on glass, the temperature generated is reduced (maximum temperature of 299 K (26 °C) on lithium niobate compared to 304 K (31 °C) on glass). As such, the radius of the heated area appears reduced. The temperatures generated are more comparable to those observed stimulating moderately populated arrays at 7.6 mW/densely populated arrays at 3.6 mW. A linear trend consistent with theoretical predictions is observed

when triangular plasmonic structures are stimulated (Figure 4.23). A deviation from predictions is noted with the behaviour of disc structures. Contrary to the simulations, the temperature generated by disc structures is significantly less than that on triangles (heating from triangle structures is 1.5× greater than from discs). Furthermore, for excitation between 0.7 and 4.7 mW, the plasmonically generated temperature remains static, suggesting a latch/rectify style response. The apparent invariant response of plasmonic structures to laser stimulation below 6.7 mW is a result of the insensitivity of the calibration curve to moderate changes in fluorescent intensity. The average intensities recorded at these powers are too similar to that observed at room temperature for the heating effect to be registered. It should be noted that if deviations from the mean temperature are considered, a more linear response again begins to emerge. Averaging the temperatures generated by different structures reveals a linear trend with a maximum error of +/- 1 K.

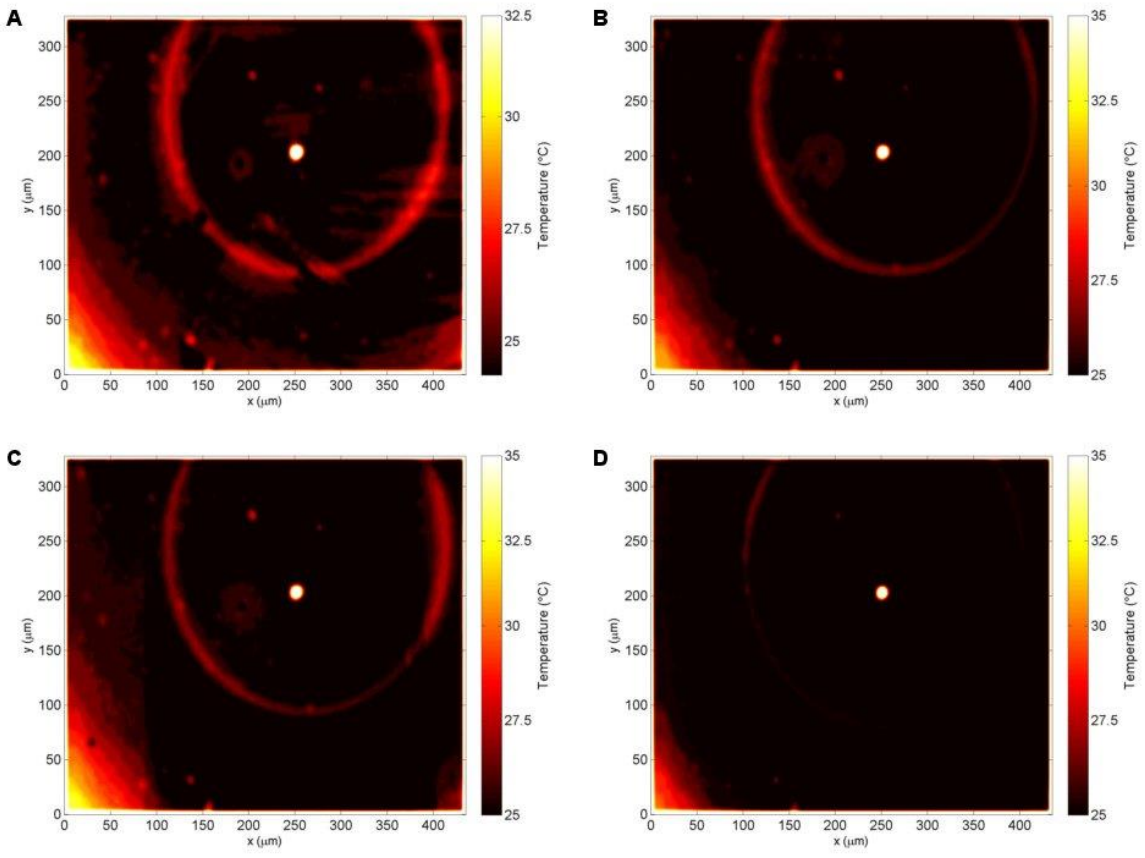

Figure 4.22: False colour images depicting change in fluorescence intensity as a result of laser stimulation of: A) 40 nm discs, B) 50 nm triangles, C) 50 nm bowties, and on D) bare lithium niobate substrate.

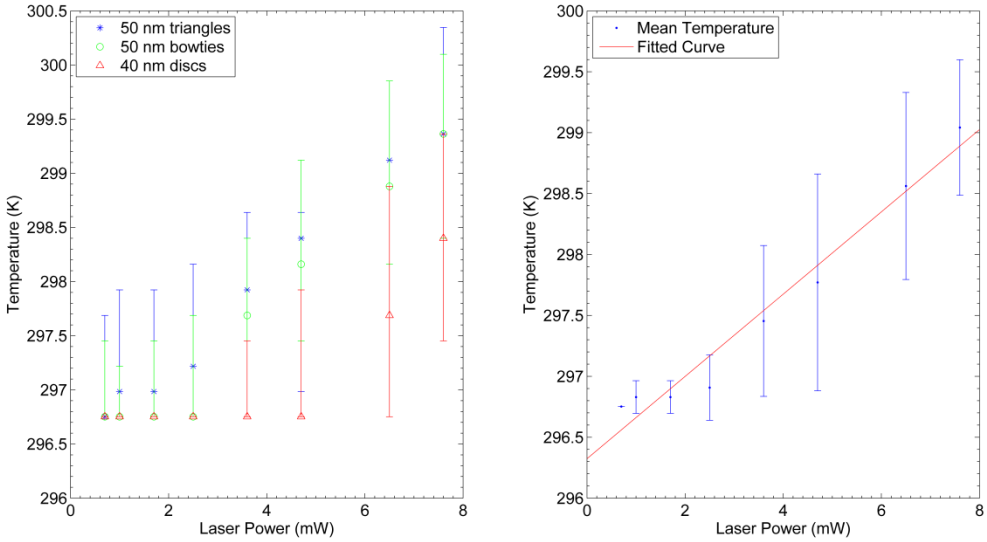

Figure 4.23: Maximum temperature generated at different laser powers resulting from plasmonic stimulation of arrays of nanostructures on lithium niobate. Left) Temperatures observed for distinct particles. Right) Mean of temperatures of all structures considered.

As lithium niobate absorbs a significant portion of photonic stimulation (up to 30% at 633 nm as indicated in Figure 4.24), there is the possibility that substantial temperatures can be generated on the substrate without plasmonic enhancement. Figure 4.22D illustrates the fluorescence intensity as a result of laser stimulation of a blank lithium niobate substrate. No change in intensity is recorded for all powers considered, indicating that the bulk temperature remains unchanged and any temperature increase generated as a result of photothermal absorption in lithium niobate is highly localised. As a result, temperature generated by photothermal absorption on lithium niobate cannot be recorded using the technique considered. Plasmonic enhancement (especially using arrays of structures) thus significantly improves the ability to generate and control temperatures using optical methods.

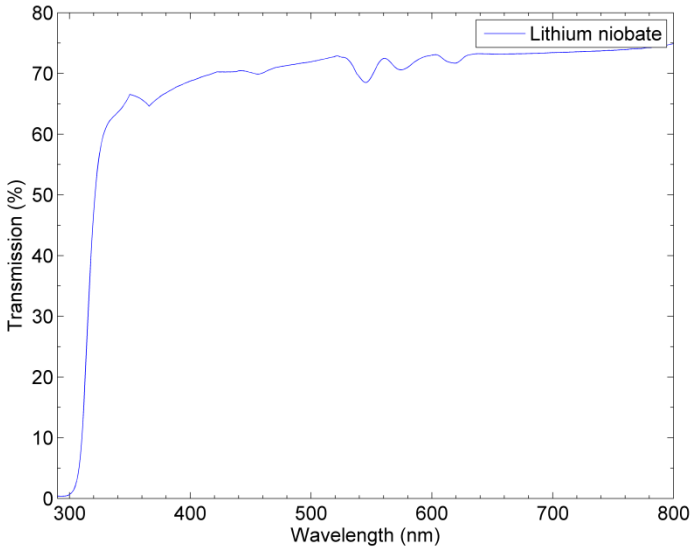

Figure 4.24: Transmission profile of lithium niobate measured using a Shimadzu UV-3101 pc spectrophotometer

4.5 Improvements to technique

The limitations of the technique presented arise from the fact that an optical response is used to characterise temperature. As such though there is little scope for improving accuracy in absolute terms, it is possible to implement some changes such that thermometry is performed closer to the diffraction limit.

4.5.1 Diffraction limit

The inability to visualise temperature changes for sparse arrays arises from the fact that in this regime, temperature generation is delocalised: particles do not act collectively and plasmonic heating occurs at a nanometre scale. The spatial resolution is thus limited by the wavelength of illumination i.e.

$$d = \frac{0.61\,\lambda}{NA}, \tag{4.7}$$

where d is the size of the smallest resolvable spot, λ is the imaging wavelength, and NA is the numerical aperture of the objective. From (4.7), the resolving limit is 500 nm, for the optical system used. This can be increased by using objectives with higher numerical aperture. There is of

course a limit to how large the numerical aperture can be feasibly made for visualisation of plasmonic heating by structures resonant at visible wavelengths. This improvement is sufficient for single thermal imaging of larger plasmonic structures (on the order of 200 nm). However, giving their size, it is not possible to quantify the heating of single plasmonic structures used in this project.

4.5.2 Point spread function and optical sectioning

Operating in a wide field configuration enables easy integration with the experimental setup detailed in Chapter 3. The large depth of field characteristic of this optical configuration suggests a possible source of the deviation of the observed to the predicted temperature. Though light present at the detector is primarily due to the object in the focal plane, diffraction means that there is some contribution from out of focus elements.

The observed fluorescence intensity is a weighted mean of the fluorescence in the depth of field:

$$\overline{I_f} = \frac{1}{DOF} \int I_f(z) \cdot f(z)\, dz, \tag{4.8}$$

where $I_f(z)$ is the fluorescence intensity at a particular distance from the focal plane in the microscope's depth of field, and $f(z)$ is a distant dependent scaling function which describes diffractive effects. In this convention, $f(z)$ is at a maximum at the focal plane where it equals 1. As defined previously, I_f is inversely related to temperature.

These relationships explain how plasmonic temperature is underestimated using this technique. The characteristic thermal field associated with plasmonic heating is non-linear exhibiting a distant dependent decay. This implies that the magnitude of the fluorescence intensity increases with distance. Thus, in contrast to uniform temperature fields (such as those obtained during calibration) contributions from out of focus elements are more significant.

Practical solutions for reducing this effect involve optical sectioning. For a sufficiently small depth of field (i.e. $DOF = dz$), the depth averaged fluorescent intensity is identical to the planar fluorescent intensity. This optical sectioning can be achieved using techniques such as confocal imaging (restricting observed light at the conjugate focal plane), or total internal reflection fluorescent microscopy (restricting fluorescent excitation using an evanescent wave). These

require a fundamental change to the optical setup which reduces the ease of deployment of this technique.

Computational optical sectioning techniques can be used to reduce the contribution of out of focus fluorescence intensities without changing the experimental setup (and can be used in conjunction with the practical sectioning techniques to improve their response). The expression describing the average intensity involves the convolution of the planar intensity with the function detailing the diffractive effects. Hence, planar intensity can be recovered if a deconvolution algorithm is applied provided there is knowledge of the diffractive response of the optical system.

The diffractive response of an optical system ($f(z)$) is encompassed in the point spread function, which is the response of an imaging system to an optical impulse (i.e. the transfer function of the imaging system). This can be gotten experimentally, by imaging a point source (e.g. fluorescent microbeads, quantum dots) at different focal lengths, or analytically with appropriate knowledge of relevant optical parameters of the imaging system (numerical aperture, working distance, emission wavelength etc.).

4.5.3 Self-referencing

Ratiometric referencing of temperature sensitive fluorescent dyes is useful for limiting the effect of changes in intensity resulting from sources other than changes in temperature, as well as magnifying the dynamic range of temperature, and improving the sensitivity of the technique. These principles are used in some degree with some fluorescence polarisation anisotropy schemes [5], and with two dye/colour fluorescence [22]. In molecular rotors such as DMABN [11], the low energy excited state and the TICT state are sufficiently energetic two support radiative energy transfer. Thus, these dyes exhibit temperature dependent fluorescent emission at two different wavelengths. This could be used in a similar manner to fluorescent polarisation anisotropy to improve the sensitivity of the technique.

4.6 Conclusion

Through numerical simulations, some key attributes of plasmonic heating have been identified. In general, experimental observations of plasmonic thermal generation support these theoretical predictions. There is a radial dependence on the magnitude of the temperature decaying with

increasing distance from the point of illumination. Temperature broadly increases with laser power, with a linear relationship best describing the interaction between both parameters. Finally, temperature and heated area increase with array density.

There is a large discrepancy between the predicted temperature and that estimated using the thermometry technique. The temperatures generated are at least one order of magnitude lower than those predicted numerically. Presuming no errors in the calibration process (e.g. estimation of the beam diameter and conversion of fluorescence intensity to temperature), the major source of the deviation appears to be due to the fact that an average temperature of the bulk is reported, as opposed to a surface temperature. The technique detailed is useful for verifying that plasmonic heating is occurring and broadly estimating the distribution. For more rigorous quantitative analysis, numerically simulated values may give a better estimation of plasmonic enhanced temperature. Implementation of the suggested improvements should bring the experimental values more in line with the predictions.

4.7 References

[1] J. Greffet, "Laws of Macroscopic Heat Transfer and Their Limits," in *Microscale and Nanoscale Heat Transfer*, S. Volz, Ed. Springer-Verlag Berlin Heidelberg, 2007, pp. 1–13.

[2] B. Cretin, S. Gomes, N. Trannoy, and P. Vairac, "Scanning Thermal Microscopy," in *Microscale and Nanoscale Heat Transfer*, S. Volz, Ed. Springer-Verlag Berlin Heidelberg, 2007, pp. 181–238.

[3] C. Gosse, Bergaud, Christian, and P. Low, "Molecular Probes for Thermometry in Microfluidic Devices," in *Thermal Nanosystems and Nanomaterials*, S. Volz, Ed. Springer-Verlag Berlin Heidelberg, 2009, pp. 301–341.

[4] X. Wang, O. S. Wolfbeis, and R. J. Meier, "Luminescent probes and sensors for temperature.," *Chem. Soc. Rev.*, vol. 42, no. 19, pp. 7834–69, 2013.

[5] G. Baffou, M. P. Kreuzer, F. Kulzer, and R. Quidant, "Temperature mapping near plasmonic nanostructures using fluorescence polarization anisotropy.," *Opt. Express*, vol. 17, no. 5, pp. 3291–3298, 2009.

[6] J. A. Levitt, P. Chung, M. K. Kuimova, G. Yahioglu, Y. Wang, J. Qu, and K. Suhling, "Fluorescence Anisotropy of Molecular Rotors," *ChemPhysChem*, vol. 12, no. 3, pp. 662–672, 2011.

[7] G. Baffou, P. Bon, J. Savatier, J. Polleux, M. Zhu, M. Merlin, H. Rigneault, and S. Monneret, "Thermal imaging of nanostructures by quantitative optical phase analysis," *ACS Nano*, vol. 6, no. 3, pp. 2452–2458, 2012.

[8] Z. Chen, X. Shan, Y. Guan, S. Wang, J. J. Zhu, and N. Tao, "Imaging Local Heating and Thermal Diffusion of Nanomaterials with Plasmonic Thermal Microscopy," *ACS Nano*, vol. 9, no. 12, pp. 11574–11581, 2015.

[9] H. Ma, P. Tian, J. Pello, P. M. Bendix, and L. B. Oddershede, “Heat Generation by Irradiated Complex Composite Nanostructures,” *Nano Lett.*, vol. 14, no. 2, pp. 612–619, Feb. 2014.

[10] D. Ross, M. Gaitan, and L. E. Locascio, “Temperature measurement in microfluidic systems using a temperature-dependent fluorescent dye.,” *Anal. Chem.*, vol. 73, no. 17, pp. 4117–23, Sep. 2001.

[11] B. Valeur, *Molecular Fluorescence: Principles and Applications*. Wiley-VCH, 2001.

[12] M. A. Haidekker, T. Ling, M. Anglo, H. Y. Stevens, J. A. Frangos, and E. A. Theodorakis, “New fluorescent probes for the measurement of cell membrane viscosity.,” *Chem. Biol.*, vol. 8, no. 2, pp. 123–131, 2001.

[13] “INRAD Lithium Niobate datasheet.” [Online]. Available: http://www.lambdaphoto.co.uk/pdfs/Inrad_datasheet_LNB.pdf. [Accessed: 01-Dec-2012].

[14] R. L. Rowley, W. V. Wilding, J. L. Oscarson, N. Giles, R. J. Rowley, T. E. Daubert, and R. P. Danner, “DIPPR Data Compilation of Pure Compound Properties,” *Design Institute for Physical Property Data*, 2001. [Online]. Available: http://dippr.byu.edu/students/. [Accessed: 15-Apr-2015].

[15] S. J. Tan, M. J. Campolongo, D. Luo, and W. Cheng, “Building plasmonic nanostructures with DNA.,” *Nat. Nanotechnol.*, vol. 6, no. 5, pp. 268–76, May 2011.

[16] R. Quidant, S. Monneret, G. Baffou, P. Berto, E. B. Urena, J. Polleux, and H. Rigneault, “Photoinduced Heating of Nanoparticle Arrays,” *ACS Nano*, vol. 7, no. 8, pp. 6478–6488, 2013.

[17] A. Bouhelier, R. Bachelot, J. S. Im, G. P. Wiederrecht, G. Lerondel, S. Kostcheev, and P. Royer, “Electromagnetic Interactions in Plasmonic Nanoparticle Arrays,” *J. Phys. Chem. B*, vol. 109, no. 8, pp. 3195–3198, 2005.

[18] P. B. Johnson and R. W. Christy, “Optical Constants of the Noble Metals,” *Phys. Rev. B*, vol. 6, no. 12, pp. 4370–4379, 1972.

[19] P. B. Johnson and R. W. Christy, “Optical constants of transition metals: Ti, V, Cr, Mn, Fe, Co, Ni, and Pd,” *Phys. Rev. B*, vol. 9, no. 12, pp. 5056–5070, 1974.

[20] G. J. Edwards and M. Lawrence, “A temperature-dependent dispersion equation for congruently grown Lithium Niobate,” *Opt. Quantum Electron.*, vol. 16, no. 4, pp. 373–375, 1984.

[21] J. R. Carruthers, G. E. Peterson, and M. G. M. Bridenbaugh, “Nonstoichiometry and Crystal Growth of Lithium Niobate,” vol. 1846, no. 1971, 1998.

[22] V. K. Natrajan and K. T. Christensen, “Two-color laser-induced fluorescent thermometry for microfluidic systems,” *Meas. Sci. Technol.*, vol. 20, no. 1, p. 15401, 2008.

5 Numerical simulations of plasmonic controlled pyro-electrokinetic phenomena

Summary

In this chapter, forces induced on a particle in microfluidic environment during pyroelectric manipulation, are discussed. Particular emphasis is placed on the magnitude of unintended forces introduced as a consequence of pyroelectric field generation, and how their presence affects trapping. Numerical simulations are used to predict the magnitude of these forces and to form a guideline for predicting which microfluidic environments support electrokinetic manipulation and the dominant mechanisms.

5.1 Introduction

To control particle motion using electrokinetics, the total primary (intentionally induced) electrical force needs to be greater than other forces a particle experiences in a microfluidic chamber. A sufficiently large electric field of the right nature (geometry, frequency etc.) is required to produce said force. The question of what constitutes a sufficiently large electric field is a nebulous concept, as the magnitude of the electrokinetic and competing forces are dependent on a number of factors and as such, their combined influence on overall particle motion cannot be generalised.

This chapter presents numerical simulations of pyroelectric field generation as a result of temperature changes, and forces on a particle in a microfluidic environment, as a means of predicting the nature of pyroelectric induced motion. A parametric approach to modelling is used in order to predict the evolution of forces with temperature change, bead size, and other relevant parameters.

5.2 Materials and methods

5.2.1 Finite element simulation

COMSOL Multiphysics was used to model pyroelectric field generation, temperature generation and fluid dynamics of the microfluidic system. Model geometry and boundary conditions are as described in Section 3.7.3. Thermal stimulation is provided by a Gaussian laser beam (w_0= 13 μm)

exciting an array of 40 nm discs with 200 nm pitch. Where a fixed temperature (341 K) is used, the laser power is at the maximum recorded experimentally (7.6 mW) unless otherwise stated. Silicone oil and silica beads are used as exemplary fluids and particles respectively. The values of relevant model parameters are summarised in Table 5.1. An exemplary silicone oil viscosity was measured using an Anton-Paar MCR-302 rheometer. The thermal properties of KF-96 [1] serve as estimates for the temperature dependent material properties of the generic silicone oil used in the model.

Table 5.1: Solvent and particle material properties used in finite element simulation

	Silicone oil	**Silica beads** [2]	**Units**
Refractive index (n)	1.495 [3]	1.46	N/A
Density (ρ)	1.05 [3]	2.06	g/mL
Thermal conductivity (κ)	0.1	N/A	W/m·K
Specific heat capacity (C_p)	2	N/A	kJ/kg·K
Viscosity (η)	109	N/A	mPa·s
Relative permittivity (ε_r)	2.2 [4]	2.8	N/A
Thermal expansion coefficient	1×10^{-3}	N/A	1/K
Dielectric expansion coefficient	-3.2×10^{-3} [5]	N/A	1/K

5.3 Results and discussion

5.3.1 Pyroelectric field generation

5.3.1.1 Surface charge and discharge

Pyroelectric field generation, and the nature and magnitude of the electric field within the surrounding fluid medium (dielectric), are dependent on two processes: charge generation and surface discharge. These processes can be explained sequentially, using the equivalent electrical circuit of the microfluidic system which is displayed in Figure 5.1.

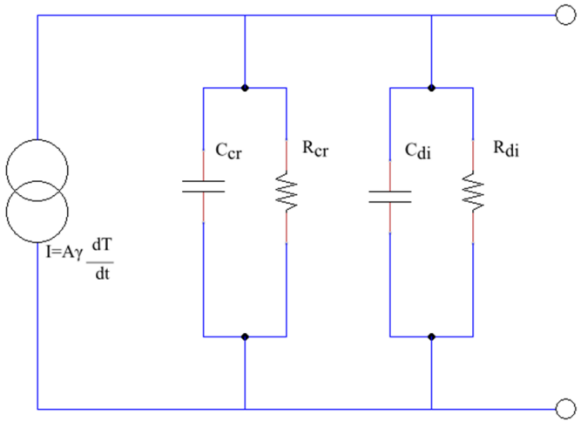

Figure 5.1: Equivalent circuit of pyroelectric crystal and fluid medium

The microfluidic system in which experiments are performed (illustrated in Chapter 3) is described using two lossy capacitors in parallel [6], biased by a temperature dependent current source where the current generated is given as,

$$I_s = A\gamma \frac{\mathrm{d}T}{\mathrm{d}t}. \tag{5.1}$$

As a result of laser excitation, temperature rises until it reaches an equilibrium state i.e. $\frac{\mathrm{d}T}{\mathrm{d}t} = 0$. Giving that the temperature change is a result of collective plasmonic nanoparticle stimulation, the characteristic thermal time scale is given by the expression below:

$$\tau_{\mathrm{th}} = \frac{D^2 \rho_s C_{ps}}{4\kappa_{\mathrm{s}}}, \tag{5.2}$$

where ρ_{s} is the substrate mass density, κ is the thermal conductivity, C_{ps} is the heat capacity, and D is the laser beam diameter. When α, the thermal diffusivity, is used (defined previously as $\frac{\kappa}{\rho\, C_p}$), (5.2) becomes:

$$\tau_{\mathrm{th}} = \frac{D^2}{4\alpha_{\mathrm{s}}}. \tag{5.3}$$

For times shorter than the characteristic thermal timescale (3.55 ms for a 26 μm laser beam in silicone oil), the pyroelectric crystal is in a charging phase. Using a combination of Kirchhoff's circuit laws and Ohm's law, the current flowing through the system is given by [7]:

$$\gamma A \frac{\mathrm{d}T}{\mathrm{d}t} = (C_{\mathrm{cr}} + C_{\mathrm{di}}) \frac{\mathrm{d}V}{\mathrm{d}t} + V\left(\frac{1}{R_{\mathrm{cr}}} + \frac{1}{R_{\mathrm{di}}}\right). \tag{5.4}$$

This yields a differential equation for the voltage in the system given as,

$$\frac{\mathrm{d}V}{\mathrm{d}t} = \frac{\gamma A}{C_{\mathrm{eq}}} \frac{\mathrm{d}T}{\mathrm{d}t} - \frac{V}{R_{\mathrm{eq}} C_{\mathrm{eq}}}, \tag{5.5}$$

where R_{eq} is the parallel combination of the pyroelectric and dielectric resistances, and C_{eq} is the parallel combination of the pyroelectric and dielectric capacitances. The solution to this differential equation gives the time dependent voltage as,

$$V(t) = \gamma A R_{\mathrm{eq}} \frac{\mathrm{d}T}{\mathrm{d}t} \left(1 - e^{-\frac{t}{\tau_{\mathrm{e}}}}\right). \tag{5.6}$$

Equation (5.6) describes a saturated voltage curve with an exponential approach, where τ_{e} is the electrical time constant (charge relaxation time) given by $R_{\mathrm{eq}} C_{\mathrm{eq}}$.

The electrical circuit behaviour from $t > \tau_{\mathrm{th}}$ differs from that previously described. In spite of illumination, temperature remains constant and no charge is generated by the pyroelectric. A combination of Kirchhoff's circuit laws and Ohm's laws in this phase gives the current in the system as,

$$0 = (C_{\mathrm{cr}} + C_{\mathrm{di}}) \frac{\mathrm{d}V}{\mathrm{d}t} + V\left(\frac{1}{R_{\mathrm{cr}}} + \frac{1}{R_{\mathrm{di}}}\right). \tag{5.7}$$

The redefined differential equation describing voltage is thus given as,

$$\frac{\mathrm{d}V}{\mathrm{d}t} = -\frac{V}{\tau_{\mathrm{e}}}. \tag{5.8}$$

The solution of which is:

$$V(t) = V e^{-\frac{t}{\tau_{\mathrm{e}}}}. \tag{5.9}$$

Equation (5.9) describes an exponentially decaying voltage, where V is the voltage generated during the charging phase i.e.

$$V = \gamma A R_{\mathrm{eq}} \frac{\Delta T}{\tau_{\mathrm{th}}} \left(1 - e^{-\frac{\tau_{\mathrm{th}}}{\tau_{\mathrm{e}}}}\right). \tag{5.10}$$

From these explanations the salient parameters are the observation time (t), the charge relaxation time (τ_{e}), and the thermal timescale (τ_{th}). In the context of continuous wave illumination, it is assumed that the stimulated plasmonic array reaches its equilibrium state very early in the observation phase (i.e. $\tau_{\mathrm{th}} \ll t$). As such, the pyroelectric crystal is predominantly in a surface discharge phase during the observation period. To ensure electrokinetic forces do not deteriorate during laser stimulation, the generated voltage and by extension, the electric field are required to be above a specific threshold throughout the observation period. If this threshold voltage is defined arbitrarily as,

$$V_{\mathrm{th}} \geq 0.9\, V, \tag{5.11}$$

the ratio of the observation period to the charge relaxation time is defined as,

$$\frac{t}{\tau_{\mathrm{e}}} \leq -\ln 0.9. \tag{5.12}$$

Thus the range of timescales under which surface discharge effects are at the arbitrarily defined minimum is given as:

$$t \leq 0.1\tau_{\mathrm{e}}. \tag{5.13}$$

The results of finite element simulations performed in a time harmonic regime, can be used to visualise the effects of solvent polarity and conductivity on the magnitude of the electric field within the dielectric, as well as the range of observation periods for which the above condition is satisfied. The simulation geometry is as defined in Section 3.7.3. Substrate parameters are defined previously. In Figure 5.2, the solvent conductivity is fixed to 10^6 S/m while polarity (in the form of electrical permittivity) and observation period (1/frequency) are varied. Note that increasing the solvent polarity reduces the electric field strength. An observation period of 10^4 Hz (10^{-4} seconds) is required in solvents of this conductivity to ensure that V is greater than V_{th}.

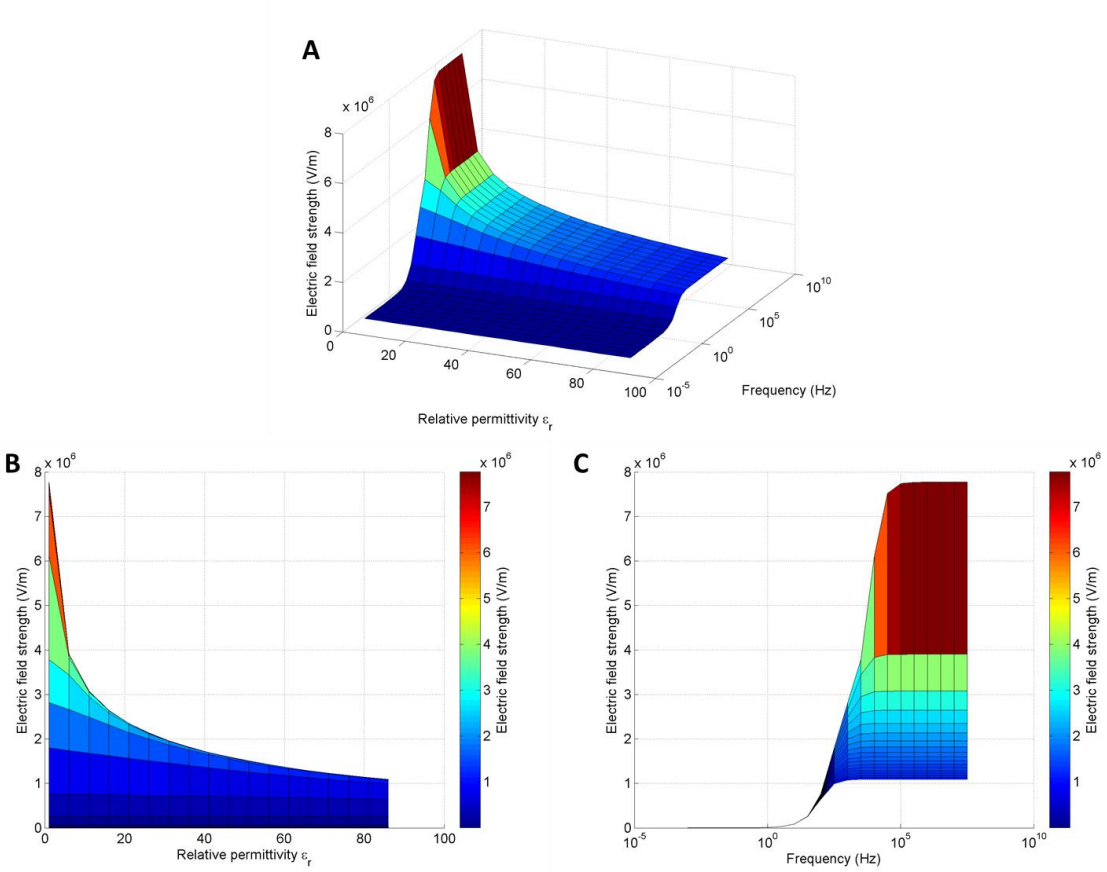

Figure 5.2: A) Electric field strength as a function of permittivity and frequency of thermal stimulation. B) 2D cross section illustrating decay of electric field with permittivity. C) 2D cross section illustrating increase and eventual saturation of electric field with frequency.

A similar set of simulations is performed with fixed frequency (10^{-3} Hz or a characteristic observation time in minutes), and varying conductivity and polarity. The results are depicted in Figure 5.3. The behaviour of electric field strength with respect to solvent polarity is unchanged. To fulfil the condition previously described ((5.11)), a solvent with an electrical conductivity of $<10^{-12}$ S/m is required.

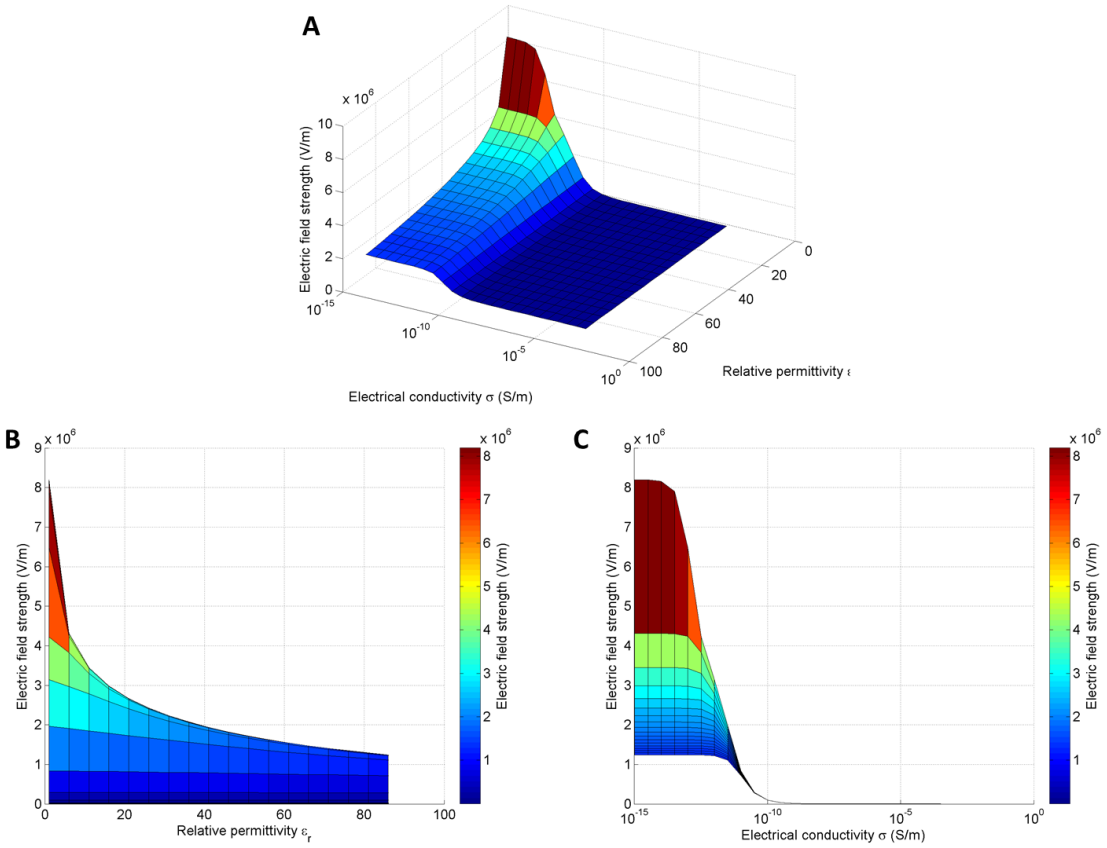

Figure 5.3: A) Electric field strength as a function of solvent permittivity and conductivity. B) 2D cross section illustrating decay of electric field with permittivity. C) 2D cross section illustrating decay with conductivity. For low conductivities electric field saturation is observed.

With the use of solvents of such low conductivity, a static approximation can be used to solve for the pyroelectrically generated voltage when $t < 0.1\tau_e$. Figure 5.4 shows the electric field behaviour calculated using only dielectric parameters (i.e. conductivities have been ignored). The values of the electric field are identical to the maximum calculated using the multivariate expression incorporating conductivities and charge relaxation time.

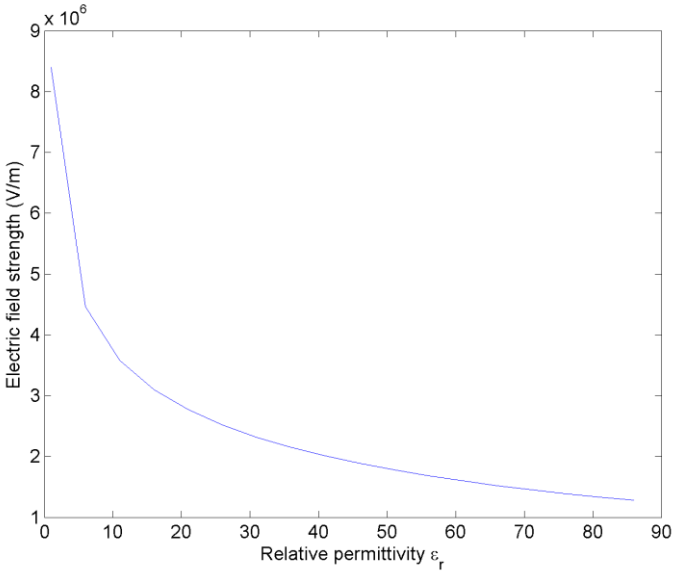

Figure 5.4: Electric field strength calculated using only dielectric parameters. Trend matches that observed when high frequencies/large fluid resistivities are used.

In the defined static condition, the pyroelectrically generated voltage is effectively constant since, as $\tau_{\mathrm{th}} \ll t$, the charging phase is practically instantaneous, and surface discharge effects are now negligible. A new expression for the voltage can be written using the pyroelectric charge, and ignoring the solvent and crystal conductivities (where the change in temperature is spatially uniform) [6]:

$$V = \frac{A\gamma\Delta T}{C_{\mathrm{eq}}}. \tag{5.14}$$

In the context of the equivalent circuit illustrated, the electric field in the dielectric is of the form:

$$E = \frac{V}{L}, \tag{5.15}$$

where L is the capacitor thickness.

Under a static approximation, the electric field within the dielectric is given by the equation below:

$$E = \frac{\gamma\Delta T}{\varepsilon_{\mathrm{di}} + \frac{\varepsilon_{\mathrm{cr}} L_{\mathrm{di}}}{L_{\mathrm{cr}}}}. \tag{5.16}$$

Hence, to maximise the efficiency of pyroelectric field generation, a dielectric fluid is required as a result of the low conductivity of lithium niobate (2.63×10^{-15} S/cm as quoted by Roditi [8]). Figure 5.5 shows particle concentration as a result of pyroelectric field generation. Though it is possible to generate electric fields pyroelectrically in other solvents, this requires modulated thermal stimulation or the ability to observe and complete experiments in periods close to, or quicker than the thermal response time.

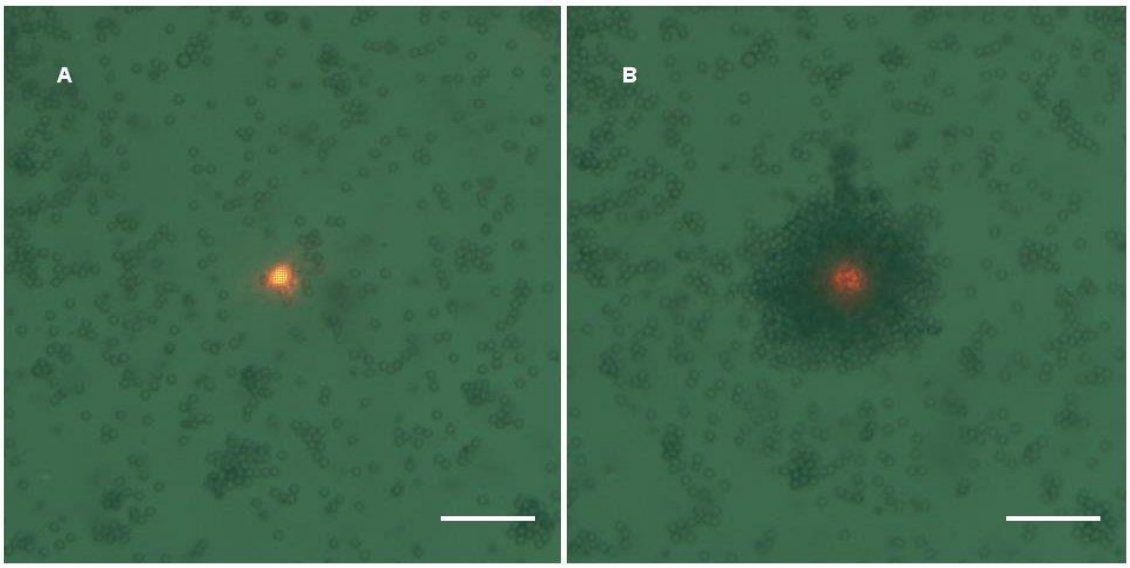

Figure 5.5: Concentration of 5 µm PMMA beads in silicone oil. This is not possible in polar, conducting solvents. A) Beads at the start of laser stimulation. B) Beads after 30 seconds of stimulation. Scale bar is 50 µm.

5.3.1.2 Spatial variations of pyroelectric field

Though the static approximation employed is able to estimate the magnitude of a pyroelectric field for a given temperature change, there is no indication of the spatial variation of this field within the dielectric, information which is key in determining which electrokinetic mechanisms can be employed for a given experimental design. This information is derived by solving Gauss's electrostatic equation, with particular emphasis on the interface between the pyroelectric crystal and fluid dielectric. The key condition is continuity of electric displacement:

$$D_{\mathrm{cr}} - D_{\mathrm{di}} = \sigma, \tag{5.17}$$

where σ is the surface charge density given by :

$$\sigma = \gamma \Delta T(r). \tag{5.18}$$

From (5.18), it can be estimated that at the fluid-pyroelectric interface, the spatial variation of the electric field mirrors the thermal field. This is confirmed by Figure 5.6, which shows a linear relationship between electric field and laser induced temperature, matching lateral positions on the solid-fluid interface.

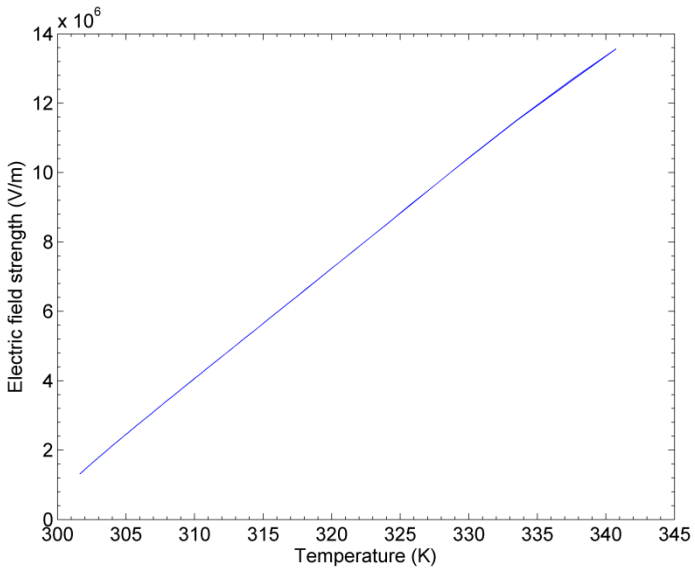

Figure 5.6: Simulated relationship between temperature and electric field strength on the surface of lithium niobate substrate.

The profile of the pyroelectric field generated as a result of stimulation from a Gaussian laser beam is shown in Figure 5.7.

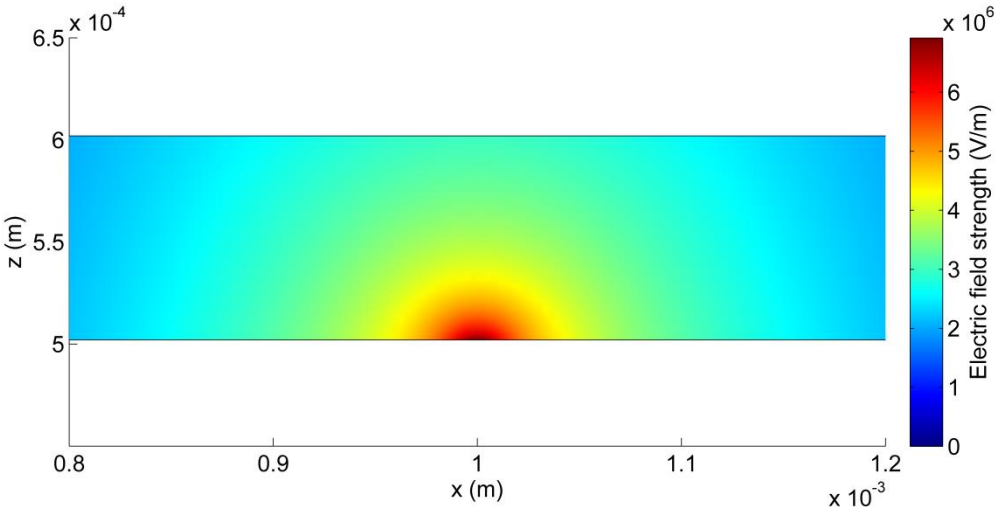

Figure 5.7: Spatial variation of electric field.

5.3.2 Dimensionless thermodynamic numbers

In the course of numerical simulation of the microfluidic system, a number of approximations have to be made to decouple thermal and mechanical expressions from each other and allow these equations to be solved independently. The validity of these approximations determines how accurately the numerical simulations model experimental behaviour. The accuracy of these approximations can be estimated using a series of dimensionless numbers, which compare the order of magnitude of relevant parameters in order to determine their respective contributions.

5.3.2.1 Reynold's number

The distinction between laminar and turbulent flow regimes is made using the Reynold's number, a dimensionless number which indicates whether inertial or viscous forces [9] dominate within a frame of reference. The Reynold's number is given by:

$$Re = \frac{\rho L v}{\eta}, \tag{5.19}$$

where L is the characteristic length of the system, v is the velocity, ρ is the volumetric mass density of the fluid, and η is the fluid's dynamic viscosity.

The transition from laminar to turbulent regimes occurs when $Re > 1$ (i.e. flow is considered laminar when $Re < 1$) [10]. Based on this definition, an inequality that defines a range of velocities under which flow is considered to be laminar can be created. This is given as:

$$v \leq \frac{\eta}{\rho L}. \tag{5.20}$$

Using some characteristic parameters of the microfluidic system under examination (L= 100 µm, η=109 mPa·s, ρ= 1.05× 10^3 kg/m^3), it can be calculated that velocities below 1 m/s are conducive to laminar flow. This suggests that inertial forces are negligible in a microfluidic system, and dynamics are dominated by viscous forces.

5.3.2.2 Peclet number

The conductive heat equation defined in Chapter 2 is used to calculate the magnitude of plasmonic heating generated. In using the conductive heat equation, it is assumed that heat transfer in the microfluidic system considered is diffusive in nature. Thus, thermally activated mass transport processes (chiefly convection) are neglected. The Peclet number defines the transition between heat convection and heat diffusion [9]. This is given by:

$$Pe = \frac{\rho C_p v L}{\kappa}, \tag{5.21}$$

where v is the fluid velocity, L is the characteristic length of the system, ρ is the fluid density, κ is the thermal conductivity and C_p is the heat capacity. When α, the thermal diffusivity is used, (5.21) becomes:

$$Pe = \frac{vL}{\alpha}. \tag{5.22}$$

The transition from diffusive heat transfer to convective heat transfer occurs at $Pe = 1$ (i.e. heat transfer is diffusive when $Pe < 1$ and convective when $Pe > 1$).

Again, an inequality can be defined to gain a range of fluid velocities where heat transfer is diffusive as:

$$v \leq \frac{\kappa}{\rho C_p L}. \tag{5.23}$$

Using the previously defined parameters, heat transfer is diffusive for velocities < 480 µm/s. This suggests that for solutions of the Navier-Stokes equation below this threshold, convection has little effect on heat transfer in the modelled systems i.e. temperature generation can be considered independently of mass transport.

5.3.3 A thermally limited trap/figure of merit

The thermal limit is used to define the stability of a trap and can be explained by considering the energy associated with different forces, or equivalently using stochastic integration techniques employed in the evaluation of the Langevin equation.

In the energy framework, particles are attracted to the point of maximum electrokinetic force (potential well), and require a disturbance from an energy with equal and opposite magnitude to displace them completely from this potential well. In a perfect system, no external stimulation (as defined in the Langevin equation) exists other than the trapping force. Hence, any deviation from the potential well is a result of thermal energy (i.e. Brownian motion) [11].

For a stable trap, the depth of the potential well is greater than the thermal energy associated with the particle. Giving that thermal energy is governed by Boltzmann statistics, it should be noted that the often used expression for this (kT) refers to an average measure of thermal processes, and instantaneous disturbances from energies higher than kT are possible and statistically probable.

A more intuitive explanation can be made using the iterative stochastic integration process. Here, the typical velocities associated with each process are compared against each other [12]. The velocity associated with the trapping force needs to be greater than that associated with Brownian motion, such that the time taken to attract/trap the particle $\ll$ the time taken for it to escape due to thermal energy.

The trapping velocity (from Stokes's drag) is given by:

$$U_{\text{ext}} = \frac{F_{\text{ext}}}{6\pi\eta r} \tag{5.24}$$

Using elementary definitions of velocity, a characteristic timescale can be derived as follows:

$$\frac{\Delta d}{\Delta t} = \frac{F_{\text{ext}}}{6\pi\eta r} \tag{5.25}$$

$$t_{\text{ext}} = \frac{6\pi\eta r \Delta d}{F_{\text{ext}}}, \tag{5.26}$$

where t_{ext} is the time it takes to a particle to travel a characteristic distance.

The Brownian timescale is given by:

$$t = \frac{3\pi\eta r(\Delta d)^2}{kT}. \tag{5.27}$$

In this expression, the mean squared displacement ($\bar{x}^2$) has been replaced by Δd, i.e. the Brownian timescale refers to the time it takes for a particle to traverse the previously defined characteristic distance purely under the influence of thermal energy.

The condition for stable trapping is thus gained by comparing the characteristic timescales as below:

$$\frac{6\pi\eta r \Delta d}{F_{\text{ext}}} < \frac{1}{10}\left(\frac{3\pi\eta r(\Delta d)^2}{kT}\right). \tag{5.28}$$

The additional 1/10 scalar is an arbitrary factor, introduced such that the external force still dominates over instantaneous high thermal energy forces. By rearranging this inequality and inserting relevant expressions for the external forces, more definite values for parameters affecting electrokinetic particle motion (e.g. electric field strength, particle surface charge density, Claussius-Mossotti factor etc.) can be derived.

5.3.4 Extrinsic forces

Figure 5.8 illustrates the interaction between extrinsic forces (those which are absent when laser excitation is removed) on a particle in a microfluidic system. Laser heating of the pyroelectric substrate induces localised surface charges, which in turn generate an electric field within the fluidic environment. In addition to the forces acting directly on the particle as a result of laser stimulation (F_p in the diagram), the electric field and temperature gradient also generate fluidic

body forces (F_f) which act indirectly on the particle because of drag. The sum of these forces dictates the direction of particle motion. The effects of individual extrinsic forces on particle motion are discussed below.

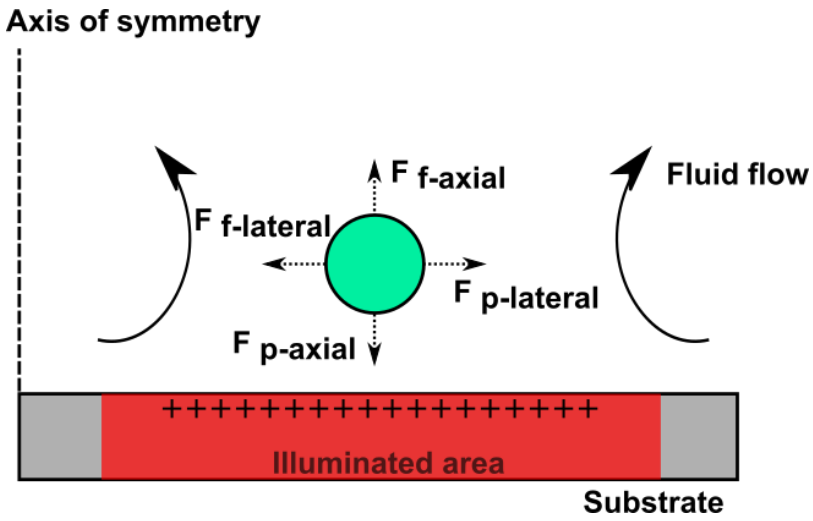

Figure 5.8: Free body diagram of externally actuated forces

5.3.2.3 DEP/EP

The dominant mechanisms controlling electrokinetic particle motion depends on the magnitude and spatial variation of the electric field and the electroneutrality of the particle in question. Based on the simulation above, the generated electric field profile has a Gaussian origin, which is sufficiently non-uniform to allow for the establishment of DEP. In anticipation of likely modes of operations of the manipulation system, and for ease of comparison with experimental results, the simulation considers positive DEP of functionally neutral silica particles ($\varepsilon_{\mathrm{p}} = 2.8$) in silicone oil ($\varepsilon_{\mathrm{m}} = 2.1$). It is anticipated that in contrast to the situation frequently described in the literature (in which the electrical conductivities of the medium and the particle are responsible for the behaviour of electrical polarisation at low frequencies), the electrical permittivity dictates the magnitude of the Claussius-Mossotti factor even at the low frequencies of operation considered, due to the extremely low resistivity of both the solvent and the particle.

Figure 5.9 and Figure 5.10 illustrate the spatial variation of the DEP force acting on a 1 µm silica bead. Note that the DEP force is very tightly confined to a 100 µm radius. The maximum occurs when beads are at the interface and decays rapidly with increasing height such that it is negligible for heights 20 µm above the interface.

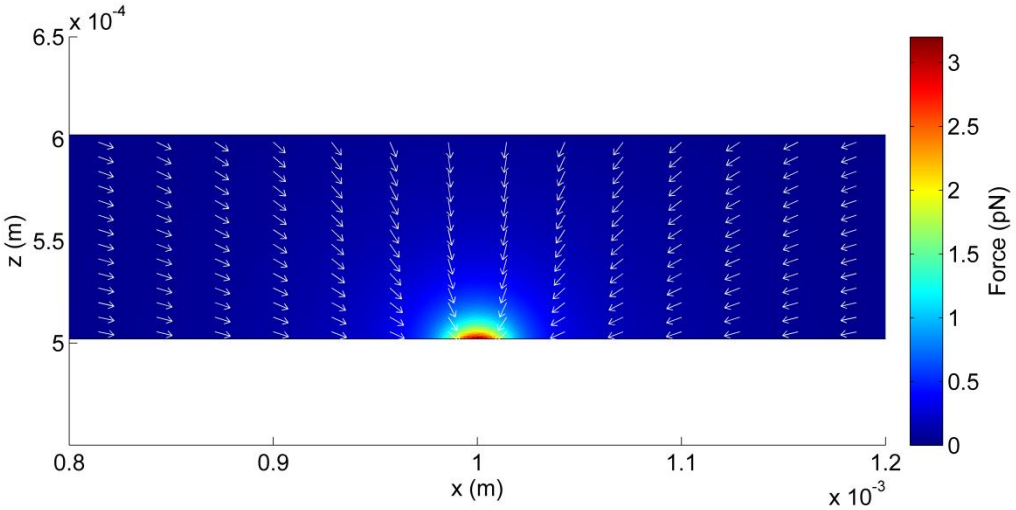

Figure 5.9: Spatial distribution of dielectrophoretic force in the absence of other forces. Arrows show particles are attracted to laser spot.

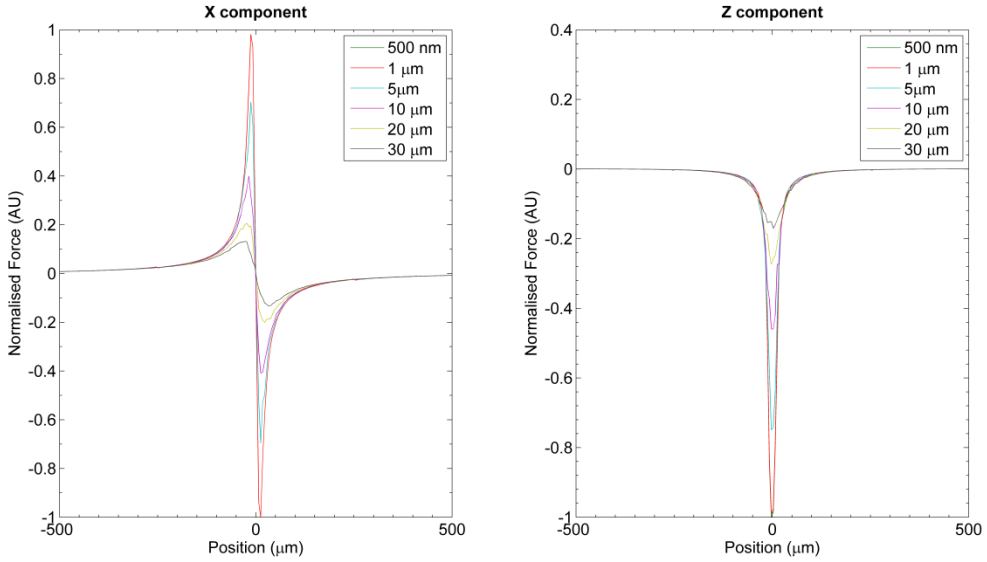

Figure 5.10: Spatial variation of horizontal (x) and vertical (z) components of dielectrophoretic force. Force is at a maximum close to the solid-fluid interface.

Dielectrophoresis is the only source of particle based electrokinetic motion in electroneutral particles. From previous discussions, it has been shown that electroneutrality of particles is not guaranteed in spite of their preparation, due to solid-surface interactions which can induce charges of a given surface density on a particle. Hence, electrophoretic behaviour is not neglected in the discussion of the electrokinetic behaviour of particles.

Using a similar technique as performed in defining the thermal limit of a trap (i.e. comparing characteristic velocities associated with electrophoretic motion and dielectrophoretic motion), the maximum surface charge density under which a given particle can be considered functionally neutral is given as:

$$\rho < \frac{r\varepsilon_{\mathrm{m}} K \nabla |E|^2}{2\,E} \tag{5.29}$$

For particles with a charge density significantly higher than those gained when (5.29) is evaluated, electrophoretic based particle motion dominates. Figure 5.11 depicts a situation in which dielectrophoresis appears to be the dominant force, characterised by pearl chaining of the silica beads. Electrophoretic behaviour is observed in Figure 5.12, where carboxylated polystyrene beads are separated from amine-functionalised beads.

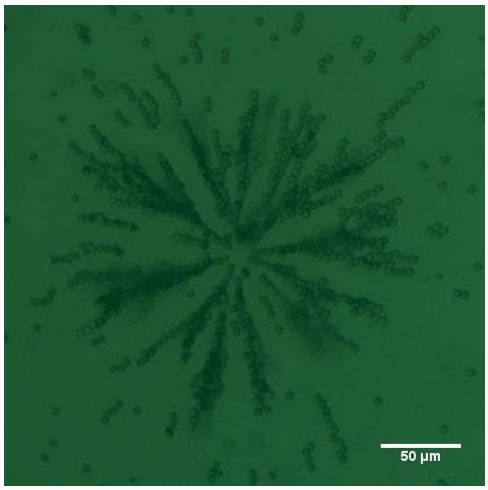

Figure 5.11: Pearl chaining of silica beads following laser stimulation characteristic of DEP.

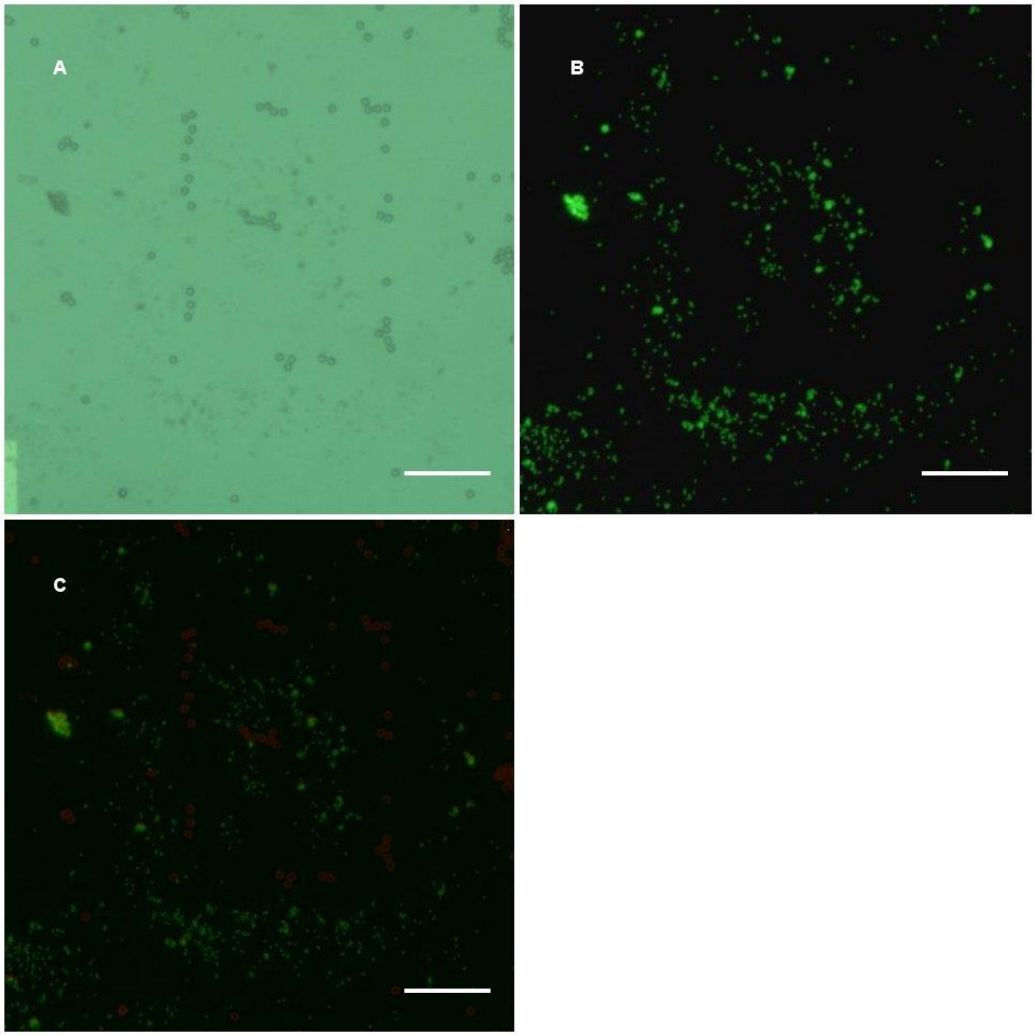

Figure 5.12: Charge and size based separation of beads owing to multiple electrokinetic phenomena (including electrophoresis) occurring simultaneously (Section 5.4). A) Bright field image depicting patterning by attraction of 5 µm carboxylated polystyrene beads. B) Fluorescent image depicting repulsion of 1 µm amine beads. C) Composite image depicting separation of 5 µm (red) and 1 µm (green) polystyrene beads. Scale bar is 50 µm.

The spatial variation of the electrophoretic force is depicted in Figure 5.13. The force vectors are identical to the electric field. The simulation considers the case where electrophoretic and dielectrophoretic motion is in the same direction. Due to the spatial variation of the electric field, the maximum electric field and maximum electric field gradient are coincident, and trapping occurs at the same point.

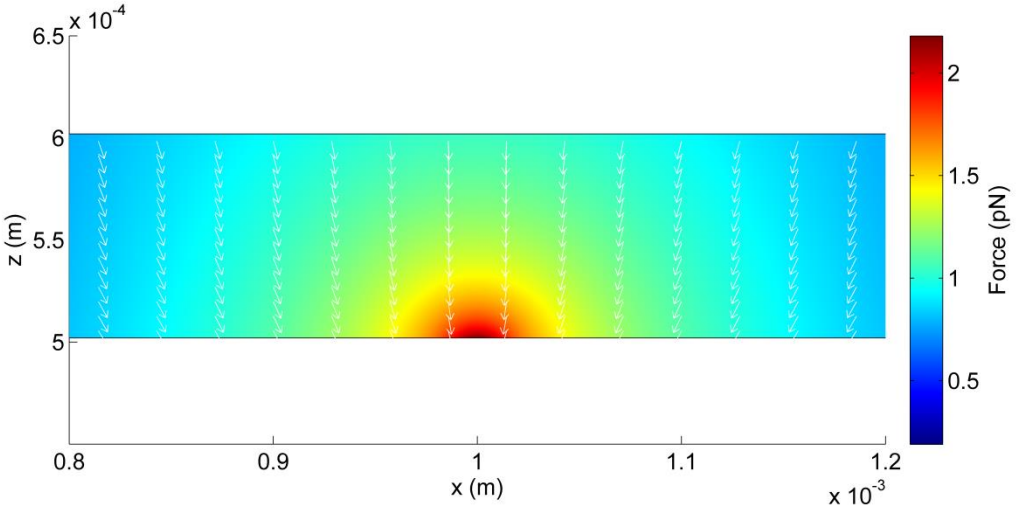

Figure 5.13: Spatial distribution of electrophoretic force in the absence of other forces. Arrows show particles are attracted to laser spot.

As the maximum electrophoretic force decays much less rapidly than the dielectrophoretic force, i.e. it is not confined to the immediate vicinity of the laser beam (Figure 5.14), it can be used as a DEP promoter, enabling long range manipulation of particles as in the simulation considered. Using electrophoresis in this manner requires prior knowledge of the sense of the pyroelectric crystal, to ensure both electrophoretic and dielectrophoretic forces act in the same direction.

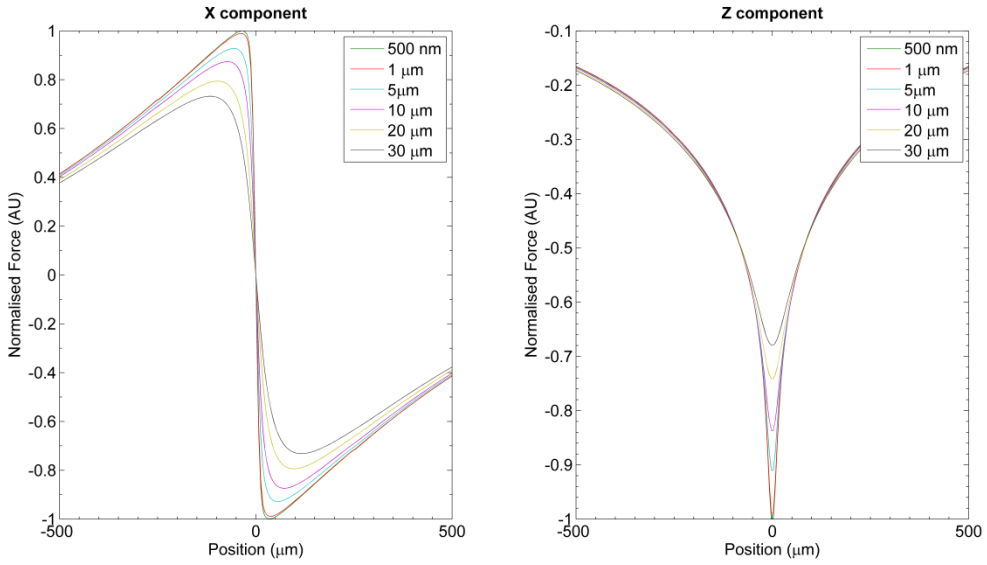

Figure 5.14: Spatial variation of horizontal (x) and vertical components of electrophoretic force. Force is at a maximum close to the solid-fluid interface.

5.3.2.4 Convection

Temperature gradients create a change in fluid density which causes natural convection. The body force associated with convection is given by:

$$f = \frac{\mathrm{d}\rho}{\mathrm{d}T}\Delta T g\hat{z} \tag{5.30}$$

Alternatively, the Boussinesq approximation can be used, which assumes density varies linearly with temperature (an approximation which can be made if the change in temperature is small enough). This is given as:

$$f = \Delta T g \rho \beta, \tag{5.31}$$

where β is the linear coefficient of thermal expansion of the fluid.

The image below shows the characteristic toroidal pattern associated with natural convection, with the arrows indicating the direction of travel. Particles are attracted to the hotspot at horizontal planes close to the solid-liquid interface.

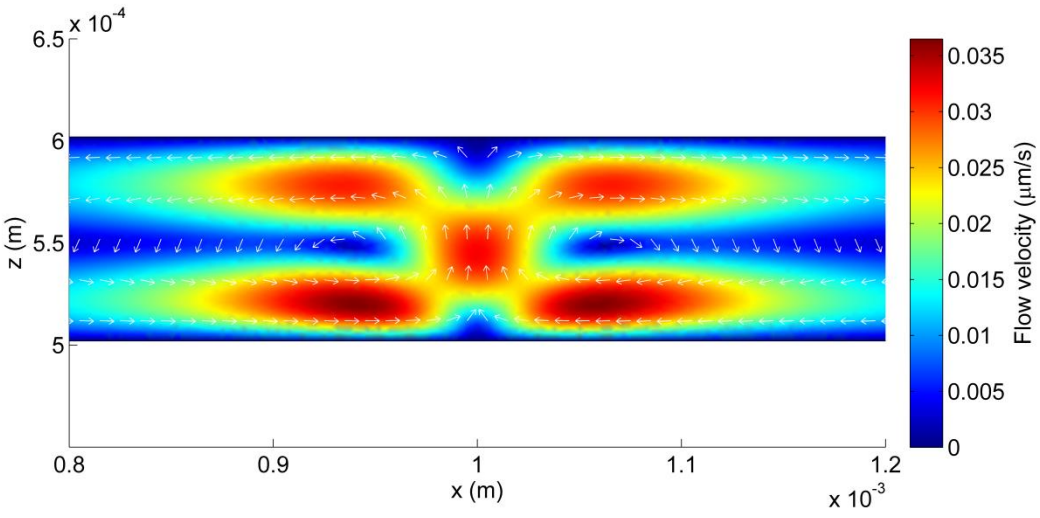

Figure 5.15: Simulated thermal convection flow pattern. Flow minimum coincides with laser spot. Lateral direction reverses for heights above 50 µm.

In comparison to dielectrophoresis and electrophoresis, convective velocity is negligible and has little effect on particle motion. As thermal convection is the only extrinsic force which occurs

strictly as a result of thermal stimulation, it is the only source present on glass and pyroelectric substrates as well as one of the main explanations for motion on glass. Giving the velocities calculated (0.04 μm/s), the effects of thermal convection on silica beads are negligible. Convection effects are however amplified on glass as a result of the substrate's poorer thermal conductivity in comparison to lithium niobate (1.38 vs 4 W/m·K). As a result, where all other factors are equal (laser power, plasmonic absorption cross section and array density, surrounding environment), the temperature generated and subsequently the velocity of convection on a glass substrate is ~4× that of lithium niobate. Hence, plasmonic convection occurs at lower laser powers on glass than lithium niobate.

5.3.2.5 Electrohydrodynamic effects

The use of non-polar, insulating materials and the quasi-static nature of the generated electric field have a marked effect on the electrohydrodynamic effects. The major characteristic of such media is the low dissociation degree of electrolytes causing low ion concentration. This reduction in ion concentration far outweighs the reduction in electrical permittivity, resulting in an increase in the size of the Debye length. As a result of this, the distribution of ions in the double layer is distorted preventing electroosmotic flow [13],[14]. Electrothermal body forces are thus the primary electrohydrodynamic effects. The characteristic slow charge relaxation time of non-polar insulating fluids means that β is functionally negligible [5][15], as Coulombic polarisation evolves very slowly in response to a perturbation. Thus, the electrothermal force is primarily a result of dielectric forces.

Figure 5.16 shows solutions of the Navier-Stokes equation with the electrothermal force as a perturbing agent. α in this case is set to -3.2× 10^{-3}, the typical value of silicone oils listed in the literature [5]. As with thermal convection, there is a characteristic toroidal flow induced in the fluid. This is much more dominant than thermal convection, being ~4 orders of magnitude greater (80 μm/s at its maximum compared to 0.04 μm/s).

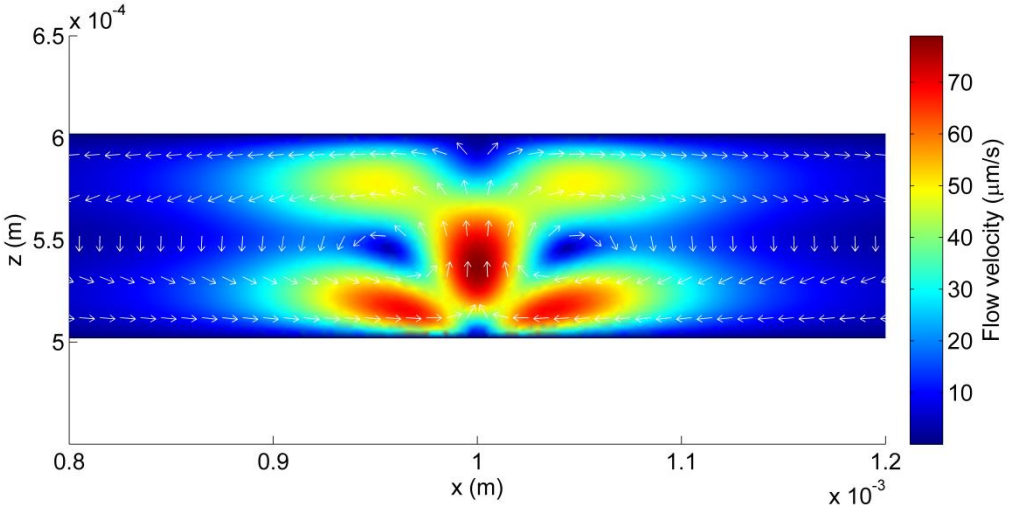

Figure 5.16: Simulated electrothermal convection pattern. Flow minimum coincides with laser spot. Lateral direction reverses for heights above 30 µm.

In common with dielectrophoresis, the magnitude of this force is independent of the surface charge of a particle. In addition to this, the displacement as a result of electrothermal convection is operational over a wider geometric space (similar to electrophoresis). As such, electrothermal convection can also be used for the long range of manipulation of particles, as illustrated in Figure 5.17. Since the force minimum is coincident with the dielectrophoretic maximum, the electrothermal force can be used to aid trapping of neutral particles, and is not necessarily competitive with the trapping mechanism. In addition, using electrothermal convection as a DEP promoter is easier to predict, as it occurs independent of particle geometry and electrical properties.

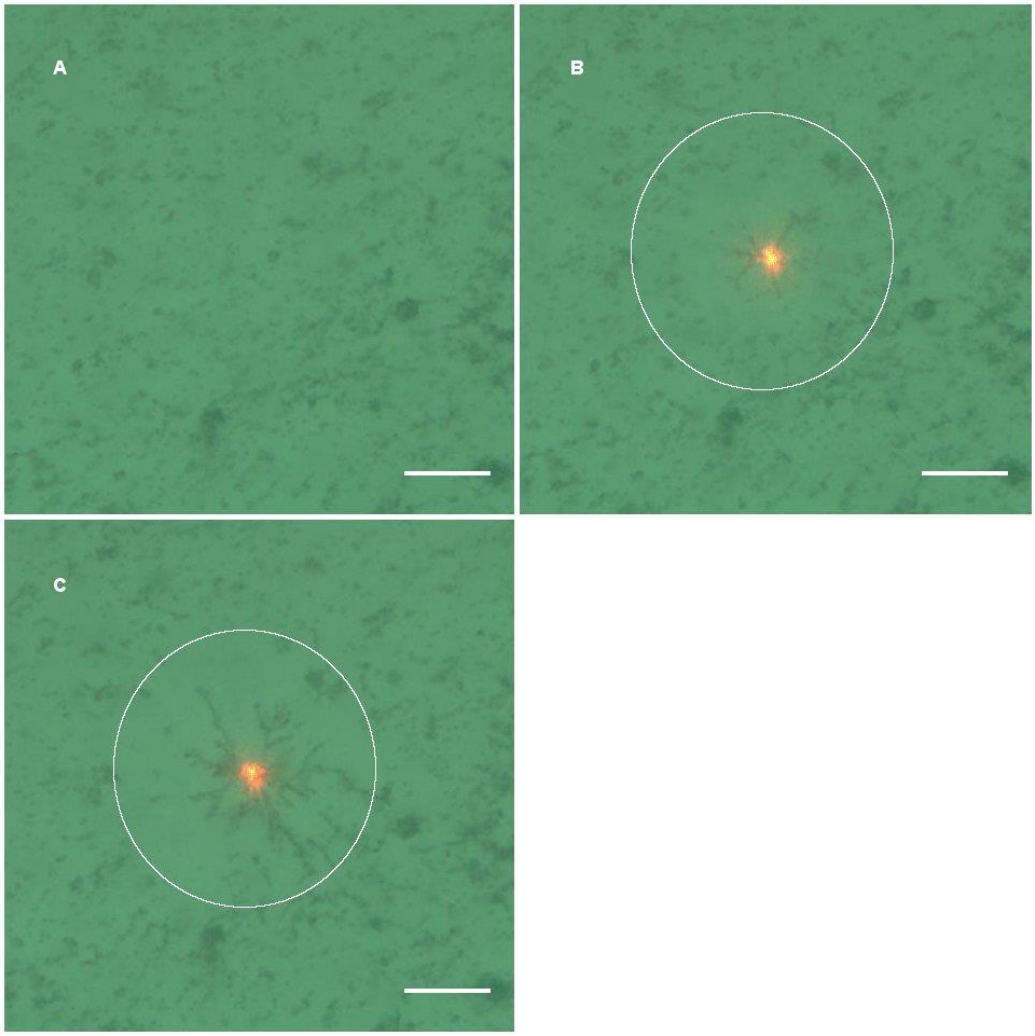

Figure 5.17: Timelapse image depicting simultaneous trapping and convection of 2.5 µm beads. Labelled circles depict the extent of the torus created as a result of convection. A) 2.5 µm beads before trapping. B) 2 seconds after stimulation begins, beads start to assemble themselves in pearl chains. Recirculation due to toroidal convection is not immediately evident. C) After 30 seconds of stimulation, the pearl chains have increased in size. The contrast between regions affected and those unaffected by laser stimulation is enhanced due to bead recirculation by convection. Scale bar is 50 µm.

5.4 Order of magnitude

Figure 5.18 depicts the characteristic velocities as a result of different forces acting on a 1 µm diameter bead, which is located 500 nm directly above the laser spot at the solid fluid interface, with respect to laser power. The threshold is gained by dividing the maximum Brownian displacement by one second. For powers less than 1.4 mW, Brownian motion is responsible for particle displacement (i.e. laser stimulation has no effect on particles). Above this power, electrophoretic motion begins to dominate. The onset of this condition is dependent on the surface charge density of the particle (this is arbitrarily set as 0.1 $\mu C/m^{-2}$ in these simulations). For a completely neutral particle of the same diameter, there is no electrophoretic motion, and

dielectrophoretic motion would occur at 3 mW. In the simulation considered, dielectrophoretic motion begins to dominate at powers above 6.55 mW. At this distance from the pyroelectric substrate, electrothermal convection is inconsequential for the powers considered.

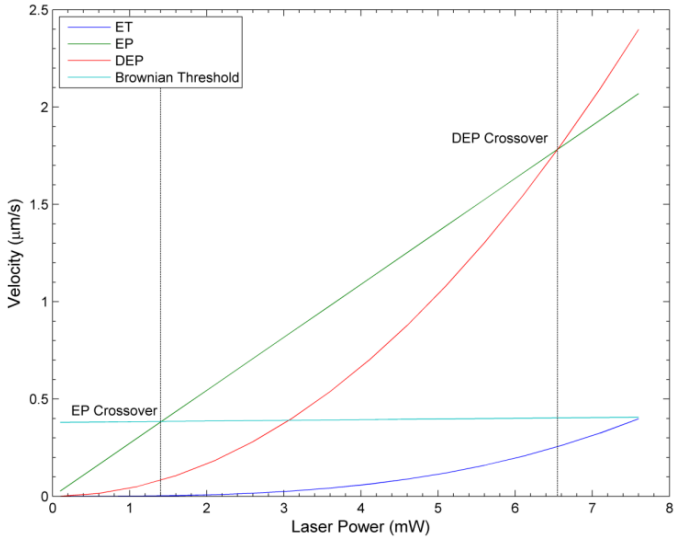

Figure 5.18: Characteristic velocities of a 1 µm bead under the influence of electrothermal (ET), electrophoretic (EP) and dielectrophoretic (DEP) forces at different laser powers. The maximum allowable displacement in 1 second due to Brownian motion is used as a threshold. Bead is located 500 nm above the solid-fluid interface.

The force regimes are defined by the relative magnitude of electrokinetic forces (e.g. electrophoresis vs dielectrophoresis), as opposed to the complete absence of all other electrokinetic forces. For instance, between 3 and 6.55 mW, particle motion is a combination of electrophoresis and dielectrophoresis. In spite of the fact that this is nominally the electrophoretic regime, the assumption that a particle displays purely electrophoretic behaviour becomes more erroneous as the laser power increases, until the dielectrophoretic force more accurately describes particle motion.

In contrast, Figure 5.19 shows the behaviour of a 1 µm silica bead for heights 5 µm above the interface. Due to the spatial decay previously encountered, dielectrophoretic behaviour is comparable to electrophoresis only at the highest power considered (i.e. 7.6 mW). The onset of electrophoretic motion remains largely unchanged, indicating that spatial decay is not quick for this force. Electrothermal behaviour, which proved largely negligible for all powers considered at 500 nm, begins to dominate at 3.7 mW, and is the primary source of bead motion for high laser powers.

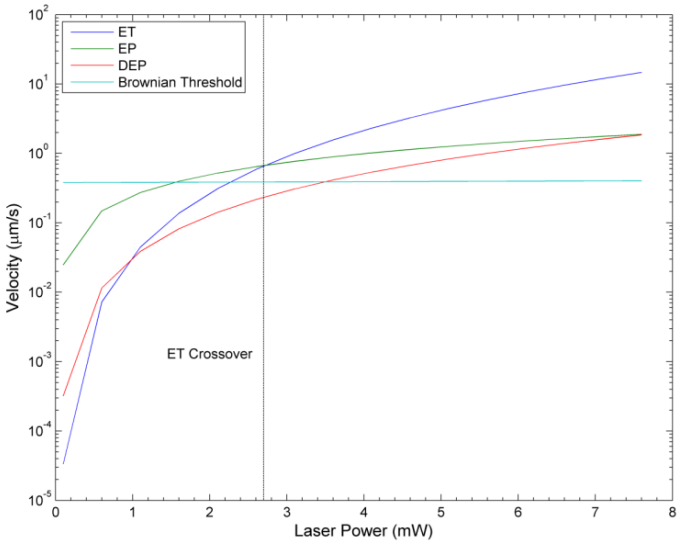

Figure 5.19: Characteristic velocities of a 1 µm bead under the influence of electrothermal (ET), electrophoretic (EP) and dielectrophoretic (DEP) forces at different laser powers. Bead is located 5 µm above the solid-fluid interface.

The relationship between the magnitude of the force and electric field explains how different forces can be activated by modifying the laser power. Brownian motion exhibits a linear increase with laser power. In comparison to the other forces discussed, the rate of increase of this is slow enough that the threshold is effectively constant for the powers and environments considered. This is a result of the large viscosity of silicone oil, as well as the fact that this disturbance is a result of purely thermal effects i.e. the conversion of thermal stimulation to an electric field using the pyroelectric effect amplifies kinetic forces. Electrophoresis has a linear relationship with electric field (and laser power by extension). Dielectrophoresis varies with the square of laser power, due to its relationship to the square of the applied electric field. While the electrothermal force varies with the square of the electric field and the temperature, neither of these parameters are independent in the analysis considered (it is theoretically possible to decouple microfluidic temperature from the pyroelectric by adjusting the resistivity of the solid-fluid interface such that thermal transmission is reduced), as both are controlled by laser stimulation through plasmonic heating. Hence, the electrothermal force varies with the cube of laser power. As laser power grows (approaches infinity), the electrothermal force becomes the dominant source of particle motion regardless of particle properties. The behaviour at more moderate laser powers is dependent on specific electrical parameters (e.g. surface charge density, Claussius-Mossotti factor and dielectric thermal expansion coefficient for electrophoresis, dielectrophoresis and electrothermal flow respectively), as seen previously (i.e. the coefficient of the various powers).

Based on previous definitions, particle size affects the magnitude of some of the discussed kinetic forces. Convection terms (thermal and electrothermal) are ignored in this analysis as they are

independent of particle size. Figure 5.20 depicts the characteristic velocity for a range of different beads located 500 nm above the solid-fluid interface. The applied laser power is 7.6 mW. Note that Brownian motion is inversely proportional to particle size (measured by the radius), thus reducing the previously defined thermal threshold. Electrophoresis is directly proportional, and dielectrophoresis is proportional to the square of particle size. Thus, in a manner similar to the analysis performed with the applied laser power, it can be surmised that dielectrophoresis more accurately describes the behaviour of larger particles.

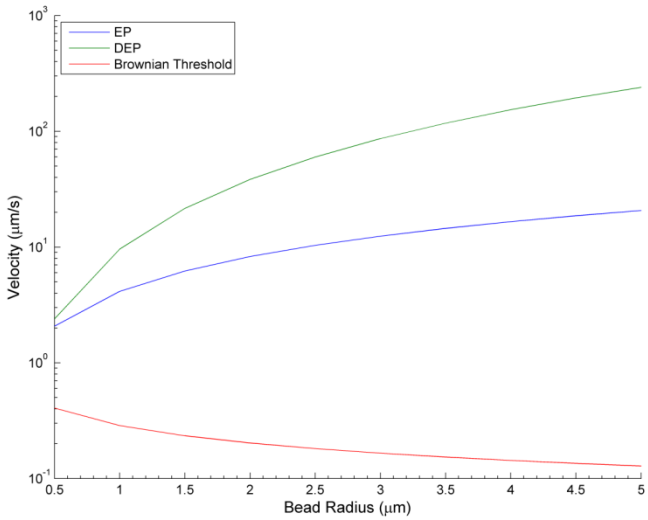

Figure 5.20: Characteristic velocities of a range of silica beads under the influence of electrophoretic (EP) and dielectrophoretic (DEP) forces at 7.6 mW. The maximum allowable displacement in 1 second due to Brownian motion is used as a threshold. Bead is located 500 nm above the solid-fluid interface.

5.5 Conclusion

In this chapter, numerical simulations have been used to model the behaviour of a microfluidic system. In order to ensure pyroelectric field generation, a dielectric fluid (low electrical conductivity and permittivity) is required to enable the transmission of electrical energy from the crystal to the fluidic environment.

The main forces on a particle in a microfluidic environment activated as a result of thermal and pyroelectric stimulation have been examined. Based on the finite element modelling performed, thermal behaviour has little effect on the motion of a particle. Thus, particle motion observed on pyroelectric substrates is a result of electrokinetic forces in some capacity.

Brownian motion is used as a baseline for distinguishing between stochastic particle motion and the broadly deterministic motion induced by external forces. A distinction has been made between what constitutes a stable trapping force and an observable electrokinetic force, thus the minimum thresholds defined for these differ. The threshold provided for stable trapping is a conservative figure; trapping is theoretically possible with any observable electrokinetic force.

The applied laser power dictates regimes in which different forces are dominant. Assuming a finite surface charge is present, electrophoretic motion appears to be more relevant at lower laser powers, particularly for smaller particles. Due to the growth rate of both processes, increasing the laser power creates a dielectrophoretic regime for particles located close to the laser spot. From the simulations, the electrothermal effect is a prominent source of motion particularly at the highest laser powers, due to the magnitude of the flow, and the fact that it acts independently of particle size and electrical properties. Though the maximum calculated flow is comparable to (and sometimes exceeds) that induced with dielectrophoresis, the spatial position of these maxima do not coincide with each other, and as such, it can be used to enable long range particle manipulation. The validity of these numerical predictions is explored experimentally in further chapters.

5.6 References

[1] "Silicone Fluid: KF-96," Shin-Etsu.

[2] "Silica Microspheres," Bangs Laboratories, Incorporated.

[3] "Silicone Oil: high temperature," *Sigma-Aldrich*. [Online]. Available: http://www.sigmaaldrich.com/catalog/product/sial/175633?lang=en&region=GB. [Accessed: 08-Feb-2015].

[4] "Material Characteristic Guide." Omega Engineering Incorporated.

[5] P. J. Stiles, "Electro-thermal convection in dielectric liquids," *Chem. Phys. Lett.*, vol. 179, no. 3, pp. 311–315, 1991.

[6] T. Z. Fullem and Y. Danon, "Electrostatics of pyroelectric accelerators," *J. Appl. Phys.*, vol. 106, no. 7, p. 74101, 2009.

[7] S. B. Lang, "Pyroelectric Thermometer for Use at Low Temperatures," *Rev. Sci. Instrum.*, vol. 40, no. 2, p. 274, 1969.

[8] "Lithium Niobate - Free of Pyro-Electric Effect." [Online]. Available: http://www.roditi.com/SingleCrystal/LiNbO3/liNBO3-Black-Wafers.html.

[9] S. Hardt and F. Schönfeld, "Microfluidics: Fundamentals and Engineering Concepts," in *Microfluidic Technologies for Miniaturized Analysis Systems*, S. Hardt and F. Schönfeld, Eds. Springer Science, 2007, pp. 1–58.

[10] S. Tao and H. Morgan, “AC Electrokinetic Micro- and Nano-particle Manipulation and Characterization,” in *Electrokinetics and Electrohydrodynamics in Microsystems*, A. Ramos, Ed. Springer Wien New York, 2011, pp. 1–28.

[11] A. Ramos, H. Morgan, N. G. Green, and A. Castellanos, “Ac electrokinetics: a review of forces in microelectrode structures,” *J. Phys. D. Appl. Phys.*, vol. 31, no. 18, pp. 2338–2353, 1999.

[12] M. P. Hughes and H. Morgan, “Dielectrophoretic trapping of single sub-micrometre scale bioparticles,” *J. Phys. D. Appl. Phys.*, vol. 31, no. 17, pp. 2205–2210, 1999.

[13] A. Ramos, “Electrohydrodynamic and Magnetohydrodynamic Micropumps,” in *Microfluidic Technologies for Miniaturized Analysis Systems*, S. Hardt and F. Schönfeld, Eds. Springer Science, 2007, pp. 59–115.

[14] A. Ramos, “Electrohydrodynamic Pumping in Microsystems,” in *Electrokinetics and Electrohydrodynamics in Microsystems*, A. Ramos, Ed. Springer Wien New York, 2011, pp. 127–156.

[15] R. J. Turnbull and J. R. Melcher, “Electrohydrodynamic Rayleigh-Taylor Bulk Instability,” *Phys. Fluids*, vol. 12, no. 6, p. 1160, 1969.

6 Arbitrary patterning of particles using pyroelectric manipulation

Summary

This chapter demonstrates arbitrary patterning of particles, achieved by scanning the stage in a predetermined route, as a means of illustrating the plasmonic enhanced electrokinetic manipulations. This is possible as a result of the intrinsic dielectric properties of lithium niobate. Patterning is performed with different materials in a range of media to demonstrate the versatility of the technique.

6.1 Introduction

Verification of pyroelectric based electrokinetic manipulation is hindered by the existence of numerous forces acting simultaneously, as has been previously discussed in Chapter 5. This makes it difficult to ascertain what is responsible for any apparent motion induced on particles. In addition to this, in the experimental framework devised, there is a further possibility that particle motion is a result of optical forces resulting from laser illumination, which further obscures identification of electrokinetics of pyroelectric origin. Hence, a demonstration where the primary motion of particles is unique to pyroelectric substrates is required.

The ability for plasmonic structures to generate heat has been established numerically and experimentally (Chapter 4), thus ascertaining that the primary prerequisite for pyroelectric manipulation can be achieved. To demonstrate this motion, the innate properties of lithium niobate (chiefly, its large electrical permittivity and high capacitance which allows the generated electric field to persist after the change in temperature has been stabilised) have been used to dynamically assemble particles into arbitrarily defined patterns, which persist in the absence of laser stimulation. The ability to create patterns in this manner distinguishes this operation from other optically controlled micromanipulation techniques.

In this chapter, evidence of pyroelectric manipulation is provided by demonstrating this patterning effect on lithium niobate. Results are compared with a glass control to ascertain that motion is not primarily due to purely optical/thermal origins. Patterning is performed in a range of media to test solvent effects on the generated electric field. The differences between patterning on and off plasmonic arrays are compared to verify the effects of plasmonic

enhancement. Patterning is performed with metallic and insulating materials to verify the effect light absorption in trapped particles has on the patterning process. Finally, the origins of the patterning mechanism, factors affecting the process, and possible applications are discussed.

6.2 Materials and methods

Plasmonic structures are fabricated using the protocol detailed in Section 3.4.3. As before, structures are designed to achieve peak plasmon resonance between 600 and 650 nm. Arrays of 60 nm discs with an interparticle spacing of 300 nm are fabricated on glass, while 40 nm discs with an interparticle spacing of 200 nm are fabricated on lithium niobate. A microfluidic chamber is constructed with the substrates supporting the plasmonic arrays and a 180 µm coverslip using 100 µm thick double sided tape as a spacer.

5 µm carboxylated silica beads are suspended in various media (further details provided below) at a concentration of 5 mg/mL.

Gold nanoparticles are suspended in mineral oil to a concentration of 1.3 mM, as dictated by the final concentration of the nanoparticles fabricated using the Turkevich-Frens method detailed in Section 3.4.2.1. The solvent swap process detailed in Section 3.6.2 is necessary to transfer nanoparticles from their native aqueous environment to mineral oils. As the gold nanoparticles are much smaller than the silica beads used in patterning, they are spun at a much higher velocity (19000 rpm compared with the 5000 rpm typically used).

Silver nanowires are suspended in mineral oil at a concentration of 0.5%. As these were supplied in IPA, an attenuated solvent swap process was sufficient to ensure miscibility of the wires in mineral oil (as IPA is of similar polarity to ethanol, nanowires can be transferred directly to mineral oil after centrifugation i.e. no need for intermediary solvent)

6.2.1 Solvents

Patterning experiments are performed with carboxylated silica beads in a range of environments of high and low electrical conductivity and relative permittivity. The solvents and relevant parameters are given in the table below. It should be noted that the conductivity information of the oils are estimates. Giving the extremely high electrical resistivity of these solvents, electrical conductivities could not be measured by conventional means, using a conductivity meter. The

values reported constitute the maximum conductivities for liquid dielectrics measurable with the conductivity meter used. Silicone oils have been reported to have conductivities of $<10^{-13}$ Sm^{-1} [1] while conductivities of $<10^{-14}$ Sm^{-1} have been reported for mineral oils and similar alkanes [2] [3]. As the conduction process in liquid dielectrics is strongly dependent on the presence of impurities [3]–[5], specific conductivities are difficult to ascertain; a range of values are frequently quoted. Giving the environment in which the experiments are performed, the upper limit of conductivity more accurately describes charge transport processes for the solvents considered. The viscosities of almond oil, silicone oil, and mineral oil were measured using an Anton-Paar MCR-302 rheometer.

Table 6.1: Relevant electrical and thermodynamic properties of solvents in which experiments are performed

Solvent	Conductivity σ (Sm^{-1})	Electrical permittivity ε	Viscosity η (mPa·s)
Deionised water	5.5×10^{-8}	80	1
Isopropyl alcohol	6×10^{-8}	18.6	1.96
HFE-7500	5.5×10^{-7}	5.8 [6]	1.24 [6]
Almond oil	$< 1 \times 10^{-12}$	2.8 [7]	76
Mineral oil	$< 1 \times 10^{-12}$	2.1 [7]	54
Silicone oil	$< 1 \times 10^{-12}$	2.2 [7]	109

6.3 Results and discussion

6.3.1 Glass control

Figure 6.1 shows the results of the attempted patterning of a 100 µm side square on a glass substrate (5 consecutive scans at 50 µm/s), using silica beads in a variety of media. As expected, no patterning is observed, as there is no pyroelectric effect associated with this substrate. Bead motion is a result of the increased thermal energy in the microfluidic system.

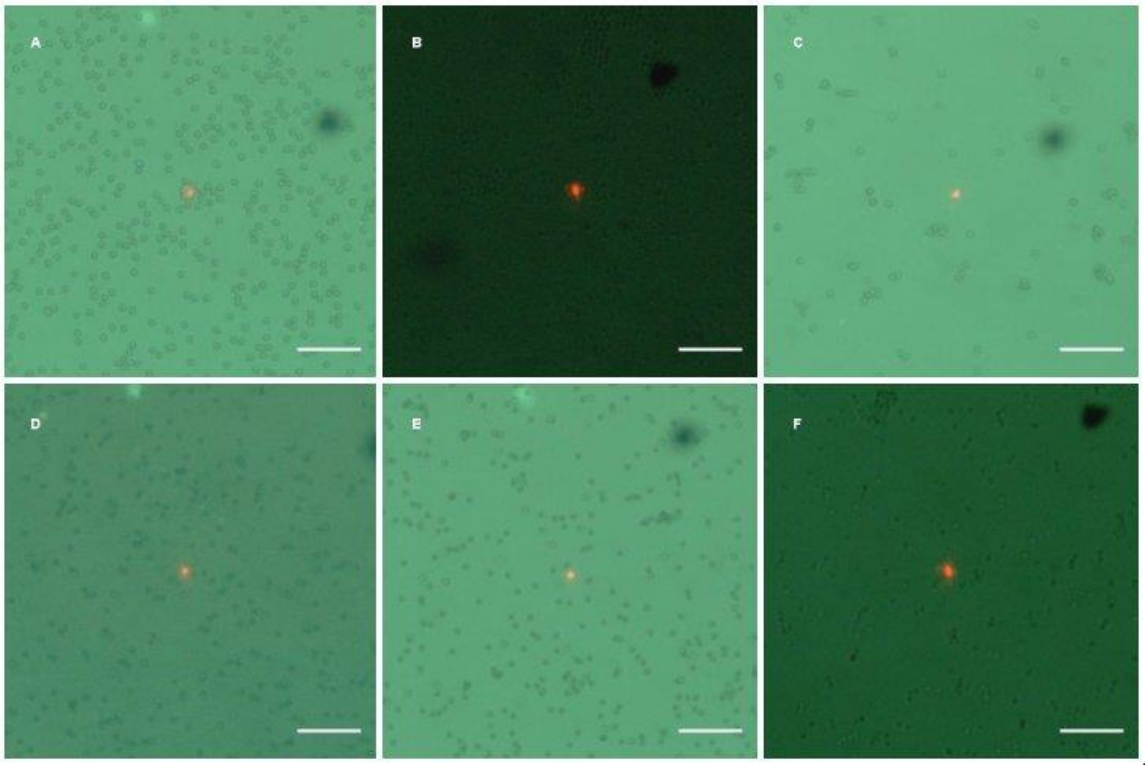

Figure 6.1: Particle behaviour after laser scanning on glass in: A) water, B) IPA, C) HFE-7500, D) almond oil, E) mineral oil, and F) silicone oil. No patterning is observed. Scale bar for all pictures is 50 µm.

Though no patterning behaviour is observed on glass, the response of particles to thermal stimulation differs according to the solvent used (as is to be expected, since they do not share the same thermodynamic properties). Since the microscope stage was moved in order to achieve the scanning effect, quantitative analysis of particle motion could only be performed on a fraction of the recorded images (otherwise, scanning motion overwhelms underlying thermal induced motion). Thermal induced motion of particles, deemed negligible in the analysis performed in Chapter 5, can be identified due to the absence of other forces.

Tracking and analysis (using the Matlab tool, msdanalyzer [8]) of particles in water, mineral oil, and almond oil reveals non-diffusive motion for the periods observed, detailed by the parabolic profile of the MSD, as illustrated in Figure 6.2D. Based on the shape of these graphs, there appears to be an underlying flow of constant velocity, as the MSD of such systems is given by [9]:

$$\bar{x}^2 = 2dDt + v^2t^2, \tag{6.1}$$

where d is the dimensionality of the problem (2 in this case), D is the diffusion coefficient, v is the flow velocity (time invariant).

The plots presented are the best predicted fit to the experimentally derived MSD of an ensemble of particles. Only the shortest video duration is considered, to minimise extrapolation errors. The particle trajectories are also depicted. Observe that in water and almond oil (Figure 6.2A and B), particle displacement is fairly uniform. In contrast, mineral oil trajectories appear to be bimodal (dot like paths and elongated rod paths). This bimodality contributes to the unexpectedly large flow velocity calculated. The greatest velocity is observed with particles in water; an unsurprising result giving the fact that it has the lowest viscosity. The flow velocity decreases with increasing solvent viscosity, as is expected from the Navier-Stokes equation.

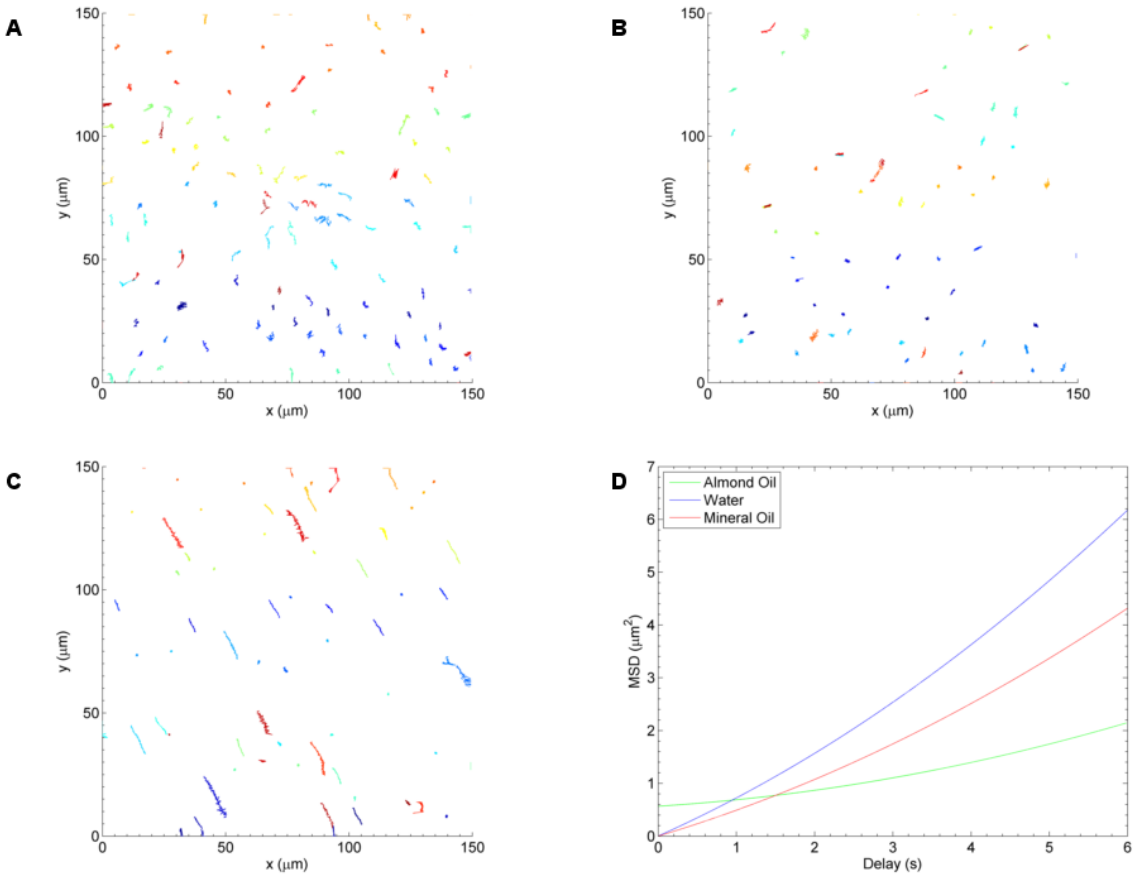

Figure 6.2: Trajectories of an ensemble of silica beads in: A) water, B) almond oil, and C) mineral oil. D) Plot of MSD of particles with respect to time-steps.

The relative poor heatsinking ability of glass is responsible for some phenomena which are not encountered on lithium niobate. Plasmonic structures are able to generate higher temperatures on glass, with equivalent laser powers, than on lithium niobate, thus magnifying thermal effects. Convective behaviour is observed most prominently in silicone oil alone, due to the high coefficient of thermal expansion. The convective flow is estimated to be 23 µm/s using PTVlab [10]. Figure 6.3 depicts the calculated flow profile. Velocity is at a minimum at the centre of the

image (corresponding to the position of the laser). Decomposing the velocity field to depict the x and y components of velocity individually, shows that the values of velocity are symmetric about the laser.

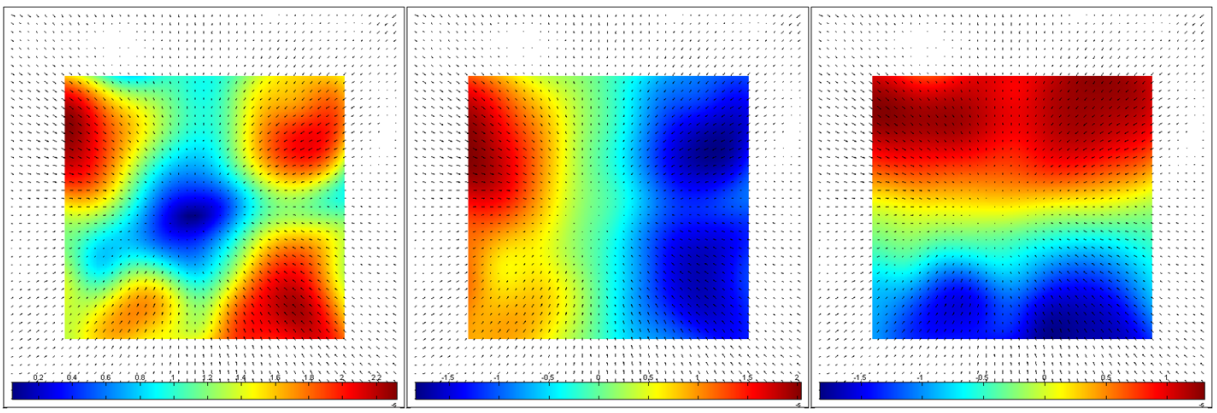

Figure 6.3: Convective flow imaged using PTV. Left) Total velocity field. Middle) x component of velocity. Right) y component of velocity.

Bubble formation is observed in IPA and HFE-7500. Based on some of the characteristics of the bubbles (size, lifetime), and the conditions surrounding their formation (i.e. continuous wave illumination), these bubbles appear to be similar in nature to those described in [11] (liquid surrounding air, rather than vapour molecules), suggesting the possibility of superheating of the liquid environment. There is a delay between switching on the laser and the beginning of recording. As a result, the onset of bubble formation is not observed at higher powers. Note that by halving the laser power to ~3.8 mW, bubble formation is stopped in HFE-7500 and delayed in IPA. Bubble formation in IPA at lower powers occurs only when the laser coincides with a cluster of particles. This suggests that silica beads act as nucleation centres, which lower the temperature threshold for bubble formation.

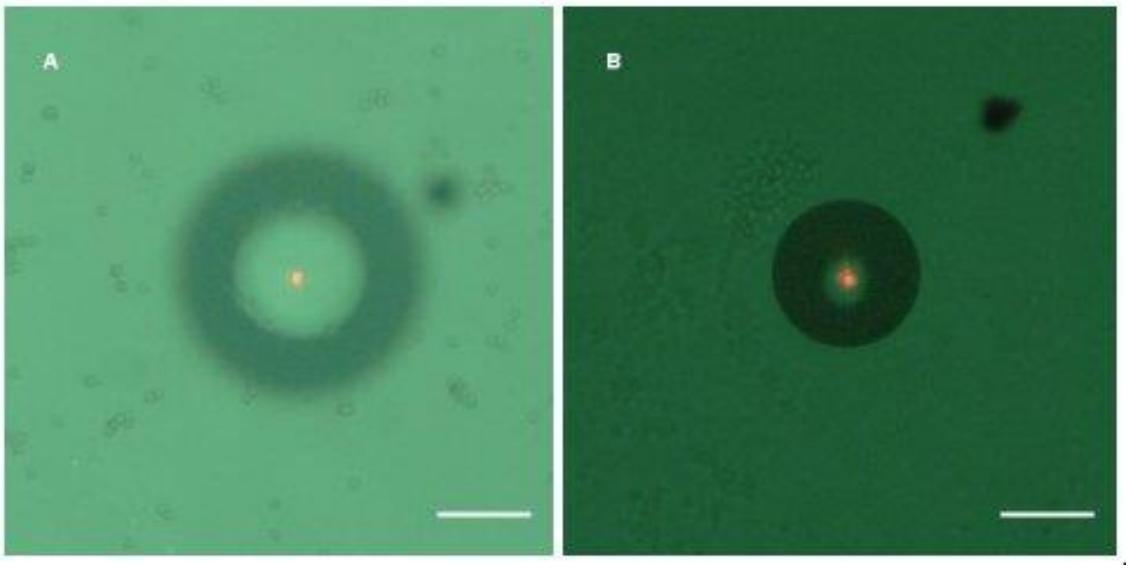

Figure 6.4: Bubble formation as a result of thermal stimulation on: A) HFE-7500 and B) IPA. Scale bar is 50 µm.

6.3.2 Lithium niobate

A 100 µm side square was patterned on a lithium niobate substrate using the same parameters. The heatsinking effect associated with the increased thermal conductivity of lithium niobate is evident when the behaviour of the fluids is considered. No plasmonic convection or bubble formation is observed in the relevant solvents. The dominant behaviour is the assembly of particles into the defined patterns. The outline of the square begins to emerge with increasing fidelity as the electrical conductivity of the medium decreases. The behaviour of particles in dielectric media can be used as evidence of the existence of multiple particle manipulation mechanisms. From previous theoretical considerations, (specifically the Peclet number) it has been shown that thermal diffusion is primarily responsible for heat transfer in microfluidic systems (the influence of convection is negligible). The characteristic thermal response time is ~10^{-3} seconds, much shorter than the observation period associated with the experimental setup (133 ms at 7.5 Hz). Hence, heating and cooling are functionally instantaneous (Chapter 4). Particle reassembly persists in the absence of thermal stimulation (most clearly seen with silicone oil). The loss of a thermal gradient within the dielectric indicates that this action is no longer a result of electrothermal forces, demonstrating that a purely electric force now controls particle motion.

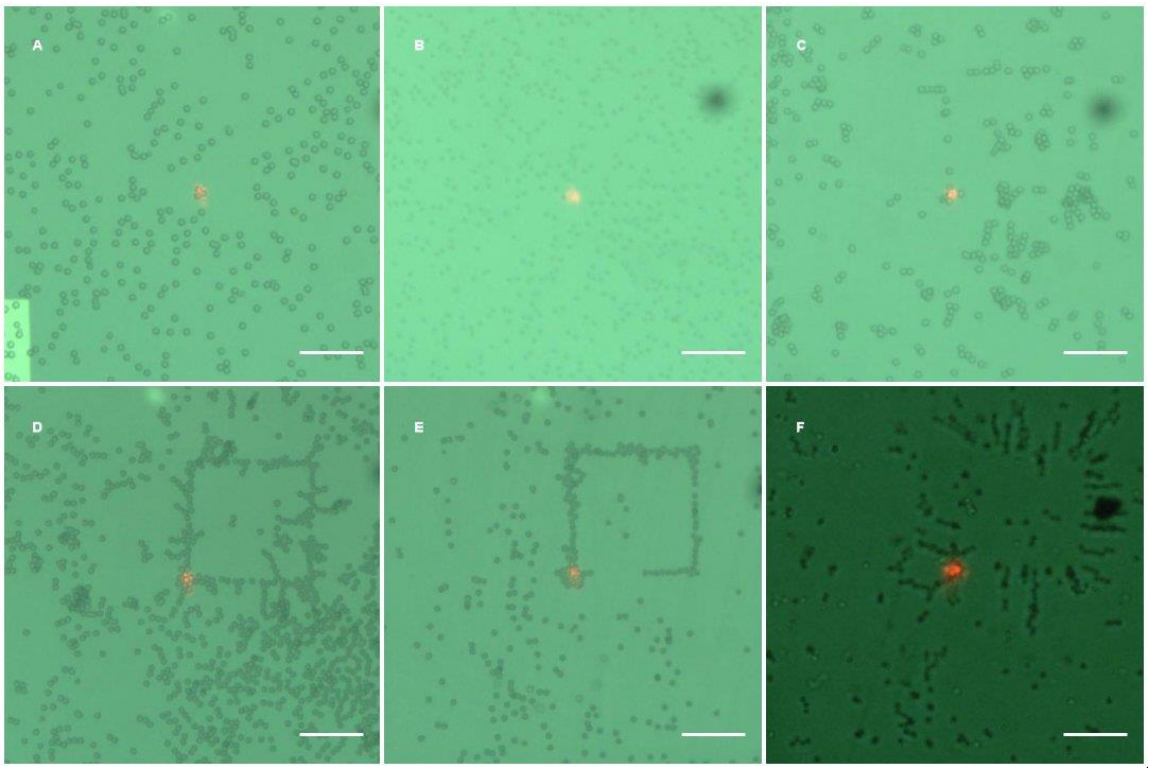

Figure 6.5: Particle behaviour after laser scanning on lithium niobate in: A) water, B) IPA, C) HFE-7500, D) almond oil, E) mineral oil, and F) silicone oil. Scale bar for all pictures is 50 µm.

6.3.2.1 Patterning process

The patterning process is facilitated by the interplay between a long range attractive force and a short range trapping force. This is consistent with the observations made using numerical simulations which indicated that different forces were dominant at varying distances from the source of stimulation. The attractive force (originating from electrothermal convection) draws in particles from a distance far exceeding the radius of the stimulating laser, locally increasing the concentration at the point of stimulation. Phenomenologically, the increased concentration is a function of the strength of attraction force, which dictates how far particles are attracted from, and the dwell time, which dictates how fast dislodged particles relocate to the laser's focal point. The characteristic increased concentration noted with the patterning process is thus accompanied by a depletion region (the size of which is a function of the attractive force), beyond which the concentration of the particles remains the same. The high contrast between regions densely and sparsely populated with particles, enables easy visualisation, and a simple qualitative assessment of the success of patterning. The trapping force acts independently of the attraction force and holds particles in place after thermal stimulation has been removed. This persistence is a consequence of the capacitive nature of electric field generation using lithium niobate and non-polar solvents, which explains how particle motion can be observed on glass substrates without

the reassembly of particles characteristic of patterning; on glass, the external force induced by laser excitation merely redistributes particles without a trapping force at the laser's focal point.

For a quantitative measure of the combined effect of the trapping and attraction forces, an enrichment factor is calculated using the integrated pixel intensity of the recorded image. Images are processed to produce binary images. The average of the integrated pixel intensity thus becomes a measure of the concentration of particles in the image. The enrichment factor is then defined as:

$$\frac{n_{after} - n_{before}}{n_{before}} \tag{6.2}$$

By taking a ratio of the change in concentration, the enrichment factor corrects for apparent variations in particle densities. This value is plotted as a function of distance from a centrally located point (further explanation of this procedure is given in Appendix E) to gain a plot which can be used to elucidate some of the characteristics of the patterning process outlined above. Though this is not the most accurate measurement (bead clustering in the z direction is underestimated, it is assumed that spaces are filled laterally), when used in conjunction with the recorded images, the success of patterning can be validated. Explanation of the key features of the graph is made easier by the fact that a simple geometric shape has been patterned.

Figure 6.6 depicts an exemplary plot using results of patterning experiments with silica beads in mineral oil (the corresponding image is depicted in Figure 6.5E). A peak in the enrichment factor occurs at 50 µm (concentration is ~1.8 times greater after stimulation), highlighting the presence of significant clustering at this point. Based on the definition of the central point, this feature indicates the presence of the patterned 100 µm side square. The width of this peak region is synonymous with the line width of the patterned object, which, along with the height of the enrichment factor, is a function of the magnitude of the combined pyroelectric forces (attractive and trapping). There are two depletion regions (characterised by negative enrichment factor) located either side of the peak. The first indicates that the patterned feature has void regions. The second depletion region is, as previously mentioned, the spatial boundary of the attractive force (beyond this concentration of particles remains essentially unchanged). In Figure 6.6, the size of the region of interest chosen (150 µm), along with the strength of the attractive force, is such that the return to the initial (background) concentration is not depicted.

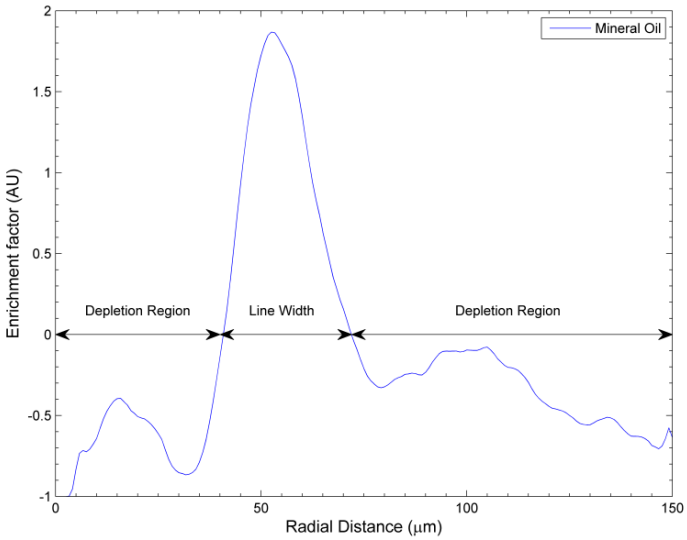

Figure 6.6: Change in particle concentration as a function of radial distance from centrally located point.

A similar analysis can be performed using graphs from the results of the other experiments depicted in Figure 6.5. In general, the plots share the same features, with the differences highlighting the particular vagaries of the patterning process in each solvent. The peak at 50 µm when HFE-7500 is used (0.5), is comparatively lower than other solvents, showing that patterning in HFE-7500 is weakest. Note that the enrichment factor close to the centre of the region of interest is ≫0, indicating the presence of some particles in the centre of the patterned object. Finally, the difference between the peak enrichment factor and the mean is small (i.e. low signal to noise ratio) indicating that patterning is difficult to confirm purely visually (without prior knowledge of any stimulation having been applied).

In contrast, patterning in almond oil is much more similar to patterning in mineral oil. The void region is clearly defined in the plot; particles do not remain in the centre of the patterned object. Though the peak enrichment factor (1× greater following stimulation) is decreased in comparison to the experiment performed in mineral oil, it is clearly differentiated from the background. The major deviation between the two solvents is that the return to the background concentration is seen in almond oil (indicated by the fact that the enrichment factor crosses the zero point after a 13 µm region of depletion), suggesting that the trapping force is smaller. This is consistent with the fact that almond oil is more viscous than mineral oil. Hence, resistance from viscous forces is larger. In addition to this, the increased permittivity of almond oil leads to a slight reduction in the magnitude of the generated pyroelectric field and a reduction in the size of the Claussius-Mossotti factor, both of which contribute to reductions in electrokinetic forces resulting in the apparent decrease in patterning ability.

The plot derived from patterning performed in silicone oil differs markedly from the previously discussed cases, due to the change in the assembly behaviour of the particles. Though the depletion regions are retained, the peak is broader (76 µm compared with 32 µm observed using mineral and almond oil) and occurs at 62.5 µm, 12.5 µm further from the centre than expected. This is a result of the distribution of the particles which are aligned perpendicular to the laser scanned route in linear pearl chains as opposed to clusters. The long pearl chains give rise to a "thicker" square i.e. a broadening of the peak enrichment factor region. The pearl chaining observed is characteristic of dielectrophoretic action [12], [13]. Particles distort the electric field in the microfluidic environment as a consequence of electrical polarisation, creating regions of high and low electric field localised around their geometry. As a result of this distortion, similar particles preferentially arrange themselves parallel to the electric field lines, resulting in the pearl chains observed. Numerical simulations performed in Chapter 5, previously highlighted the fact that several electrokinetic mechanisms exist simultaneously as a result of pyroelectric stimulation. It was explained that close to the crossover powers, the model of particle motion deviates from the behaviour dictated by the regime as other electrokinetic forces become more relevant. This ambiguity explains why pearl chaining is observed in only one of the solvents used; silicone oil is the only one in which the generated electric field is sufficient to make electrophoretic trapping of silica beads irrelevant.

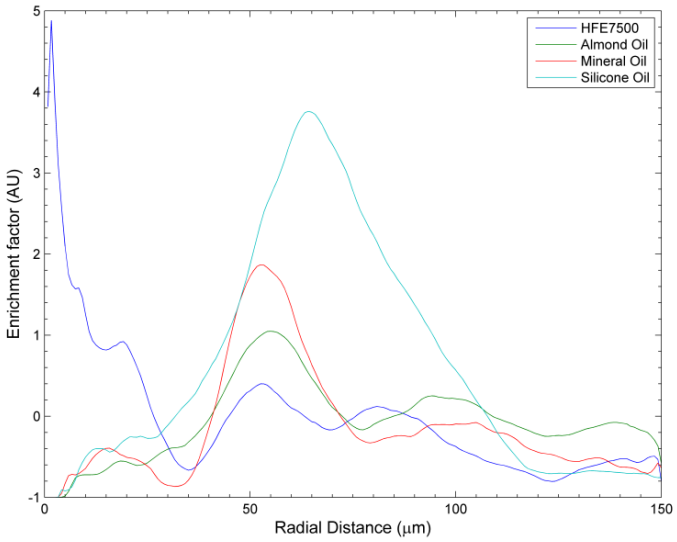

Figure 6.7: Effects of surrounding solvents on radial distribution of particles.

6.3.3 Metallic patterning

Patterning using metallic (conductive particles) is performed as a further demonstration of the versatility of the micromanipulation technique. In the experiments discussed, mineral oil is used as a representative dielectric liquid, as viscous resistances are lowest in this medium (a phenomenon observed when silica particles are patterned). The inherent high conductivity and permittivity associated with metallic particles maximises the Claussius-Mossotti factor. Thus, though no charged carrier species (such as the carboxyl group previously used on with silica beads) are adsorbed onto particles, this non-functionalisation has little bearing on the ability to keep particles in place; the trapping force is expected to be largely dielectrophoretic (as observed previously with beads in silicone oil).

The metallic nature of the particles introduces new interparticle relationships not previously considered. Plasmonic enhancement of the laser beam causes heating in the fluid (separate from that intentionally introduced to induce the pyroelectric effect). Giving their symmetrical geometry, these effects are more keenly felt with gold nanoparticles as opposed to silver nanowires (60 nm × 10 μm). Though the nanoparticles fabricated are resonant at 532 nm in their native aqueous environment, their peak resonance broadens and redshifts when they are transferred to mineral oil (illustrated in Figure 6.8). This is a result of the change in refractive index of the surrounding medium as well as the fact that during the solvent swap process, the gold nanoparticles undergo particle aggregation which increases their apparent size. The diameter after solvent swap is measured to be 144 nm.

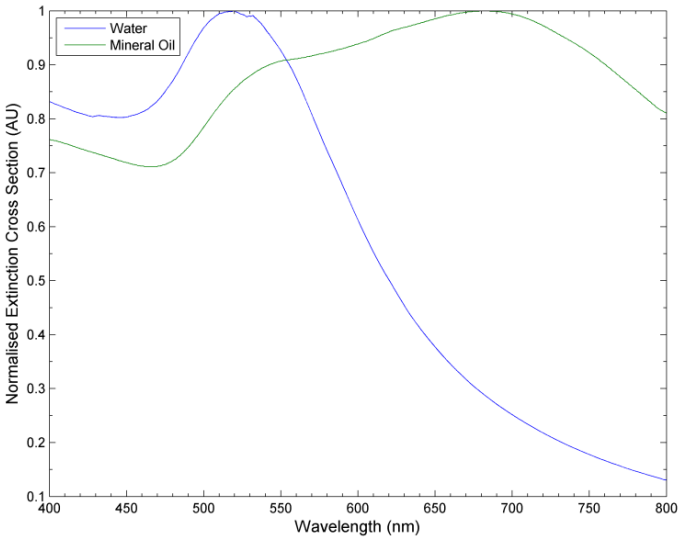

Figure 6.8: Plasmonic spectra of gold nanoparticles in water and mineral oil. The change in refractive index and irreversible aggregation caused by modifying the solvent broadens the plasmon resonance peak.

As with experiments performed using silica beads, there is no evidence of patterning when glass is used as a control substrate. The laser scans a 100 µm square side four times consecutively at 50 µm/s. As the particles used are much smaller (~80× in the case of the short axis of the silver nanowires and ~35× in the case of gold nanoparticles) than silica beads, it is difficult to identify any underlying flow conditions; a degree of clustering (particularly with gold nanoparticles) would be required to reliably observe particles in a bright field configuration, which is not seen uniformly throughout the volume of the microfluidic chamber for the concentrations used.

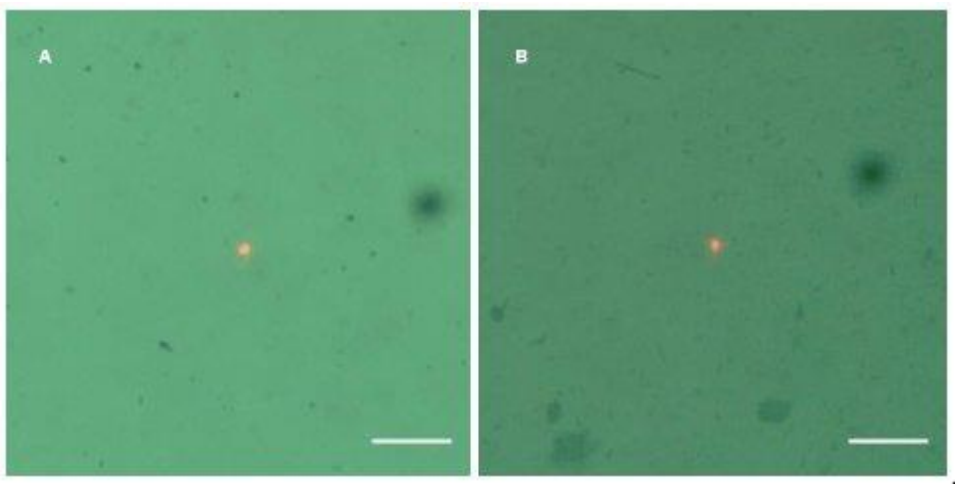

Figure 6.9: Patterning behaviour of metallic particles in mineral oil on glass. A) Gold nanoparticles and B) silver nanowires are considered. No patterning is observed. Scale bar is 50 µm.

In contrast, patterning is evident on lithium niobate substrates. Figure 6.10 depicts the results of substrate scanning. Due to the size of the nanoparticles used, there is a high contrast between non-patterned (where individual particles are hard to perceive) and patterned areas (the clustering previously mentioned helps in identifying particles). As a result, the enrichment factor calculated is far greater than with silica beads.

As a result of their geometric anisotropy, particle assembly with silver nanowires is more haphazard than all other cases considered. A combination of the fact that the initial orientation of particles is random, and the fact that the dielectrophoretic trapping force induces a torque on anisotropic particles [12], [13], causes silver nanowires in the main to align their long axis perpendicular to the laser spot and pearl chaining to occur subsequently. This is more evident at the start of the patterning process when the laser spot is static.

Any additional heating caused by the plasmonic stimulation of the particle has no effect on the ability to trap particles.

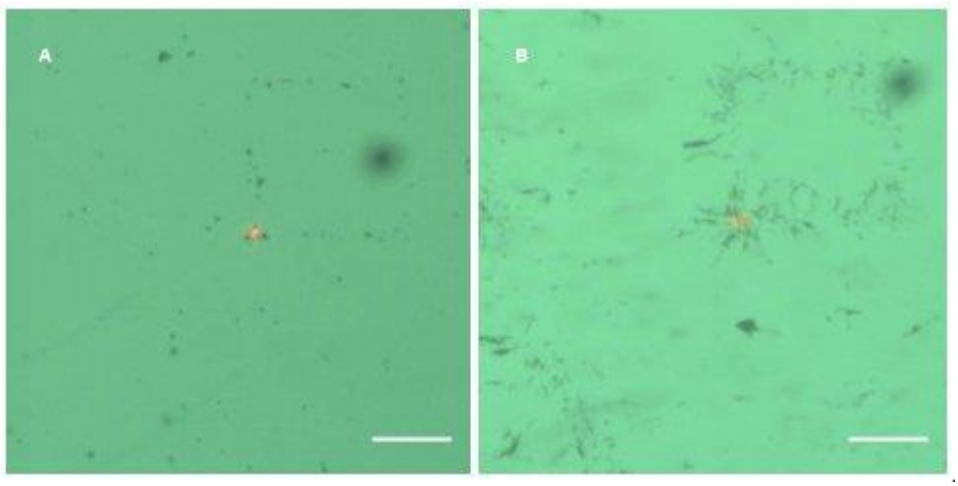

Figure 6.10: Patterning behaviour of metallic particles in mineral oil on lithium niobate. A) Gold nanoparticles and B) silver nanowires are considered. Scale bar is 50 µm.

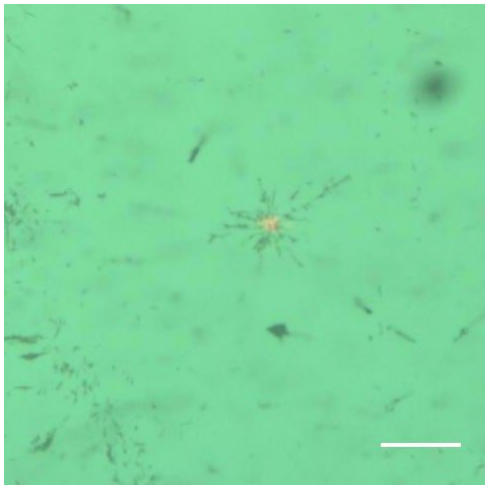

Figure 6.11: Pearl chaining of silver nanowires observed at the beginning of the patterning process. Scale bar is 50 µm

6.3.4 Effects of scanning speed on pattern resolution

The primary application for the demonstrated patterning effect is as a photoresist free optofluidic lithographic technique. Arbitrary patterning can be used in a similar manner to dip-pen nanolithography for the patterning of biomolecules such as proteins, viruses, and DNA [14]. Arrayed molecules can be used for the study of cellular interactions [15], or as scaffolds for the self-assembly of other entities [16],[17] Alternatively, metallic particles can be patterned for the fabrication of transparent conductive electrodes for use as touch screens and photovoltaic thin films [18], [19].

The ability to control resolution is important if patterning is to be adapted for lithographic purposes. By considering the laser route to be formed of a grid of infinitesimally spaced elements, it can be shown that the scan speed is inversely proportional to the dwell time. Hence, by varying this parameter, its effect on the resolution of the pattern can be shown. Based on the patterning process discussed previously, long dwell times result in larger clusters of particles, and a larger depletion region as particles are able to traverse further distances to a central point. The behaviour of silica beads, silver nanowires and gold nanoparticles in mineral oil are considered.

Figure 6.12 depicts the effects of scanning speed on pattern integrity for experiments performed using silica beads in mineral oil. These results are the closest adherents to the proposed hypothesis i.e. in general, the enrichment factor decreases as scanning speed increases. There are some deviations to this behaviour, notably, with a 20 µm/s scanning speed. Note however, that particle enrichment begins earlier and line thickness is wider than observed with other experiments, suggesting that the lateral assembly of particles is more significant at this speed. In addition to this, the peak enrichment factor occurs at a different point (45 µm in comparison to

50 µm in all other cases considered), and its subsequent decay is of a different nature to that observed in the remainder of the experiments. These deviations suggest that the patterns are of a different nature.

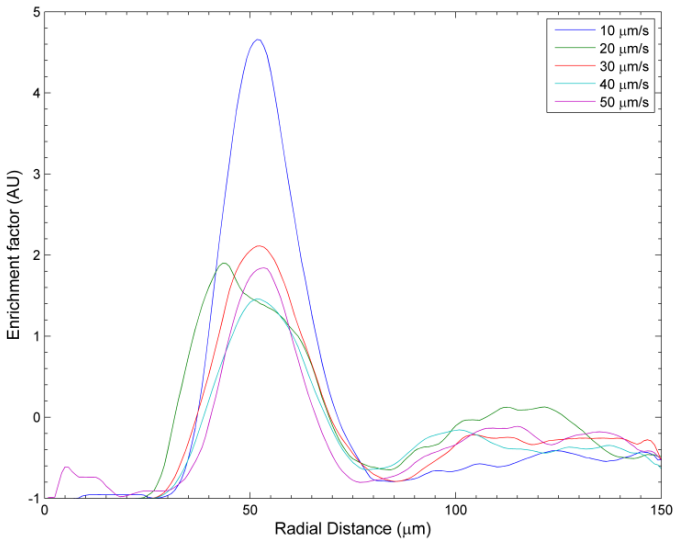

Figure 6.12: Effects of scanning speed on radial distribution of silica beads

A potential source of the deviation from the initial hypothesis is the effect of viscous resistance which was not accounted for in the initial analysis. Long dwell times mean that particles preferentially assemble in clusters, as they accumulate roughly at a single point. As a result, the concentration of particles in the area to be patterned is non-uniform leading to unevenly covered patterns (Figure 6.13). The low viscous resistance characterised by slow moving speeds means that the weaker trapped beads (i.e. those at the edges of a cluster) are able to follow the laser spot. As transported particles reach a critical density, some are deposited in new positions filling the spaces between larger clusters. Patterns thus become more uniform with successive laser scans. For larger speeds, patterning is more uniform; particles accumulate at a series of central locations. However, the distance between these locations is such that no gaps are perceived in the final pattern (Figure 6.14). The anomalous decrease in enrichment factor appears to indicate a crossover where dwell time is long enough to support the more clustered behaviour but the scanning speed is too fast to allow complete redistribution of particles on successive passes. This results in incomplete patterns, which somewhat explains the modified nature of the plot of enrichment factor observed. Though the normalisation process performed in calculating the enrichment factor is aimed at mitigating the effects of variable particle density, it crucially does not account for the effect this has on the completion of a particular pattern, or how incomplete

patterns are encoded. Note that scanning at 10 µm/s also creates incomplete patterns. However, where there is particle clustering, it is much greater than observed at faster speeds such that averaging gives the suggestion of a complete structure.

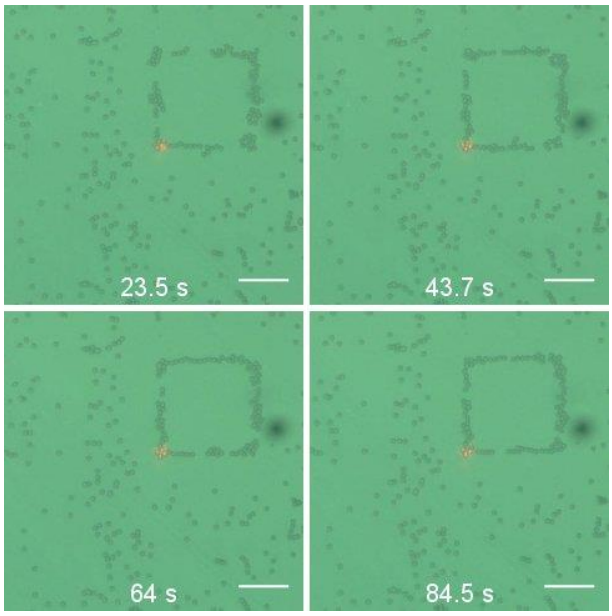

Figure 6.13: Evolution of patterned object for successive complete scans performed at 20 µm/s. Scale bar is 50 µm. Gaps exist in square and are filled in with successive scans.

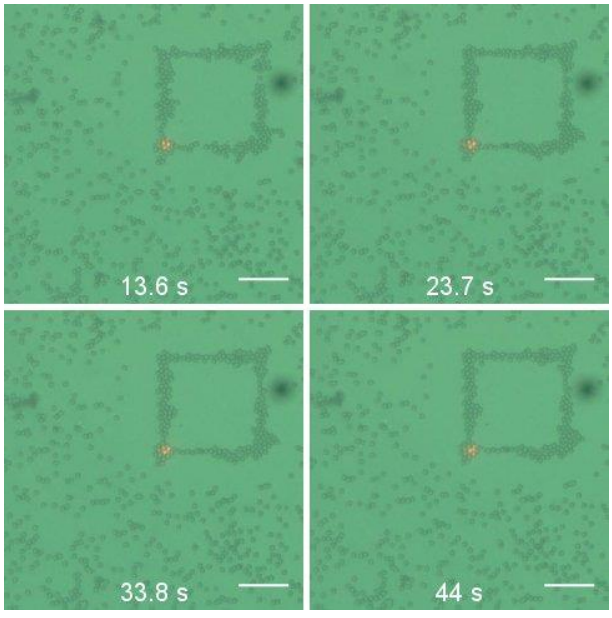

Figure 6.14: Evolution of patterned object for successive complete scans performed at 40 µm/s. Scale bar is 50 µm.

The effects of scanning speed on the resolution of gold nanoparticle patterns are similar to that observed with silica beads. Though the enrichment factor is at a maximum with the slowest scan

speeds, it does not decrease monotonically. There is a drop in enrichment factor for 30 µm/s scan speeds before a subsequent rise. Unlike silica beads, trapped gold nanoparticle clusters do not follow the moving laser spot, thus the variable effect of scanning speed on pattern resolution is not solely a result of particle clustering and redistribution. Rather, there are periodic expulsions of particles from a cluster. These appear to be a result of sudden increases in temperature due to plasmonic heating of trapped particles. As the magnitude of plasmonic heating is dependent on the density of excited particles, there appears to be a critical concentration requirement for the disruptive convection behaviour. The polydispersity of the particles means critical concentration does not rise consistently, making the periodicity of these expulsions appear to be random. Thus, while the large clustering associated with slower scanning speeds makes particle expulsions more likely, these expulsions are not improbable when faster scans are performed. In addition, the longer dwell times mean that expelled nanoparticles are more able to be recovered at slow scanning speeds.

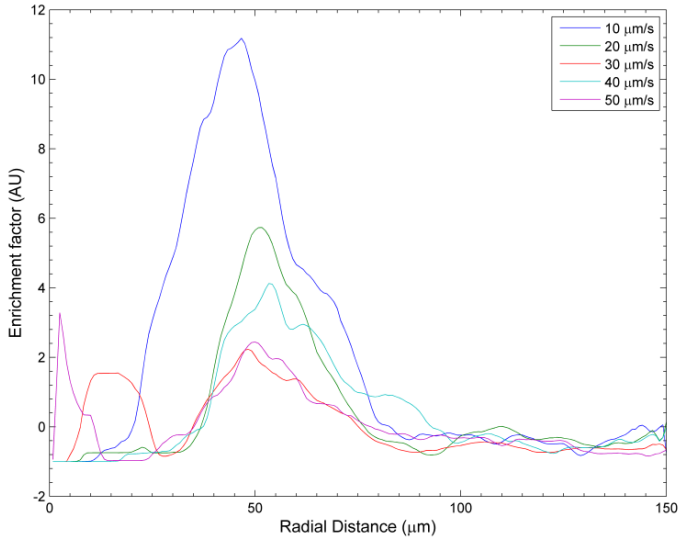

Figure 6.15: Effects of scanning speed on radial distribution of gold nanoparticles

The plots of enrichment factor derived using silver nanowires are markedly different to those observed with gold nanoparticles and silica beads for reasons outlined in Section 6.3.3. As with gold nanoparticles the behaviour with respect to scanning speed is also affected by plasmonic heating effects. The consequences of this appear to be more marked than with gold nanoparticles, as a result of the initial concentration of silver nanowires used. Hence, though patterning is evident at slower speeds, the broadening of the peaks causes a loss of definition. The process appears to be more controllable at faster speeds as the final concentration of particles is limited, thereby reducing the self-trapped plasmonic induced heating.

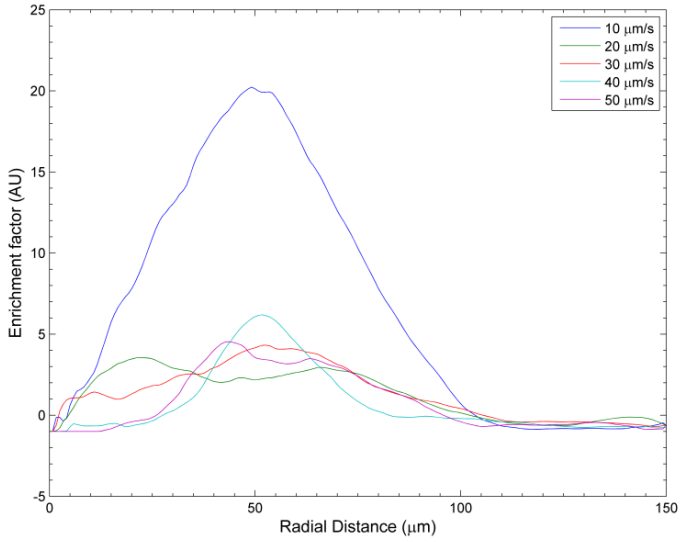

Figure 6.16: Effects of scanning speed on radial distribution of silver nanowires

6.3.5 Patterning on bare LN

What appears to be anomalous motion of silica beads is observed when laser excitation of the pyroelectric is not coincident to the plasmonic arrays. This motion appears to suggest that the patterning is a result of the optically activated electrical properties of lithium niobate i.e. the photovoltaic effect. Like the optically actuated pyroelectric effect, the photovoltaic effect is dependent on excitation intensity. Thus, the electric field generated by the lithium niobate substrate has pyroelectric and photovoltaic components. The photovoltaic current density is given as,

$$j = \kappa \alpha I, \tag{6.3}$$

where κ is the Glass constant [20], α is the wavelength specific absorption coefficient of lithium niobate, and I is laser intensity.

Since undoped lithium niobate wafers have been used in the course of these experiments, any photovoltaic effect is a result of the intrinsic antisite defects [21], [22] (anomalous location of lithium and niobium ions in the lithium niobate lattice) in the crystal. As a result, the glass constant [20] (which is dependent on the concentration and nature of the doping species) is small. This fact, coupled with the low absorption coefficient at the wavelength considered, means that the electric field generated by the photovoltaic effect is less than that generated by the

pyroelectric effect. Hence, regardless of the composition of the sources of the electric field, the pyroelectric effect would appear to be the cause of motion for undoped lithium niobate substrates operating in visible wavelengths [22], [23]. A further indicator that this anomalous patterning is a result of the pyroelectric effect, is the fact that particle reassembly occurs instantaneously. With photovoltaic patterning, a delay on the order of several seconds to minutes is expected, related to the drift and diffusion processes occurring internally in the crystal, which induce the space charge condition that is the source of photovoltaic electric fields.

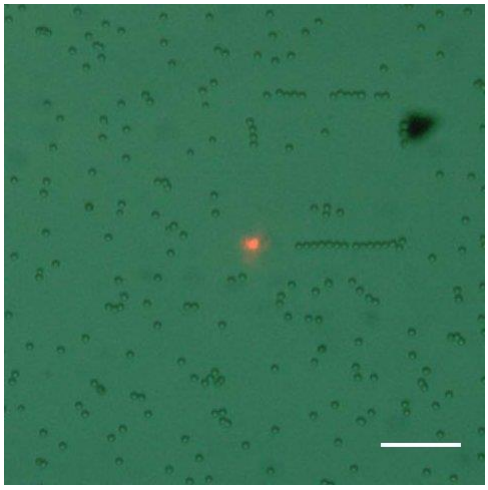

Figure 6.17: Representative image of patterning performed on bare lithium niobate substrate. Scale bar is 50 µm

From pictorial evidence, patterning on bare lithium niobate is minimal. This is reinforced by the graphical evidence in which the enhancement factor peaks at 1.35 (compared to 5 for experiments performed on plasmonic arrays in mineral oil). In the main, the enrichment factor oscillates erratically around zero, indicating that the signal to noise ratio of the patterned object is low. This reduction in concentration is primarily a result of a reduction in the attraction force due to the fact that heating is lowered without plasmonic enhancement. Note that the depletion regions measured are in general smaller (5 µm is the maximum width observed) than in experiments with plasmonic enhancement. The patterned object is thus primarily a result of redistribution of silica beads already in the path of the laser scanned route.

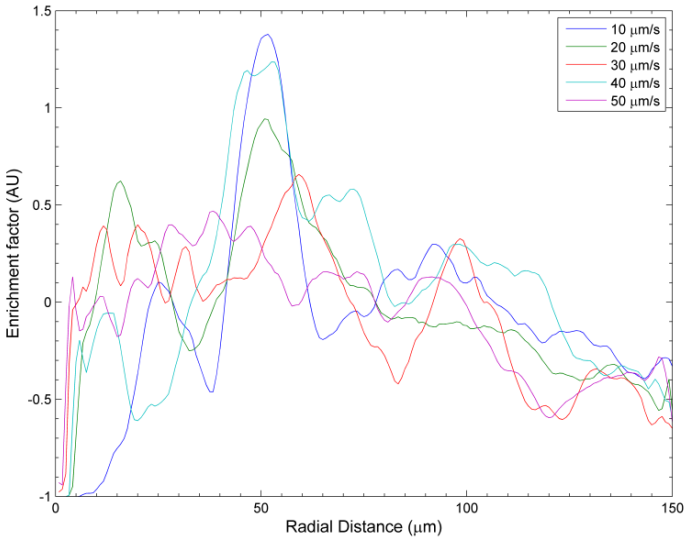

Figure 6.18: Effects of scanning speed on radial distribution of silica beads patterned on lithium niobate without plasmonic enhancement.

6.4 Conclusion

Dynamic particle reassembly has been demonstrated in a range of microfluidic environments, using pyroelectric manipulation for patterning purposes. The experiments were performed using metallic and insulating particles illustrating the versatility of the technique. Though self-induced plasmonic heating of nanometric metallic particles is possible, this does not hinder the ability to create patterns using these objects (though it appears trapping efficiency of large concentrations of metallic particles is reduced). An explanation of the mechanics of the patterning process, based on observations and previous simulations, has been devised. Patterning is made possible by a dual attraction (electrothermal convection) and trapping force (a combination of electrophoresis and dielectrophoresis depending on the solvent and the nature of the particle used). The long range attraction force increases the concentration of particles at the laser spot and the trapping force ensures they remain in place. By comparing patterning behaviour of silica beads in mineral oil with and without plasmonic arrays, the effect of plasmonic enhancement on the patterning process (i.e. magnification of forces) is realised. This effect is seen most obviously in the localisation of trapping behaviour, as the long range attraction force is greatly reduced. The concentration of particles in the region scanned is reduced, and as a result, it is difficult to distinguish the pattern from its surrounding environment. Finally, a degree of control over pattern resolution has been demonstrated by modifying the scanning speed (i.e. controlling the dwell time of the laser at a specific point). A potential avenue for further investigation is the use of

discrete elements (defined pattern grid, modulated laser beam linked to scanning speed, explicit dwell times) for finer control of the patterning process.

6.5 References

[1] H. B. Zhang, M. J. Edirisinghe, and S. N. Jayasinghe, "Flow behaviour of dielectric liquids in an electric field," *J. Fluid Mech.*, vol. 558, no. 2006, pp. 103–111, 2006.

[2] E. O. Forster, "Electric Conduction in Liquid Hydrocarbons. III. Comparison of Saturated and Unsaturated Hydrocarbons," *J. Chem. Phys.*, vol. 40, p. 91, 1964.

[3] E. R. Booser, Ed., *CRC Handbook of Lubrication: Theory and Practice of Tribology, Volume II Theory and Design*. CRC Press, 1983.

[4] D. W. Swan, "A review of recent investigations into electrical conduction and breakdown of dielectric liquids," *Br. J. Appl. Phys.*, vol. 13, no. 5, pp. 208–218, 1962.

[5] A. Kitahara and A. Watanabe, Eds., *Electrical Phenomena at Interfaces: Fundamentals, Measurements, and Applications*. Marcel Dekker, Inc., 1984.

[6] "Product Information: 3M Novec 7500 Engineered Fluid," 3M.

[7] "Material Characteristic Guide." Omega Engineering Incorporated.

[8] N. Tarantino, J. Tinevez, E. F. Crowell, B. Boisson, R. Henriques, M. Mhlanga, F. Agou, A. Israël, and E. Laplantine, "TNF and IL-1 exhibit distinct ubiquitin requirements for inducing NEMO–IKK supramolecular structures," *J. Cell Biol.*, vol. 204, no. 2, pp. 231–245, 2014.

[9] M. J. Saxton, "Modeling 2D and 3D diffusion.," in *Methods in Membrane Lipids*, vol. 400, Humana Press, 2007, pp. 295–321.

[10] A. Patalano and B. Wernher, "PTVlab (Particle Tracking Velocimetry - lab) - File Exchange - MATLAB Central." [Online]. Available: https://www.mathworks.com/matlabcentral/fileexchange/41235-ptvlab--particle-tracking-velocimetry-lab-.

[11] G. Baffou, J. Polleux, H. Rigneault, and S. Monneret, "Super-heating and micro-bubble generation around plasmonic nanoparticles under cw illumination," *J. Phys. Chem. C*, vol. 118, no. 9, pp. 4890–4898, 2014.

[12] T. B. Jones, *Electromechanics of Particles*. Cambridge University Press, 1995.

[13] N. G. Green, "Dielectrophoresis and AC Electrokinetics," in *Electrokinetics and Electrohydrodynamics in Microsystems*, A. Ramos, Ed. Springer Wien New York, 2011, pp. 61–84.

[14] K. Salaita, Y. Wang, and C. A. Mirkin, "Applications of dip-pen nanolithography," no. 1, pp. 145–155.

[15] K. Lee, S. Park, C. A. Mirkin, J. C. Smith, and M. Mrksich, "Protein Nanoarrays Generated By Dip-Pen Nanolithography," *Science*, vol. 295, no. 5560, pp. 1702–1705, 2002.

[16] S. J. Tan, M. J. Campolongo, D. Luo, and W. Cheng, "Building plasmonic nanostructures

with DNA.," *Nat. Nanotechnol.*, vol. 6, no. 5, pp. 268–76, May 2011.

[17] S. W. Chung, D. S. Ginger, M. W. Morales, Z. Zhang, V. Chandrasekhar, M. A. Ratner, and C. A. Mirkin, "Top-down meets bottom-up: Dip-pen nanolithography and DNA-directed assembly of nanoscale electrical circuits," *Small*, vol. 1, no. 1, pp. 64–69, 2005.

[18] A. R. Madaria, A. Kumar, and C. Zhou, "Large scale, highly conductive and patterned transparent films of silver nanowires on arbitrary substrates and their application in touch screens.," *Nanotechnology*, vol. 22, no. 24, p. 245201, 2011.

[19] E. C. Garnett, W. Cai, J. J. Cha, F. Mahmood, S. T. Connor, M. Greyson Christoforo, Y. Cui, M. D. McGehee, and M. L. Brongersma, "Self-limited plasmonic welding of silver nanowire junctions.," *Nat. Mater.*, vol. 11, no. 3, pp. 241–9, 2012.

[20] A. M. Glass, D. Von Der Linde, and T. J. Negran, "High-voltage bulk photovoltaic effect and the photorefractive process in LiNbO3," *Appl. Phys. Lett.*, vol. 25, no. 4, pp. 233–235, 1974.

[21] T. Volk and M. Wohlecke, *Lithium Niobate: Defects, Photorefraction and Ferroelectric Switching*. Springer-Verlag Berlin Heidelberg, 2008.

[22] M. Carrascosa, A. Garcia-Cabanes, M. Jubera, J. B. Ramiro, and F. Agullo-Lopez, "LiNbO3: A photovoltaic substrate for massive parallel manipulation and patterning of nano-objects," *Appl. Phys. Rev.*, vol. 2, no. 4, 2015.

[23] R. Gerson and D. A. Bryan, "Bulk Photovoltaic Effect in Commercial Lithium Niobate Crystals," *Proc. SPIE, Los Alamos Conf. Opt.*, vol. 380, pp. 261–265, 1983.

7 Measurement of pyroelectric forces

Summary

This chapter details the results of trapping experiments performed in static and dynamic environments, in an effort to characterise the pyroelectric trapping force. The observed behaviour is compared against controls on Pyrex substrates, and substrates without plasmonic heating, to quantify the effects of plasmonic enhancement.

7.1 Introduction

From previous observations, pyroelectric induced trapping consists of distinct phases of varying nature. As a result, the trapping force cannot be sufficiently characterised with a single experiment. The aim of this chapter is to characterise the pyroelectrically induced force by performing more quantitative based assessments of bead motion. The behaviour of silica beads (3, 4 and 5 μm in diameter) in mineral oil is considered specifically, with experiments performed in differing solvents serving as counterpoints to test hypotheses on the source of electrokinetic motion. Again, experiments are performed on glass substrates, as well as lithium niobate substrates without plasmonic enhancement.

Three complementary approaches based on single particle tracking are used to quantify the magnitude of forces and explain the dynamics of bead motion. Results from finite element simulations (Chapter 5) are used as initial estimates to model trajectories of beads and to compare against experimental results.

7.2 Materials and methods

7.2.1 Image capture and processing

Images are recorded with a 40×, 0.5 NA (for drag force experiments) objective or a 20× 0.5 NA objective (for attraction experiments) at 15 frames per second using the setup described in Section 3.3. Image processing is performed as described in Section 3.8.1, and particle tracking is performed as described in Section 3.8.2.

7.2.2 Sample preparation

Beads in solution (3 and 4 µm) undergo the solvent swap described in Section 3.6.2. Beads are suspended in solvents to a concentration of 0.05% (0.5 mg/mL). The sparse concentration used allows for easier identification of individual beads, when tracking through the entire observation process.

Plasmonic structures are fabricated using the protocol detailed in Section 3.4.3. As before, structures are designed to achieve peak plasmon resonance between 600 and 650 nm. Arrays of 60 nm discs with an interparticle spacing of 300 nm are fabricated on glass while 40 nm discs with an interparticle spacing of 200 nm are fabricated on lithium niobate. A microfluidic chamber is constructed with the substrates supporting the plasmonic arrays, and a 180 µm coverslip, using 100 µm thick double sided tape as a spacer, as described in Section 3.6.1.

7.2.3 Zeta potential measurements

The zeta potential of silica beads was measured using the Malvern Zetasizer instrument, to verify their surface charge. The results of these measurements are detailed below. These are converted to a surface charge density using the zeta potential as the surface potential. Zeta potential is uniformly negative (anionic nature of silica beads due to presence of hydroxyl groups). A discrepancy between the zeta potential of 3 µm beads and 4/5 µm beads is observed. The surface charge density is more comparable to that of a carboxylated 5 µm silica bead i.e. a bead with additional functional groups. It is possible that the apparent increase in charge density is a result of increased number of particles arriving at the electrode, which affects the results reported. The possible implications of increased surface charge density on bead motion are discussed further in proceeding sections.

Table 7.1: Surface charge densities calculated using reported zeta potentials

Sample name	Electrophoretic mobility (µm·cm/Vs)	Zeta potential (mV)	Surface charge density (mC/m^2)
3 µm	-4.429	-56.4	17
4 µm	-1.323	-16.8	0.262
5 µm	-1.343	-17.1	0.267
5 µm (carboxylated)	-3.489	-44.4	10

7.3 Results and discussion

7.3.1 Mean squared displacement

In a similar manner to Chapter 6, the mean squared displacement (from msdanalyzer [1]) is used to elucidate the dynamics of pyroelectrically induced bead motion. The mean squared displacement is the average change in bead position for a given period of time (delay time/ time lag) i.e. [2]

$$MSD(t) = MSD(n\Delta t) = \frac{1}{N}\sum_{i=0}^{N-1}(x_{i+n} - x_i)^2 + (y_{i+n} - y_i)^2, \quad (7.1)$$

where the minimum value, Δt is the minimum resolvable period between successive images (i.e. frames per second of video), n is a variable integer which defines the delay between successive frames, and N is the number of time points of $n\Delta t$ separation in the observation period. Considering particle motion in this way allows characteristic motion of particles to be realised, as stochastic motion (e.g. diffusion and Brownian motion) can be resolved. A summary of MSD functions for commonly observed particle motion is given in [2] and shown below.

Table 7.2: MSD functions for typically observed forms of microparticle motion

Motion	MSD Function
Diffusive	$\langle r^2\rangle = 2dDt$
Directed	$\langle r^2\rangle = 2dDt + v^2t^2$
Anomalous	$\langle r^2\rangle = \Gamma t^{\alpha}$
Confined	$\langle r^2\rangle = \langle r^2\rangle_0[1-\exp(-t/\tau)]$

For purely diffusive motion, the mean squared displacement has a linear relationship with time. A quadratic relationship describes the motion of particles impelled by a constant flow, and an exponential decay defines confined motion (with the time constant (τ) defining the magnitude of confinement). The factor, $\langle r^2\rangle_0$, is often replaced by 2dDt as particles confined in a trap exhibit diffusive motion for time periods below τ.

This analysis presumes that the diffusion coefficient is constant. Implicit in this assumption is that temperature is constant (or the effect of temperature change is negligible). When this is not the case, bead motion is anomalous, and the correlation of MSD to delay time is given by a power law. In such cases, purely diffusive motion is insufficient to describe the kinetic behaviour of microparticles. The power law is indicative of an additional underlying process; transport

processes are somehow correlated in time and no single diffusion coefficient describes the entirety of their kinetic behaviour [2]. This can be the result of a number of factors such as spatial variation of temperature, and active transport processes. The magnitude of the exponent, α, determines superdiffusive (bead motion faster than diffusion), and subdiffusive (bead motion slower than diffusion) conditions. For superdiffusion, $\alpha > 1$, and the MSD diverges with increasing time. For sub-diffusion, $\alpha < 1$, and the MSD converges to a point (as is the case with confined motion).

7.3.1.1 Glass control

Confined motion of beads is observed when stimulation is performed on glass substrates. Incorporating a smoothing filter to reduce localisation error from systemic instrumentation error (such as, camera and microscope jitter, localisation, error in particle identification process, point spread function [3]), suggests a time constant of 0.4 seconds. This appears to be an artefact from the filtering algorithm. Without filtering, the MSD function calculated is constant for all delay times, indicating that the characteristic time constant is less than the minimum temporal increment i.e. 0.066 s. The sources of instrumentation error are primarily high frequency components. The filtering algorithm is thus discriminatory of short large changes in displacement. The filtering algorithm is avoided when the magnitude of particle velocity cannot be estimated before observation. Note that changing laser power has no effect on the nature of bead motion as can be seen in Figure 7.1.

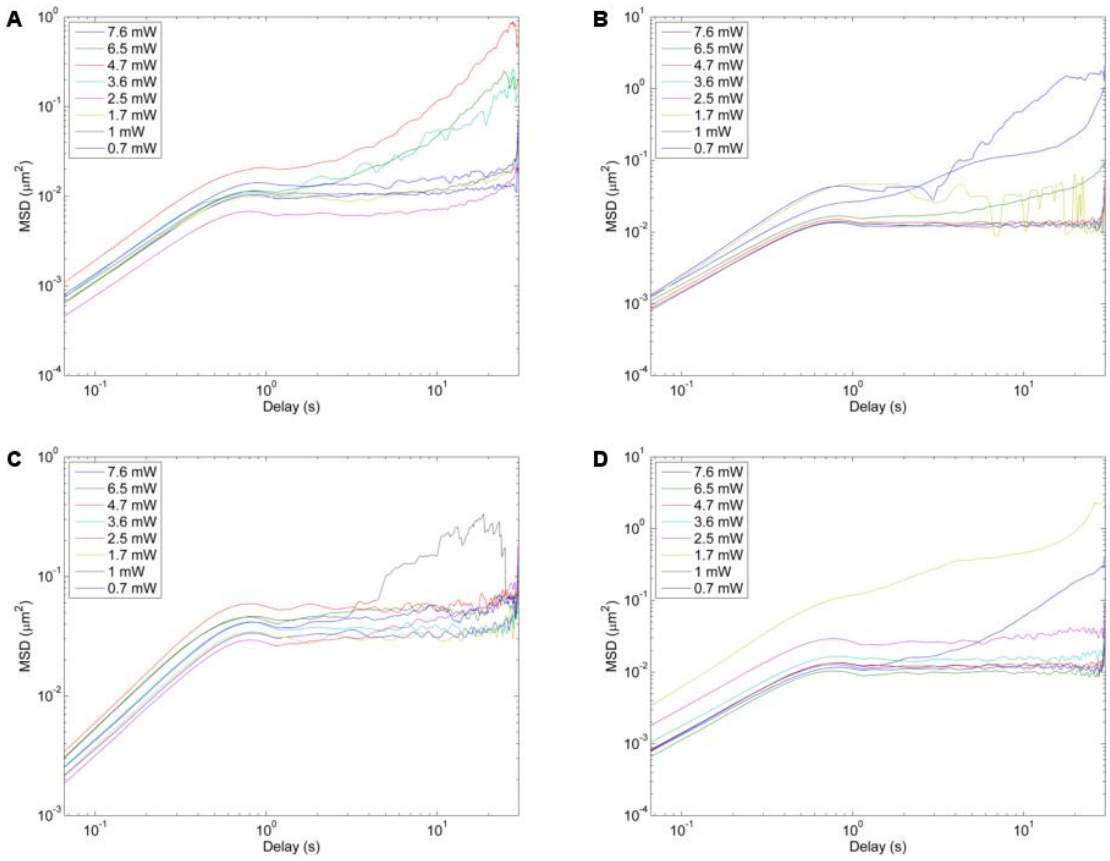

Figure 7.1: Mean squared displacement profile of the motion of: A) 3 μm, B) 4 μm, C) 5 μm beads in mineral oil, and D) 5 μm beads in almond oil as a result of stimulation of plasmonic arrays on glass.

Based on the definition of the MSD and its relation to diffusion, in all cases considered, the nature of confinement should change with increasing laser power as the increased thermal energy, coupled with the reduced solvent viscosity (typically modelled as being inversely proportional to a power of temperature), increases the diffusion coefficient, and subsequently the uncertainty in particle position. Results indicate that this is not the case. Though, the MSD varies with laser power, there is no correlation between the two parameters, suggesting that the changes in peak MSD observed are more likely a result of outliers modifying the average rather than an attribute of plasmonic stimulation. This result suggests that the solvent viscosity is practically constant in the temperature region in which the experiments are performed. The bead motion observed in isolated experiments appears to be in large part a result of movement from out of focus beads. This out of focus motion is observed particularly with 3 μm beads at high laser powers, which suggests that its presence here is a result of bead sedimentation. Sedimentation is also more apparent in previous experiments, as a result of the objective used. The lower magnification and NA used to perform those experiments meant that a larger depth of field could be observed. Hence, out-of-focus beads are clearer, and sedimentary bead motion is observed for a statistically significant period of time.

The square root of the MSD calculated remains largely static within the 100–300 nm range (Figure 7.2). Note that major deviations occur primarily with experiments where there is some evidence of isolated sedimentation. The values appear valid when compared with the resolution these experiments where performed (0.3125 µm/pixel), and the knowledge that the particle tracking allowed for sub pixel localisation. These experimental values are used as a baseline for defining the minimum allowable deviation from a stationary position when stimulation has no effect on beads. Thus, a deviation of greater than 0.3 µm in 30 seconds of stimulation is required to categorically state that the pyroelectric effect is responsible for bead motion.

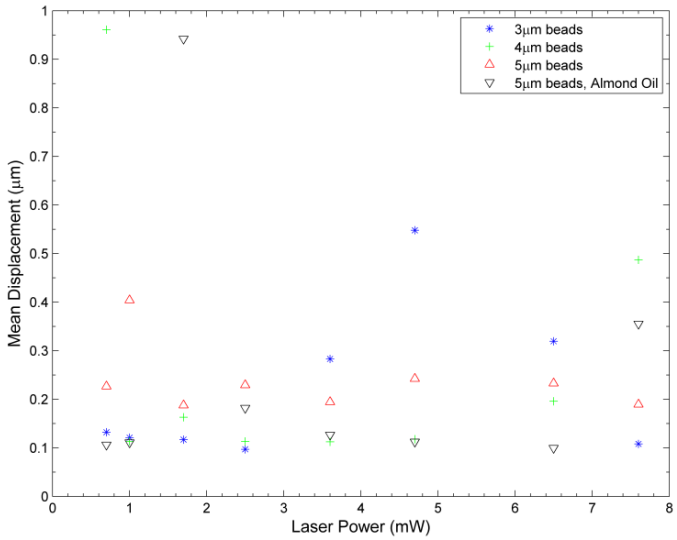

Figure 7.2: Calculated displacement of beads from initial position following 30 seconds of stimulation for a range of laser powers

7.3.1.2 Lithium niobate

The nature of the MSD curves derived from experiments performed on lithium niobate deviate markedly from the simple functions described in Section 7.3.1, suggesting that bead motion is more complex than the models listed indicate, as none of these sufficiently describe the derived MSD functions. The experimental observations made can be used to explain the deviations from the models.

Figure 7.3 displays trajectories (presented without stationary beads) recorded with excitation at 7.6 mW. This information is displayed in Figure 7.4, which gives projections of bead positions for the entirety of an observation period. The intensity of the beads is a function of their speed. Stationary beads appear brighter as they remain in position for longer. Figure 7.4A–C) shows the

recordings with stationary beads. In Figure 7.4D–F) stationary beads are removed. Tracks in general, congregate around a central point (75 µm, 75 µm), the location of the laser spot in the cropped and processed image sequence. Note that for the smaller beads (3 µm and 4 µm), tracks are haphazard, as silica beads oscillate about the laser spot. These oscillations are not observed with 5 µm beads. At lower powers, the magnitudes of the oscillations reduce and eventually disappear.

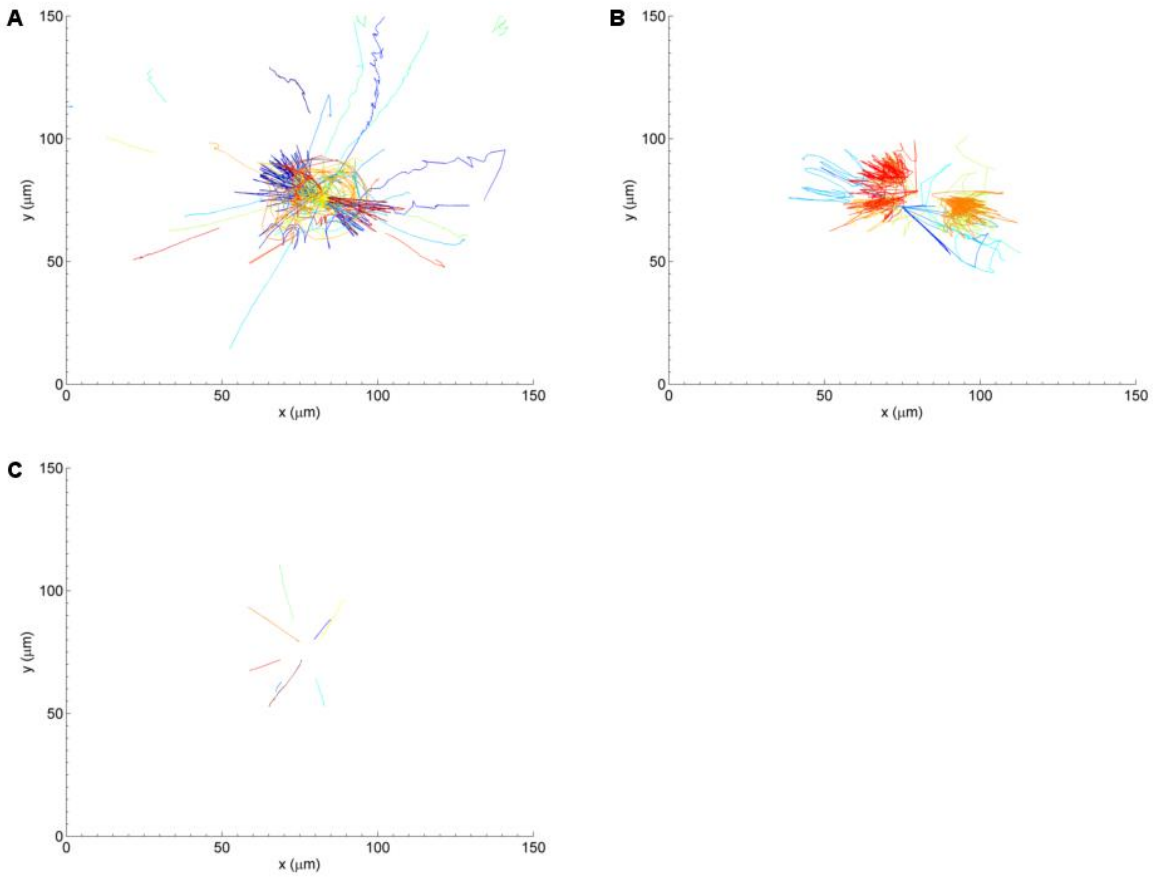

Figure 7.3: Trajectory of beads around laser spot as a result of plasmon enhanced pyroelectrically induced forces at 7.6 mW for: A) 3 µm beads, B) 4 µm beads, and C) 5 µm beads in mineral oil.

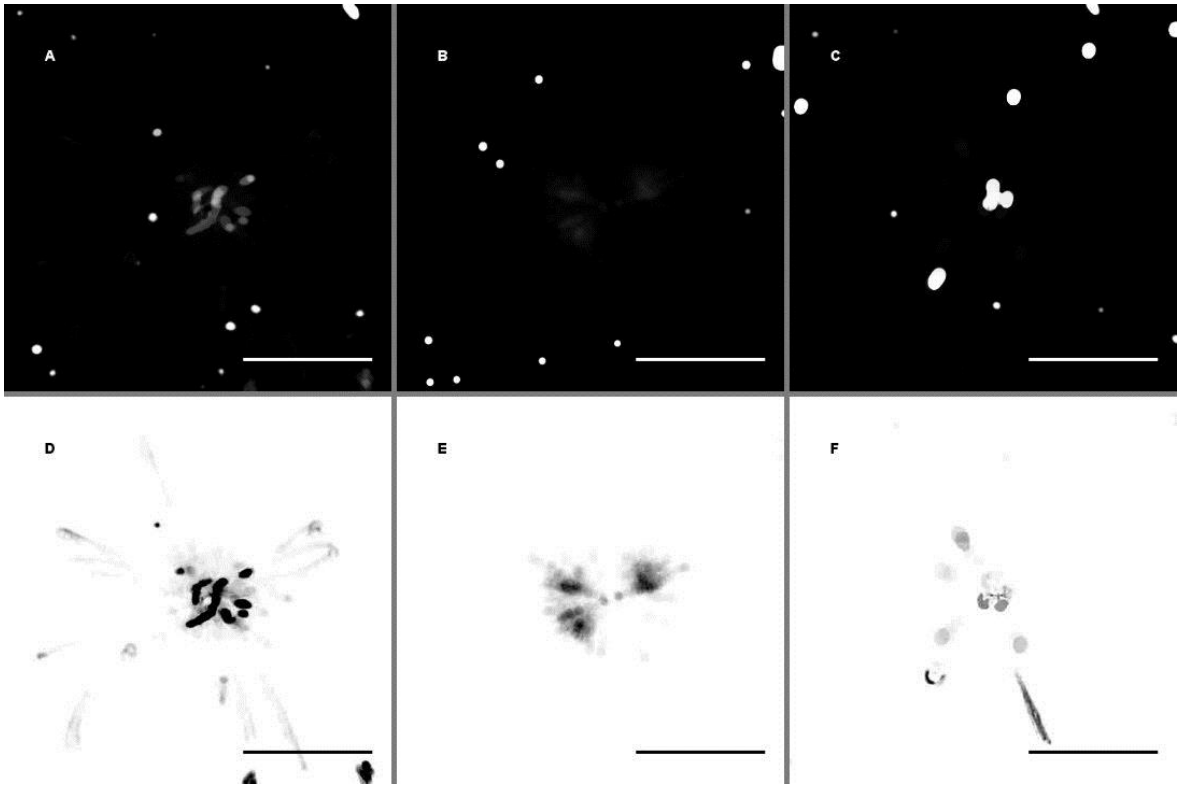

Figure 7.4: Projections of recorded particle motions using plasmonic enhancement for: A) 3 µm beads, B) 4 µm beads, and C) 5 µm beads. Recorded particle motions of: D) 3 µm beads, E) 4 µm beads, and F) 5 µm beads without the contribution of stationary beads. Bead intensity is reduced as particles are in constant motion. Scale bar is 50 µm.

The MSD curves of these experiments are presented in Figure 7.5. The results presented neglect the contribution from stationary beads. Neglecting this contribution does not affect the overall MSD profiles presented; static beads apply an offset, which reduces the maximum but does not otherwise change its evolution with respect to time delay.

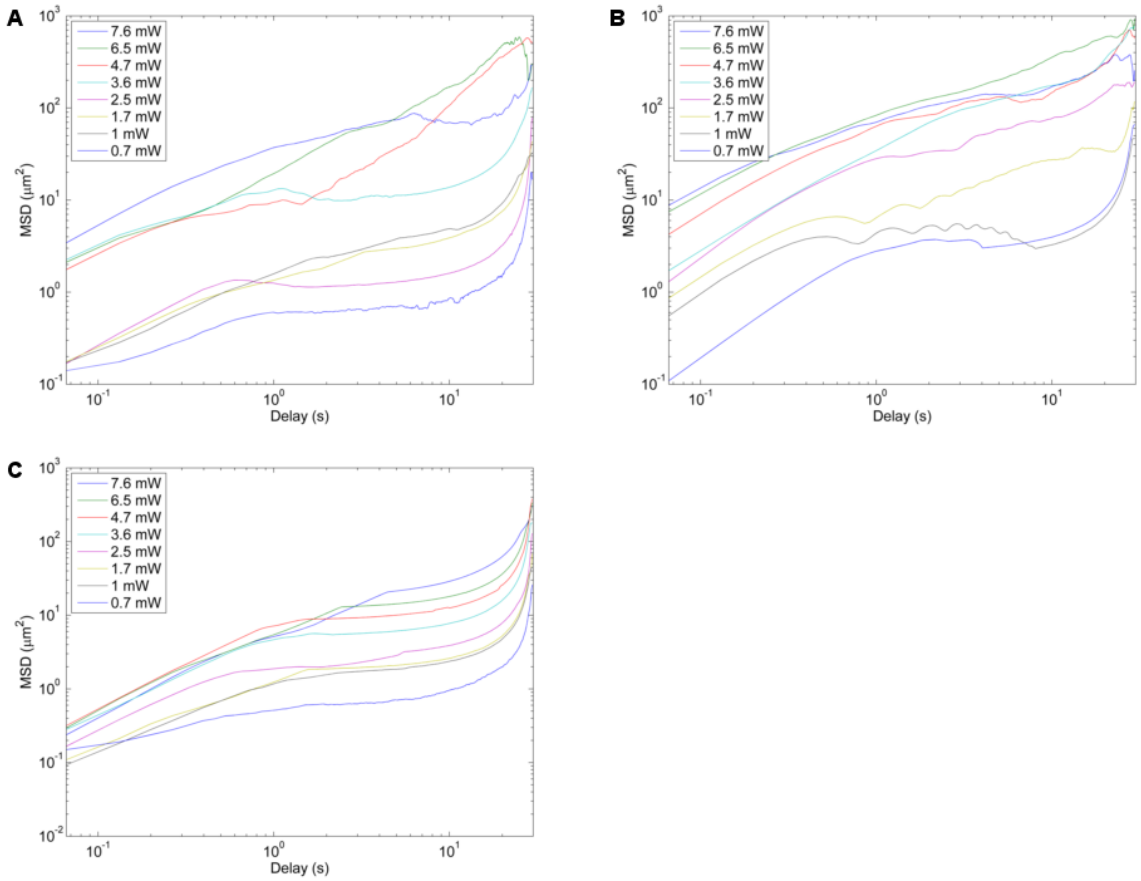

Figure 7.5: Mean squared displacement profile of the motion of: A) 3 µm, B) 4 µm, and C) 5 µm beads in mineral oil as a result of stimulation of plasmonic arrays on lithium niobate.

With the exception of the curves obtained using 3 and 4 µm beads at high laser powers, MSD curves generally exhibit a saddle profile. Bead motion is characterised by attraction and subsequent trapping at a central location. At short delay times, the gradient of the MSD curve is indicative of the underlying diffusive motion present throughout the experiment. The deviation from purely diffusive motion arises as a result of the directed motion of beads towards the laser spot caused by the attractive force. The plateau region signifies that beads are trapped; displacement remains static in spite of increasing delay time. The magnitude of the MSD in the plateau region indicates the distance travelled. MSD begins to increase again at longer time scales as a result of the fact that initial bead position differs from the final position. At longer delay times, the MSD is more reflective of isolated changes in position since fewer results are responsible for the mean.

Similar profiles were obtained from analytical simulations as illustrated in Figure 7.6. This behaviour is simulated in Matlab using the discretised Langevin equation (Appendix F). DEP is modelled as a harmonic potential with distance dependent trap stiffness, calculated using results from finite element simulations. Stochastic thermal motion is modelled with a Gaussian random

number generator with variance determined by the thermal energy of the bead. Using these parameters, the unusual MSD curves are recovered. The simulations were performed with beads randomly distributed (with a uniform probability function) in the observation space. The distances of each individual bead from the centrally located laser spot is thus different (Figure 7.6A). This variability in particle position is reflected in the fact that differing MSD curves are recorded for individual particles (Figure 7.6B). From this simulation, it can subsequently be inferred that the decay constants indicating confined motion are dependent on the time it takes beads to travel to the laser (i.e. decay constant is dependent on the distance from laser and particle velocity).

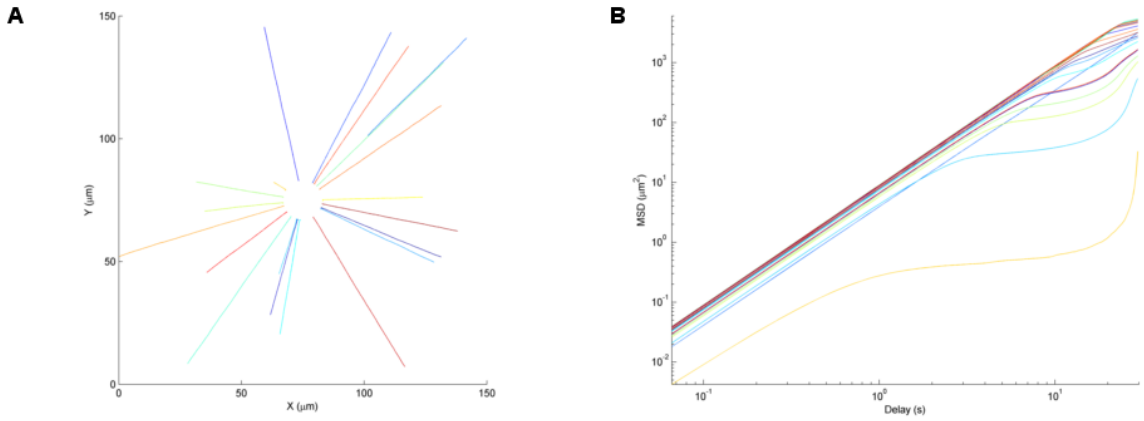

Figure 7.6: Simulated behaviour of randomly distributed 5 μm beads. A) Trajectories of bead towards trap centre. B) Corresponding MSD curves of individual particles.

The differing nature of the profiles obtained using smaller beads, can be explained in the context of the proposed operation of pyroelectric induced motion, namely the presence of independent attraction and trapping forces. Chapter 5 suggests the long range attraction force is a result of electrothermal convection, while the short range trapping force is a result of DEP. Smaller beads do not remain at the site of the laser spot due to an insufficiently large trapping force. As this force (DEP) scales with volume, 5 μm beads are unaffected. Oscillations are not observed at lower powers, signalling the switch over from an electrothermal to a dielectrophoretic regime as discussed previously.

The behaviour of beads on unpatterned lithium niobate clarify these observations. The loss of plasmonic enhancement means thermal generation is less efficient. The generated temperature and pyroelectrically induced forces are thus reduced. Due to its dependence on magnitude of temperature as well as electric field, the attraction force (controlled by electrothermal convection) reduces quicker than DEP (a cubic dependence on laser power was previously noted compared to a square dependence for DEP). As a result of the inefficient heat generation

associated with photothermal absorption, trapping of smaller beads at higher powers is observed (Figure 7.7 and Figure 7.8). Hence, the characteristic saddle like MSD curves associated with attraction and trapping are largely recovered (Figure 7.9).

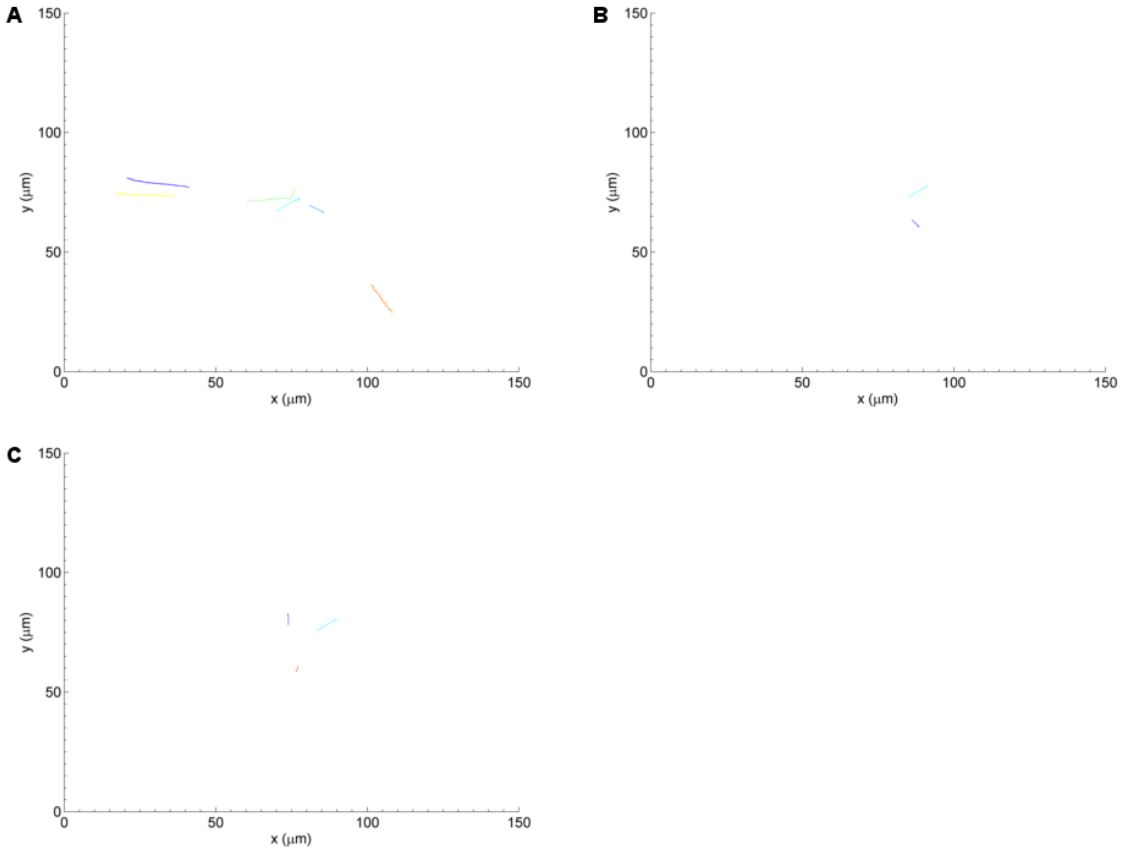

Figure 7.7: Trajectory of beads around laser spot as a result of photothermal pyroelectrically induced forces at 7.6 mW for: A) 3 µm beads, B) 4 µm beads, and C) 5 µm beads in mineral oil.

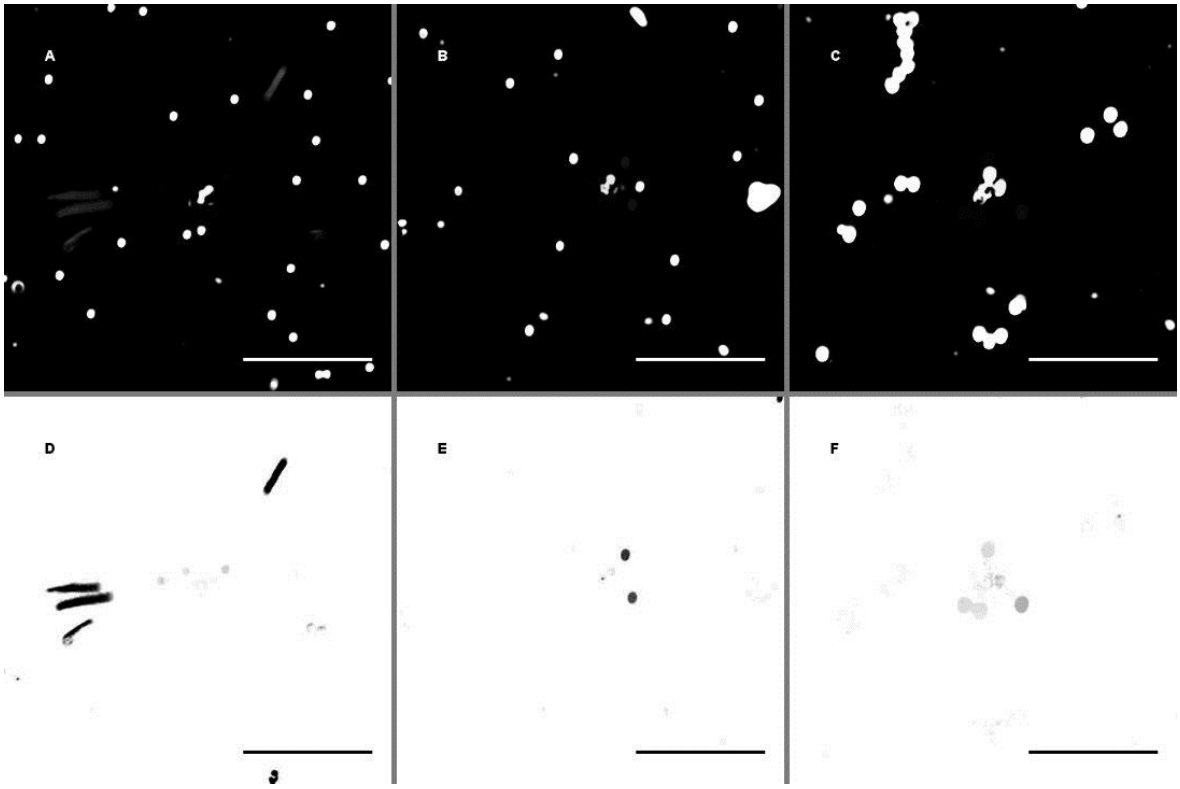

Figure 7.8: Projections of recorded particle motions using photothermal absorption for: A) 3 µm beads, B) 4 µm beads and C) 5 µm beads. Recorded particle motions of: D) 3 µm beads, E) 4 µm beads, and F) 5 µm beads without the contribution of stationary beads. Bead intensity is reduced as particles are in constant motion. Scale bar is 50 µm.

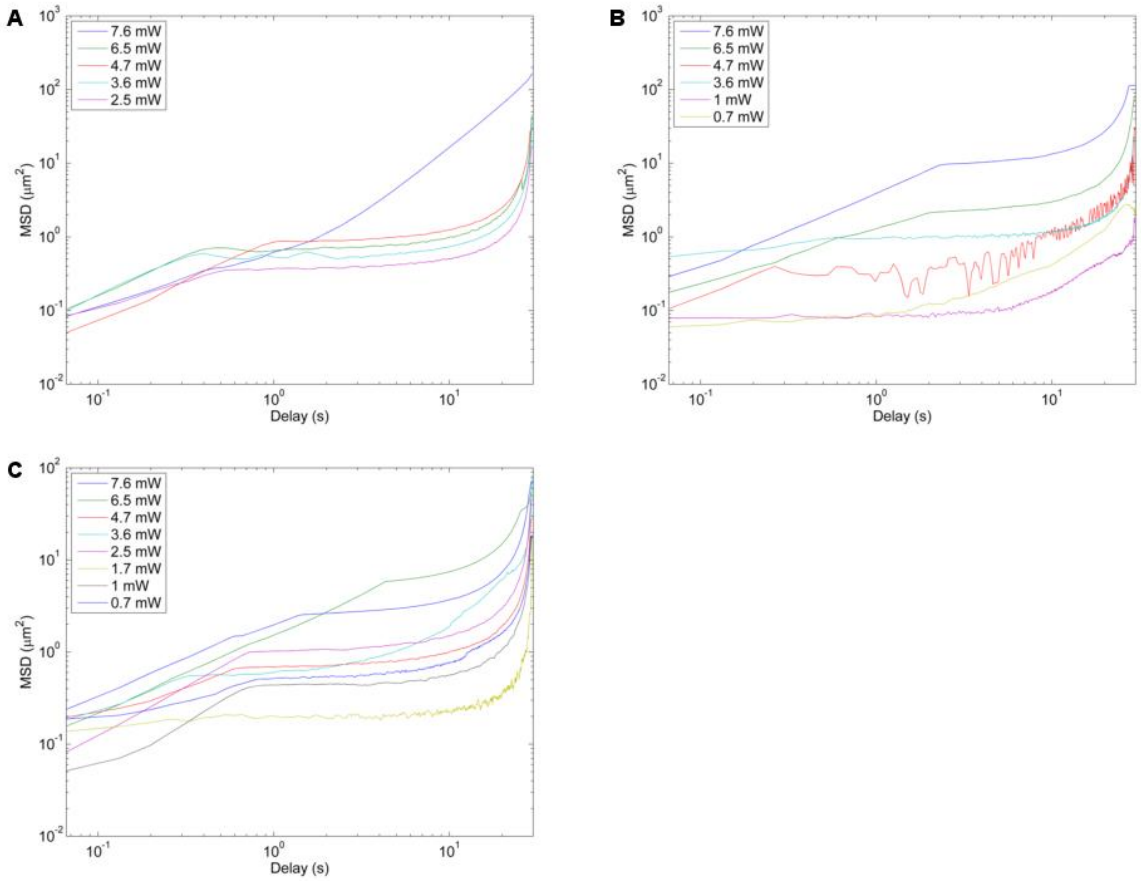

Figure 7.9: Mean squared displacement profile of the motion of: A) 3 µm, B) 4 µm, C) 5 µm beads in mineral oil as a result of photothermal absorption of unpatterned lithium niobate. Observed profiles are more uniform. No bead motion is recorded at lower powers for 3 and 4 µm beads.

The behaviour of neutral 5 µm beads in almond oil is recorded as a further test of the suggested hypothesis. The increased permittivity of the solvent means that its dielectric response is comparable to that of the silica bead i.e. relative polarisability as indicated by the Claussius-Mossotti factor (and subsequently the magnitude of the DEP force) has been reduced. The reduction of the DEP component of particle motion is evident in the recorded behaviour. Particles are repelled from the central laser spot in the majority of cases considered (Figure 7.12A and Figure 7.13A). In isolated cases, where beads are trapped at this location prior to stimulation (Figure 7.11), bead concentration is observed, suggesting prior interparticle relationships (for instance, Van der Waals forces) also aid in trapping. Repulsion does not lead to a substantial difference in the appearance of the recorded MSD profiles (Figure 7.10) as this metric does not distinguish between the direction of travel.

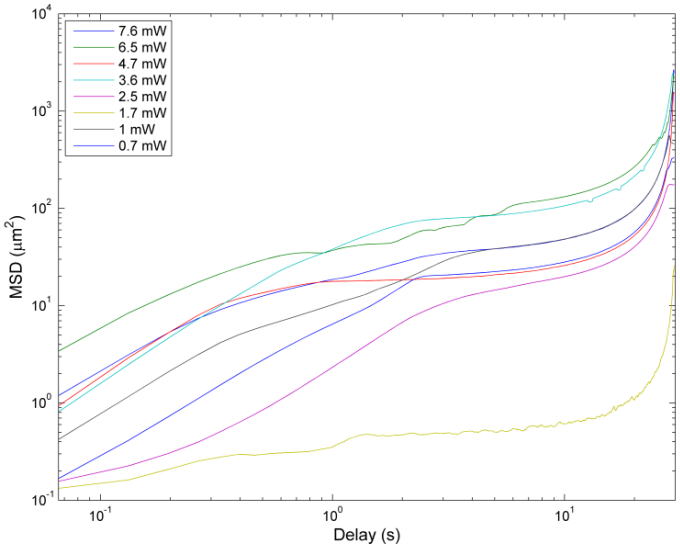

Figure 7.10: Mean squared displacement profile of bead motion in almond oil for a range of laser stimulation powers. Profile is roughly the same even though beads are repelled from the laser.

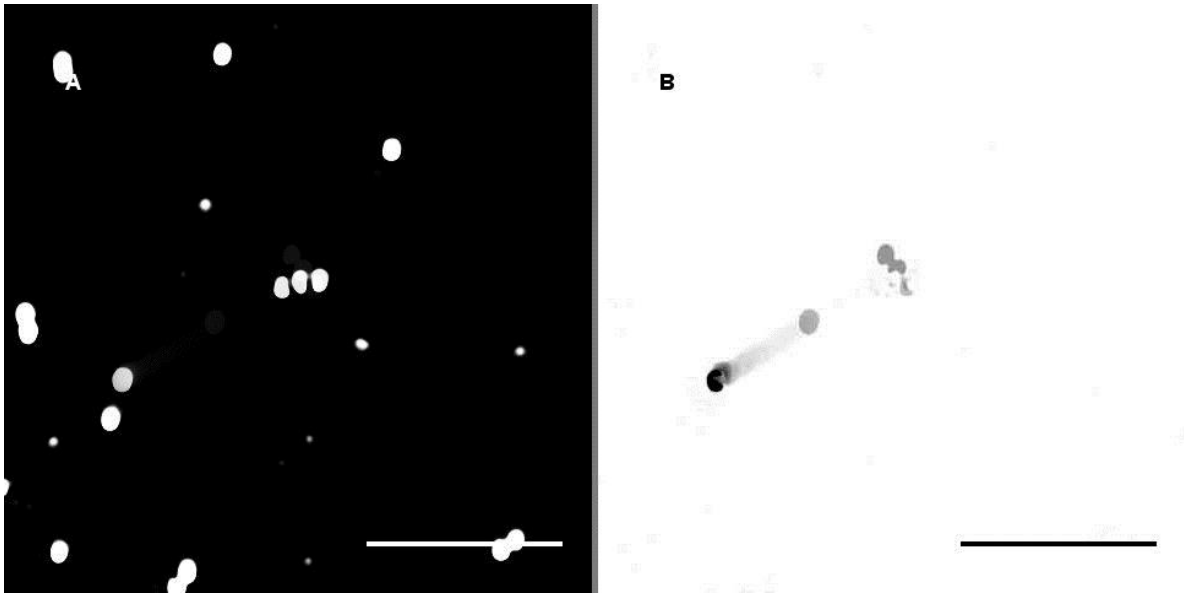

Figure 7.11: Average projection of position of 5 μm silica beads in almond oil during stimulation. A) With and B) without static beads. Beads located at the centre of the image are clustered prior to stimulation and are thus not repelled from the laser spot. Scale bar is 50 μm.

Previous demonstrations of particle manipulation using almond oil (performed during patterning experiments detailed in Chapter 6) depicted attraction of beads towards a central point rather than repulsion. Figure 7.12B and Figure 7.13 show that this attraction behaviour is retrieved when carboxylated silica beads are used in place of the neutral beads (as was the case with the demonstrations presented in Chapter 6). The change from attraction to repulsion suggests that surface charge density aids in trapping. The precise cause of this change remains to be

investigated. However, it was previously noted that the concatenation of events which enable dielectrophoretic and electrothermal motion induced by pyroelectric fields, also enable electrophoresis. It is thus possible that carboxylated beads are trapped electrophoretically as a result of their increased surface charge density. In addition to this, surface charge density controls surface conductance and polarisability of particles in aqueous solvents. A similar relationship between charge density and polarisability can be described for non-polar media. The modification in polarisability could lead to an increase in the Claussius-Mossotti factor, which also aids trapping. The effects of electrothermal convection do not completely disappear, repulsion is noted for beads initially located 30 µm away from the laser spot.

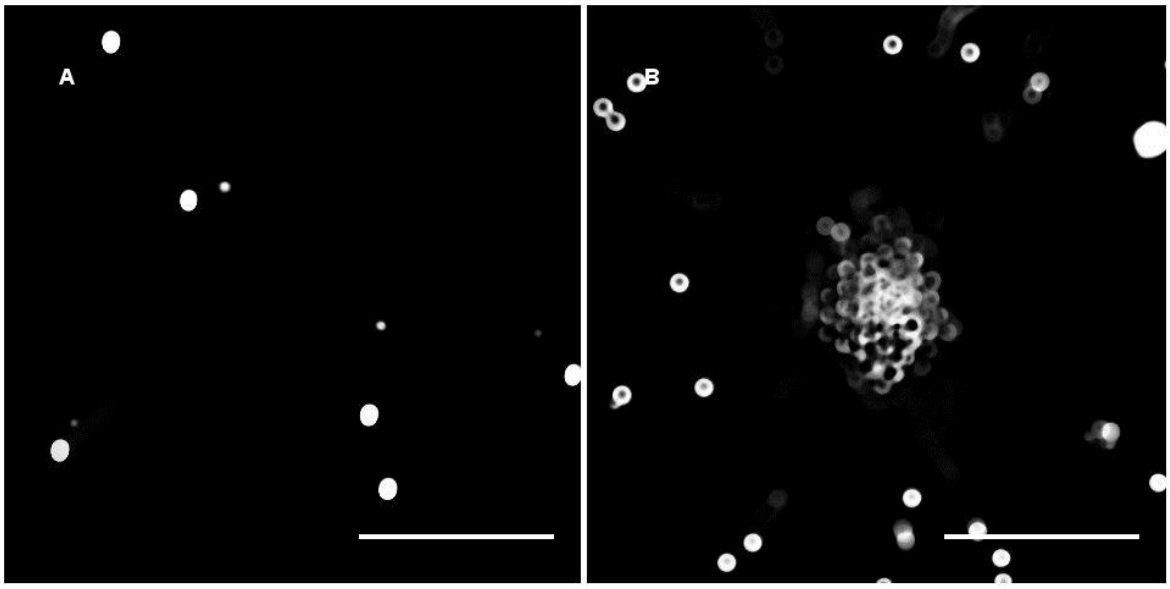

Figure 7.12: Effects of carboxylation of beads on observed motion in almond oil. A) Beads are repelled from centre. B) Carboxylated beads cluster at the trap centre. Beads initially located 30 µm from centre are still repelled. Scale bar is 50 µm.

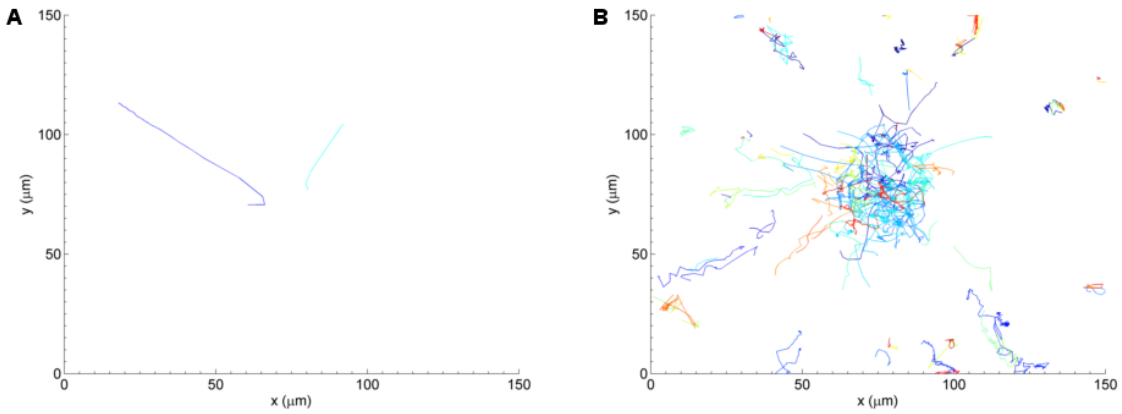

Figure 7.13: Recorded trajectory of: A) natively charged and B) carboxylated 5 μm silica beads. The small particle separation of beads located at the laser spots hampers particle tracking, thus trajectories are haphazard. Paths located 30 μm from the origin show repulsion of beads. Short trajectories are result of repulsion in the z direction; tracking stops abruptly as beads quickly leave the focal plane.

Finally, the behaviour of carboxylated silica beads in mineral oil is recorded (Figure 7.14). Unlike the case where almond oil is used, there is little substantive difference to the previous observations made using neutral beads on plasmonically patterned lithium niobate substrates. The marked difference occurs when comparing particle behaviour on unpatterned LN to patterned LN. Bead motion is not observed at lower powers on unpatterned LN, suggesting greater sensitivity of carboxylated beads to plasmonic enhancement.

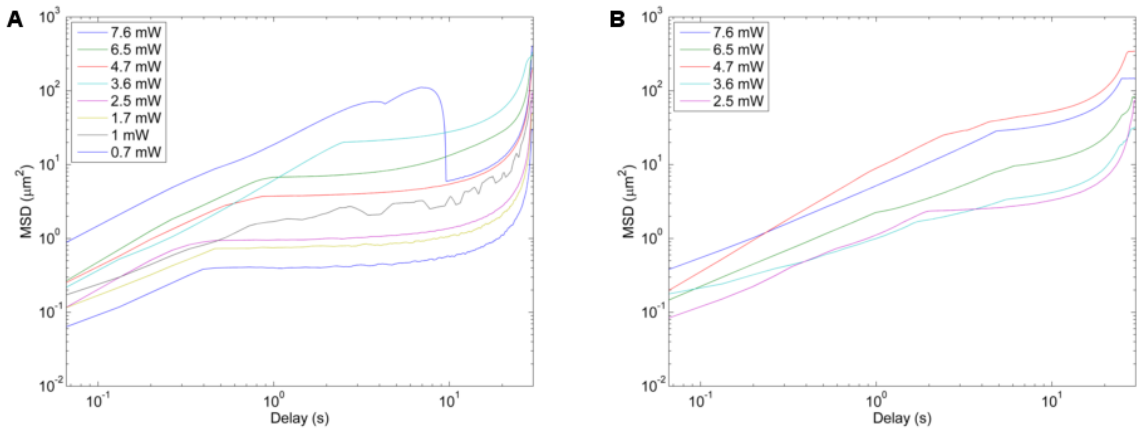

Figure 7.14: Mean squared displacement profiles of carboxylated 5 μm beads due to: A) plasmonic enhanced heating and B) photothermal absorption. No bead motion is recorded for powers below 2.5 mW when plasmonic enhancement is removed.

7.3.2 Effective trap radius

Having considered the dynamics of bead motion by analysing the MSD profiles, the attraction force is characterised by calculating the radial displacement of beads from the trap centre i.e. defining an effective trap radius [4]. This is defined as the furthest point away from the laser where beads move further than 300 nm or faster than 300 nm/30 s i.e. the point at which bead motion is purely confined. Within this radius, the sum of the externally induced forces is greater than stochastic Brownian motion. Only positive DEP i.e. attraction to the laser spot, is considered in this analysis. The motion of an ensemble of beads during laser stimulation is recorded for 30 seconds (450 frames at 15 frames per second). Three repetitions are performed at each laser power. The error bars denote the standard error to the mean (standard deviation/√number of moving beads).

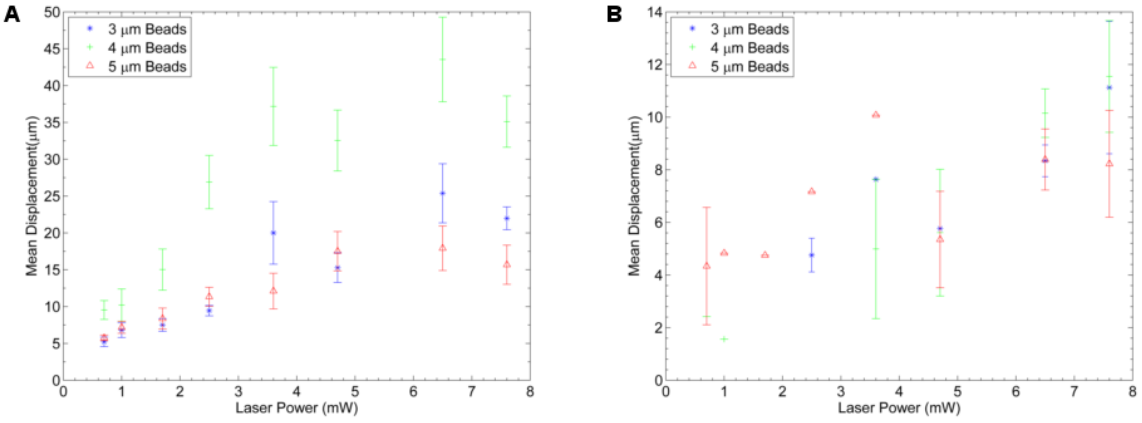

Figure 7.15: Mean displacement of beads set in motion as a result of pyroelectrically induced forces controlled by: A) plasmonic enhanced heating and B) photothermal absorption.

It is observed that with plasmonic enhancement, the mean displacement (effective trap radius) increases with laser power. Figure 7.15 suggests a somewhat linear relationship between displacement and laser power, in contrast to the cubic and quadratic relationship of ETF, and DEP, respectively. With plasmonic enhancement, the expansion rate of the trap radius slows, suggesting a saturation type condition. One is able to observe larger displacements using 3 and 4 μm beads with plasmonic enhancement compared to 5 μm beads. This is because the oscillatory motion of smaller beads enables them to traverse larger distances as they are unencumbered by static friction. Without plasmonic enhancement, beads travel a shorter distance to the trap centre.

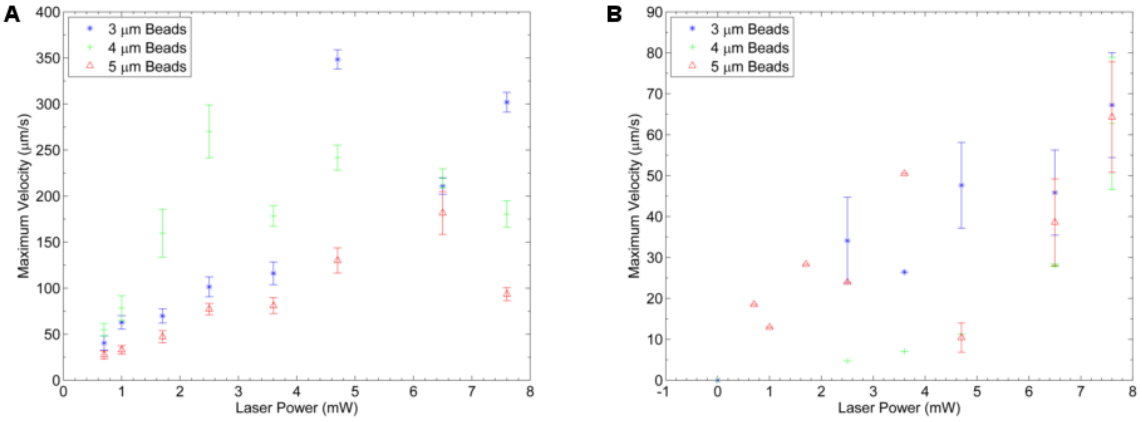

Figure 7.16: Maximum velocity of beads set in motion as a result of pyroelectrically induced forces controlled by: A) plasmonic enhanced heating and B) photothermal absorption.

Maximum particle velocity does not vary substantially with size (Figure 7.16), suggesting that this attribute is a function of electrothermal convection. 3 µm and 5 µm beads give the best indication of monotonic results. Errors arise for a number of reasons, such as the camera exposure time and the frame rate of the recorded video (i.e. the sampling interval) [5]. In these experiments the largest error source appears to be the speed of particle oscillations, which creates difficulty in following one bead for the entirety of the observation period. This leads to an overestimation of the number beads undergoing oscillations, which increases the maximum speed reported. This phenomenon is observed with 4 µm beads. Velocities substantially decrease without plasmonic enhancement, due to the reduction in generated temperature, and subsequently, electric field.

By comparing inertial and viscous contributions, one can determine which forces are largely responsible for particle motion. The range of accelerations for which viscous forces are substantially (10×) greater than inertial than forces is given by:

$$a \leq \frac{0.9\eta v}{2r^2\rho}, \tag{7.2}$$

where η is the fluid viscosity, v is the particle velocity, ρ is the particle's mass density, and r is its radius. The minimum acceleration indicative of inertial dependent motion is calculated using the maximum bead size and a velocity of 5 µm/s. This calculation suggests a baseline acceleration of ~9 m/s^2 indicates inertial dominant motion. This far exceeds the typical accelerations observed which are in the region of 100 µm/s^2. This indicates that the maximum approach velocity of beads is able to quantify attraction force with Stokes's drag equations. Calculations suggest values of attraction force in the region of 10^2 pN (Figure 7.17), a range which is substantially higher (up to

two orders of magnitudes greater than optical tweezers [6], for example) than the pN and fN magnitudes typical of other optical manipulation techniques. The similarity of the recorded particle velocities to those reported in the literature [7]–[9], is due to the fact that experiments are performed in viscous paraffinic environments in contrast to the aqueous solvents used more frequently.

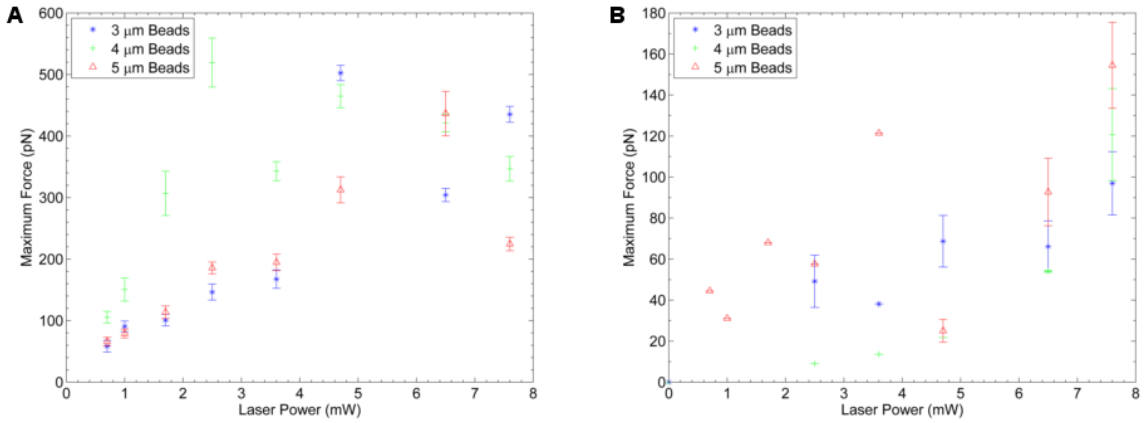

Figure 7.17: Total attraction force (calculated using Stokes's drag) on beads set in motion as a result of pyroelectrically induced forces controlled by: A) plasmonic enhanced heating and B) photothermal absorption.

The particle velocities (Figure 7.18) and thus, the calculated attraction forces (Figure 7.19), recorded using carboxylated silica beads are similar to previous results from experiments using neutral beads, suggesting that the increase in surface charge density has minimal effect on their magnitude. This observation is consistent with the proposed electrothermal convection origin of the long range attraction force, which is independent of the electrical parameters of silica beads. The major deviation from previous result is the width of the effective trap radius, which is increased (30 µm maximum is recorded compared to 15 µm observed previously) when non-functionalised beads are used; a likely result of additional propulsion of electrophoretic origin. The increased surface charge density also causes some interfacial effects, which further explain the widening of the trap radius. As a result of the increased surface charge density the contact between the particle and substrate is reduced (due to a charge induced repulsive force). Static friction is less dominant as a result of this; beads are able to be transported from further distances in a similar way to how smaller particles undergoing oscillatory motion displayed larger trap radii.

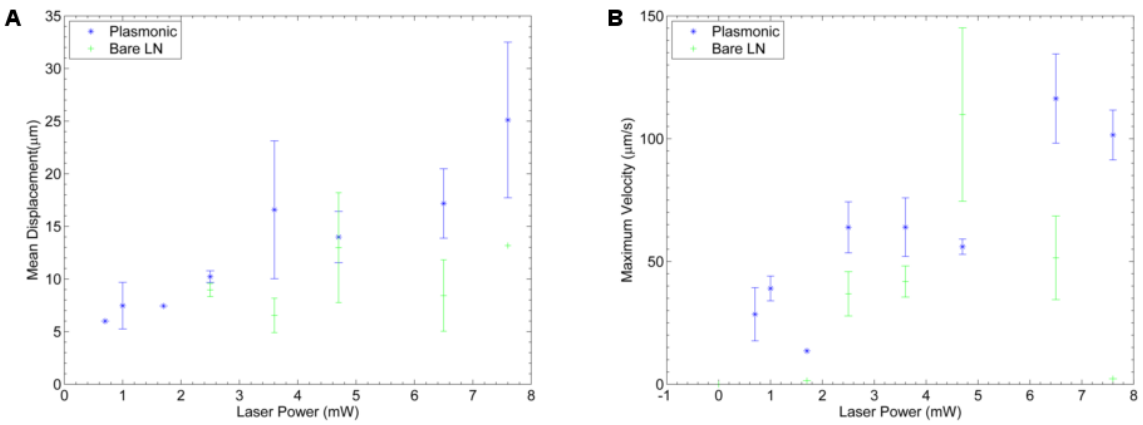

Figure 7.18: Effect of carboxylation on: A) mean displacement and B) maximum velocity of 5 µm silica beads in mineral oil.

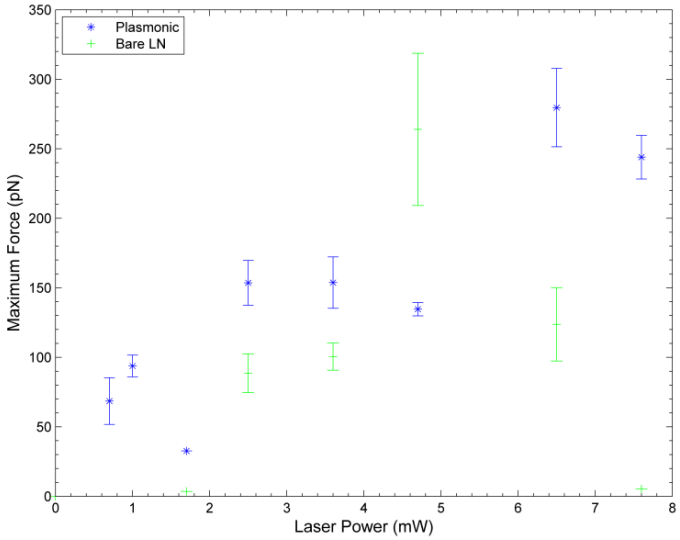

Figure 7.19: Pyroelectrically induced attraction force (calculated using Stokes's drag) on carboxylated 5 µm silica beads with and without plasmonic enhanced heating.

Table 7.3: Evolution of various indicators of attraction with laser power. Trap radius and velocity give an indication of the magnitude of force controlling the bead's approach towards the trap centre.

Bead diameter	Force (pN/mW)		Velocity (µm/s/mW)		Radius (µm/mW)	
	Patterned	Bare	Patterned	Bare	Patterned	Bare
3 µm	55.55	11.86	38.52	8.22	2.804	1.033
4 µm	31.48	11.91	16.37	6.196	4.461	1.399
5 µm	39.29	12.04	16.35	5.011	1.672	0.535
5 µm (carboxyl)	29.27	13.05	12.18	5.431	2.412	0.7193

Table 7.3 summarises how various parameters evolve, assuming a linear relationship with laser power. These results are broad estimates, errors arise due to the track identification errors previously noted, and the nature of the particle tracking algorithm used. Particle tracking is optimised for identification of Brownian motion in large particle ensembles [5]. The non-linear characteristic of superdiffusive motion requires sparse concentrations, to minimise misidentification of particles. Hence, relatively large standard errors to the mean are recorded in spite of repetitions. Nevertheless, a broad characterisation of some facets of bead behaviour in response to plasmonic enhanced pyroelectric field is gained using the effective trap radius. Different approaches are used to derive other relevant information.

7.3.3 MSD of statically-trapped beads

The mean squared displacement is used in a more traditional manner to estimate the magnitude of the trapping force. Using the MSD for this purpose is possible due to a slight change in the experiment parameters; the motion of beads which are already trapped (in an equilibrium state) is recorded. As the approach to this state is ignored, the information encoded in the MSD is thus different. Rather than this being a measure of how far a particle travels to a central point, the MSD now reflects how far a bead deviates from the trap centre. Using a finite difference implementation (programmed in Matlab) of the Langevin equation (Appendix F), the trajectory of trapped beads can be modelled numerically. The optical trap is described by a harmonic potential; beads are free to diffuse for a given characteristic distance, the magnitude of which defines the force of the trap (trap stiffness). The characteristic curve of such traps is given in Figure 7.20D.

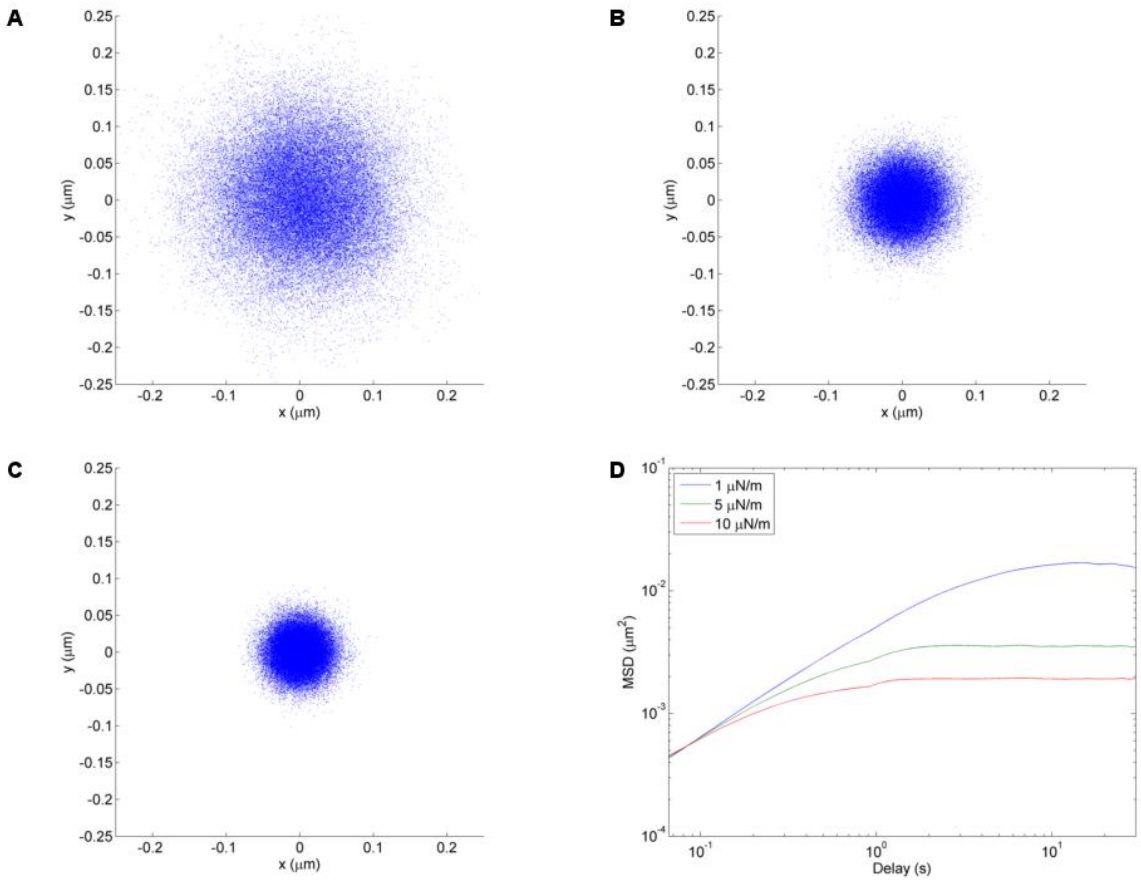

Figure 7.20: Simulated trajectories of 5 μm bead in an optical trap with: A) κ = 1 μN/m, B) κ =5 μN/m, and C) κ = 10 μN/m. D) MSD curves associated with bead motion confined by defined optical traps.

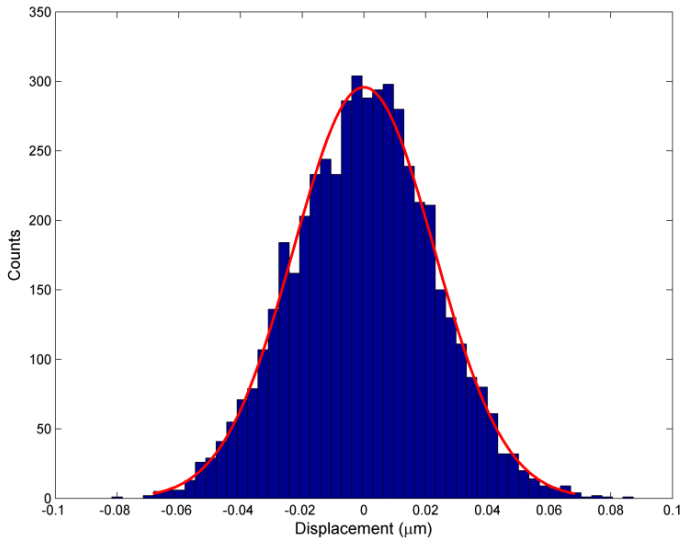

Figure 7.21: Histogram of particle displacements from trap centre in a 10 μN/m trap.

Figure 7.20 displays the trajectory of a 5 μm diameter bead in mineral oil in various optical traps as density plots. Beads experience increasing confinement as trap stiffness increases. The plateau

in the MSD curves represents the confinement region. The time it takes to reach this plateau (i.e. trap time constant) is given by [10], [11]:

$$\tau = \frac{6\pi nR}{\kappa} \tag{7.3}$$

Observing at periods shorter than this reveals diffusive motion of particles in trap. Conversely, if the observation/sampling period is much longer than this no diffusive motion is noted; beads appear static. The spring constant can be recovered using equipartition theorem [12]. Thermal energy is equal to potential energy of the spring, hence:

$$\kappa = \frac{kT}{< x^2 >}, \tag{7.4}$$

where k is Boltzmann's constant, T is temperature, and $< x^2 >$ is the mean squared displacement at the plateau region. An estimate of the maximum trapping force can be made by defining the maximum displacement from the trap centre. The MSD is a measure of the variance in particle displacement from the trap centre. The maximum displacement can thus be estimated as 3× the standard deviation (the square root of the MSD), as the motion of the bead in the trap is governed by a normal distribution (Figure 7.21); hence, trapping force is given by:

$$F = \frac{3kT}{\sqrt{< x^2 >}}, \tag{7.5}$$

assuming that the trap stiffness is constant in the regions this describes.

Five repetitions at each laser power (with and without plasmonic enhancement) are performed. Only particles which are "trapped" at the beginning of observation period are tracked. To ensure particles are trapped, the laser is initially placed away from candidate particles. After this, only particles which have been drawn to the laser spot are considered. Simulated values of temperature are used to estimate the trapping force.

When the approach to the laser's focal point is ignored, more information on the nature of confinement is revealed. For powers above 3.7 mW, MSD calculated for 3 and 4 µm is two orders of magnitude greater than those encountered otherwise, as a result of their oscillatory motion (Figure 7.22). Based on the previously defined equation for force, this increase in MSD suggests that the trapping force is ~10% of that encountered in other situations (assuming all other factors such as viscosity and temperature are equal).

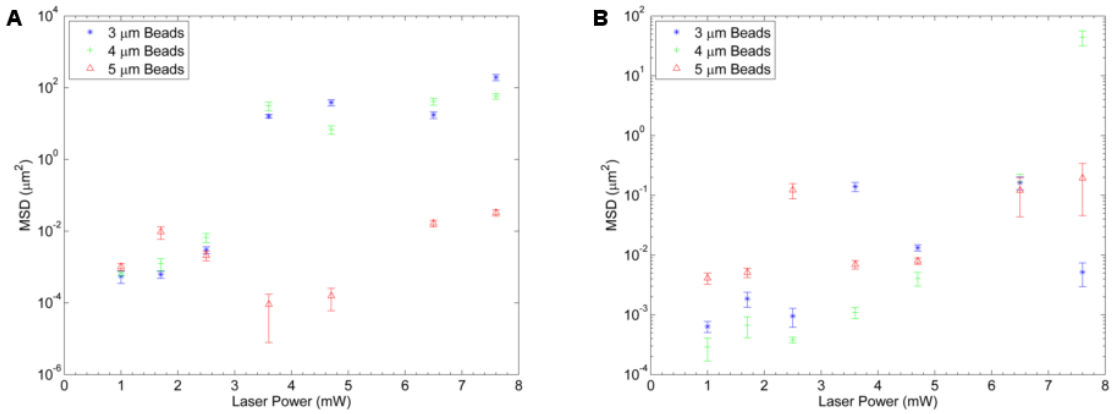

Figure 7.22: Observed mean squared displacement for natively charged silica beads in mineral oil. A) With and B) without plasmonic enhanced heating.

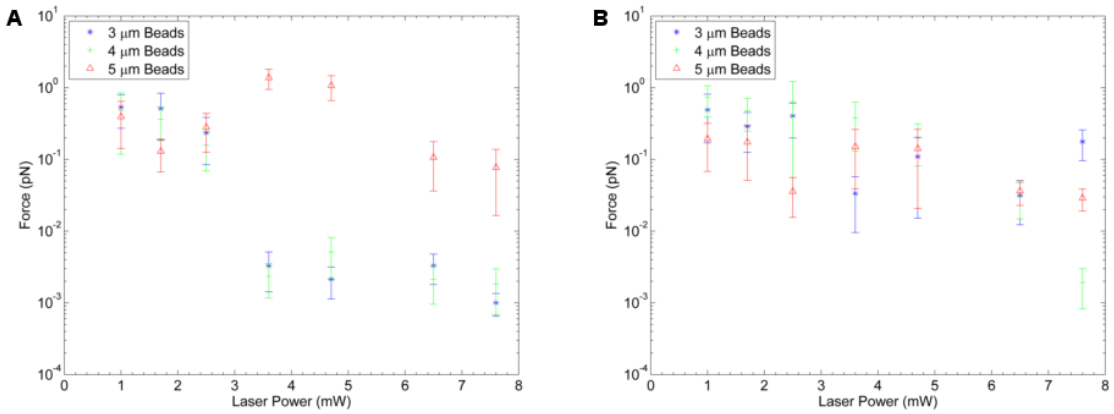

Figure 7.23: Calculated trapping force for natively charged silica beads in mineral oil. A) With and B) without plasmonic enhanced heating.

A seemingly counterintuitive trend is observed when unpatterned lithium niobate substrates are used i.e. the trapping force appears to decline slowly with increasing laser power (Figure 7.23B). Note that as a pyroelectrically induced trap is being used, laser power is synonymous with generated temperature. The implications of this were discussed previously; the increased thermal energy coupled with reduced solvent viscosity increases the uncertainty in particle position as the diffusion coefficient is reduced. No evidence of this uncertainty is observed on the glass control on which this effect should be starker, giving the greater heating efficiency associated with this substrate (discussed in Chapter 4). Thus, only a marginal increase in diffusivity is expected, attributable to the increased thermal energy in the system. The slight decrease in trapping force is somewhat in line with the apparent linear evolution of trap radius with laser power. A faster evolution with time (e.g. cubic, square dependence) would be indicative of a similar relationship

between laser power and electric field. Were this the case, one would expect the confinement to increase with laser power as the increase in electrically controlled trap stiffness is faster than thermal variations. The slow decline in confinement is thus indicative of a situation where the electrically induced trap stiffness evolves at a similar rate as diffusion.

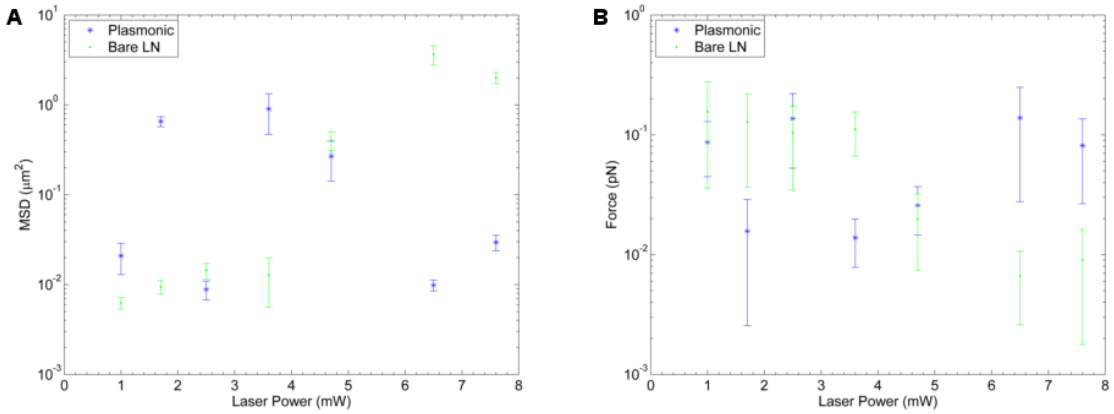

Figure 7.24: Effects of carboxylation on: A) mean squared displacement and B) trapping force for 5 µm silica bead in mineral oil.

For 5 µm beads, carboxylation has little effect on the recorded trapping force once particles have been corralled to the trap centre. Recorded values remain relatively static in the 0.1 pN range (Figure 7.24B). A possible explanation for the relative insensitivity of the MSD and force to the change in laser power is the maximum resolvable force achievable with this technique, which is dictated by the resolution of the equipment used. At worst, particle identification algorithms are only accurate to half a pixel [5]. The image resolution recorded is 0.15625 µm/pixel, thus, particle locations are accurate to 75 nm. Assuming the maximum temperature of the microfluidic system is 350 K, the maximum resolvable force with the imaging system is:

$$F = \frac{3 \times k \times 350\ K}{75 \times 10^{-9}\ m} \tag{7.6}$$

$$F \approx 0.5\ pN \tag{7.7}$$

The maximum forces reported with this technique are of a similar magnitude to this limit (values higher than the maximum can be attributed to improvements in particle localisation made as a result of sub pixel optimisation algorithms). This suggests that the results presented underestimate the actual magnitude of the trapping force as displacements significantly smaller than 75 nm (and improved confinements) cannot be reliably detected.

7.3.4 Dynamically trapped beads

Escape velocity measurements [13], [14] were performed by sinusoidally varying the position of the stage in the x direction in order to quantify the cumulative effects of the discussed electrokinetic phenomena on trapping stability. Maximum escape force is given by the Stokes's drag equation ($F = 6\pi\eta Rv$), where v is the velocity at which bead stops following the laser spot. As $v = \frac{dx}{dt}$, the escape velocity can be estimated by collating positions and times for which bead appears to be in motion to gain an overall trapping force.

Sinusoidal stage variation is approximated by controlling stage acceleration and amplitude. The stage is moved 30 µm from its initial position (i.e. its peak to peak amplitude is 30 µm). Thus, the harmonic variation of stage position and velocity with respect to time is:

$$x(t) = 15\cos(\omega t) \tag{7.8}$$

$$\frac{dx}{dt} = -15\omega\sin(\omega t), \tag{7.9}$$

where ω is $2\pi f$ and f is the frequency of the wave. Maximum velocity occurs at $\sin(\omega t) = 1$, i.e. $v = 15\omega$.

The frequency is verified using fast Fourier transform (FFT) analysis in Matlab to be 0.3847 Hz (2.6 s^{-1}), which increases to 0.4439 Hz (2.25 s^{-1}) in isolated cases. The increase in frequency has little effect on the ability to quantify force using sinusoidal stage variation. A +/- 0.0072 Hz error in the reported frequency is estimated, based on the FFT algorithm using interpolation to increase the number of samples from 200 to 256, such that the number of samples used is given by a power of 2.

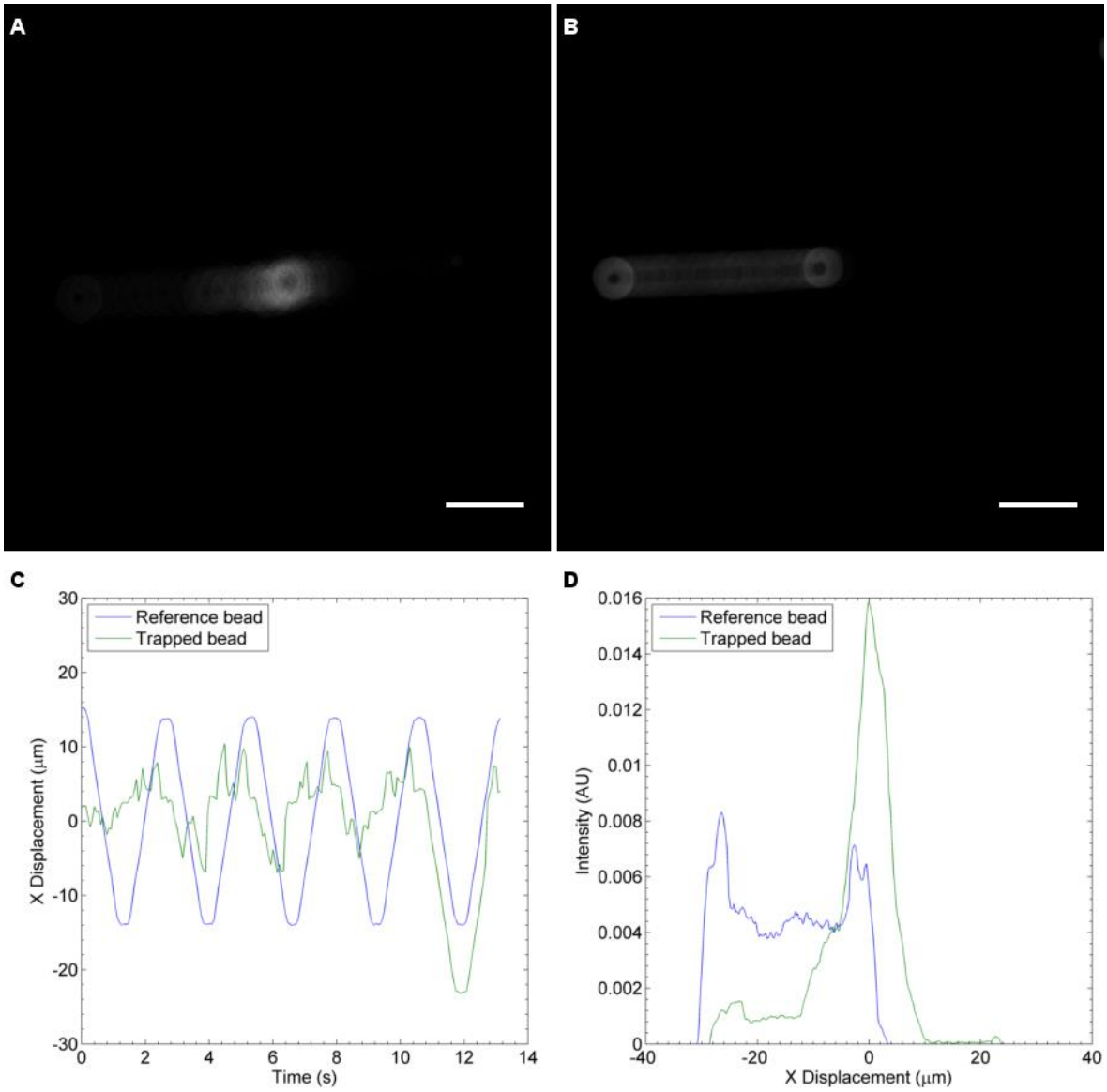

Figure 7.25: Behaviour of 5 μm silica bead in and out of plasmonic enhanced pyroelectric trap. Scale bar is 10 μm. A) z projection of trapped bead motion. B) z projection of reference bead motion which mirrors the movement of the stage. Bead is largely static and remains in the location of the laser spot. C) Position of trapped and reference bead with respect to time (offset has been removed). D) Probability density function of location of reference and trapped bead over 5 sinusoidal cycles.

Figure 7.25 illustrates the behaviour of silica beads with sinusoidal drag force. A and B are projections of the bead for all time points. As the trapped bead is located predominantly at the laser spot (located centrally in the image), the intensity of the bead is at a maximum at this point. The reference bead follows the motion of the stage. As such, the maximum bead intensity is lower, and the bead appears as a line of points, which is its trajectory over the observation period. C shows this information as a graph. The position of the reference bead mirrors the sinusoidal motion of the stage. In contrast, though the time dependent nature of bead motion is observed, the amplitude of the trapped bead is suppressed. D is a probability density function of bead displacement from trap centre. As the reference bead is in motion throughout the entirety of the

observation period, a uniform probability density function is expected. However, peaks are observed at 0 and -30 µm (i.e. maxima and minima of x(t) trace), suggesting that the bead remains at these points for longer periods of time. This is a result of the reduced velocities at the maxima and minima, and is thus dependent on the spatial and temporal resolution of the microscope stage and camera system. Images are recorded at a resolution of 6.4 pixels/µm and 1 frame/0.066 s. Hence, the minimum resolvable speed is 0.15625 µm/0.066 s (1.2 µm/s). Below this speed, beads appear stationary.

The probability density function is used to estimate maximum pyroelectric induced force in the following way. Note that for a perfect trap (constant trap stiffness and instant response time), the probability of observing a bead at the zero point, the position of the laser ($P(x = 0)$), is dependent on the trapping force i.e.

$$P(x = 0) \propto F \tag{7.10}$$

$$P(x = 0) = \frac{n}{N}, \tag{7.11}$$

where n is the number of observations made at $x = 0$, and N is the total number of observations made.

Multiplying this by T (total time) gives the amount of time bead spends in trap:

$$t_{trap} = \frac{n}{N}\, T. \tag{7.12}$$

Similarly, multiplying by T_π (time period for one sinusoidal cycle) gives the amount of time bead spends in trap in one sinusoidal cycle:

$$t_\pi = \frac{n}{N}\, T_\pi. \tag{7.13}$$

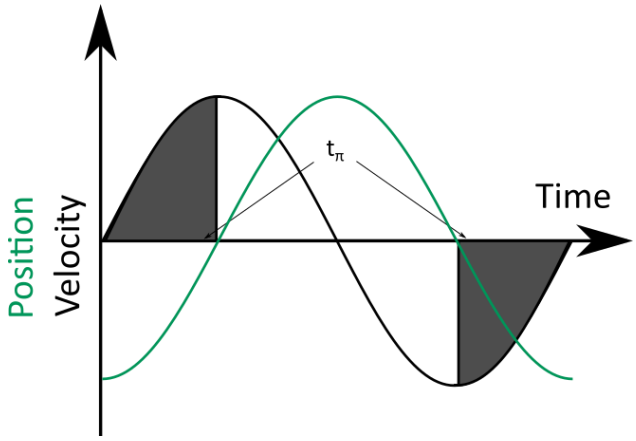

Figure 7.26: Illustration of method to determine escape velocity. Bead is trapped for velocities encapsulated in shaded areas. Intercept of position graphs highlights when bead leaves and returns to trap.

Figure 7.26 offers an illustration explaining the previously stated expressions. The green trace is the relative position of the stage with reference to the laser point and the black trace is its corresponding velocity. The shaded portion of the graph specifies when the bead is trapped i.e. t_π. At a critical velocity, the drag force exceeds the trapping force and the bead motion mirrors that of the stage. Though there are points in the intervening period when the drag force is less than the trapping force, the bead is no longer trapped as it is not coincident with the laser spot; the bead is only trapped when the stage is once again aligned with laser (in the illustrations, where the position=0). Hence, due to the symmetry of the sine curve and the mass of the beads (which dictate that inertial forces are negligible in comparison to viscous forces), the force of the trap is given by:

$$F_{trap} \propto \frac{\mathrm{d}x}{\mathrm{d}t}\Big|_{\frac{t_\pi}{2}}. \tag{7.14}$$

The velocity at $\frac{t_\pi}{2}$ is thus given by:

$$\frac{dx}{dt} = A \sin\frac{(\omega\, t_\pi)}{2} \tag{7.15}$$

$$\frac{dx}{dt} = A \sin\frac{n\pi}{N} \tag{7.16}$$

$$\frac{dx}{dt} = A \sin(P(x=0)\pi). \tag{7.17}$$

Thus, $P(x=0)$ lies in the range:

$$\arcsin\left(\frac{1.2}{15\omega}\right) \leq \frac{P(x=0)}{2} < 0.25, \tag{7.18}$$

$$\frac{P(x=0)}{2} = 0.5. \tag{7.19}$$

The above analysis has treated the probability density function as if it consisted of discrete elements. Though such a function can be recovered (due to the finite spatial and temporal resolution of the image capture system), it is better to consider the probability of finding the bead in a range of positions as trapping does not confine the bead to a singular point; it is free to move for a given distance. For the results presented, 2.5 µm is the maximum possible deviation from the centre of the trap (the radius of the largest bead such that the bead's edge is coincident with the trap centre [15]), i.e.

$$P(-2.5 \leq x \leq 2.5) \approx P(x=0) = \frac{n}{N}. \tag{7.20}$$

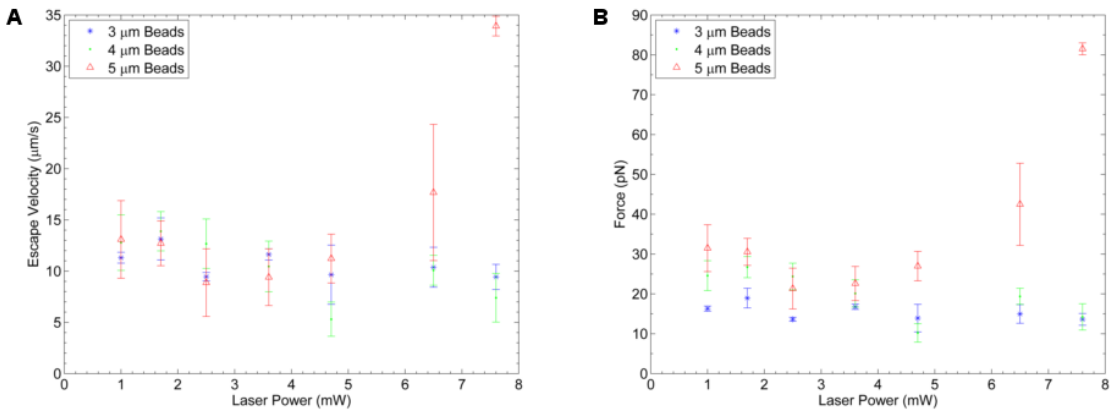

Figure 7.27: Characterisation of overall trapping force for collection of silica beads with plasmonic stimulation. A) Observed escape velocities. B) Corresponding escape force calculated using Stokes's law.

Figure 7.27 shows the escape velocity results obtained from experiments performed using a range of silica beads on plasmonic arrays. For 3 and 4 µm beads, escape velocity bears little relationship to applied laser power. Maximum escape velocity is recorded as ~12 µm/s, corresponding to a total force of 20 pN for 3 µm beads, and 28 pN for 4 µm beads. This estimate is somewhat misleading, since as has previously been mentioned, trapping does not accurately describe the behaviour of these beads at high powers. Though these beads do not remain in one location even when the trap is static, they tend to return to the laser spot provided the motion of the stage does not transport them too far away from their initial position. For 5 µm silica beads, there

appears to be a parabolic relationship between laser power and escape force. The maximum escape force is recorded as 90 pN at the highest laser power used for stimulation.

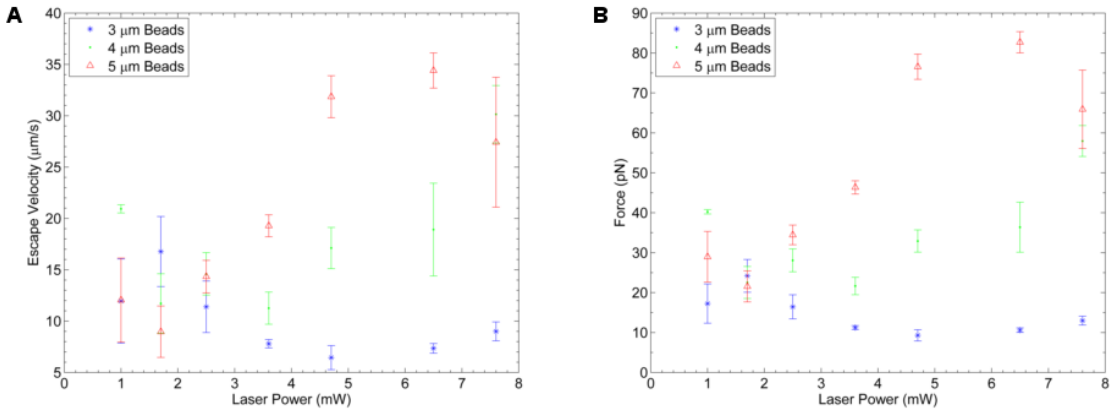

Figure 7.28: Characterisation of overall trapping force for collection of silica beads without plasmonic stimulation. A) Observed escape velocities. B) Corresponding escape force calculated using Stokes's law.

The situation when stimulation is applied on bare lithium niobate mirrors the results of experiments already discussed, in the sense that the oscillatory motion of 3 and 4 µm beads is removed and trapping behaviour is once again recovered (Figure 7.28). The cumulative trapping force appears to be size dependent as values of 90, 65, and 15 pN are calculated for 5, 4, and 3 µm beads, respectively. In addition, trapping of 5 µm beads is improved in comparison to when plasmonic enhancement is used. Though the maximum escape forces calculated are similar with and without plasmonic enhancement, the intensity of laser illumination required to create the strongest traps is reduced when stimulation is performed without plasmonic enhancement.

This improved capability to trap against a flow when using bare LN can be explained with reference to the operation regimes described in Chapter 5. The electrothermal flow which is responsible for long range attraction of beads has a deleterious effect on stable trapping as it overwhelms the dielectrophoresis. As DEP is size dependent, the onset of this condition is delayed when larger particles are used. The slight drop in escape force between 6 and 7 mW is perhaps indicative of the increasing dominance of electrothermal effects. Carboxylation appears to improve trapping efficiency (Figure 7.29). Though the maximum escape forces recorded with and without plasmonic enhancement are of a similar magnitude, these are recorded with lower powers when plasmonic enhancement is used. The reveal of a drop in escape velocity suggests trapping force does not rise indefinitely, as secondary thermal effects begin to affect trap stiffness.

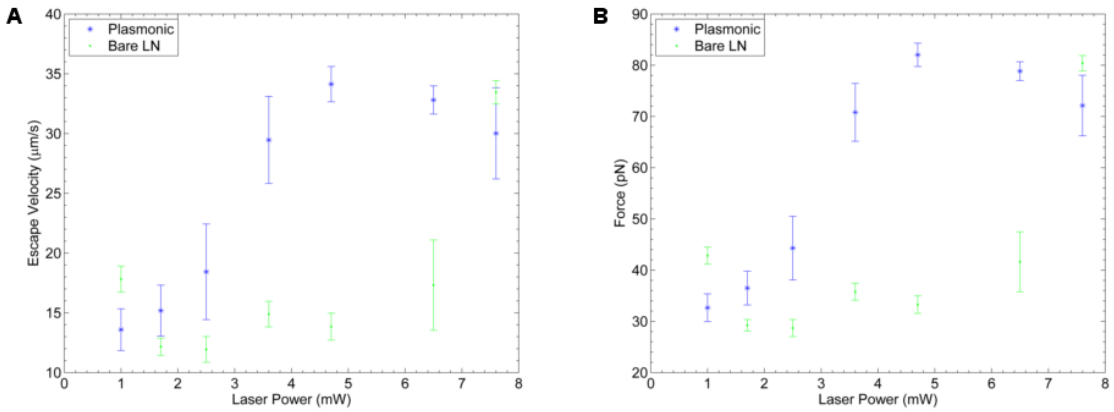

Figure 7.29: Characterisation of overall trapping force for 5 µm carboxylated silica beads with and without plasmonic stimulation. A) Observed escape velocities. B) Corresponding escape force calculated using Stokes's law.

7.4 Conclusion

In this chapter, three different experimental/analytical approaches for characterising the pyroelectric induced force on a particle have been considered. Taking an overview of the MSD of the entire kinetic process highlights distinct trapping and transportation phases of motion. The oscillatory motion of small beads at high powers indicates that different forces are in control of motion in each phase. The attraction force evolves quicker than the trapping force (located at the laser). Thus, though smaller beads are unable to remain at the trap centre, they continually return to this point. Hence, oscillatory motion is observed. The trapping force is dielectrophoretic in origin and is thus size dependent. The oscillatory motion is thus not observed with larger beads, as the trapping force is sufficient to hold them in place. The behaviour of beads in almond oil further suggests dielectrophoretic control of the trapping force; by changing solvent permittivity the trap force is weakened, thus, neutral beads are repelled although similar objects are attracted to the laser in mineral oil. Attraction is recovered with carboxylated particles. The overall dynamic profile of carboxylated beads in mineral oil appears similar to neutral beads. The mass of the beads studied indicate that inertial forces are negligible (particularly for the accelerations considered) and Stokes's drag equations can be used to estimate force associated with particle. The speed with which silica beads approach the laser spot (~10^2 µm/s), suggests that the maximum attraction force (recorded at the point of closest approach to the laser) is on the order of 0.1 nN.

Using the MSD of beads in a static trap to quantify the trapping force gives values on the order of 0.1 pN. This value is much less than the magnitude calculated for attraction force, further

suggesting both actions can be considered independently. The viscosity of the solvents used is such that this trapping force does not lead to substantial particle displacements. Note that the slow movement of particles means that this experiment is conducted close to the detection limit of the imaging system used. It is therefore possible that the values calculated represent an underestimation of the actual trapping force. Poor correlation between MSD and laser power is perhaps indicative of operation close to detection limit as the results recorded become more representative of instrumentation error.

Finally, using an escape velocity style measurement to quantify the combined trap force in a dynamic environment suggests forces of 10 pN are required to dislodge particles from the trap. Note that the counterintuitive weakening of the trap noticed when plasmonic enhancement is used, is now observed with 5 µm (the manifestations of this are less drastic as trapping is still possible unlike with smaller beads).

The experiments suggest trapping forces in the range of pN are possible using the technique. In some instances, a deleterious effect on the ability to trap when plasmonic enhancement is used is observed. Though this is more evident using smaller beads, escape velocity measurements suggest that a similar (less pronounced) effect occurs with larger beads. In these situations, the advantage of plasmonic enhancement is the ability to control motion in larger areas of the microfluidic chamber, enabling high throughput manipulation. The addition of carboxyl groups improves trapping suggesting that the deleterious effects of plasmonic enhancement are not universal. Beads smaller than those used in the experiments detailed above can be controlled provided their surface charge density is sufficiently large.

7.5 References

[1] N. Tarantino, J. Tinevez, E. F. Crowell, B. Boisson, R. Henriques, M. Mhlanga, F. Agou, A. Israël, and E. Laplantine, “TNF and IL-1 exhibit distinct ubiquitin requirements for inducing NEMO–IKK supramolecular structures,” *J. Cell Biol.*, vol. 204, no. 2, pp. 231–245, 2014.

[2] M. J. Saxton, “Modeling 2D and 3D diffusion.,” in *Methods in Membrane Lipids*, vol. 400, Humana Press, 2007, pp. 295–321.

[3] X. Michalet, “Mean square displacement analysis of single-particle trajectories with localization error: Brownian motion in an isotropic medium.,” *Phys. Rev. E. Stat. Nonlin. Soft Matter Phys.*, vol. 82, no. 4 Pt 1, p. 41914, 2010.

[4] Y. Lu, Y. Huang, J. A. Yeh, and C. Lee, “Controllability of Non-Contact Cell Manipulation by Image Dielectrophoresis (iDEP),” *Opt. Quantum Electron.*, vol. 37, no. 13–15, pp. 1385–1395, 2006.

[5] J. Crocker and D. G. Grier, “Methods of Digital Video Microscopy for Colloidal Studies,” *J.*

Colloid Interface Sci., vol. 179, no. Ccd, pp. 298–310, 1996.

[6] S. Maruo, “Manipulation of Microobjects by Optical Tweezers,” in *Microfluidic Technologies for Miniaturized Analysis Systems*, S. Hardt and F. Schönfeld, Eds. New York: Springer Science, 2007, pp. 275–314.

[7] A. Jamshidi, P. J. Pauzauskie, P. J. Schuck, A. T. Ohta, P. Chiou, J. Chou, P. Yang, and M. C. Wu, “Dynamic manipulation and separation of individual semiconducting and metallic nanowires,” *Nat. Photonics*, vol. 2, pp. 86–89, 2008.

[8] A. T. Ohta, P. Chiou, T. H. Han, J. C. Liao, U. Bhardwaj, E. R. B. Mccabe, F. Yu, R. Sun, and M. C. Wu, “Dynamic Cell and Microparticle Control via Optoelectronic Tweezers,” *J. Microelectromechanical Syst.*, vol. 16, no. 3, pp. 491–499, 2007.

[9] P. Chiou, A. T. Ohta, and M. C. Wu, “Toward all optical lab-on-a-chip system : optical manipulation of both microfluid and microscopic particles,” *Proc. SPIE*, vol. 5514, pp. 73–81, 2004.

[10] B. Lukic, S. Jeney, Z. Sviben, A. J. Kulik, E. L. Florin, and L. Forro, “Motion of a colloidal particle in an optical trap,” *Phys. Rev. E - Stat. Nonlinear, Soft Matter Phys.*, vol. 76, no. 1, pp. 1–9, 2007.

[11] G. G. Volpe, “Simulation of a Brownian particle in an optical trap,” *Am. J. Phys.*, vol. 81, no. 3, p. 224, 2013.

[12] N. G. Walter, Ed., *Single Molecule Tools, Part B: Super-Resolution, Particle Tracking, Multiparameter and Force Based Methods*. Elsevier, 2010.

[13] A. A. M. Bui, A. B. Stilgoe, N. Khatibzadeh, A. Timo, M. W. Berns, and H. Rubinsztein-dunlop, “Escape forces and trajectories in optical tweezers and their effect on calibration,” *Opt. Express*, vol. 23, no. 19, pp. 24317–24330, 2015.

[14] K. Visscher, S. P. Gross, and S. M. Block, “Construction of Multiple-Beam Optical Traps with Nanometer-Resolution Position Sensing,” *IEEE J. Sel. Top. Quantum Electron.*, vol. 2, no. 4, pp. 1066–1076, 1996.

[15] H. Felgner, O. Mu, and M. Schliwa, “Calibration of light forces in optical tweezers,” *Appl. Opt.*, vol. 34, no. 6, pp. 977–982, 1995.

8 Conclusion

Summary

A summary of the key findings of the thesis and informed speculation on the direction of future work is presented. Also included, where possible, are illustrative results explaining why the identified future directions could be implemented.

8.1 Summary

In this thesis, the pyroelectric properties of lithium niobate have been combined with plasmonic heating to enable microfluidic manipulation. In contrast to other optical manipulation techniques, microfluidic manipulation can be achieved with modest intensities, and without an external electrical signal source biasing the substrates. In comparison to the photovoltaic effect, thermally generated pyroelectric fields appear instantaneously meaning that dynamic reconfiguration of particles is possible. In addition, unlike photorefractive optoelectronic tweezing, no additional doping is required to allow control of the pyroelectric effect with visible wavelengths; the use of plasmonic enhancement enables the selection of operational wavelengths distinct from those dictated by the intrinsic properties of the pyroelectric crystal selected.

To verify the existence of plasmonic heating, fluorescent thermometry was performed using a molecular rotor. Using this technique, the dependence on the magnitude of heat generated on the array density of plasmonic structures is confirmed. Though the technique as implemented is only able to elucidate broader trends, it is nevertheless useful in confirming some of the theoretical assumptions made on the nature of plasmonic heat generation.

Numerical models of electrokinetic behaviour are created based on the theoretical considerations of pyroelectric field generation. The results of these simulations suggest the coexistence of multiple electrokinetic phenomena whose effects are controlled by parameters such as incident laser power, particle polarisability, and surface charge. The simulations also dictate the solvent environment required to ensure the generation of a pyroelectric field sufficient for electrokinetic manipulation.

Electrokinetic function with plasmonic enhanced pyroelectric is demonstrated by arbitrarily patterning shapes in a range of microfluidic environments using electrically conducting and insulating particles. These experiments also provide practical proof of some of the conjectures

made as a result of numerical simulations, mainly the need for non-polar, insulating solvents for pyroelectric field generation. This arbitrary patterning is useful for optofluidic fabrication applications.

A range of experiments based on particle tracking are used to characterise the behaviour of beads undergoing pyroelectric motion. The dominant mechanisms used to achieve the effects described appear to be a combination of DEP and electrothermal convection. Though surface charge on particles is not required, this was found to aid stable trapping of electrically insulating and non-polar microparticles (particularly of < 5 µm). Close to the solid liquid interface, these forces combine constructively to enable long range transport, and stable trapping of microparticles at a central location.

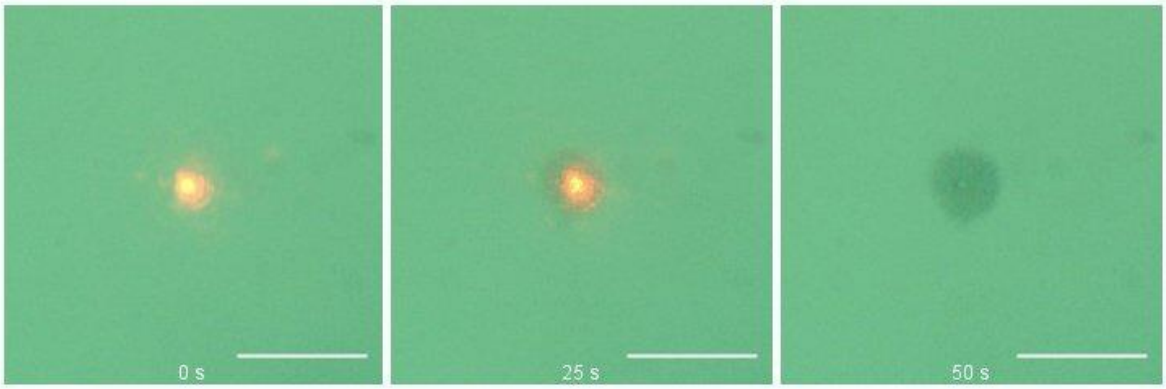

Figure 8.1: Timelapse image of pyroelectric induced attraction of 540 nm silica beads. Carboxylation aids trapping of smaller beads. Scale bar is 50 µm

8.2 Further Work

A key feature of the described technique is the microfluidic environment required to enable particle manipulation. Electrically insulating, non-polar fluids are required to ensure the generated electric field persists for a long enough period to allow successful particle manipulation. This prerequisite limits some of the biological applications the technique can be employed with. Though solvents such as mineral oil are used in specific biological applications (e.g. mineral oil with DNA), in general the non-physiological environment places undue stress on cells and biomolecules, causing them to act atypically, and as such, are often times avoided (so as not to influence functions of interest). Biologically relevant solvents are typically several orders of magnitude more conductive than the liquid dielectrics used for demonstration [1]. As such, the

major avenue for further investigation is in the development of methods to allow the use of this technique in environments other than the ones employed in this thesis.

A possible solution is in the use of frequency modulated laser stimulation instead of continuous wave illumination. Careful selection of the laser's repetition rate (linking this to the thermal relaxation time) enables the generation of harmonic temperature fields [2]. Pulsed illumination can subsequently be used to create persistent electric fields in more polar, conductive solvents, provided that the frequency of the temperature field is comparable to the charge relaxation time of the pyroelectric substrate. As well as increasing the range of usable solvents which support this technique, such a scheme might prove advantageous when the ease of use of is considered; the frequency of operation can be selected to maximise/minimise certain electrokinetic effects, which need not all occur simultaneously if they prove to be a hindrance.

The use of plasmon-enhanced pyroelectrics for the direct control of fluids [3] (droplet and digital microfluidics), suggest applications for the technique where the limited (at present) range of solvents which can support microfluidic manipulation in the manner discussed in the thesis is irrelevant. Evidence of pyroelectric field effects on fluids was observed incidentally during the fabrication process, which necessitated the implementation of a discharge time required to allow the lithium niobate substrate to neutralise before the application of the second layer of PMMA resist. This effect can be used in a more structured way for the control of picolitre quantities of fluids. Droplet microfluidics, specifically for the control of water in oil emulsions with dielectrophoretic forces, can be employed to move discrete volumes containing biologically relevant material in environments proven to support pyroelectric field generation.

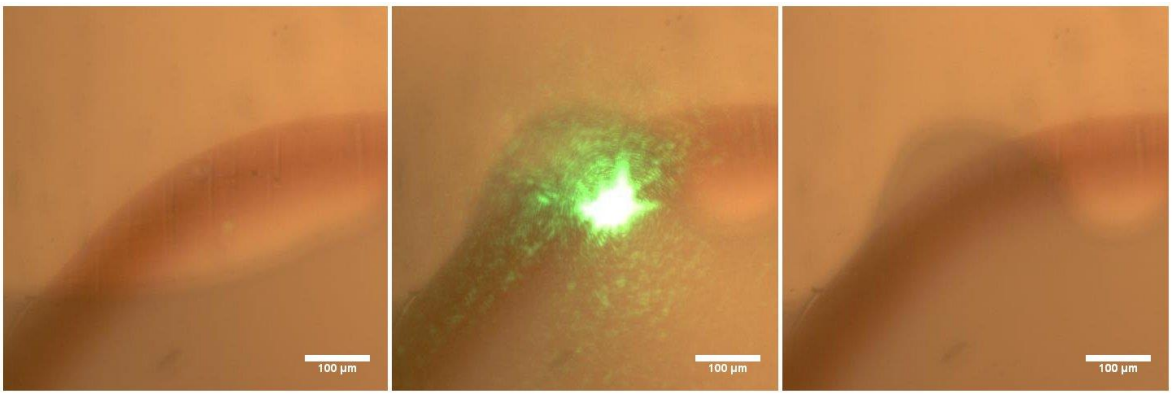

Figure 8.2: Electrowetting type function of almond oil as a result of stimulating gold colloid. Reduced plasmon resonance (525 nm compared to 633 nm used elsewhere) necessitates a change in excitation wavelength.

Though careful engineering of the structure of plasmonic entities has been employed throughout this thesis, this need not be the case depending on the degree of wavelength discrimination required. The single most important parameter in ensuring the ability for plasmonic thermal generation to create enough heat for microfluidic manipulation is the pitch/density of arrays. Thus, any plasmonic structure can theoretically be used for enhancement of the pyroelectric effect provided the density is large enough to generate appreciable temperatures. This fact potentially simplifies the fabrication process, as electron-beam fabrication is not necessarily required in all cases. Figure 8.3 demonstrates pyroelectric manipulation with the stimulation of colloidal gold. The laser is loosely focussed, thus optical density is greatly reduced. The two dimensional array associated with planar structures is replaced by a quasi-3D array which improves heat generation.

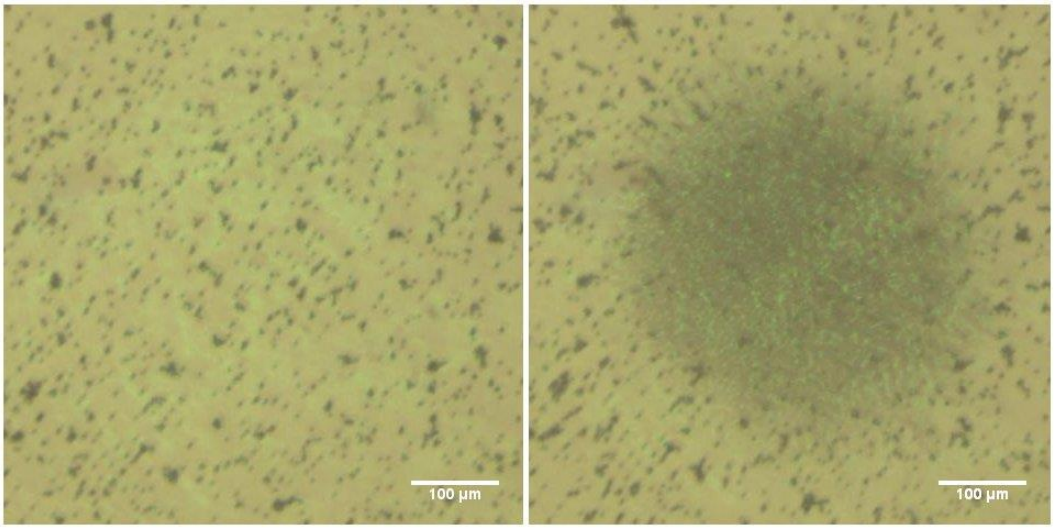

Figure 8.3: Assembly of silica beads in mineral oil as a result of unfocussed laser stimulation of gold colloids. Reduced plasmon resonance (525 nm compared to 633 nm used elsewhere) necessitates a change in excitation wavelength.

A similar effect is observed on isolated occasions when high power broadband illumination is used on gold colloids. Though the absorption at a specific resonant wavelength may be reduced, heat power in general increases as it is due to the absorption properties of the plasmonic structure over a range of wavelengths i.e.

$$Q = \int \sigma_{\mathrm{abs}}(\lambda) I(\lambda) d\lambda, \tag{8.1}$$

where Q is heat power, σ_{abs} is the wavelength dependent absorption cross section, and I is the intensity of illumination at a specific wavelength.

The ability to manipulate particles with broadband plasmonic excitation enables easier realisation of reconfigurable electrodes using standard office equipment (digital projectors), instead of more specialised optics (spatial light modulators).

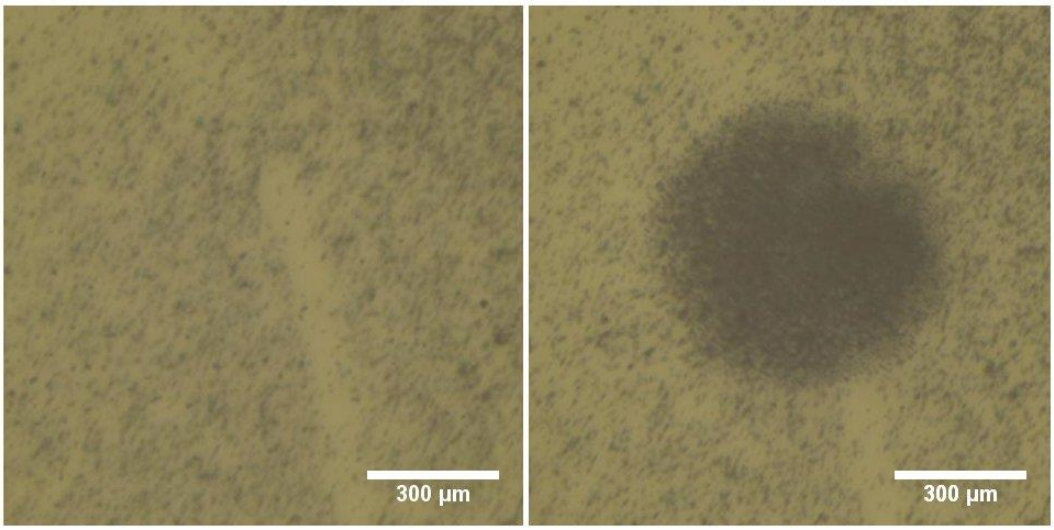

Figure 8.4: Assembly of silica beads in mineral oil as a result of stimulation with high intensity white light source. The size of the bead cluster is dictated by the focussing objective used for stimulation.

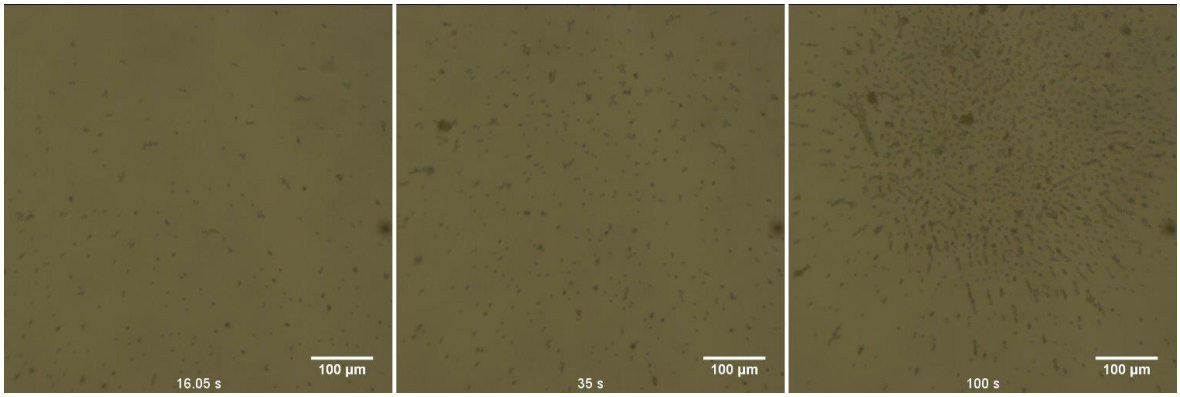

Figure 8.5: Time lapse image of bead assembly with white light stimulation. Note uniform background as no laser stimulation is used. Following stimulation, silica beads populate the frame.

Finally, the microfluidic manipulation demonstrated has been performed using pyroelectric crystals. Though the mechanical robustness of these materials make them easy to handle, they possess other qualities which complicate the fabrication process e.g. the thickness dependent capacity makes fabrication of plasmonic structures comparatively more difficult; their comparatively large refractive index limits the minimum plasmon resonance (for instance, it is more difficult to reliably fabricate plasmonic structures resonant around 500 nm). A possible solution is the replacement of ceramic pyroelectrics with polymers. Thin film pyroelectric

polymers (e.g. PVDF, and its copolymers [4][5]) deposited on glass substrates, can be used as an electronically active superstrate playing a similar role to amorphous silica on ITO in optoelectronic tweezers. Separating the pyroelectric layer from the glass substrates enables the ability to control thickness (by spin coating for example), and means finer control of electrical properties (e.g. capacitance, resistance). At the same time, electron beam lithography of plasmonic structures becomes more trivial. Alternatively, planar plasmonic fabrication can be ignored entirely in favour of the use of colloidal particles. Plasmonic enhancement occurs by effectively doping the polymer with a predetermined concentration of materials when it is in a liquid state. The structure of the thin film following deposition and annealing subsequently determines the distribution of colloidal plasmonic particles.

8.3 Conclusion

The above is a summary of potential avenues for further study based largely on observations encountered in the course of investigation. These have focussed on technical improvements, and extensions to make a more comprehensive platform for microfluidic manipulation using pyroelectric materials. Even without these improvements, the technique can be used readily for a range of purposes. For instance, the arbitrary patterning (highlighted in Chapter 6) can be employed in optofluidic fabrication schemes and localised concentration of particles can be used to improve sensitivity of biosensors. Plasmon enhanced-pyroelectric manipulation is thus a complementary addition to the already established optical manipulation techniques.

8.4 References

[1] R. Pethig, “Review article-dielectrophoresis: status of the theory, technology, and applications.,” *Biomicrofluidics*, vol. 4, no. 2, pp. 1–35, Jan. 2010.

[2] P. Berto, M. S. A. Mohamed, H. Rigneault, and G. Baffou, “Time-harmonic optical heating of plasmonic nanoparticles,” *Phys. Rev. B*, vol. 90, no. 3, p. 035439, Jul. 2014.

[3] P. Ferraro, S. Grilli, L. Miccio, and V. Vespini, “Wettability patterning of lithium niobate substrate by modulating pyroelectric effect to form microarray of sessile droplets,” *Appl. Phys. Lett.*, vol. 92, no. 21, p. 213107, 2008.

[4] S. H. Bae, O. Kahya, B. K. Sharma, J. Kwon, H. J. Cho, B. Ozyilmaz, and J. H. Ahn, “Graphene-P(VDF-TrFE) multilayer film for flexible applications,” *ACS Nano*, vol. 7, no. 4, pp. 3130–3138, 2013.

[5] M. I. Akcan and C. Topacli, “Pyroelectric and dielectric properties of spin-coated thin films

of vinylidene fluoride- Trifluoroethylene copolymers," *Polym. Int.*, vol. 50, no. 7, pp. 835–840, 2001.

Appendix A Further plasmonics

A.1 Surface plasmon resonance

Surface plasmon resonance is a coupled oscillation of a metal's plasmons to photonic excitation confined to the interface between the metal and a dielectric. The confinement of the oscillation to the boundary suggests some form of waveguiding, hence, the excitation necessary for achieving the surface plasmon resonance effect are particular solutions for the Helmholtz equation [1]:

$$\nabla^2 E + k_0^2 \varepsilon E = 0, \tag{A.1}$$

where k_0 is the wave-vector of free space defined as $\frac{\omega}{c}$, and c is the speed of light in vacuum. A one-dimensional plane wave approximation can be used to describe electromagnetic wave excitation. In the geometry displayed in Figure A.1, the interface lies at the z=0 coordinate. The electromagnetic wave is polarised in the z direction, propagates in the x direction and is spatially invariant in the in-plane y direction, thus the general mathematical description of this plane wave with time harmonic dependence is [1]:

$$\boldsymbol{E}(\boldsymbol{x}, \boldsymbol{y}, \boldsymbol{z}) = E\hat{\boldsymbol{z}} e^{-i(\beta x + \omega t)}, \tag{A.2}$$

where β is the component of the wave vector in the direction of wave propagation i.e. $\beta = k_x$.

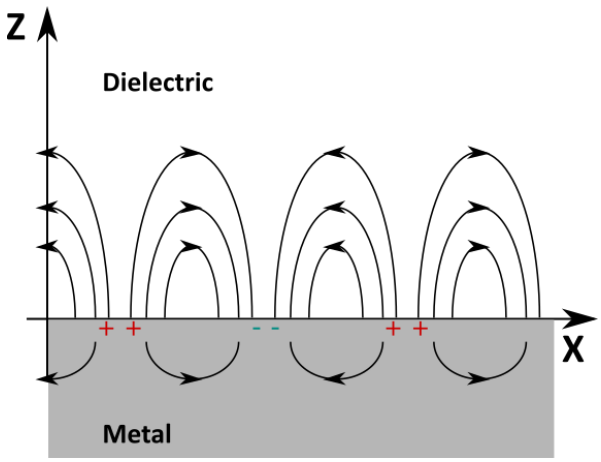

Figure A.1: Schematic illustration of geometry and conditions for SPR [2]. Image depicts charge distribution and electric field lines from propagating surface plasmon.

Due to the coupling between electric and magnetic fields as defined by Maxwell's equations, solutions to this equation are of two forms; transverse magnetic (TM or p) wave modes where electromagnetic field components, $E\hat{\boldsymbol{x}}$, $E\hat{\boldsymbol{z}}$ (electric field), and $H\hat{\boldsymbol{y}}$ (magnetic field), are non-zero, and transverse electric (TE or s) wave modes where electromagnetic field components, $H\hat{\boldsymbol{x}}$, $H\hat{\boldsymbol{z}}$, and $E\hat{\boldsymbol{y}}$, are non-zero. Analysis of the necessary boundary conditions (continuity of magnetic and perpendicular electric fields at the metal dielectric interface) shows that no surface modes exist for TE wave modes; surface plasmon resonance is only possible with TM wave modes [1].

The dispersion relation for a surface plasmon polariton is derived by considering the boundary conditions for TM wave modes and is written as [1]:

$$\beta = k_0 \sqrt{\frac{\varepsilon_{\text{metal}}\varepsilon_{\text{dielectric}}}{\varepsilon_{\text{metal}} + \varepsilon_{\text{dielectric}}}} \tag{A.3}$$

The wave vector for an SPP highlights a further characteristic of surface plasmon resonance. To excite an SPP with a photon, the frequency and momentum of each wave need to be matched i.e. a coincidence of the wave vectors is required at the surface of the metal (Figure A.2). The dispersion relation for a photon in a dielectric is given by [1]:

$$k_{\text{dielectric}} = k_0 \sqrt{\varepsilon_{\text{dielectric}}} \tag{A.4}$$

From (A.4) it is clear that a photon cannot directly excite a surface plasmon since $\beta \neq k_{\text{photon}}$ (due to the dependence of β on the dielectric function of metals defined previously, $\beta > k_{\text{photon}}$).

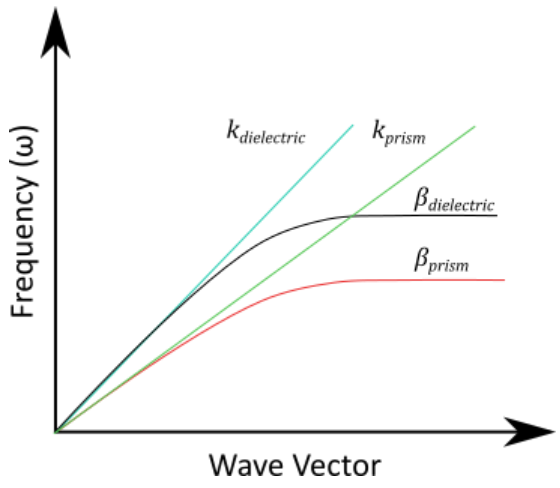

Figure A.2: Dispersion relations of photons and surface plasmons [1]. Photonic excitation of a metal's surface plasmon can only be achieved when the wave vectors resonantly match (as with the wave vector of a photon in a prism coupler

and the plasmon at metal-dielectric interface). Note, photonic excitation of a surface plasmon is not possible when the dielectric interface is the same as the dielectric medium through which the photon travels

Surface plasmon resonance requires coupling through an intermediary dielectric to match the phase of the plasma oscillations to that of the incident light. Often times a prism with an electrical permittivity higher than the dielectric medium at whose interface the surface plasmon polariton is required is used. The dispersion relation for the prism, and the requisite conditions for resonant coupling are:

$$k_{\text{prism}} = k_0\sqrt{\varepsilon_{\text{prism}}} \tag{A.5}$$

$$\beta = k_{\text{prism}} \sin\theta, \tag{A.6}$$

where θ is the angle the prism-refracted ray makes with the normal of the surface of propagation ($k_{\text{prism}} \sin\theta$ is the component of the photon's wave vector in the prism in the direction of SPP propagation). For the same reasons a coupling medium is necessary (i.e. the need for phase-matching), SPPs cannot be excited at the interface between the prism and the metal. Thus two coupling schemes exist, illustrated in Figure A.3; the Otto configuration in which the metal dielectric interface is sandwiched by the base of the prism [1], and the Kretschmann configuration in which the metallic thin film is deposited directly onto the prism and SPPs propagate on the opposing metal surface [1].

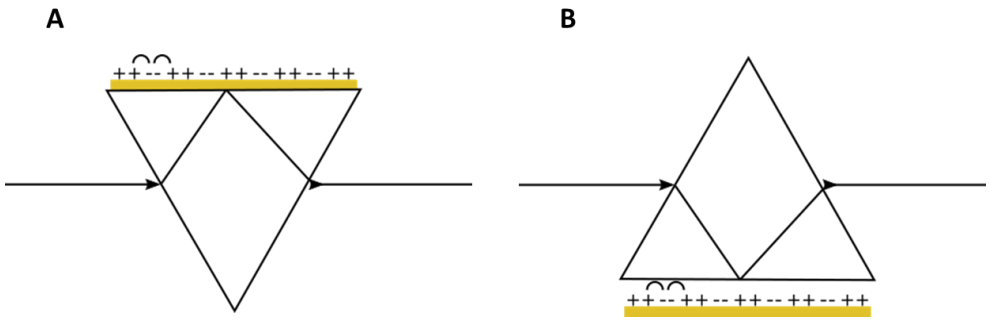

Figure A.3: : Coupling geometries for SPR [1]. A) Kretschmann configuration. B) Otto Configuration. Phase matching of light wave to metal's surface plasmon is achieved by exciting with an evanescent wave.

A.2 Plasmonic heating using pulsed illumination

When plasmonic nanostructures are illuminated by pulses on the order of nanoseconds, the uniform temperature approximation is invalidated, and internal energy transfer processes need to be considered, to gain an accurate estimate of the generated temperature. Broadly speaking, temperature generation from a metallic nanoparticle is completed in three sequential stages [3],

[4]. First, a fraction of the incident photonic excitation is absorbed by the free electrons of the excited metals. The energy of the electron gas reaches a Fermi-Dirac distribution within ~100 fs of initial excitation. This process creates an internal non-equilibrium state due to the energy mismatch between the electron gas and the encompassed metallic volume. The second stage of temperature generation addresses this as the electron gas is cooled through collisions with the phononic lattice leaving a nanoparticle with uniform internal temperature (a process which is completed in ~2 ps). Finally, the temperature of the nanoparticle decays to its steady state through diffusion to the surroundings (the timescale of this process has been discussed previously). From this consideration of internal processes, it is apparent that the maximum nanoparticle temperature is reached sometime during the intermediary energy transfer stages, and that at steady state, the surrounding environment acts as a heatsink for the metal. The maximum temperature increase is stated as [3],

$$\delta T_{\mathrm{NP}}^{0} = \frac{\sigma_{\mathrm{abs}} F}{V \rho_{\mathrm{NP}} C_{p_{\mathrm{NP}}}}, \tag{A.7}$$

where F is the fluence i.e. intensity/frequency and V is the volume of the nanoparticle.

A.3 References

[1] S. A. Maier, *Plasmonics: Fundamentals and Applications*. Springer Science, 2007.

[2] K. A. Willets and R. P. Van Duyne, “Localized surface plasmon resonance spectroscopy and sensing.,” *Annu. Rev. Phys. Chem.*, vol. 58, pp. 267–97, Jan. 2007.

[3] G. Baffou and R. Quidant, “Thermoplasmonics: using metallic nanostructures as nanosources of heat,” *Laser Photon. Rev.*, vol. 17, pp. 1–17, 2013.

[4] M. L. Brongersma, N. J. Halas, and P. Nordlander, “Plasmon-induced hot carrier science and technology,” *Nat. Nanotechnol.*, vol. 10, no. 1, pp. 25–34, 2015.

Appendix B Theory

B.1 Derivation of polarisability of sphere

The polarisability of a sphere gives mathematical origins of the Claussius-Mossotti factor in dielectrophoresis, as well as the localised electric field enhancement in LSPR. As stated in Chapter 2, a quasi-static approximation is made such that the polarisability of the sphere can be derived using Laplace's equation. The geometry of the problem is depicted in Figure B.1. Though a fluid medium is stated in Figure B.1, this can be generalised to a dielectric medium when considering the origins of localised electric field enhancement in LSPR.

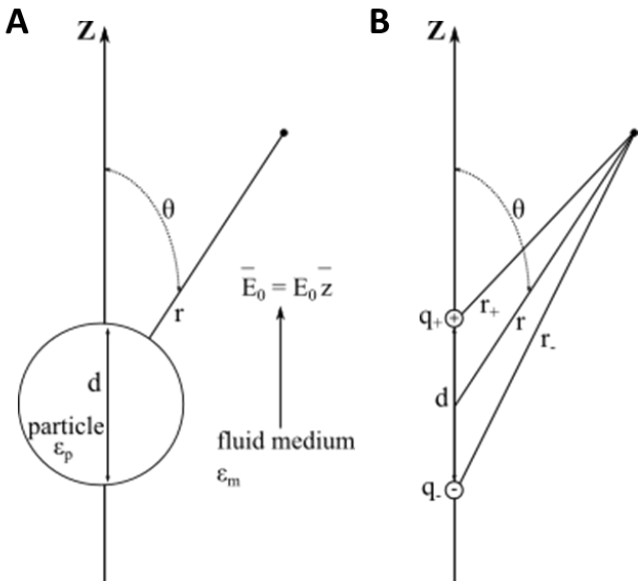

Figure B.1: Geometry for calculating polarisability of sphere. A) Sphere in electric field in a dielectric fluid. B) Equivalent dipole for calculating the effective dipole moment

The dipole moment of a sphere can be derived by considering the effect a sphere of permittivity, ε_{p}, has on the electric field of the surrounding medium of permittivity, ε_{m}, as illustrated in Figure B.1A. As the sphere has axial symmetry, the electric field is described in polar form as a function of radial coordinate, r, and polar angle, θ. The electric field defined is uniform and is consequently divergence and curl free [1]. As such, it can be shown that the electric field can be written as a series of electric potentials which satisfy Laplace's equation. These potentials are [1]:

$$\phi_1 = -E_0 r\cos\theta + \frac{A\cos\theta}{r^2}, \qquad r > \frac{d}{2} \tag{B.1}$$

$$\phi_2 = -Br\cos\theta\,, \qquad r < \frac{d}{2}, \tag{B.2}$$

where ϕ_1 is the potential outside the sphere, ϕ_2 is the potential inside the sphere, and A and B are unknown coefficients whose value can be determined (after imposing appropriate boundary conditions i.e. continuity of electrostatic potential and continuity of normal displacement flux density at the interface between the sphere and immersed medium) to be [1]:

$$A = \frac{\varepsilon_\mathrm{p} - \varepsilon_\mathrm{m}}{\varepsilon_\mathrm{p} + 2\varepsilon_\mathrm{m}} R^3 E_0 \tag{B.3}$$

$$B = \frac{3\varepsilon_\mathrm{m}}{\varepsilon_\mathrm{p} + \varepsilon_\mathrm{m}} E_0, \tag{B.4}$$

where R is the radius of the sphere (i.e. $R = \frac{d}{2}$).

The potential outside the sphere can be thought of as the sum of the electrostatic potentials of the applied electric field with the electrostatic potential induced by the sphere (which is considered to be a dipole). Using Coulomb's law and the superpositioning principle, the potential induced by the equivalent dipole (with geometry defined as in Figure B.1B) is [1]:

$$\phi = \frac{q}{4\pi\varepsilon_\mathrm{m} r_+} - \frac{q}{4\pi\varepsilon_\mathrm{m} r_-}. \tag{B.5}$$

The relationship between r and r_+/r_- is given by simple geometry as [1],

$$\frac{r}{r_\pm} = \left[1 + \left(\frac{d}{2r}\right)^2 \mp \frac{d}{r}\cos\theta\right]^{-\frac{1}{2}}. \tag{B.6}$$

Thus, using a Maclaurin series expansion to first order, the induced dipole potential can be written as [1],

$$\phi = \frac{p\cos\theta}{4\pi\varepsilon_\mathrm{m} r^2}. \tag{B.7}$$

The effective dipole moment can thus be defined in terms of the particle's properties by equating the general form of the induced dipole potential to that calculated using the dipole charges as [1],

$$p = 4\pi\varepsilon_\mathrm{m} A \tag{B.8}$$

$$p = 4\pi\varepsilon_{\mathrm{m}} \frac{\varepsilon_{\mathrm{p}} - \varepsilon_{\mathrm{m}}}{\varepsilon_{\mathrm{p}} + 2\varepsilon_{\mathrm{m}}} R^3 E_0. \tag{B.9}$$

B.2 Charge density and surface potential

The double layer is electrically equivalent to a parallel plate capacitor because of the separation of charges. The potential drop across this layer can theoretically be calculated as follows [2]:

$$Q = qA = C \cdot \psi \tag{B.10}$$

$$C = \frac{\varepsilon A}{d} \tag{B.11}$$

$$\psi = \frac{qA}{C} = \frac{qAd}{\varepsilon A} = \frac{qd}{\varepsilon}, \tag{B.12}$$

where, q is the surface charge density, ε is the absolute permittivity of the liquid medium, A is the area of the surface, and d is the double layer thickness

In practice, the double layer thickness is not known, and the potential has to be calculated using elementary Coulombic interactions. The electrical potential (ψ) at a distance x away from the surface can be calculated using Poisson's equation as,

$$\frac{d^2\psi}{dx^2} = \frac{\rho}{\varepsilon}. \tag{B.13}$$

ρ is the volume charge density in the liquid which is dependent on the thermal motion of ions. These ions thus follow a Boltzmann distribution as described below [3]:

$$n_+ = n_0 \exp\left[\frac{-ze\psi}{kT}\right] \tag{B.14}$$

$$n_- = n_0 \exp\left[\frac{+ze\psi}{kT}\right], \tag{B.15}$$

where n_+ and n_- are the distributions of positive and negative ions respectively, n_0 is the bulk concentration of ions, z is the valence of the ionic species, e is the charge of an electron, k is Boltzmann's constant and T is the temperature in the liquid.

The volume charge density for a symmetric electrolyte (i.e. positive ions and negative ions have equal valence) is thus given as [3]:

$$\begin{aligned}\rho &= ze(n_+ - n_-)\\ &= zen_0\left(\exp\left[\frac{-ze\psi}{kT}\right] - \exp\left[\frac{+ze\psi}{kT}\right]\right)\\ &= 2zen_0 \sinh\frac{ze\psi}{kT}.\end{aligned} \tag{B.16}$$

Once this charge density expression is input into Poisson's equation, a solution for the potential (after applying appropriate boundary conditions at $x = \infty, \frac{d\psi}{dx} = 0$ and at $x = 0, \frac{d\psi}{dx} = \psi_0$) is written as [3],

$$\psi = \frac{2kT}{ze}\ln\frac{(1 + \gamma\exp[-\kappa x])}{(1 - \gamma\exp[-\kappa x])}, \tag{B.17}$$

where κ is the reciprocal of the double layer thickness ($\frac{1}{d}$) and is written as,

$$\kappa = \left(\frac{2e^2 n_0 z^2}{\varepsilon kT}\right)^{\frac{1}{2}}, \tag{B.18}$$

and γ is defined as,

$$\gamma = \frac{\exp\left[\frac{ze\psi_0}{2kT}\right] - 1}{\exp\left[\frac{ze\psi_0}{2kT}\right] + 1}. \tag{B.19}$$

This expression for the potential can be computed with appropriate distances to find the zeta potential. In practice, the location of the shear plane is not known. The Stern plane is thus used as an initial estimate when deriving the zeta potential analytically. Due to the decay of potential with distance, ζ is slightly less than ψ_s as the shear plane is located a short distance away from the solid surface.

As the volume charge density in the liquid is a result of electrostatic attraction of counter-ions towards the surface, it follows that solid surface charge density and liquid charge density are connected. The relationship is given as [3],

$$q = (8n_0\varepsilon kT)^{\frac{1}{2}}\sinh\frac{ze\psi_0}{2kT} \tag{B.20}$$

B.3 Langevin equation

The motion of a particle under the influence of the forces considered can be described using the Langevin equation i.e. Newton's equation of motion with additional terms for linear dissipation and stochastic forces. The Langevin equation is thus described as [4],

$$m\frac{\mathrm{d}v}{\mathrm{d}t} = F_{\mathrm{ext}} - fv + F_{\mathrm{r}}(t), \tag{B.21}$$

where F_{ext} refers to external forces, fv is the friction/viscous force and $F_{\mathrm{r}}(t)$ is the stochastic thermal force.

Two further properties of the thermal force are needed to fully describe the Langevin equation. These are:

$$< F_{\mathrm{r}}(t) >= 0 \tag{B.22}$$

$$< F_{\mathrm{r}}(t)F_{\mathrm{r}}(t') \geq B\delta(t-t') \tag{B.23}$$

$$B = 2fkT,$$

where f is the coefficient of friction, k is Boltzmann's constant, and T is the surrounding temperature.

The first property is a function of the random nature of thermal induced collisions, such that over time, the average of this force is zero. The second property describes the independent nature of collisions separated in time.

The expression when $F_{\mathrm{ext}} = 0$ describes the Brownian/diffusive motion of a particle. Dividing both sides of the equation by m gives a differential equation for the thermal induced velocity of a particle:

$$\frac{\mathrm{d}v}{\mathrm{d}t} = \frac{1}{m}\big(-fv + \eta(t)\big). \tag{B.24}$$

Solving this equation shows that velocities are stochastic (as a result of the dependence on a stochastic thermal variable). Hence, in characterising the effects of Brownian motion, there is an uncertainty in the actual velocity of a specific particle and subsequently, the displacement of particles due to thermal energy which is gotten by solving the following integration:

$$x = x_0 + \int_0^t v(t')\mathrm{d}t', \tag{B.25}$$

where x_0 is the initial position of the particle and $v(t)$ is the velocity variable calculated using the Langevin equation. Solving this reveals particle displacement has a Gaussian distribution.

B.4 Crystal structure of lithium niobate

Lithium niobate can have either a hexagonal unit cell (the conventional notation used in the remainder of this discussion displayed in Figure B.2) or a rhombohedral one, depending on the chosen axis of orientation. In the hexagonal unit cell, the c axis is defined as the one about which the crystal has rotational symmetry which is the z axis in Cartesian notation. In Cartesian notation, the x axis can be chosen to be any axis orthogonal to the z axis (i.e. the minor axis). Once these have been chosen, the y axis is selected such that the crystal has right handed symmetry.

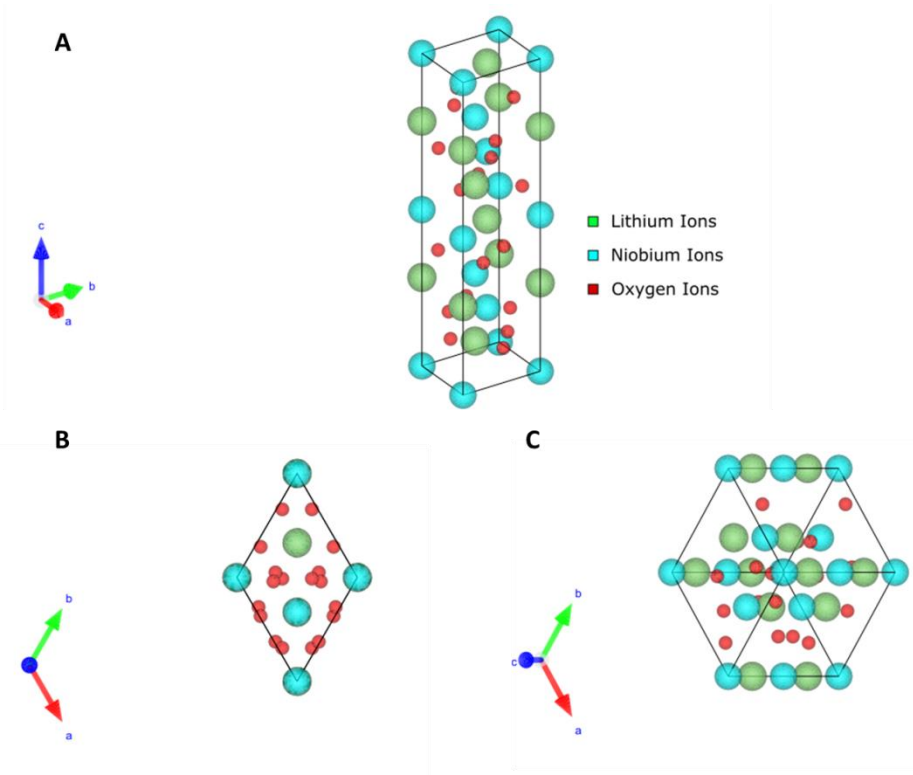

Figure B.2: Unit cell of lithium niobate Crystal plotted using Vesta with parameters from [5]**. A) Unit cell in three dimensions. B) Two dimensional projection showing origins of rhombohedral unit cell. C) Two dimensional projection showing origins of hexagonal unit cell.**

When in a crystal lattice, the oxygen atoms form octahedral layers, the interstitials of which are filled with lithium and niobium ions. It is the position of the lithium and niobium ions in respect to

the oxygen layers which gives rise to the pyroelectric effect in lithium niobate. In the paraelectric phase (above the Curie temperature: 1200 °C [5]), the positions of these ions are fixed (lithium lies in an oxygen layer a c/4 (c=1.38 nm [5]) axis away from niobium (Figure B.3)), and the crystal has no spontaneous polarisation. In the ferroelectric phase, the interstitials formed by the oxygen layers are filled a third each by lithium, niobium, and vacancies (due to the stoichiometry of lithium niobate) in the following configuration {…Nb,V,Li,Nb,V,Li,e.t.c}. Lithium and niobium ions are free to move in this configuration with the resulting charge separation causing the spontaneous polarisation.

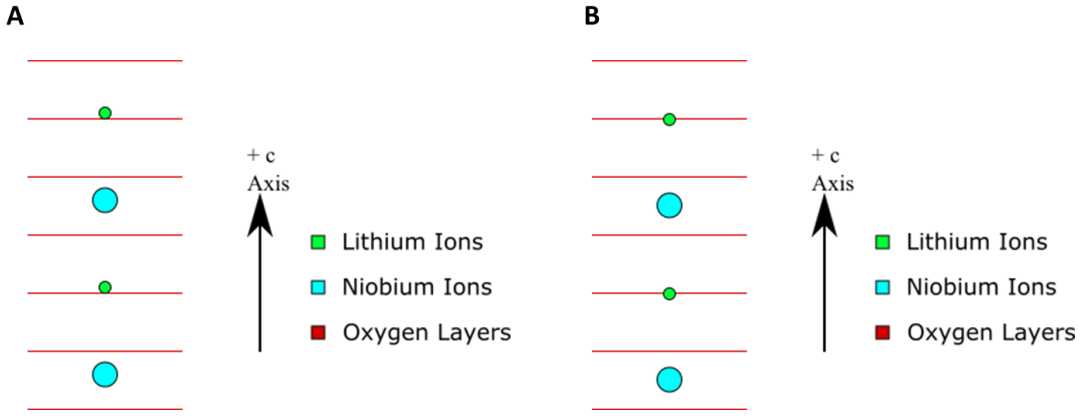

Figure B.3: Lattice configuration of lithium niobate [5]**. A) Ferroelectric phase of lithium niobate. B) Paraelectric phase of lithium niobate.**

The direction of the c axis is defined by how the crystal faces normal to it are polarised in response to heating (compression). The positive c direction is directed out of the +c face i.e. the face which becomes more negative upon heating; as the crystal is heated (becomes more compressed), lithium and niobium ions move closer to their paraelectric positions reducing the polarisation of the crystal. As a result, there is an excess of negative screening charge at the +c face (the converse is true for the cooling behaviour).

B.4.1 Crystal cut

The orientation of the Cartesian axes of a unit cell in relation to a lithium niobate wafer defines its cut. Under the normal definition, the z axis of a wafer is perpendicular to the face with the largest surface area (i.e. the flat face of the wafer), i.e. the length of the z direction is synonymous with the thickness of the crystal. x and y directions are orthogonal to the z axis in such a manner as to form a set of right handed symmetry. The cut of the lithium niobate wafer is defined by which of

the wafer's axes is parallel to the c axis of a unit cell (e.g. the z axis of a z cut lithium niobate wafer is parallel to the unit cell's c axis).

The cut of the wafer has important repercussions on the ability to generate the pyroelectric effect. As has been seen, spontaneous polarisation is due to the displacement of lithium and niobium ions in relation to the oxygen layer, as a result of contractions of the unit cell. In the simplest consideration of these contractions, motion is decoupled in the dimensions. In this case, it can be shown that when these contractions are applied perpendicular to the c axis, they compress and expand the oxygen layers and have no effect on the relative position of the lithium and niobium ions. Hence, it would appear that there is no pyroelectric effect when non z-cut crystals are used. Though coupling of motion is not forbidden, z cut crystals remain optimal for producing the pyroelectric effect.

B.5 References

[1] T. B. Jones, *Electromechanics of Particles*. Cambridge University Press, 1995.

[2] H. A. Pohl, *Dielectrophoresis: The behaviour of neutral matter in nonuniform electric fields*. Cambridge University Press, 1978.

[3] D. J. Shaw, *Introduction to Colloid and Surface Chemistry*. Butterworth-Heinemann, 1992.

[4] T. Tome and M. J. de Oliveira, "Langevin Equation," in *Stochastic Dynamics and Irreversibility*, Springer International Publishing, 2015, pp. 43–71.

[5] R. Weis and T. Gaylord, "Lithium niobate: summary of physical properties and crystal structure," *Appl. Phys. A*, vol. 203, pp. 191–203, 1985.

Appendix C Instrument operation

C.1 Hitachi S4700-SEM

Visual inspection of fabricated plasmonic structures was performed using a scanning electron microscope- the Hitachi-S4700. The minimum resolution of an optical microscope is dictated by the diffraction limit given by Equation (4.7), which dictates that practically speaking, features of below ~200 nm cannot be resolved using conventional optical microscopy.

The electron microscope operates due to the wave particle duality of the electron, (an elementary particle). Its wavelength is given by the de Broglie equation as,

$$\lambda = \frac{h}{mv}, \tag{C.1}$$

where h is Planck's constant, m is the mass of the electron, and v its velocity which is related to accelerating voltage by:

$$v = \sqrt{\frac{2eV}{m}}, \tag{C.2}$$

where V is the accelerating voltage and e is the charge of an electron.

Due to the low mass of electrons, their wavelength in comparison light is greatly reduced. In addition, these wavelengths can be controlled by adjusting the acceleration voltage. For acceleration voltages in the 10^2 kV range, wavelengths in the pm range are possible (compared to 100 nm typical of photonic illumination). Electron beam wavelength does not significantly exceed this value due to the increased significance of relativistic effects as electron velocity increases [1]. The resolution of electron microscopes is in the region of nanometres; lower than typical microscopes, but higher than dictated by the Rayleigh limit, due to defects from objectives [1].

In the Hitachi S4700, electrons are produced by applying the acceleration voltage to a cold cathode tungsten tip and are focussed using an electromagnetic objective lens. An image of the specimen is produced by raster scanning the electron beam over the sample

The micrograph is constructed by detecting the secondary and back scattered electrons resulting from the interaction between the electron beam and the sample [1]. The SEM has two detectors: one positioned behind the objective (through the lens) and one next to the sample.

To reduce charge build up (which causes beam deflections and adversely affects the operation of SEM [1]) and enhance contrast, insulating materials, such as glass, are coated with a thin layer of metal to increase their surface conductivity prior to observation in the SEM.

C.2 Vistec VB6 and Belle

Electron beam lithography is similar in principle to photolithography. Features are patterned by exposing a resist (chemically active material sensitive to electromagnetic stimulation) coated substrate to appropriate excitation which defines the desired pattern. Following exposure, unaltered resist is removed by chemical development. The patterned substrate undergoes further processing as necessary (such as dry and wet etching, metallisation). Electron beam lithography is capable of creating smaller features than photolithography (nm vs μm) due to the smaller wavelength associated with electronic stimulation.

Electron beam lithography is a direct write process (i.e. no mask is used); the electron beam is scanned over a route determined by software containing the CAD pattern. The Vistec VB6 is a vector scanning tool. The electron beam only writes and travels to positions defined by software. The tool is thus capable of higher resolutions in comparison to raster scanning instruments (electron beam travels everywhere but is selectively blanked to write in correct positions).

The VB6 accelerates electrons at 100 kV through a minimum spot size of 4 nm and writes 1.2 mm wide fields by electron beam deflection. Stage moves are required to create patterns larger than 1.2 mm. Stitching is required to accurately pattern geometries which traverse two 1.2 mm wide fields. The VB6 has a 15 nm stitch accuracy.

The final undiscussed parameter is the electron beam dose which is the charge required to expose the resist, such that it is fully altered, to reveal the defined geometry. This is selected in belle, and is measured in units of μC/cm.

Designs of geometric patterns created in the CAD tool, L-Edit, are fractured into a series of trapezoidal pixels more representative of the electron beam spot. The resolution of the final patterned object is dependent on the beam spot size and the number of pixels used to create, a function of the beam step size,

$$BSS = VRU \times Resolution, \quad \text{(C.3)}$$

where resolution is 1.25 nm (the minimum stepping resolution of the electron beam).

The VRU (variable resolution unit), and spot size are also selected in belle to maximise the writing speed while ensuring resolution is acceptable.

A final factor which affects patterning resolution is electron scattering. As a result of this effect, patterned resist is broader in dimensions than the electron spot. This broadening causes features to lose their definition (the gap between closely spaced features such as bowties can be removed as a result of this broadening). The effects are mitigated by increasing the electron beam energy and reducing the thickness of resist layers when fabricating small features. A proximity error correction algorithm can also be applied when is being fractured. This modifies the dose close to the edges so that the exposed area matches the CAD pattern. The distribution of the dose is calculated using simulated results of electron scattering in the appropriate resist-substrate combination.

C.3 Plassys MEB 400s

Evaporation of gold, titanium and aluminium was carried out using either the Plassys MEB 400s or the MEB 550s electron beam evaporator (schematic illustration in Figure C.1) in the James Watt Nanofabrication Centre. Though the capabilities of both tools differ (different metals are available for evaporation in each tool, the Plassys MEB 550s has an ion gun for substrate cleaning and etching; maximum substrate size is bigger on the MEB 550s tool), they operate in identical manners when evaporating the aforementioned metals.

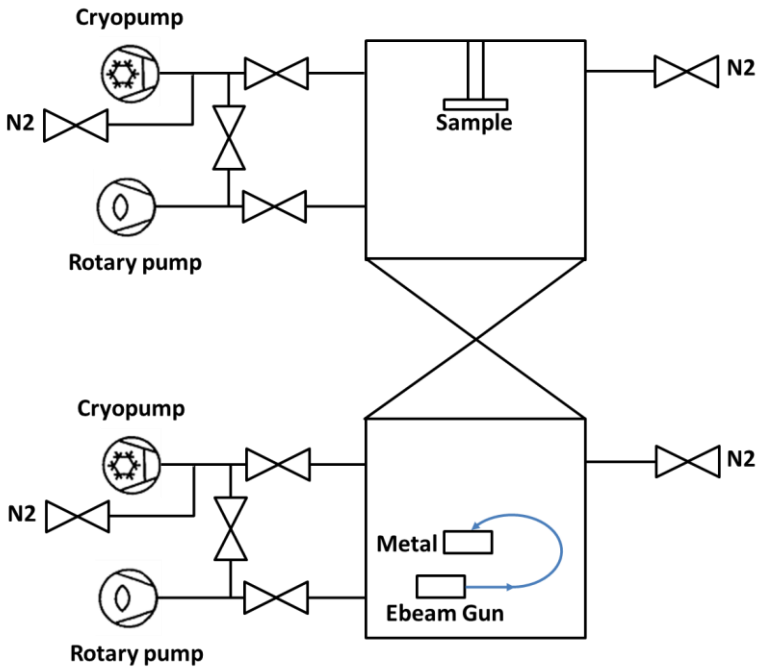

Figure C.1: Block diagram of Plassys tool.

Samples are placed in the sample chamber which is subsequently evacuated to a pressure of ≤ 2 × 10^{-6} mbar using first a rotary pump and then a cryopump. Evaporation is performed in a high vacuum environment to maximise the mean free path of the particles. This is required to be longer than the distance between the sample and the metal crucible (~30 cm) to ensure metal vapours reach the target unimpeded. The high vacuum environment also reduces the build-up of contaminant (e.g. oxide) layers which hinder the ability to deposit multiple layers of metal on each other. A high powered electron beam from a 10 kW source heats up the metal to vaporisation. The evaporation rate is monitored using a quartz crystal device. Once this is stable (between 0.3 and 0.5 nm/s depending the metal being evaporated), the shutter masking the metal crucible from the substrate is opened, allowing metallisation. The substrate is rotated during evaporation ensuring even metal coverage. Control of the Plassys (evaporation rate, metal thickness, beam current) is fully automated ensuring repeatability between different runs.

C.4 Malvern Zetasizer ZS90

The Malvern Zetasizer is a multifunctional tool which uses appropriate spectroscopic techniques to measure size, zeta potential, and molecular weight of colloidal particles. Only the first two parameters are measured with this tool in the course of the thesis. The mode of operation is determined using software. Appropriate experiment parameters (temperature, refractive index)

are selected in the accompanying software. Operational principles and instrument configuration are detailed below.

C.4.1 Size

Size measurements are performed using dynamic light scattering. Laser illumination of an ensemble of colloidal beads produces a characteristic speckle pattern due to the interference of light scattered by individual particles. As the particles are undergoing Brownian motion, this speckle pattern fluctuates in intensity with a characteristic delay time as different particles change in position. An auto correlator is used to compute the specific relationship between rate of fluctuation and particle diameter. The intensity signal is compared against itself at varying defined time points. For short delay times, the change in particle position is small, thus, the intensity of the speckle pattern is near identical for adjacent time points, and the autocorrelation coefficient ~1. At longer delay times, the change in particle position is greater, and the autocorrelation coefficient is zero (i.e. there is no relationship between the signals compared at the times indicated).The delay time is a function of the particle's diffusivity given by the Stokes-Einstein equation:

$$d_{\mathrm{H}} = \frac{kT}{3\pi\eta D}, \tag{C.4}$$

where k is Boltzmann's constant, T is the temperature in Kelvin, η is the viscosity of the dispersant solvent, d_{H} is the particle's hydrodynamic diameter, and D is its diffusion coefficient. These parameters must be noted for accurate calculation of the size of particles in a sample.

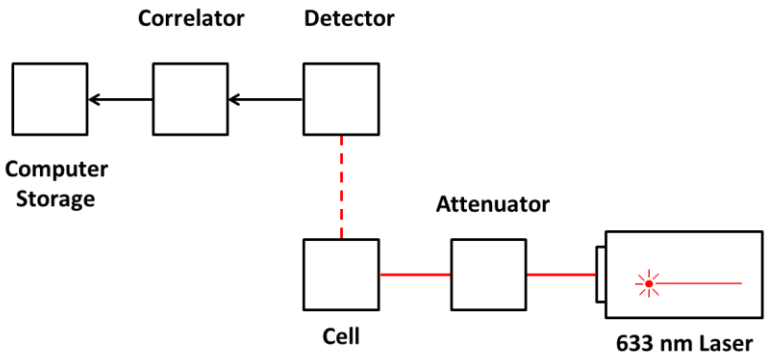

Figure C.2: Dynamic Light Scattering Block Diagram [1].

Figure C.2 is a general block diagram of a dynamic light scattering experiment in the Malvern Zetasizer instrument. Laser light is passed through an attenuator to the cell containing the samples. The attenuator position is adjusted automatically using software to ensure scattered light intensity is able to produce a resolvable signal from the detector. The detector is positioned at 90° from the cell and consists of a photomultiplier (which converts scattered intensity to a voltage) and filter circuits. The electronic signal is relayed to the correlator, a digital signal processing unit which creates a function relating fluctuations in intensity to change in time. Finally, this function is passed on to the program in computer storage for analysis.

C.4.2 Zeta potential

Zeta potential is calculated by measuring the electrophoretic mobility of a sample using phase analysis light scattering, an interferometric technique based on laser Doppler velocimetry. Laser illumination is split into an incident beam, which illuminates a sample of colloidal particles, and a reference beam. Light scattered by the incident beam (at a 17° angle [1]) is heterodyned with the reference beam producing an interference pattern. Similar to dynamic light scattering, the interference pattern evolves with time. The characteristic frequency of this evolution is proportional to particle velocity. Rather than this being governed by Brownian motion, it is controlled by the electrophoretic mobility of colloidal particles, as samples are placed in a cell through which an electric field flows. Using Henry's equation, the electrophoretic mobility can subsequently be used to calculate the zeta potential, and further, the surface charge density. These parameters are noted in computer software prior to analysis.

In the phase analysis technique, the position of the reference beam is modulated at a characteristic frequency. Hence, rather than calculating the velocity from the absolute interference evolution frequency, the frequency relative to the reference (i.e. the phase shift) is used, allowing for accurate estimation of the sign of the zeta potential. In addition, the Zetasizer performs consecutive measurements in high and low frequency electric fields, to distinguish between phase shifts caused due to electrophoretic mobility, and those resulting from electro-osmosis (i.e. charged cell walls).

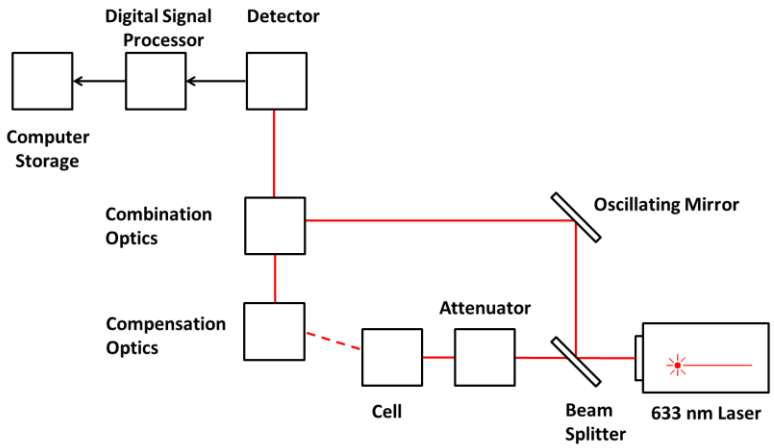

Figure C.3: Phase analysis Light scattering block diagram [1]**.**

Figure C.3 is a block diagram of the phase analysis light scattering technique. Laser illumination is split using a beam splitter to get a reference and a scattering beam. The position of the reference beam is modulated using the oscillating mirror. As with dynamic light scattering, an attenuator is used to control the intensity of scattered light ensuring a resolvable signal is observed by the detector. Compensation optics are required to correct for diffraction effects (as a result of cell wall thickness) and maintain the alignment of the scattered beam with the reference beam during optical mixing, which is performed using combination optics. The resulting interference pattern is converted to an electrical signal using the detector, which is processed and analysed using the digital signal processor, and the software in computer storage.

C.5 Shimadzu UV-3101 pc

Optical characterisation of fabricated plasmonic structures was carried out using a Shimadzu UV-3101 pc. As the tool is a double beam device, extinction measurements are carried out by comparing the intensity of light at the reference arm to that at the sensing arm. Results are displayed as a transmittance value (3.3) or a dimensionless absorption (3.4).

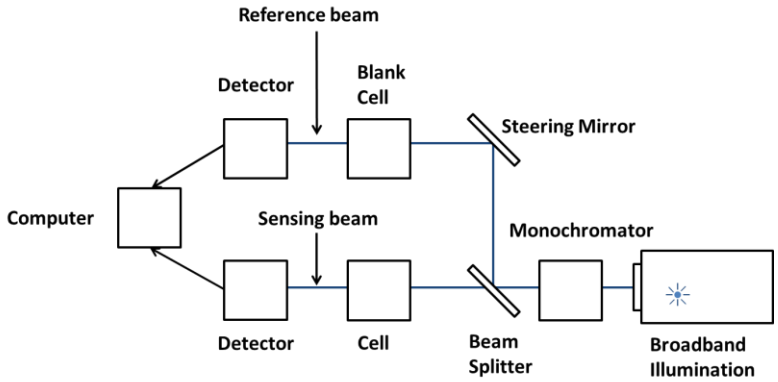

Figure C.4: Block diagram of dual-beam spectrophotometer

Figure C.4 is a block diagram of a typical dual beam device. Broadband illumination is decomposed into single wavelength using a monochromator. A beam splitter divides the coherent light into a reference and a sensing beam. The photodetectors measure the intensity of transmitted light.

The system consists of two light sources (Tungsten and Deuterium lamp), a grating-monochromator and two photodetectors to allow spectral characterisation in the 190–3200 nm range. The majority of measurements are performed in the visible region (400–800 nm) thereby removing mechanical artefacts due to switching of the grating, light source or detector. Of these three, only the wavelength at which grating change occurs is fixed (1792 nm). Light source and detector change occur in the 282–393 nm and 750–895 nm range, respectively, with the precise wavelength selected by the user.

C.6 References

[1] R. F. Egerton, *Physical Principles of Electron Microscopy: An introduction to TEM, SEM, and AEM*. New York: Springer Science, 2005.

[2] “Zetasizer Nano Series User Manual.” Malvern Instruments, 2004.

Appendix D Simulation parameters

D.1 Johnson and Christy values for gold and titanium refractive index

Refractive indices of gold and titanium in the visible wavelength range, as reported by Johnson and Christy, are tabulated below. A cubic spline interpolation method is used by COMSOL to find values at a specific wavelength.

Table D.1: Johnson and Christy refractive indices of gold and titanium [1], [2]

Wavelength (eV)	Refractive Index			
	Gold		Titanium	
	n	***k***	***n***	***k***
1.51	0.16	5.083	3.21	4.01
1.64	0.14	4.542	3	4.01
1.76	0.13	4.103	2.86	3.96
1.88	0.14	3.697	2.76	3.84
2.01	0.21	3.272	2.67	3.72
2.13	0.29	2.863	2.6	3.58
2.26	0.45	2.455	2.54	3.43
2.38	0.62	2.081	2.44	3.3
2.5	1.04	1.833	2.36	3.19
2.63	1.31	1.849	2.32	3.1
2.75	1.38	1.914	2.27	3.04
2.88	1.45	1.948	2.21	3.01
3	1.46	1.958	2.14	2.98
3.12	1.47	1.952	2.08	2.95

D.2 Sellmeier equations for lithium niobate refractive index

The temperature independent Sellmeier equation for the ordinary and extraordinary refractive indices of lithium niobate is given as [3],

$$n^2 = A_1 + \frac{A_2}{(\lambda^2 - A_3^2)} - A_4\lambda^2 \tag{D.1}$$

In this equation, λ is the vacuum wavelength in micrometres. The remaining coefficients are summarised in Table D.2.

Table D.2: Sellmeier coefficients for calculating ordinary and extraordinary refractive indices of lithium niobate [3]

	ordinary	extraordinary
A1	4.9048	4.582
A2	0.11775	0.09921
A3	0.21802	0.2109
A4	0.027153	0.02194

D.3 References

[1] P. B. Johnson and R. W. Christy, "Optical Constants of the Noble Metals," *Phys. Rev. B*, vol. 6, no. 12, pp. 4370–4379, 1972.

[2] P. B. Johnson and R. W. Christy, "Optical constants of transition metals: Ti, V, Cr, Mn, Fe, Co, Ni, and Pd," *Phys. Rev. B*, vol. 9, no. 12, pp. 5056–5070, 1974.

[3] G. J. Edwards and M. Lawrence, "A temperature-dependent dispersion equation for congruently grown Lithium Niobate," *Opt. Quantum Electron.*, vol. 16, no. 4, pp. 373–375, 1984.

Appendix E Patterning explanation

Quantitative measurement of line thickness is gotten by radially averaging the pixel intensity. Though key features can be gotten by taking an average across a line section, the degree to which they represent the totality of the image is dependent on $\mathrm{d}l$ (the fundamental line width), the position of the line and the uniformity of the patterned object. As the choice of where to place the line section becomes an arbitrary decision, the linear average collected becomes less representative of the entire image. If the linear mean intensity of the entire image is used, the signal to noise ratio of the patterned object needs to be sufficiently high to ensure pattern detection. To quantify pattern resolution, an approach based on the radial profile is used to simplify some of these concerns.

The radial profile of a region of interest from a pair of images recorded before the scanning process begins and after the scanning process is complete is obtained. The region of interest is defined such that the centre of the patterned object coincides with the centre of the region of interest. The radial profile plot algorithm plots the following function which is the average pixel intensity of all pixels at a distance r from the centre:

$$\overline{f(r)} = \frac{\mathrm{d}l}{2\pi r}\int f(r,\theta)\mathrm{d}\theta, \tag{E.1}$$

where $f(r,\theta)$ is a function describing the pixel intensity at a specific polar coordinate where r is distance from the centre and $\mathrm{d}l$ is the pixel width such that $\frac{\mathrm{d}l}{2\pi r}$ is the number of pixels in a circle of radius r. The radial profile plot is thus a measure of the average pixel intensity of a series of concentric circles enclosing the centre of the region of interest.

Before stimulation, particles are randomly distributed i.e. there is no correlation between radial distance and integrated pixel intensity. The mean of the above function, when calculated with the relevant image (i.e. before stimulation), is used as a measurement of the initial concentration of the particles. An enrichment factor (which is the measurement of line thickness) is defined as follows:

$$EF = \frac{\overline{f(r)_{\mathrm{after}}} - \overline{f_{\mathrm{before}}}}{\overline{f_{\mathrm{before}}}} \tag{E.2}$$

A negative enrichment factor is indicative of depletion i.e. less particles are found in this position after stimulation than they are before.

Appendix F Simulating stochastic motion

F.1 Discretising the Langevin equation

The trajectory of a particle, which exhibits stochastic motion, can be simulated using iterative processes to compute the Langevin equation for the position of the particle at different points in time. For simplicity, the overdamped Langevin equation is considered, such that inertial contributions are ignored [1], [2]. In this case the Langevin equation is,

$$fv = F_{\mathrm{ext}} + F_{\mathrm{r}}(t), \tag{F.1}$$

where f is the frictional coefficient of the particle, v is the velocity of the particle, F_{ext} is the external force, and $F_{\mathrm{r}}(t)$ is the stochastic thermal force.

By noting that $v = \frac{\mathrm{d}x}{\mathrm{d}t}$, (F.1) can be written equivalently as,

$$\frac{\mathrm{d}x}{\mathrm{d}t} = \frac{1}{f}\big(F_{\mathrm{ext}} + F_{\mathrm{r}}(t)\big). \tag{F.2}$$

(F.2) is discretised as follows:

$$\frac{x_{\mathrm{n}} - x_{\mathrm{n-1}}}{\Delta t} = \frac{1}{f}\left(F_{\mathrm{ext}} + \frac{F_{\mathrm{r}}}{\sqrt{\Delta t}}\right), \tag{F.3}$$

due to the properties of the thermal force [3].

Hence, the sequence generator which provides the new position of a particle is:

$$x_{\mathrm{n}} = x_{\mathrm{n-1}} + \frac{F_{\mathrm{ext}}}{f}\Delta t + \frac{F_{\mathrm{r}}}{f}\sqrt{\Delta t}. \tag{F.4}$$

From [3] (as a consequence of the properties described by (B.22) and (B.23)), the stochastic thermal force is defined by a Gaussian distribution, scaled by $\sqrt{2fkT}$. (F.4) can thus be written as,

$$x_{\mathrm{n}} = x_{\mathrm{n-1}} + \frac{F_{\mathrm{ext}}}{f}\Delta t + \sqrt{2D\Delta t}\, w_{\mathrm{n}}, \tag{F.5}$$

where D is the diffusion coefficient given by (2.39), the Stokes-Einstein equation, and w_{n} is a random number generator with a Gaussian distribution.

To ensure the simulation is valid, Δt is selected such that it lies in the following range [1]:

$$\frac{m}{f} < \Delta t < \frac{f}{k'} \tag{F.6}$$

where m is the mass of the particle, and k is a scalar potential which can be used to describe the external force. Δt is thus required to be greater than the momentum relaxation time but smaller than the characteristic time scale of the external force [1].

F.2 Matlab script simulating bead motion in an optical trap

```
close all
clear all
clc

% Simulation parameters
SPACE_UNITS = '\mum';
TIME_UNITS = 's';
N_PARTICLES = 5;

% Particle parameters
b_r = 1.5e-6;              % bead radius (m)
eta = 54e-3;               % viscosity (Pa.s)
kb = 1.38e-23;             % Boltzmann's constant (J/K)
T = 300;                   % Temperature (K)
gamma = 6*pi*eta*b_r;      % Friction coefficient
rho =2.06e6;               % silica bead density (g/m^3)
m = rho*(4/3)*pi*b_r^3;    % mass of silica bead
tau = m/gamma;             % Momentum relaxation time
D = kb*T/gamma;            % Diffusion Coefficient (m^2/s)
k = 1e-6;                  % trap stiffness (N/m)
phi=gamma/k;               % Trap time scale
dt =66e-3;                 % time step (s)
```

```
x_bar=sqrt(2*D*dt); % Thermal scale factor

N_TIME_STEPS = 1e3;

tracks = cell(N_PARTICLES,1); % Array of particle positions

x0=0;
y0=0;
ini= [x0 y0]; % Trap centre

for i= 1: N_PARTICLES
    time= (0:N_TIME_STEPS-1)' * dt;
    X=zeros(N_TIME_STEPS,2);
    X(1,:)= [0 0];  % Initialise position such that particle is in trap at the
                    % beginning of simulation


        for j= 2:N_TIME_STEPS
            dX_brownian = x_bar*randn(1,2);    % Compute stochastic deviation
                                               % using Gaussian pseudorandom
                                               % number generator
            dX_directed = (-k*dt*(X(j-1,:)-ini))/gamma; % Compute deterministic
                                                        % motion
            dX= dX_brownian +dX_directed;      % Compute total change in position
            X(j,:)=X(j-1,:)+dX;                % Update position
        end

        X=1e6*X;                          % Convert from m to µm
        tracks{i} = [time X];             % Save computed trajectory
        scatter(X(:,1),X(:,2),2,'.b');  % Plot computed trajectory
        hold all
end

axis equal

xlabel('x (\mum)','FontSize',14); % Label x axis
ylabel('y (\mum)','FontSize',14); % Label y axis
```

F.3 Matlab script simulating bead approach to optical trap

```
close all

clear all

clc


% Simulation parameters

SPACE_UNITS = '\mum';

TIME_UNITS = 's';

N_PARTICLES = 20;

N_TIME_STEPS = 450;

SIZE = 150e-6;

tracks = cell(N_PARTICLES,1);


% Particle parameters

b_r= 1.5e-6;              % bead radius (m)

eta=109e-3;               % viscosity (Pa.s)

kb= 1.38e-23;             % Boltzmann's constant (J/K)

%T=317;                   % Temperature (K)

gamma= 6*pi*eta*b_r;      % Friction coefficient

rho=2.06e6;               % silica bead density (g/m^3)

m= rho*(4/3)*pi*b_r^3;    % mass of silica bead

tau= m/gamma;             % Momentum relaxation time

dT = 0.066;               % time step (s)


% External force parameters

b_str= num2str(1e6*b_r*2);

fname= strcat('spatial_variation_FDEP_x_',b_str,'um.txt');
```

```
T= importdata('spatial_variation_T_x_1um.txt'); % Import temperature distribution
T= T.data;                                       % Import temperature distribution
Tr=fit(T(:,1),T(:,2),'SmoothingSpline');         % Interpolate temperature
                                                 % distribution
F_DEP=importdata(fname);   % Import force field
F_DEP=F_DEP.data;          % Import force field
k=diff(F_DEP(:,2))./diff(F_DEP(:,1));          % Convert force to potential
kr=fit(F_DEP(1:199,1),k,'SmoothingSpline');    % Interpolate potential


phi=gamma/max(abs(k)); % Minimum trap time scale


x0=75e-6;
y0=75e-6;
ini= [x0 y0]; % Coordinates of trap centre


for i= 1: N_PARTICLES


    time= (0:N_TIME_STEPS-1)' * dT;
    X=zeros(N_TIME_STEPS,2);
    X(1,:)= SIZE.*rand(1,2);      % Randomise initial particle position
                                  % using uniform pseudorandom
                                  % number generator
    r=sqrt(((X(1,2)-y0)^2)+((X(1,1)-x0)^2));   % Find radial distance
                                               % to trap centre
    D = kb*Tr(r)/gamma; % Position dependent diffusion Coefficient m^2/s
    x_bar=sqrt(2*D*dT); % Thermal scale factor


        for j= 2:N_TIME_STEPS
            dX_brownian = x_bar*randn(1,2); % Compute stochastic deviation
```

```
                                        % using Gaussian pseudorandom
                                        % number generator
            dX_directed = (-kr(r)/gamma)*(X(j-1,:)-ini)*dT; % Compute
                                                    % deterministic
                                                    % deviation
            dX= dX_brownian +dX_directed; % Compute total change in position
            X(j,:)=X(j-1,:)+dX;                     % Update particle position
            r=sqrt(((X(j,2)-y0)^2)+((X(j,1)-x0)^2)); % Update radial distance
            D = kb*Tr(r)/gamma;                     % Update diffusion
                                                    % coefficient
            x_bar=sqrt(2*D*dT);                     % Update thermal scale
                                                    % factor
         end


        X=1e6*X;                % Convert from m to µm
        tracks{i} = [time X];   % Save trajectory
end


ma = msdanalyzer(2, SPACE_UNITS, TIME_UNITS);  % Initialise msdanalyzer
ma = ma.addAll(tracks);                        % Add all trajectories
ma.plotTracks                                  % Plot trajectories
ma.labelPlotTracks                             % Label plot
xlim([0 150]);                                 % Fix x axis maximum to 150 µm
ylim([0 150]);                                 % Fix y axis maximum to 150 µm
```

F.4 References

[1] G. G. Volpe, “Simulation of a Brownian particle in an optical trap,” *Am. J. Phys.*, vol. 81, no. 3, p. 224, 2013.

[2] M. Schmiedeberg, J. Roth, and H. Stark, “Brownian particles in random and quasicrystalline

potentials: how they approach the equilibrium.," *Eur. Phys. journal. E*, vol. 24, no. 4, pp. 367–377, 2007.

[3] T. Tome and M. J. de Oliveira, "Langevin Equation," in *Stochastic Dynamics and Irreversibility*, Springer International Publishing, 2015, pp. 43–71.